Quantum Optical Storage and Processing Using Raman Gradient Echo Memory

Mahdi Hosseini

A thesis submitted for the degree of
Doctor of Philosophy in Physics

Advisors: Prof. Ping Koy Lam
and Dr. Ben Buchler

Department of Quantum Science

Australian
National
University

May 2012

دور چون با عاشقان افتد تسلسل بایدش

Declaration

This thesis is an account of research undertaken between 20 October 2008 and 13 January 2012 at The Department of Quantum Science, Faculty of Science, The Australian National University, Canberra, Australia.

Except where acknowledged in the customary manner, the material presented in this thesis is, to the best of my knowledge, original and has not been submitted in whole or part for a degree in any university.

Mahdi Hosseini
May, 2012

Acknowledgements

"If I have seen further it is only by standing on the shoulders of giants."

Isaac Newton

I started my PhD in the group of Prof. Ping Koy Lam after people like Gabriel Hétet and Magnus Hsu had already poured sweat into establishing a stunning research lab. Gabriel, together with the rest of the team developed the theory of the Rb-based gradient echo memory technique and implemented the initial experiment. By the time I joined the group, we were in a stage where different ideas could be put into practice. I am grateful for all of the things that Gabriel taught me and the knowledge he passed on to me at the start of my PhD.

Ping Koy and Ben, I could not really ask for better supervisors. You are more than just advisors; you are amazing scientists, inspiring mentors and wonderful friends. Ben, I owe you a debt of gratitude that I will never really be able to pay back. I certainly benefited from your insight and expertise in the past years. Your patience and perfectly rational explanations showed me the way towards being a good scientist. Ping Koy, you always enlightened me through your broad knowledge and your deep intuitions about my project and what was necessary to achieve the project goals. I thank you for allowing me the space and freedom I needed to work and for continued support and guidance from day one. Nothing I say here can do any justice to what you did for me, but I hope you know how much I appreciate it all.

I admire greatly the support from Prof. Hans Bachor during my PhD. I am indebted to Joe Hope, Matthew Sellars, John Close, Nick Robins, and Graham Dennis for giving me the tools that turned out to be essential for my research, and for the valuable discussions throughout these years. Many thanks to my colleagues: Ben Sparkes, Geoff Campbell, and Daniel Higginbottom. I very much enjoyed working, sharing the lab, and laughing with you. I greatly appreciate the interactions and discussions I had with Stojan Rebic and Jason Twamley. I would also like to thank our great administrator, Amanda White, for her administrative help during the last months of my PhD. Sincere thanks to Ben Buchler, Ping Koy Lam, Ben Sparkes, Olivier Pinel, Julien Bernu, Milos Rancic, Ellen McIlveen, Geoff Campbell and Helen Chrzanowski for the time they took to read and comment on my thesis. Special thanks to the people of our office: Ben, Geoff, Helen, Olivier and Daniel; without you, I would never have been such an expert at chess and Carcassonne. The endless discussions we had in our office, and 10:30 free coffee we never missed were great distractions from work.

Genuine thanks to my affectionate parents for believing in me and for their limitless love and mental support. Lastly and most importantly, special thanks to my wonderful wife, Boshra, for always being there for me. Boshra, your encouragement, love and support are powerful sources of inspiration and energy. Without you, I would be a different person today.

Abstract

The non-interacting and high-speed nature of light makes it an ideal carrier of information that is essential for transmission of quantum information. Indeed, many proposals and demonstrations of quantum cryptography rely on the use of fibre-optic networks. Construction of a memory that can store light and preserve its quantum properties will be useful in a range of quantum information systems such as secure quantum communication and quantum computation. This is why a quantum memory for light is a remarkable objective.

The key to quantum memory is to store the probability amplitude of the possible outcomes of measurement but without measurement. An important criterion for a quantum memory is that the efficiency of the recall must exceed 50%. This is the crucial no-cloning limit for security of information, since it guarantees that nobody can access the information by copying it. This benchmark is important because any kind of deterministic amplification of quantum information is fundamentally impossible. On-demand retrieval of information and ability to controllably manipulate the quantum information are also important for quantum applications.

When light is absorbed by atoms, it is actually possible to reverse the absorption process. In our memory system: light is absorbed by an ensemble of atoms and, using careful conditioning and control, we can cause the stored light to be regenerated and released at a later time. This is done by applying a gradient of magnetic field along the atomic ensemble that is the basis for our optical memory. To recall the light we flip the sign of the gradient field. This kind of reversible absorption is called photon echo, hence the name of our scheme: The Gradient Echo Memory (GEM). This simple protocol is used in our experiment and can be applied to a range of different atomic systems.

We have extended the GEM protocol and experimentally implemented a memory using three-level atoms. We used an off-the-shelf Rb vapour cell operating above room temperature as the memory medium. In this realisation, we broke the efficiency record with 87% recall of the input light pulse. Moreover, through complete state tomography of coherent states we have demonstrated the ability of our memory to noiselessly store quantum states of light.

We have also demonstrated that the memory can store a string of pulses and then recall the pulses ondemand in arbitrary order allowing re-sequencing of the stored information. Furthermore, we have shown that pulses could be time-compressed, time-stretched or split into multiple smaller pulses and selectively recalled in several pieces. This technique enables the construction of an optical random-access memory for quantum information. Moreover, the scheme to manipulate the spectral properties of optical data, stored inside the memory, has been introduced. We have also investigated the possibility of obtaining large nonlinear phase shifts between single photons inside the memory. Such strong interactions can be used for the implementation of universal quantum gates.

Contents

Declaration iii

Acknowledgements v

Abstract vii

1 Introduction and Motivation 3

2 Theory of Atom-Light Interaction 9
2.1 Quantum Optics Theory . . . 9
2.1.1 Quantisation of field and energy . . . 10
2.1.2 Optical quadratures . . . 11
2.1.3 The Heisenberg uncertainty principle . . . 11
2.1.4 Quantum superposition and entanglement . . . 11
2.1.5 The density operator . . . 12
2.1.6 Quantum optical states . . . 15
2.1.7 Wigner function representation . . . 16
2.1.8 Detection of optical quantum states . . . 19
2.1.9 Photon statistics of optical states . . . 22
2.1.10 Maximum likelihood reconstruction in homodyne measurement . . . 23
2.2 Atom-light interaction . . . 24
2.2.1 Interaction with a two-level atom . . . 24
2.2.2 Dressed state picture . . . 26
2.2.3 Bloch sphere . . . 26
2.2.4 Spin and photon echo . . . 28
2.2.5 Free induction decay . . . 29
2.2.6 Adiabatic following . . . 30
2.3 Optical Bloch Equations . . . 30
2.4 Light interaction with a Λ-atom . . . 33
2.4.1 Electromagnetically induced transparency . . . 34
2.4.2 Raman scattering . . . 38
2.4.3 Light shift . . . 38
2.5 Summary . . . 39

3 Literature Review on Optical Storage 41
3.1 Delay and storage in optical waveguides . . . 41
3.1.1 Optical Fibres and Cavities . . . 41
3.1.2 Stimulated Brillouin Scattering . . . 42
3.1.3 Trapped light in a metamaterial waveguide . . . 44
3.2 Transmissive Atomic Memories . . . 45
3.2.1 EIT light storage . . . 46
3.2.2 Light storage using four wave mixing . . . 50

3.2.3 Off-resonant Faraday interaction . . . 51
3.3 Absorptive Atomic Memories . . . 53
3.3.1 Off-resonance Raman memory . . . 53
3.3.2 Pulse photon echo storage . . . 54
3.3.3 Controlled Reversible Inhomogeneous Broadening . . . 56
3.3.4 Atomic frequency comb . . . 58
3.4 Optomechanical light storage . . . 60
3.5 DLCZ protocol . . . 61
3.6 Summary . . . 64

4 Gradient Echo Memory; Theory and Experimental Techniques 67
4.1 Theoretical description of GEM . . . 68
4.1.1 Basic concepts . . . 68
4.1.2 Model . . . 68
4.1.3 Three-level atoms . . . 71
4.2 Atomic vapour properties . . . 75
4.2.1 ^{87}Rb Atomic level structure . . . 75
4.2.2 Broadening phenomena in atomic vapour . . . 76
4.2.3 Interaction of Rb with external magnetic fields . . . 84
4.3 Experimental techniques . . . 84
4.3.1 Experimental setup . . . 84
4.3.2 First observation of echo in warm vapour . . . 87
4.3.3 Slow light contribution . . . 89
4.3.4 Summary . . . 89

5 Light Storage in the Polariton Picture 91
5.1 The EIT dark-state polariton . . . 92
5.2 GEM Normal mode . . . 94
5.2.1 Steering of the GEM polariton . . . 95
5.2.2 Polariton-Polariton interaction . . . 98

6 Spectral Processing of Stored Light 101
6.0.3 Self-induced frequency shift . . . 101
6.1 Controlled frequency shifting . . . 104
6.1.1 Experimental observation of frequency shift . . . 105
6.2 Bandwidth manipulation . . . 106

7 Arbitrary Manipulation of Optical Bits 109
7.1 Time sequencing . . . 110
7.1.1 Arbitrary retrieval . . . 111
7.1.2 Optical conveyor belt . . . 113
7.2 Experimental Implementation . . . 113
7.2.1 Experimental results . . . 115
7.3 Backward retrieval and stationary light . . . 117
7.4 Conclusion . . . 123

8 High Efficiency Light Storage 125
8.1 Experimental arrangement . . . 125
8.2 High efficiency storage results . . . 126
8.2.1 Atomic decoherence . . . 128
8.3 Multi-pulse storage . . . 130
8.3.1 A pillar that pacifies the oceans . . . 131
8.4 Conclusion . . . 132

9 Atom-Light Interference 133
9.1 Introduction . . . 133
9.2 Method . . . 135
9.2.1 Time-domain interference . . . 135
9.2.2 Frequency-domain interference . . . 139
9.3 Summary . . . 140

10 Four-wave mixing in a double-Λ system under the GEM condition 143
10.1 FWM in double-Λ systems . . . 143
10.2 FWM and EIT in a dense atomic sample . . . 145
10.3 FWM and Raman absorption in a dense atomic sample . . . 146
10.3.1 Polarisation effects on FWM . . . 148
10.3.2 Angular dependency of FWM in a Doppler broadened medium . . . 149
10.3.3 The effect of inhomogenous broadening on FWM . . . 151

11 Introduction to Quantum Information Technology 155
11.1 Quantum Information Technology . . . 155
11.1.1 The quantum bit . . . 156
11.1.2 Quantum gates . . . 156
11.1.3 Quantum computation . . . 157
11.1.4 Quantum communication . . . 159

12 Quantum Measurements 165
12.1 Quantum performance prediction . . . 166
12.2 Experiment and method . . . 166
12.2.1 Noise measurement . . . 167
12.3 State Tomography . . . 169
12.3.1 Photon number distribution and Wigner function . . . 169
12.3.2 Fidelity Measurements . . . 170
12.3.3 T-V representation . . . 173
12.4 Conclusion . . . 174

13 Nonlinear Polaritonic Interaction 177
13.1 Introduction . . . 177
13.2 XPM between single photons inside nonlinear fibre . . . 179
13.3 XPM in EIT media . . . 180
13.4 XPM between light and atomic coherence . . . 181
13.4.1 GEM-based XPM experiment . . . 181
13.5 XPM between two stored photons . . . 184
13.5.1 Analytical solution . . . 185
13.5.2 Numerical simulation . . . 187

13.5.3 Quantum simulation . . . 188
13.5.4 Discussion . . . 189
13.6 Conclusion . . . 189

14 Summary, Conclusion and Future Direction 191
14.1 Summary and conclusion . . . 191
14.2 Future directions . . . 191
14.2.1 Observation of stationary light . . . 191
14.2.2 Simultaneous storage of two frequency sidebands . . . 192
14.2.3 Storage of a single photon, squeezing and entanglement . . . 192
14.2.4 GEM in dipole trap . . . 192

A Appendix A: Experimental details 193
A.1 Rb vapour properties . . . 193
A.2 Magnetic coil design . . . 193
A.2.1 Single coil design . . . 195
A.2.2 Multiple coil design . . . 196
A.3 Oven design for the filtering cell . . . 196
A.4 The effect of re-pumping on storage . . . 198
A.5 Combining and separating beams using ring cavities . . . 199
A.6 Optimum storage . . . 199

B Appendix B: AC Stark gradient echo memory in cold atoms 201
B.1 Introduction . . . 201
B.2 Scheme . . . 201

C Appendix C: XMDS programming 205
C.1 Sample XMDS script . . . 205
C.2 Sample XMDS2 script . . . 208

Bibliography 213

List of Figures

1 Room temperature quantum memory 2

1.1 Thesis structure 5

2.1 Wigner representation 17
2.2 No-cloning fidelity limit 19
2.3 Homodyne detection setu 19
2.4 Phase-insensitive heterodyne 21
2.5 Poisson distribution 22
2.6 Dressed picture 27
2.7 Bloch sphere representation 27
2.8 Sequences of spin echo in Bloch sphere representatio 28
2.9 Free induction decay 29
2.10 Three level atom 33
2.11 Susceptibility plot 37
2.12 Stokes and anti-Stokes Raman scattering 38

3.1 SBS data storage sequence 43
3.2 Rainbow storage 45
3.3 EIT storage 46
3.4 EIT pulse shaping 47
3.5 Storage of squeezing 48
3.6 Single photon storage using EIT 49
3.7 Delay of entanglement 51
3.8 Memory based on the off-resonant Faraday interaction 52
3.9 Storing entanglement in atomic spins 53
3.10 Three-pulse photon echo 55
3.11 Interference of echoes 56
3.12 Proposed AFC memory 57
3.13 AFC quantum projection measurements 59
3.14 Optomechanically induced transparency 60
3.15 DLCZ scheme 62
3.16 Entanglement between four atomic ensembles 63

4.1 Time-reversing atomic spin cartoon 67
4.2 GEM scheme 69
4.3 Bloch sphere representation of gradient echo technique 69
4.4 Efficiency plot of a two-level GEM system 71
4.5 Λ atom interacting with two laser fields 72
4.6 Quasi-two-level atom 73
4.7 Efficiency plot of Λ-GEM 75
4.8 Atomic level structure of ^{87}Rb and saturation absorption 76

4.9 EIT and Raman linewudth in a Doppler broadened medium 78
4.10 Crossing angle between optical and atomic beams 78
4.11 Angular dependency of EIT 80
4.12 Angular dependency of GEM 80
4.13 Magnetic coil configuration around the Rb cell 85
4.14 Experimental results of Raman and EIT lines 86
4.15 First result of photon echo generated using warm vapour cell 87
4.16 Slow light contribution 88

5.1 Plasmons in The Lycurgus Cup in the British Museum 92
5.2 EIT normal mode 93
5.3 GEM normal mode 96
5.4 Switching of GEM polariton 97
5.5 Level structure used for interference of atomic coherences 98
5.6 Interference of atomic coherences 99

6.1 Microscopic light storage 102
6.2 Frequency shift and gradient 103
6.3 Memory phase shift 104
6.4 Controlling frequency shift 105
6.5 Theoretical frequency shifting of echo 106
6.6 Experimental frequency shifting of echo 107
6.7 Bandwidth manipulation of echo signal 108

7.1 Optical conveyor belt 109
7.2 First in first out storage 111
7.3 Optical pulse sequencer 112
7.4 Setup for optical pulse sequencing experiment 114
7.5 FID and Raman line 115
7.6 Experimental FILO and FIFO storage 116
7.7 Experimental pulse sequencing results 117
7.8 Shape mirroring 118
7.9 Forward and backward propagating light in the EIT medium 119
7.10 Experimental setup for producing backward propagating echo 120
7.11 Forward and backward propagating light in the GEM medium 121
7.12 Stationary light in GEM system 122

8.1 Setup for hight efficiency storage experiment 127
8.2 Raman Absorption line and input-echo pulses in dense atomic medium . . . 128
8.3 Coupling field effect on efficiency and noise 129
8.4 20 pulse storage 130
8.5 Monkey King 131

9.1 Schematic representation of atom-light interference in the memory 134
9.2 Setup for RF signal preparation 135
9.3 Interference between electric field and atomic excitations 137
9.4 Interference shown in space-time 138
9.5 Atom-light interference fringes from time-based interference 138
9.6 Interference fringes from frequency-based interference 140

10.1 Four-wave mixing in double-Λ system . . . 144
10.2 FWM in EIT medium . . . 147
10.3 FWM in GEM medium . . . 148
10.4 General FWM scheme in Rb atoms . . . 149
10.5 Polarisation effect on FWM . . . 150
10.6 Amplification measured in GEM . . . 150
10.7 Angular dependency of FWM in GEM . . . 151
10.8 Inhomogenous broadening effect on FWM . . . 151
10.9 Probe and Stokes field inside broadened Raman line . . . 152

11.1 Qubit representation in Bloch sphere . . . 156
11.2 Implementation of Fredkin gate using a nonlinear medium . . . 157
11.3 CNOT gate . . . 157
11.4 Generation of Bell states using a Hadamard and a C-NOT gates . . . 157
11.5 Few implemented quantum computing devices . . . 158
11.6 General principles of an idealised quantum repeater . . . 160

12.1 Implied quantum memory performance for coherent state storage. . . . 166
12.2 Noise measuremnet . . . 167
12.3 Quadrature amplitude as a function of local oscillator phase . . . 168
12.4 Density matrix elements for input and output pulses . . . 170
12.5 Photon number distribution for input and output pulses . . . 171
12.6 Fidelity of the memory for various optical states . . . 172
12.7 T-V diagram for warm Rb memory . . . 174

13.1 Setup for implementing Fredkin gate and cluster states using XMP . . . 178
13.2 XPM in DEIT system . . . 181
13.3 XPM interaction level scheme . . . 182
13.4 XPM experiment setup . . . 183
13.5 XPM experiment . . . 184
13.6 Level scheme for XPM in memory . . . 185
13.7 Numerical simulation of nonlinear phase shift between single photons . . . 187

A.1 Atomic-level structure of ^{87}Rb . . . 194
A.2 Number density of ^{87}Rb . . . 194
A.3 Geometry of the solenoids . . . 195
A.4 Switching circuit . . . 196
A.5 Magnetic field of an eight-segmented coil . . . 197
A.6 Schematic design of oven for the filtering cell . . . 197
A.7 Experimental setup for backward propagating repumping beam . . . 198
A.8 Setup for combining and separating of sideband frequencies . . . 199
A.9 Fourier transform of an Raman line . . . 200

B.1 Proposed setup of the ac-Stark GEM . . . 203

List of Tables

4.1 Buffer gas-induced frequency shift 81

11.1 Quantum memory: state of the art 163

12.1 Experimental parameter table 173

A.1 ^{87}Rb physical properties 193

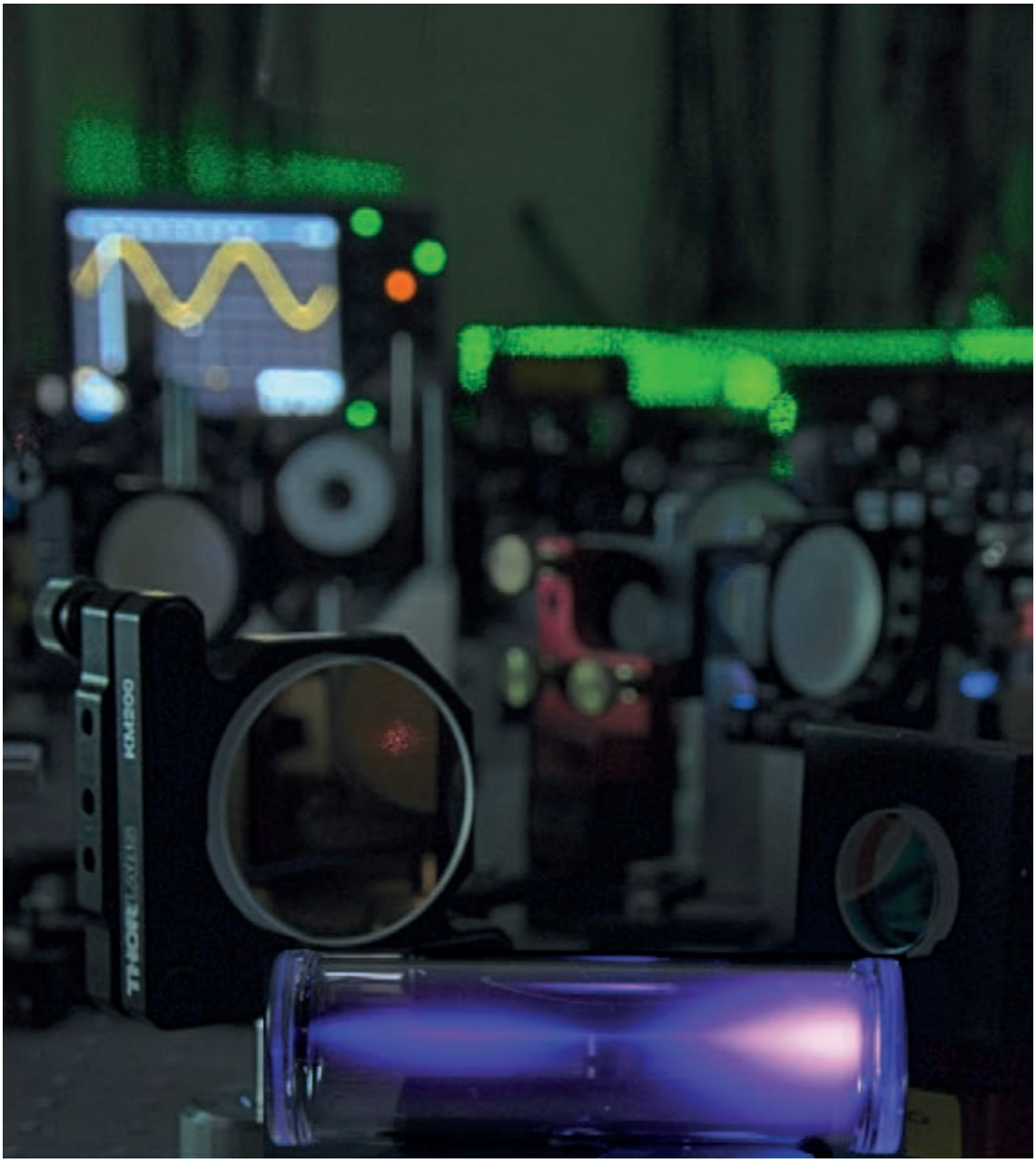

Figure 1: Thousands of kilometres of light conveying large amount of information can be stopped and stored coherently in a few-cm-long gaseous memory operating above room temperature.

Chapter 1

Introduction and Motivation

"I wanted to rock back and forth between myth and distant futures, yesterday, today, and tomorrow. It felt a bit like prophecy and a bit like storytelling".

George Murray (poet)

Storing information has been important to humanity since the time when the most sophisticated artificial memory was a cave wall. The evolution of human intelligence increases the need for more sophisticated memories every day. Nowadays we are surrounded by storage devices, such as hard disks, DVDs and phones. Information in all of our digital technology is encoded in a binary format (0s and 1s).

The non-interacting and high-speed nature of light makes it an ideal carrier of information. The bandwidth and versatility of optical devices has revolutionised communication in the past decades. In conventional optical information systems, data storage is not a problem. One can just detect the light and store the information in an electronic memory.

There is, however, a new frontier emerging: quantum information technology. Quantum information technology promises vastly more powerful computing and perfectly secure cryptographic systems, but there are complications. Principal amongst these is that one cannot record quantum information in a regular memory. A quantum memory must preserve the quantum properties of the information. Many proposals and demonstrations of quantum communication and computation rely on the use of photons for carrying quantum information. If we can construct a memory that could store light and preserve the quantum state of that light, then it will be directly applicable to a range of quantum information systems. This is why a quantum memory for light will prove a significant breakthrough. Apart from the intriguing applications, a coherent memory for the fastest particles in the universe is fundamentally interesting.

According to the Heisenberg uncertainty principle, performing measurement on a system will impact the state of the system. For instance, if quantum information is encoded into the amplitude and phase of photons, measuring amplitude or phase of even a small fraction of the photons will destroy the information. Therefore, unlike the conventional memories, storage of quantum information cannot be achieved by measuring the information and then storing the results of the measurement. The key to quantum memory is that, regardless of any factor, you can never know or measure what you have stored.

Another important criterion for a quantum memory is that the efficiency of the recall must exceed 50%. This is the crucial no-cloning limit for the security of information since it guarantees that the transmitted information cannot be stolen by secretly reading out the memory. Light can travel without absorption or loss for great distances in transparent media such as optical fibres. One way to store light is, therefore, to use an enormous coil of fibre. Such a device, while feasible, is just a delay line. For a useful optical quantum

memory we also require the ability to recall on demand and even to manipulate the information. The trick is to stop the light somehow and then release it later as required.

Atoms provide an ideal quantum interface for photonic interactions. The marriage of optics and atomic physics has initiated a wide range of applications in technology. The invention of the laser has revolutionised various aspects of technology. Interaction between atoms and light can be controlled in such a way as to manipulate the properties of one using the other. In particular, the ability to stop and manipulate photons using atoms has attracted a lot of interest in science and technology in the last decade.

A few milliseconds of laser light propagating in free space spreads over hundreds of kilometres of the space. Recent progress in scientific research has provided the power to compress and store such a long propagating optical field into a centimetre-long atomic memory. This is equivalent to a medium with a refractive index of millions. Furthermore, the properties of such a memory can be controlled externally in order to manipulate properties of the stored light. Using the electromagnetically induced transparency (EIT) technique, for example, the light can be slowed down a hundred million times from its vacuum speed. This is done by controllably tuning the refractive index of an atomic medium.

Furthermore, atoms can preserve the quantum nature of the light thanks to its coherent interaction with photons. Photons can carry information encoded, for example, into their different polarisation states. If the photon is in an equal superposition of horizontal and vertical polarisations of light, it means that, upon measurement, there is a 50% chance of finding the photon in the vertical polarisation, and a 50% chance of finding it in the horizontal polarisation. The only way that a classical memory (like a computer hard disk) can store such information is to perform a measurement first on the photon, find the polarisation of the photon, and store the final result of the measurement; therefore all classical memories in the market, at maximum, can store only 50% of quantum information. Conversely, a quantum memory can store the probability distribution of the photon polarisation states so that after storage the retrieved photons represent the same probability distribution as the input photons. In a quantum memory, information can be mapped into atomic coherence. In this example, the correlation between polarisation of photons can be imprinted into electrons inside atoms which are in a superposition of two atomic energy states. The stored information in the form of atomic coherence can be converted to an optical field and retrieved from the memory on demand.

The field of quantum information technology is one of the primary applications of quantum memory devices where storing information carrying quantum signatures is crucial to any step of information processing. Since photons are the best carriers of information, the need for an optical quantum memory has motivated many groups around the world to pursue its implementation. Substantial research has been dedicated to the development of quantum memory using various methods and resources. These will be summarised in Chap. 3.

In this thesis we investigate a promising technique for coherent manipulation and storage of optical pulses in an ensemble of warm Rb atoms. This scheme of optical storage is known as gradient echo memory (GEM). The structure of the thesis is schematically described in Fig. 1.1. The thesis is divided in to 3 parts. Part I includes a general introduction to light storage and contains 2 chapters. The basic concepts and background theory are introduced in Chap. 2. In Chap. 3, we provide a review on the optical storage and quantum storage literature. In Part II of the thesis containing 6 chapters dedicated to semi-classical light storage using GEM technique. In Chap. 4 we describe the theoretical

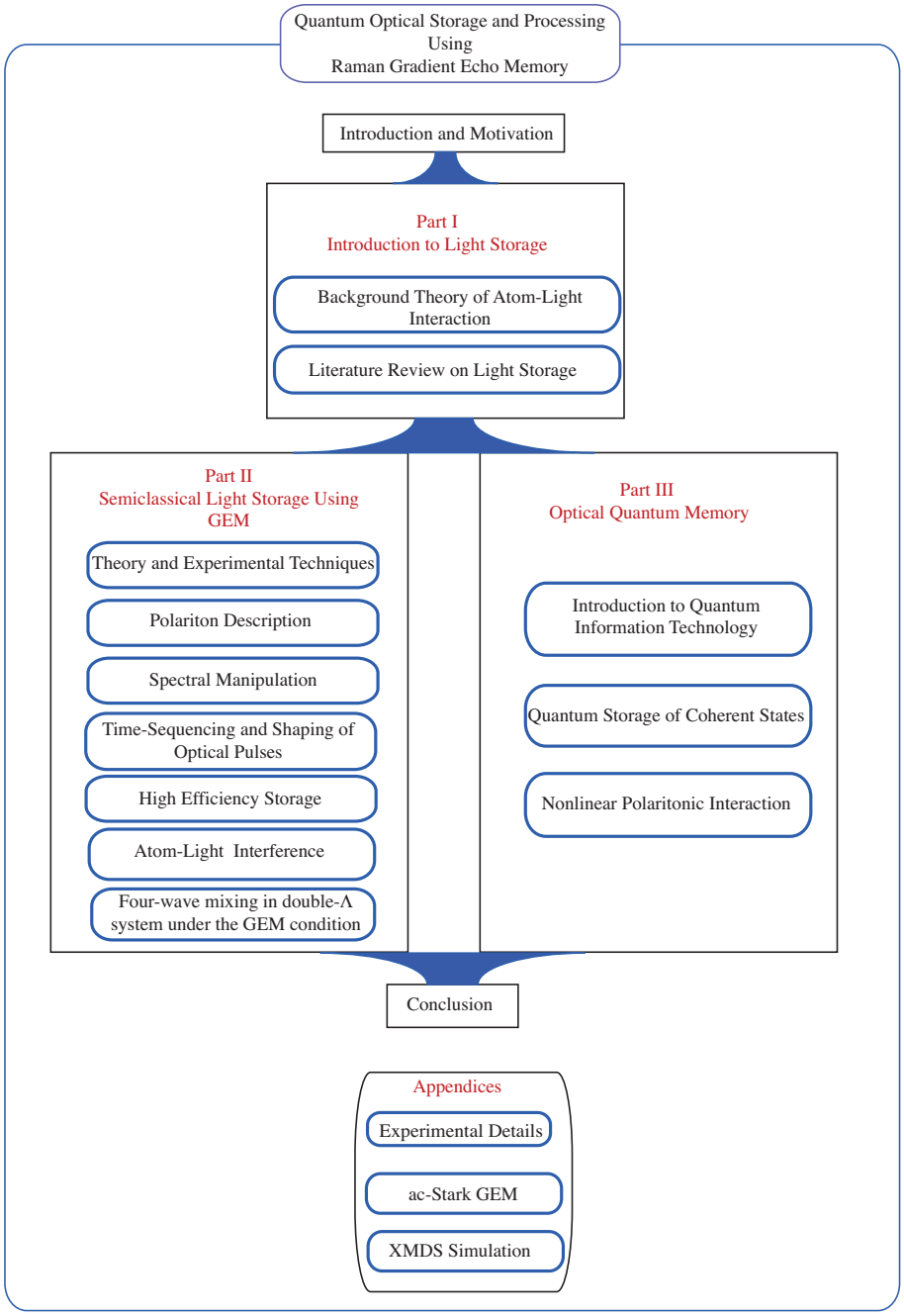

Figure 1.1: Thesis structure

framework and experimental methods required for light storage. In Chap. 5 we describe the physics of the system by associating a quasi-particle with the light-atom interactions inside the memory. In Chap. 6 we investigate the spectral manipulation that can be done on the input data pulses using GEM. In Chap. 7, we explain how the memory can be used as a pulse sequencer. The experimental evidence of high efficiency storage is provided in Chap. 8. Interference of atomic optical fields in the memory is studied in Chap. 9. We investigate the effect of four-wave mixing on storage using GEM in Chap. 10. Part III of the thesis includes 4 chapters in which we focus on quantum application of our memory system and we study quantum properties of the memory. In Chap. 11 we provide

an introduction to quantum communication technology and the motivation for quantum memory study. In Chap. 12 we study quantum storage of optical states. In Chap. 13 we investigate the possibility of non-linear cross phase modulation between two single photons inside the memory. Finally in Chap. 14 we provide an overall conclusion of the thesis.

The majority of this thesis has been published by, submitted to, or accepted for publication in international journals. Some selected articles resulted from the work done during my Ph.D. and included in this thesis are:

- Photon echoes generated by reversing magnetic field gradients in a rubidium vapor G. Hétet, M. Hosseini B. M. Sparkes, D. Oblak, P. K. Lam, and B. C. Buchler, Opt. Lett. 33 No.20, 2323 (2008).

- Coherent optical pulse sequencer for quantum applications M. Hosseini, B. M. Sparkes, G. Hétet, J. J. Longdell, P. K. Lam and B. C. Buchlerm Nature 461, 241-245 (2009).

- Precision spectral manipulation of optical pulses using a coherent photon echo memory B. C. Buchler, M. Hosseini, G. Hétet, B. M. Sparkes, P. K. Lam, Opt. Lett. 35, 1091 (2010).

- High efficiency coherent optical memory with warm rubidium vapour M. Hosseini, B. M. Sparkes, G. Campbell, B. C. Buchler, P. K. Lam, Nat. Commun. 2, 174 (2011).

- High Efficiency Gradient Echo Memory with 3-Level Atoms B. C. Buchler, M. Hosseini, G. Htet, B. M. Sparkes, J. J. Longdell, M. J. Sellars and P. K. Lam, AIP Conf. Proc. 1363, pp. 383-388; doi:10.1063/1.3630216 (2010).

- A Room Temperature Quantum Optical Memory M. Hosseini, B. Sparkes, G. Campbell, B. Buchler, and P. K. Lam, International Conference on Quantum Information, OSA Technical Digest (CD), paper QTuG1 (2011).

- Unconditional room temperature quantum memory M. Hosseini, G. Campbell, B. M. Sparkes, B. C. Buchler, P. K. Lam, Nat. Phys. 7, 794-798 (2011).

- Time and frequency domain polariton interference G. Campbell, M. Hosseini, B. M. Sparkes, P. K. Lam, and B. C. Buchler, New J. of Phys. 14, 033022 (2012).

- Light Storage and Manipulation using Raman Gradient Echo Technique M. Hosseini, B. M. Sparkes, G. Campbell, B. C. Buchler, P. K. Lam, Accepted for publication in J. Phys. B. (2011).

- Quantum Memory with Built-in Cross Phase Modulation M. Hosseini, B. M. Sparkes, S. Rebic , J. Twamley, B. C. Buchler, P. K. Lam, arXiv:1112.2010[quant-ph] (2011).

-A Room Temperature Quantum Memory M. Hosseini, G. Campbell, B. M. Sparkes, P. K. Lam and B. C. Buchler, in Proceedings of the International Quantum Electronics Conference and Conference on Lasers and Electro-Optics Pacific Rim 2011, (Optical Society of America, 2011), paper I354.

Other articles resulted from the work done during my Ph.D. are:

- ac Stark gradient echo memory in cold atoms B. M. Sparkes, M. Hosseini, G. Hétet, P. K. Lam, and B. C. Buchler , Phys. Rev. A 82, 043847 (2010).

- Experimental demonstration of coherent spectral manipulation of optical pulses using the gradient echo memory scheme B. M. Sparkes, C. Cairns, M. Hosseini, D. Higginbottom, G. Campbell, O. Pinel, P. K. Lam, and B. C. Buchler, Accepted for publication in Phys. Rev. X (2012).

- Spatial mode storage in a gradient echo memory D. B. Higginbottom, B. M. Sparkes, M. Rancic, O. Pinel, M. Hosseini, P. K. Lam, B. C. Buchler, arXiv:1204.3981 [quant-ph] (2012).

- Quantum benchmarking with realistic states of light N. Killoran, M. Hosseini, B. C. Buchler, P. K. Lam, and N. Lütkenhaus, arXiv:1205.1424 [quant-ph] (2012).

Part I
Introduction to Light Storage

Chapter 2

Theory of Atom-Light Interaction

"Whenever a theory appears to you as the only possible one, take this as a sign that you have neither understood the theory nor the problem which it was intended to solve."

Karl Popper

It is indeed possible to manipulate the external, as well as internal, degrees of freedom of atoms using photons. Understanding interactions between electromagnetic fields and atoms is fundamental for interpretation of various phenomena in nature. Particularly in this thesis, atom-light interactions are the main phenomena that govern the physics of the system and are thus crucial to introduce.

In this chapter we discuss the basic ideas and concepts required to understand how the laser field interacts with atomic systems. We start by looking at semi-classical and quantum properties of optical fields in Sec. 2.1. Interaction of light and atomic fields is considered in Sec. 2.2. For further information regarding the quantum optics theory and atom-light interactions I suggest Ref. [1, 2] to the reader.

2.1 Quantum Optics Theory

The field of quantum optics started in 1899 when Max Planck modelled blackbody radiation and found that light might be quantised. Later on, Bohr showed that the atomic energy levels were also quantised, in the sense that they could only emit discrete amounts of energy. Following these developments, there was a considerable amount of interest in the understanding of the interaction between light and matter that not only formed the basis of quantum optics but was also crucial for the development of quantum mechanics as a whole.

It is only quite recently that the quantum properties of laser light and its role in studying various aspects of quantum physics have been understood. Among the major breakthroughs made in quantum optics are squeezing, quantum non-demolition (QND) and entanglement, which have attracted a lot of interest in the past decade thanks to their application in quantum information technology [1] and quantum metrology [3].

The ability to generate and detect light with less quantum fluctuations than the vacuum (squeezed light) makes optics a fertile testing ground for quantum measurement theory. An ideal laser source emits a light field that has an amplitude and phase fluctuations identical to those of vacuum fluctuations. The amplitude or phase noise of a laser can be reduced below the shot noise (fluctuations of the number of detected photons) level so that the output of the laser may exhibit sub-Poissonian statistics (see Sec. 2.1.9). In other words, the amplitude or phase fluctuations may be reduced below the vacuum fluctuations. The generation of squeezed states requires a nonlinear phase-dependent interaction. In 1985 R.E. Slusher [4] first observed the squeezed states at the Bell Laboratories using four-wave mixing in atomic sodium. This was soon followed by demonstrations of squeezing in an optical parametric oscillator by H.J. Kimble [5] and by four-wave mixing in optical fibres by M.D. Levenson [6]. Squeezing, like photon anti-bunching, is a consequence of the quantisation of the light field. The application of squeezed light in optical interferometry was first demonstrated in experiments by Grangier [7], Kimble [5] and others.

The idea of QND is to measure the value of an observable without disturbing it, so that subsequent measurements can be made with equal accuracy as the first. Demonstrations of quantum non-demolition measurements have been achieved in optics in experiments by M.D. Levenson and P. Grangier [8].

Quantum entanglement is associated with the peculiar nonclassical correlations that are possible between separated quantum systems.

Below we introduce some basic concepts and theory of quantum optics that are required for the rest of the thesis.

2.1.1 Quantisation of field and energy

Quantum mechanics postulates that the electromagnetic (EM) field consists of discrete energy wave packets or photons. One way to derive the quantisation of the EM field is to use its equivalence to an infinite set of harmonic oscillators. Each harmonic oscillator is quantised using the canonical procedure [1]. Eigenstates of the Hamiltonian are states of definite energy satisfying

$$\hat{\mathcal{H}}|n\rangle = \hbar\omega(\hat{a}^\dagger\hat{a} + 1/2)|n\rangle = E_n|n\rangle \tag{2.1}$$

where the non-hermitian operators $\hat{a}^\dagger$ and $\hat{a}$ are defined by

$$\begin{aligned} \hat{a} &= 1/\sqrt{2m\hbar\omega}(m\omega\hat{x} + i\hat{p}) \\ \hat{a}^\dagger &= 1/\sqrt{2m\hbar\omega}(m\omega\hat{x} - i\hat{p}) \end{aligned} \tag{2.2}$$

where m and ω are effective mass and frequency of the oscillator. In the case of the electromagnetic field, the eigenstate of the energy is a representation of the field as a sum over modes at frequencies ω_i , each with a definite number n_i of excitations, or quanta. Therefore, the energy of the electromagnetic field can be written as

$$E = \hbar\sum_i \omega_i(n_i + 1/2) \tag{2.3}$$

In order to quantise the electromagnetic field one needs to solve the Maxwell equations for the electric (E) and magnetic (H) fields in terms of basis functions $e^{i(\mathbf{k}.\mathbf{r}-\omega_k t)}$. The electric and magnetic field operators, using the analogy of the harmonic oscillator, are given by

$$\begin{aligned} \hat{\mathbf{E}} &= \sqrt{\frac{\hbar}{2\epsilon_0 V}}\sum_k \epsilon_k\sqrt{\omega_k}\hat{a}_k u_k(r)e^{-i\omega_k t} + H.c. \\ \hat{\mathbf{H}} &= \sqrt{\frac{\hbar}{2\epsilon_0 V}}\frac{1}{c\mu_0}\sum_k (\hat{k}\times\epsilon_k)\sqrt{\omega_k}\hat{a}_k u_k(r)e^{-i\omega_k t} + H.c. \end{aligned} \tag{2.4}$$

where $u_k(r) = \frac{e^{i\mathbf{k}.\mathbf{r}}}{\sqrt{2\pi}}$ is the spatial mode, $\omega_k = c|k|$, V is the quantisation volume, and ϵ_k is a unit polarisation vector. The operator $\hat{\mathcal{E}}_k$ depends on mode k of the electromagnetic field, and V is the interaction volume. Each eigenstate $|n_k\rangle$ of the Hamiltonian satisfies

$$\hat{\mathcal{H}}_k|n_k\rangle = \hbar\omega_k(\hat{a}_k^\dagger\hat{a}_k + 1/2)|n\rangle \tag{2.5}$$

The term $\hat{a}_k^\dagger\hat{a}_k$ represent the total number of photons in the system. The factor of 1/2 accounts for vacuum fluctuations of the field.

2.1.2 Optical quadratures

In optical phase space, operators that represent the real and imaginary parts as

$$\hat{x} = \frac{\hat{a}^\dagger + \hat{a}}{\sqrt{2}} \tag{2.6}$$

$$\hat{p} = i\frac{\hat{a}^\dagger - \hat{a}}{\sqrt{2}} \tag{2.7}$$

define quadratures of the complex amplitude. The quadratures satisfy the commutation relation

$$[\hat{x}, \hat{p}] = i \tag{2.8}$$

x and p are in fact the amplitude and phase quadratures of the electromagnetic field.

2.1.3 The Heisenberg uncertainty principle

"The more precisely the position is determined, the less precisely the momentum is known in this instant, and vice versa." Heisenberg, uncertainty paper, 1927 [9].

Heisenberg's uncertainty principle is one of the fundamental concepts of quantum physics, and is the basis for the initial understanding of fundamental uncertainties in one's ability to measure more than one quantum observable at a time. Attempting to measure a particle's position to the highest degree of accuracy, for example, leads to an increased uncertainty in measurement of the particle's momentum to an equal degree of accuracy. For any non-commuting observables (for example $\hat{x}$ and $\hat{p}$) with commuting relationship $[\hat{x}, \hat{p}] = i\hbar$, the Heisenberg's Principle is typically written mathematically in the form of

$$\delta\hat{x}.\delta\hat{p} \geq \hbar/2 \tag{2.9}$$

This principle can appear in other forms for other non-commuting quantum observables, like amplitude and phase quadratures of a laser field. δ here represents the standard deviation.

2.1.4 Quantum superposition and entanglement

In classical mechanics the state of a system is essentially a list of the system's properties; more precisely, it is the specification of a set of parameters from which the list of properties can be reconstructed, for example the amplitude and phase of a laser field. The quantum state of a system should be understood as a probability amplitude for the measurement outcomes of the system.

Quantum superposition is an expression that defines an event's final outcome as the combination of all possible outcomes. All the possible outcomes put together define a quantum superposition event. If a system, for instance, is in superposition between spin up and down of an atom we can write the spin state as

$$|\psi\rangle = \alpha|\uparrow\rangle + \beta|\downarrow\rangle \tag{2.10}$$

that means by measuring the spin of the atom, one can find the system in "up" state ($|\uparrow\rangle$) with probability of $|\alpha|^2$ and in "down" state ($|\downarrow\rangle$) with probability of $|\beta|^2$, where $|\alpha|^2 + |\beta|^2 = 1$.

Quantum entanglement is a physical concept associated with the peculiar nonclassical correlations that are possible between separated quantum systems. Two systems are entangled, if the properties of the system as a whole can no longer be described by the state of each part in isolation. In other words, a system composed of multiple parts $A, B, ...$ is entangled if it is in a state Ψ that

cannot be described as a tensor product $\Psi = \Psi_A \otimes \Psi_B \otimes ...$, where Ψ_i denotes the wave-function of part i.

Entanglement forms one of the cornerstones of the new field of quantum information. Quantum entanglement is applied to enhance and to extend the power of conventional information processing. Quantum information usually carries the entanglement and superposition as two signatures of quantum mechanics. A pair of quantum systems in an entangled state can be used as a quantum information channel to perform computational tasks that are impossible for classical systems. The general study of the information-processing capabilities of quantum systems is the subject of quantum information theory.

Entanglement can be measured, transformed, and purified. For example, the strong correlations between entangled particles enable one to transfer the quantum properties from one particle to another by *quantum teleportation*. Based on Heisenberg's principle one cannot measure conjugate quantum observables of a system simultaneously. However, by applying a clever application of entanglement, one can take an alternative route to overcome some difficulties associated with this principle. The degree of entanglement, which can be monitored independently, allows one to check whether an eavesdropper is listening or whether the transmission is really secure. This is known as *quantum key distribution* (QKD). This perspective of quantum optics is further discussed in Chap. 11.

There exist four maximally entangled states, known as Bell states, that can be written as

$$\begin{aligned} |\Phi^{\pm}\rangle &= 1/\sqrt{2}(|00\rangle \pm |11\rangle) \\ |\Psi^{\pm}\rangle &= 1/\sqrt{2}(|01\rangle \pm |10\rangle) \end{aligned} \tag{2.11}$$

where $|0\rangle$ and $|1\rangle$ are two particular states of two entangled systems.

The EPR paradox

"If, without in any way disturbing a system, we can predict with certainty... the value of a physical quantity, then there exists an element of physical reality corresponding to this physical quantity."
Einstein, Podolsky and Rosen (1935) [10]

In their argument, Einstein, Podolsky and Rosen introduced a physical description that nature should obey: one system can influence the properties of a distant system, at most, with the speed of light and a measurement result is predetermined, even if we do not perform the measurement. Then they pointed out that the results of measurement on entangled particles, when obeying the above conditions, lead to contradictions with Heisenberg's uncertainty principle. Shortly after, in response to this paradox, Schrödinger described entanglement as the essence of quantum mechanics exhibiting the difference to classical mechanics in the most pronounced way [11]. Two entangled particles have to be seen as a whole. If one focuses on only one of the two, just as EPR had done, one misses important features of the coupled system. This argument is known as the EPR paradox.

2.1.5 The density operator

The density operator is a generalisation of the wave function to include the possibility of uncertainty in the preparation of the wave function. In other words, it includes information about all possible ways that a wave function can collapse. If we know only that the system is described by an ensemble of quantum states, $|\Psi_n\rangle$, with probabilities p_n, then the appropriate density operator is

$$\hat{\rho}(t) = \sum_n p_n |\Psi_n(t)\rangle\langle\Psi_n(t)| \tag{2.12}$$

here $\hat{\rho}$ is the density operator and for any complete set of basis states it can be represented as a matrix (the density matrix). If the complete set of basis states $\{|i\rangle\}$ is orthonormal, we can write

$$\hat{\rho} = \sum_{ij} |i\rangle\langle i|\hat{\rho}|j\rangle\langle j| = \sum_{ij} |i\rangle\rho_{ij}\langle j| \tag{2.13}$$

The diagonal matrix element ρ_{ii} are the probabilities of finding the system in state $|i\rangle$; the off-diagonal elements ρ_{ij} are often described as coherences between states i and j. The density operator is Hermitian, i.e. $\hat{\rho}^\dagger = \hat{\rho}$ and therefore it has real eigenvalues. If the states $\{|\Psi_n\rangle\}$ are orthonormal, these eigenvalues are just the p_n. The eigenvalues must therefore lie between 0 and 1. Assuming the states $|\Psi_n\rangle$ are properly normalised, the sum of the probabilities p_n is 1, and one can then write

$$\mathrm{Tr}[\hat{\rho}] = \sum_i \langle i|\hat{\rho}|i\rangle = \sum_n p_n \sum_i |\langle i|\Psi_n\rangle|^2 = \sum_n p_n = 1 \tag{2.14}$$

The expectation value of any operator $\hat{O}$ can be calculated if $\hat{\rho}$ is known:

$$\begin{aligned} \langle\hat{O}\rangle &= \sum_n p_n \langle\Psi_n|\hat{O}|\Psi_n\rangle \\ &= \sum_{ij}\sum_n p_n \langle\Psi_n|i\rangle\langle i|\hat{O}|j\rangle\langle j|\Psi_n\rangle \\ &= \sum_{ij} O_{ij}\rho_{ji} = \mathrm{Tr}[\hat{O}\hat{\rho}] \end{aligned} \tag{2.15}$$

The time-dependence of the density operator (in a closed system) is given by:

$$\begin{aligned} \frac{\partial\hat{\rho}}{\partial t} &= \sum_n p_n(\partial_t|\Psi_n(t)\rangle)\langle\Psi_n(t)| + |\Psi_n(t)\rangle(\partial_t\langle\Psi_n(t)|) \\ &= \frac{1}{i\hbar}\sum_n p_n \hat{H}|\Psi_n(t)\rangle\langle\Psi_n(t)| - \frac{1}{i\hbar}\sum_n p_n|\Psi_n(t)\rangle\langle\Psi_n(t)|\hat{H} \\ &= \frac{1}{i\hbar}[\hat{H},\hat{\rho}] \end{aligned} \tag{2.16}$$

where $\hat{H}$ is the Hamiltonian of the system. This equation holds in the Schrödinger representation, where the wave functions are time-dependent but the operators are not. The solution to this equation may be formally written

$$\hat{\rho}(t) = \hat{U}(t,t_0)\hat{\rho}(t_0)[\hat{U}(t,t_0)]^\dagger \tag{2.17}$$

where $\hat{U}$ is a unitary operator. It is worth mentioning that this equation might look like the equation for the time-dependence of an operator $\hat{O}$ in the Heisenberg representation:

$$\frac{d\hat{O}}{dt} = \frac{\partial\hat{O}}{\partial t} + \frac{1}{i\hbar}[\hat{O},\hat{H}] \tag{2.18}$$

but it is, indeed, very different.

Reduced density matrix

Consider two systems A and B, each with their Hilbert space H_A and H_B, so the total Hilbert space of the composed system is $H_A \otimes H_B$. The reduced density matrix appears in the frame of composed systems. In a tensor product basis $|\psi_{A_i}\rangle \times |\psi_{B_j}\rangle$, the total density matrix ρ is written as

$$\hat{\rho} = \sum_{ij}\sum_{kl} \rho_{ij}^{kl} |ij\rangle\langle kl| \tag{2.19}$$

We can define the reduced density matrix for system A only as

$$\hat{\rho}_A = \sum_{i}\sum_{k} \sigma_{ik} |i\rangle\langle k| \tag{2.20}$$

where σ_{ik} is the partial trace over system B, $\sigma_{ik} = \sum_j \rho_{ij}^{kj}$.

All observables which are only related to A can be calculated with only the reduced density matrix of A, $\hat{\rho}_A$.

Entangled state

In general, in Hilbert space $H_A \otimes H_B$ we can write the state of a system as

$$|\psi\rangle_{AB} = \sum_{i,j} c_{ij} |i\rangle_A \otimes |j\rangle_B \tag{2.21}$$

This state can be separated into two states defined by Hilbert spaces H_A and H_B if $c_{ij} = c_i^A c_j^B$, and we can write $|\psi\rangle_A = \sum_i c_i^A |i\rangle_A$ and $|\psi\rangle_B = \sum_j c_j^B |j\rangle_B$. The two systems are inseparable or "*entangled*" if $c_{ij} \neq c_i^A c_j^B$.

Consider two basis vectors, for instance, $\{|0\rangle_A, |1\rangle_A\}$ of H_A and two basis vectors $\{|0\rangle_B, |1\rangle_B\}$ of H_B, one possible entangled state might have the following form:

$$\frac{1}{\sqrt{2}}\Big(|0\rangle_A \otimes |1\rangle_B - |1\rangle_A \otimes |0\rangle_B\Big) \tag{2.22}$$

For discrete variables, the entanglement is usually characterised by measuring the correlation of properties of single particles. The entanglement condition in a continuous variable (CV) regime can be written [12] as

$$\mathrm{Var}[\hat{x}_+ + \hat{x}_-] + \mathrm{Var}[\hat{p}_+ - \hat{p}_-] < 2 \tag{2.23}$$

where canonical quadrature operators obey $[\hat{x}_\pm, \hat{p}_\pm] = i$. For a vacuum state $\mathrm{Var}[\hat{x}_{vac}] = \mathrm{Var}[\hat{p}_{vac}] = 1/2$. Var here is variance function.

Pure and mixed states

A pure quantum state is a state that can be represented as a linear superposition of basis states, $|i\rangle$. A pure quantum state is given by

$$|\psi\rangle = \sum_i \lambda_i |i\rangle \tag{2.24}$$

The density matrix elements for a pure state are given by $\rho_{ij} = \lambda_i \lambda_j$ and $\mathrm{Tr}[\rho] = \sum_i \lambda_i$. The density matrix of a pure state $|\psi\rangle$ has only one nonzero eigenvalue. Hence if ρ is of order n, then one of its eigenvalues is 1 and all other eigenvalues are 0. In consequence, the density matrix of a pure state has the special property that $\mathrm{Tr}[\rho] = 1$ and $\rho^2 = \rho$.

A quantum state may not be always a pure state. A mixed quantum state is a statistical distribution of pure states. For the density matrix of a mixed state we have

$$\rho = \sum_{\psi} P_{\psi} |\psi\rangle\langle\psi| \tag{2.25}$$

where P_ψ is probability of finding the system in state ψ and therefore $\sum_\psi P_\psi = 1$. Also, for a mixed state

$$Tr[\rho^2] < 1 \tag{2.26}$$

2.1.6 Quantum optical states

Quantum states have certain features that cannot be understood by classical theory. The non-classical nature of a quantum state can exhibit itself in different ways. In quantum optics, manifestations of the nonclassical states of light include, for instance, the photon anti-bunching, the sub-Poissonian distribution of photon numbers (see Sec. 2.1.9), the degree of quadrature squeezing, and oscillations of the photon number distribution.

The Fock state

Any quantum state in Fock space can be written as a superposition of a well-defined number of particles, i. e. the number basis $|N\rangle$, $N = 1, 2, ...$, which is a complete orthonormal basis. A Fock state is an eigenstate of the number operator and can be defined as

$$|\psi_n\rangle_F = 1/\sqrt{N!}(a_0^\dagger)^N|0\rangle$$

In the case of an optical Fock state, the variance in the photon number is zero and the photon number is completely determined. It is true that the photon number is directly related to the energy, but this does not imply that the amplitude of the electromagnetic fields is completely determined. This is because the frequency of the photon is undetermined. A Fock state is not a wavelike field in the classical sense. The field's frequency cannot be specified due to the field's random phase.

The coherent state

Due to its quantum nature, the electric field of a freely propagating light wave carries some intrinsic quantum noise. This can be understood by considering Heisenberg's uncertainty relation. The operators of phase- and amplitude- quadrature of the light field do not commute, similar to the position and momentum of a particle. The product of phase- and amplitude-uncertainty has a fixed lower limit. States of the light field with the smallest possible amount of overall quantum noise are called minimum uncertainty states. An example of such a state is the coherent state. The light emitted by an ideal monomode laser is a coherent light exhibiting noise in amplitude and phase quadratures equal to that of the vacuum. This means that the uncertainty in either the amplitude or phase quadrature measurement of the laser light is equal to the vacuum fluctuation. The resulting distribution of the amplitude and phase of a coherent state can be described by a Gaussian distribution. Mathematically a coherent state can be written as

$$|\alpha\rangle = e^{-|\alpha|^2/2} e^{\alpha a_0^\dagger}|0\rangle \tag{2.27}$$

This is a superposition of states with a definite particle number (Fock states).

The squeezed state

An interesting demonstration of Heisenberg's uncertainty principle can be given by reducing the quantum noise in one quadrature of the coherent laser field (for example the phase) at the expense of increasing it in the complementary observable (i.e. the amplitude). This can be done using nonlinear interaction, for example parametric amplification and de-amplification. These generated states of the light field are called squeezed states, since the quantum noise in one quadrature becomes squeezed.

Squeezed states have been investigated in many experiments in past years, since they can be used to reduce the amount of noise in specially designed optical precision measurements [7, 5]. The possibility of overcoming the quantum limit in optical detection by making phase-sensitive measurements, which utilises only the quadrature with reduced quantum fluctuations, has attracted attention. Two entangled beams can also be generated, for instance, by interfering two squeezed beams at a beam splitter.

The squeezing operator is given by

$$\hat{S}(r,\theta,t) = exp(\frac{r(e^{-2i\theta}\hat{a}(t)^2 - e^{2i\theta}\hat{a}^\dagger(t)^2)}{2}) \tag{2.28}$$

where r is the squeezing parameter and θ is the squeezing quadrature angle. The squeezed vacuum is obtained by applying the squeezing operator on a vacuum state. The squeezed vacuum and displaced squeezed states are given respectively by

$$\begin{aligned} |0,r,\theta,t\rangle &= \hat{S}(r,\theta,t)|0\rangle \\ |\alpha,r,\theta,t\rangle &= \hat{D}(\alpha)\hat{S}(r,\theta,t)|0\rangle \end{aligned} \tag{2.29}$$

where $\hat{D} = e^{\alpha\hat{a}^\dagger - \alpha^*\hat{a}}$ is the displacement operator. The squeezing factor, r, is real and positive and can be directly related to the standard deviation of the squeezed quadrature in frequency domain

$$\Delta\hat{X}_\theta(\omega) = e^{-r(\omega)}. \tag{2.30}$$

2.1.7 Wigner function representation

Quasi-probability functions are important to study the quantum features of the state under consideration. One of these functions is the Wigner function. The density matrices of a system can be equivalently represented as the Wigner function. This function was found and developed by L. Szilard and E.P. Wigner in 1932 [13]. The Wigner function is a phase space distribution similar to the Maxwell-Boltzmann distribution of position and momentum of an ensemble of particles known from classical statistical mechanics. However, it is not a probability distribution and due to the non-commutativity of its position and its momentum (i.e. phase- and amplitude-quadrature in the case of the light field) it may take on negative values. The negativity in the Wigner function, written in amplitude and phase space, is a quantum signature of the system. The wave packet is the density projection of the Wigner function distribution under various phase angles. The Wigner function can be determined from experimental quadrature noise measurements via tomographical reconstruction techniques.

The Wigner distribution $P(x,p)$ is defined as:

$$P(x,p) = \frac{1}{\pi\hbar}\int_{-\infty}^{\infty} \Psi^\star(x+y)\Psi(x-y)e^{2ipy/\hbar}dy \tag{2.31}$$

The Wigner function of a general Gaussian state is given by [14]

$$W(\alpha) = \frac{2}{\pi\sqrt{V^+V^-}} e^{[-\frac{2}{V^+}(\alpha_r\cos\phi+\alpha_i\sin\phi-\delta_r)^2-\frac{2}{V^-}(\alpha_i\cos\phi+\alpha_r\sin\phi-\delta_i)^2]} \tag{2.32}$$

where $V^{\pm}$ are variances of two orthogonal distributions of amplitude and phase. The above equation describes a coherent state of amplitude $\delta = \delta_r + i\delta_i$ when $V^{\pm} = 1$. ϕ is the phase of the state. For a pure squeezed state we have $V^+ \times V^- = 1$ and $V^+ \neq V^-$.

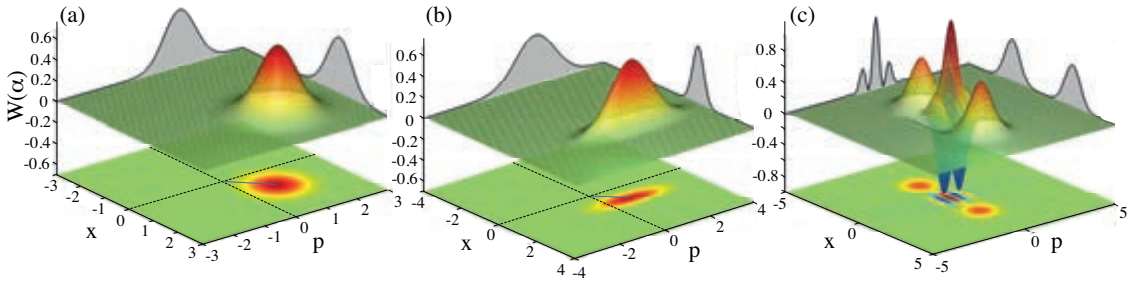

Figure 2.1: Wigner representation of (a) a coherent state (b) a squeezed state, (c) a superposition of two coherent states. Projection of the Wigner function in the x-p plane shows the size of the uncertainty in the two quadratures.

For a coherent state (Fig. 2.1 (a)), the corresponding phase space distribution is symmetric and Gaussian. The ball-on-stick representation of a coherent state is shown in the $x-p$ plane of Fig. 2.1 (a). The length of the stick is equal to $\sqrt{n}$ and size of the ball represents the uncertainty in amplitude (x)-phase(p) plane. The corresponding phase space distribution of a squeezed state has an elliptical shape as shown in Fig. 2.1 (b) for displaced squeezed state.

Besides the Wigner representation, there are other distribution functions such as the Glauber-Sudarshan P-function [15] and Q function [16]. As for the quasi-probability distribution, the P function is highly singular, involving an infinite sum of higher order derivatives of a delta function and represents the probability density to find a state. The Q function is always non-negative and does not exhibit a clear signal for non-classicality. One notices that Wigner distribution (W) is narrower than Q, and P distribution is narrower that W.

Coherent superposition

Studies on nonclassical properties of the quantum superposition of coherent states are of great interest because of their applications in quantum information theory such as quantum communication. A familiar example of such states is the superposition of two classical-like coherent states of the same amplitude but with a phase difference of 180^o

$$|\psi\rangle = N(|\alpha\rangle - e^{-i\phi}|-\alpha\rangle)$$

For $\phi = 0$, the above equation describes the odd coherent state, while for $\phi = \pi$, it describes the even coherent state. The Wigner representation of superimposed coherent states is given by

$$W^{\pm}(\beta) = N_{\pm}^2[W_{|\alpha\rangle}(\beta) + W_{|-\alpha\rangle}(\beta) + W_{int}(\beta)] \tag{2.33}$$

where $N_{\pm}^2 = 1/(2\pm 2e^{-2|\alpha|^2})$ is a normalisation constant and $W_{|\pm\alpha\rangle}(\beta)$ denotes the Wigner function of the single coherent state. The term $W_{int}(\beta)$ accounts for quantum interference between the two coherent states.

Fig. 2.1 (c) shows the Wigner representation of two superimposed coherent states, i.e. Schrödinger cat states. When the Wigner function takes on negative values, it is a clear sig-

nature of nonclassicality. Fringes at the centre of the plot are the result of quantum interference between two states. The larger the two states are, the finer the fringes will be. The generation of optical Schrödinger cat states is important for applications in quantum communications [17, 18], and quantum computing [19, 20].

Overlap

The fidelity of a final state to its initial one is a criterion of teleportation. The fidelity can be obtained by calculating the overlap between the two states. In general cases where the Gaussian states are input, the classical fidelity $\mathcal{F}_c$ and quantum fidelity $\mathcal{F}_q$ are defined [14] as

$$\mathcal{F}_c = [\int d^2\alpha \sqrt{P_1(\alpha)P_2(\alpha)}]^2 \tag{2.34}$$

$$\mathcal{F}_q = |Tr[\sqrt{\sqrt{\rho_1}\rho_2\sqrt{\rho_2}}]|^2 \tag{2.35}$$

where P_1 and P_2 are probability distributions of a system, and ρ_1 and ρ_2 are density matrices. If the two density matrices belong to two pure states, i. e. $\rho_1 = |\psi\rangle\langle\psi|$ and $\rho_2 = |\phi\rangle\langle\phi|$, then $\mathcal{F}_q = |Tr[\sqrt{\rho_1\rho_2\rho_2}]|^2 = |\langle\phi|\phi\rangle|^2$.

The density matrix can also be equivalently represented as a Wigner function. In the case when the input states are pure, the noise added to the state causes a significant change to the Wigner function describing the output state, with the result being a poor overlap between the input and output states. In the case of a pure input state the fidelity is given by the overlap of their Wigner functions

$$\mathcal{F}_q = |\langle\psi_2|\psi_1\rangle|^2 = \pi \int d^2\alpha W_{in}(\alpha)W_{out}(\alpha) \tag{2.36}$$

In the case of a Gaussian state, knowing the input quadrature variances of $V_{in}^{\pm}$ and output variances of $V_{out}^{\pm}$, it is possible to estimate the fidelity of the system. It can be shown [14] that the overlap between the input and output states is

$$\mathcal{F}_q = 2e^{-\frac{2\delta_x^2}{V_{in}^+ + V_{out}^+} - \frac{2\delta_y^2}{V_{in}^- + V_{out}^-}} / (\sqrt{(V_{in}^+ V_{out}^- + 1)(V_{in}^- V_{out}^+ + 1)} - \sqrt{(V_{in}^+ V_{in}^- - 1)(V_{out}^+ V_{out}^- - 1)}) \tag{2.37}$$

where $\delta_{x/y}$ is the quadrature value difference of the input and output states in phase space. The x (+) and y (-) represent amplitude and phase quadratures. This expression can be used to calculate the fidelity of any Gaussian distribution states such as coherent or squeezed sates. Using this expression we have plotted the fidelity between two Gaussian states (input and output states) as a function of loss and mean photon number in Fig. 2.2 (a) and (b), respectively.

No-cloning limit

Quantum mechanics postulates that cloning a quantum state is impossible [21]. This principle is important in understanding some quantum key distribution protocols [22]. Attempts to clone quantum information using, for instance, splitters and linear amplifiers result in quantum back-action. This cloning operation will add a vacuum of noise to conjugate variables and therefore the fidelity between the initial and final states will be deteriorated. Considering this noise penalty, the *no-cloning fidelity limit* [23] can be calculated, above which the output of a quantum device or channel is the best possible copy.

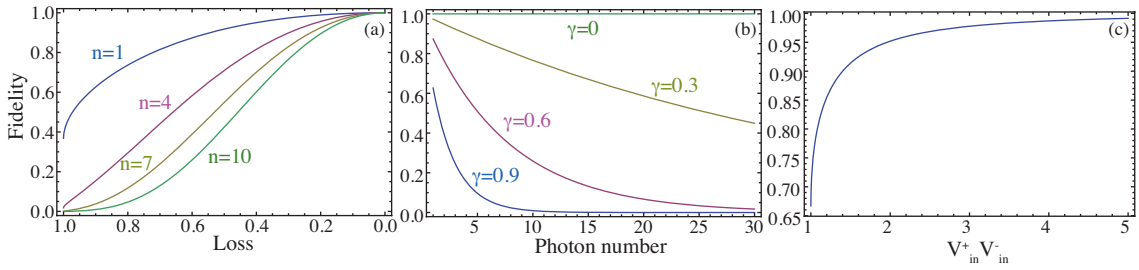

Figure 2.2: (a) Fidelity between two optical coherent states as a function of relative intensity loss plotted for different mean photon numbers. (b) Fidelity between two coherent states as a function of mean photon number plotted for different values of relative intensity loss γ. (c) No-cloning fidelity limit as a function of input variance normalised to vacuum noise.

For coherent states, the cloning fidelity limit is about 2/3 (0.68%) for Gaussian (non-Gaussian) cloners [24, 25]. If the input variances of the two quadratures are larger than the vacuum fluctuation (incoherent source) the no-cloning fidelity limit is different and can be calculated using Eq. 12.2. Figure 2.2 (c) shows the no-cloning fidelity limit calculated using Eq. 12.2, assuming one vacuum of noise added to both quadratures, as a function of input quadrature variances.

2.1.8 Detection of optical quantum states

Homodyne detection

Ordinary photodetectors detect light intensity or photon flux n; homodyne detection by contrast measures the quadrature values of the electric field. It is a particularly important technique for the study of phase-sensitive phenomena. Consider two beams, a weak signal field and a strong light field known as a local oscillator (LO), interfering on a beamsplitter.

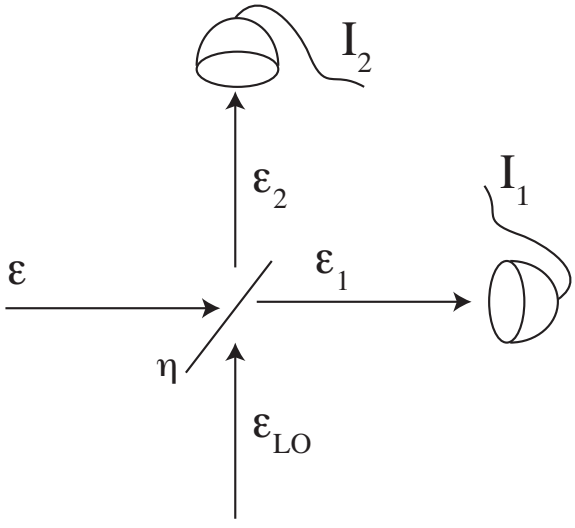

Figure 2.3: Homodyne detection setup

Balanced homodyne detection is usually preferred to eliminate the contribution of the local oscillator noise. In this case, two photodiodes are used after a 50:50 beam splitter as

shown in Fig. 2.3; the sum and difference of photocurrents are electronically obtained. If the signal port is blocked, the difference of photocurrents exhibits the shot noise level of the local oscillator beam, even if the actual noise level of that beam is different. The latter noise level can be obtained in addition by taking the sum of the photocurrents. That sum exhibits the same noise as for direct detection of the local oscillator beam with a single photodiode. When the signal beam interferes with the LO beam, the difference in the signal of the detectors allows one to simply compare the signal noise with the shot noise limit. For the squeezed quadrature of light, the sum of the photocurrents exhibits a lower noise than the difference. In many cases, the local oscillator power is made so high that the corresponding shot noise provides a large signal-to-noise ratio.

Consider setup depicted in Fig. 2.3 where two optical modes

$$\mathcal{E}_{LO}(t) = (\mathcal{E}_{LO} + \delta X1_{LO}(t) + i\delta X2_{LO}(t))e^{i\phi_{LO}} \tag{2.38}$$

$$\mathcal{E}(t) = \mathcal{E} + \delta X1(t) + i\delta X2(t) \tag{2.39}$$

interfere on a beamsplitter with a reflectivity of η where ϕ is the phase difference between the LO and the signal beam. The amplitude of the light on one arm of the interferometer is given by

$$\mathcal{E}_1(t) = \sqrt{\eta}\mathcal{E}_{LO}(t) + \sqrt{1-\eta}\mathcal{E}(t) \tag{2.40}$$

and therefore the intensity measured by the detector is

$$\begin{aligned} I_1 = \langle \mathcal{E}_1(t)^\dagger \mathcal{E}_1(t)\rangle = \eta\langle \mathcal{E}_{LO}(t)^\dagger \mathcal{E}_{LO}(t)\rangle + (1-\eta)\langle \mathcal{E}(t)\mathcal{E}(t)^\dagger\rangle \\ +\sqrt{\eta(1-\eta)}(\langle \mathcal{E}_{LO}(t)\rangle\langle \mathcal{E}(t)^\dagger\rangle + \langle \mathcal{E}(t)\rangle\langle \mathcal{E}_{LO}(t)^\dagger\rangle) \end{aligned} \tag{2.41}$$

which can be approximated assuming$|\mathcal{E}_{LO}| \gg |\mathcal{E}|$ and $\eta = 1/2$ to

$$I_1 \simeq 1/2[|\mathcal{E}_{LO}|^2 + \mathcal{E}_{LO}(\delta X1(t)\cos\phi_{LO} + \delta X2(t)\sin\phi_{LO}))]. \tag{2.42}$$

Similarly, the current for the other detector can be found. The difference current I_- is then given by

$$I_- = \mathcal{E}_{LO}(\delta X1(t)\cos(\phi_{LO}) + \delta X2(t)\sin(\phi_{LO})) \tag{2.43}$$

which only represents amplitude fluctuations of the weak field while fluctuations in the LO field are eliminated.

Homodyne detection can also be used to measure quadrature values of a pulsed signal field. In this case, the amplitude of the pulse varies depending on the phase of the LO and by integrating I_- over the pulse duration Δt. One can associate a single quadrature value with the entire pulse. The integration will effectively limit the measurement bandwidth to $1/\Delta t$. Alternatively, one can obtain quadrature values corresponding to different parts of the signal pulse.

Heterodyne detection

Heterodyne detection is a slight modification to homodyne detection where the signal and the LO fields have different frequencies. Consider two optical beams mixing on a photodiode. We can write the classical amplitude of the two beams as, $E_s(t) = E_s e^{i(\omega_s t+\phi)}$ and $E_{LO}(t) = E_{LO} e^{i(\omega_{LO} t+\phi)}$. Neglecting terms oscillating at 2ω, the ac photodetector current is given by:

$$I_{ac} = (E_s + E_{LO})^2 \simeq E_s E_{LO} \cos(\Delta\omega t + \phi) \tag{2.44}$$

which indicates a signal beating with a frequency equal to the frequency difference between the signal and LO field, $\Delta\omega = \omega_s - \omega_{LO}$. Here, ϕ is the phase difference between the signal and LO. This signal can be demodulated using analogue or digital demodulation to arrive at a signal similar to the homodyne signal. The demodulated signal will be sensitive to the phase, ϕ, and its amplitude will fluctuate if the optical path is not locked. The heterodyne signal can be demodulated in a way that cancels the effect of the change in the relative phase between the LO and the signal. This is done by splitting the RF signal in two parts and demodulating one with $\sin(\Delta\omega t)$ and the other with $\cos(\Delta\omega t)$. Afterwards, squaring the signals and adding them together will result in a ϕ-independent output signal. This demodulation method is schematically shown in Fig. 2.4.

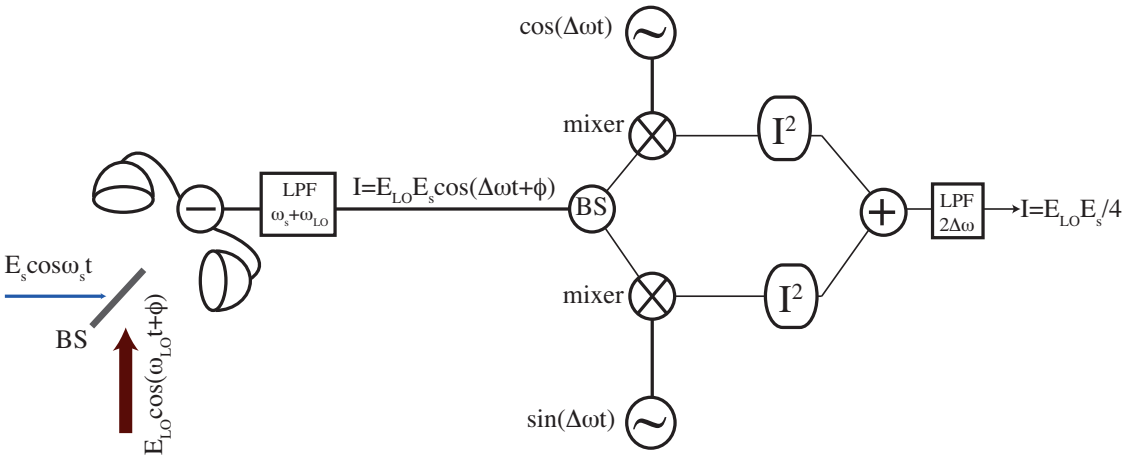

Figure 2.4: Schematic setup for demodulation of the heterodyne signal in order to perform phase insensitive measurement. The square operation can be done digitally. LPF: low pass filter, BS: beam splitter, I^2: square operation on the signal.

Using heterodyne detection for quantum measurements, one can measure the amplitude and phase of a signal simultaneously, at the expense of one added vacuum of noise. Simultaneous measurement of the two quadratures also provides information about the photon statistics of the state [26]. The annihilation and creation operators of an arbitrary field may be expressed in the Heisenberg picture as a sum of the amplitude and phase quadrature operators. We have $\hat{A}(t) = \bar{A} + \delta\hat{A}(t)$ and $\hat{A}^\dagger(t) = \bar{A}^\dagger + \delta\hat{A}^\dagger(t)$. The variance of an arbitrary input field in the frequency domain is given by

$$V^{\pm}(\omega) = \langle \delta A(\omega)^\dagger \delta A(\omega) + \delta A(-\omega)^\dagger \delta A(-\omega) \pm \delta A(-\omega)\delta A(\omega) \pm \delta A(-\omega)^\dagger \delta A(\omega)^\dagger \rangle + 1. \tag{2.45}$$

The average number of photons in both the positive and negative sidebands (at frequency ω) for a continuous variable measurement of the variances is given [26] by

$$\bar{n}(\omega) = \frac{V^{+}(\omega) + V^{-}(\omega) - 2}{4}. \tag{2.46}$$

2.1.9 Photon statistics of optical states

The Poisson distribution is used to model the number of events occurring within a given time interval. An ideal laser light source is a coherent state and has a Poisson distribution, and a thermal radiation source has Bose-Einstein distribution. For the Poisson distribution, the expectation value and variance of the photon number are equal. On the other hand, the variance of the thermal photon number distribution goes beyond its expectation value and follows Maxwell-Boltzmann distribution. The photon number distribution of an amplitude-squeezed state is sub-Poissonian.

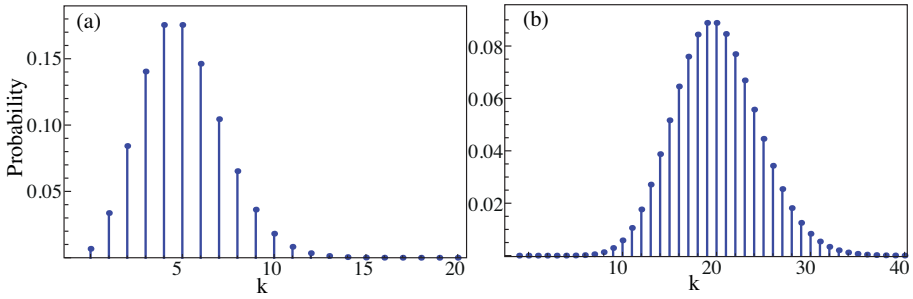

Figure 2.5: Poisson distribution shown for (a) $\lambda = 5$ and (b) $\lambda = 20$

The formula for the Poisson probability function is

$$P_{\lambda}(k) = e^{-\lambda}\lambda^{k}/k! \tag{2.47}$$

where λ is the shape parameter which indicates the average number of events in the given time interval and k is an integer value. The number distribution of any coherent state is Poissonian.

Figure 2.5 is the plot of the Poisson probability density function for two values of λ as a function of k. In general, the photon number distribution of a squeezed state is given [27] by

$$P(n) = |\langle n|\alpha, r, \theta\rangle|^2 \tag{2.48}$$

where

$$\langle n|\alpha, r, \theta\rangle = \sqrt{\frac{e^{in\theta}\tanh r^{n}}{2^{n} n!\cosh r}}\exp(-1/2(|\alpha|^2 + (\alpha^{\star})^2 e^{i\theta}\tanh r))H_n[\frac{\alpha + \alpha^{\star}e^{i\theta}\tanh r}{\sqrt{2e^{i\theta}\tanh r}}] \tag{2.49}$$

and $H_n[x]$ are the Hermite polynomials. This photon distribution can be broader or narrower than the Poissonian distribution evident for coherent states, depending on the coherent amplitude α and the quadrature of the squeezing θ.

2.1.10 Maximum likelihood reconstruction in homodyne measurement

The quantum state of a system can be accurately described if the measurement is complete, i.e. all of the projectors corresponding to the data yield the decomposition of the unity operator. Provided that the data do not exhaust all the values, the measurement is incomplete. In this case, the full quantum description of a system may be accomplished using the maximum likelihood (MaxLik) estimation [28, 29, 30]. The method is to perform set of measurements on various known quantum states and then estimate the unknown measurement from the collected data.

Reconstruction corresponds to normalisation of incompatible observations that are done on the subspace where the measured projectors reproduce the identity operator ($\hat{R}$). This approach handles noisy data corresponding to realistic incomplete observation with finite resolution. In other words one can determine "what quantum states seem to be most likely for that measurement". This type of reconstruction can be used to estimate the quantum state of a system using quadrature homodyne measurement.

This detection of discretised quadrature components reproduces the identity operator as

$$\hat{R} = \sum_i \hat{\Pi}(x_i) \tag{2.50}$$

where x_i denotes the position of a particular bin in x-coordinate and

$$\hat{\Pi}(x_i|\theta) = \Delta x \sum_{n=0}^{\infty} \sum_{m=0}^{n} \phi_{nm}(x_i)\eta^m(1-\eta)^{n-m}\frac{n!}{m!(n-m)!}|n\rangle\langle n|, \tag{2.51}$$

$$\phi_{nm}(x|\theta) = \frac{1}{2^{(m+n)}n!m!\sqrt{\pi}}e^{-i(n-m)\theta}e^{-x^2}H_m^2(x)H_n^2(x). \tag{2.52}$$

Here η denotes the detection efficiency and H_m is the Chebyshev-Hermite polynomial of mth order. By analogy to the ordinary binomial distribution, we may call the random number m the number of successes in a series of n independent experiments. The reconstruction of ρ can be done using iterative method solving the nonlinear equation for density matrix

$$\hat{R}(\hat{\rho})\hat{\rho} = \hat{\rho} \tag{2.53}$$

In this derivation, the condition of normalisation, $Tr[\hat{\rho}] = 1$, is used such that

$$\hat{R} = \sum_i \frac{f_i}{\rho_{ii}}\hat{\Pi}(x_i|\theta) \tag{2.54}$$

$$\rho_{ii} = Tr[\hat{\rho}\hat{\Pi}(\hat{x_i}|\theta)] \tag{2.55}$$

where f_i is the probability amplitude of measuring quadrature value x_i. This method is used to reconstruct the density matrix elements from the experimental quadrature data.

2.2 Atom-light interaction

Atoms are an exceptional medium for development of an efficient coherent interface with light. Theoretical treatment of this problem provides a framework that can be used to analyse atom-light interaction as it appears in quantum optics. A fully self-consistent quantum mechanical treatment of atoms interacting with electromagnetic fields requires that we treat the field, as well as the matter, quantum mechanically. In many cases we can use a simplified theory called semiclassical theory in which the atoms are treated quantum mechanically, while the fields are taken to be c-number solutions of the classical Maxwell equations.

Atomic operators

To theoretically investigate atom-light interactions, it is convenient to define some atomic operators similar to electromagnetic field operators. These operators are Pauli vectors defined by

$$\hat{\sigma} = \hat{\sigma}_x \bar{i} + \hat{\sigma}_y \bar{j} + \hat{\sigma}_z \bar{k}. \tag{2.56}$$

The Pauli spin matrices, $\hat{\sigma}_x$, $\hat{\sigma}_y$ and $\hat{\sigma}_z$ represent the intrinsic angular momentum components of electron spin. We define atomic operators as

$$\hat{\sigma}_+ = \hat{\sigma}_x + i\hat{\sigma}_y = |e\rangle\langle g| \tag{2.57}$$
$$\hat{\sigma}_- = \hat{\sigma}_x - i\hat{\sigma}_y = |g\rangle\langle e| \tag{2.58}$$
$$\hat{\sigma}_z = |e\rangle\langle e| - |g\rangle\langle g| \tag{2.59}$$

where g and e denote ground and excited states of a two-level atom, respectively. The operators $\hat{\sigma}^{\pm}$ are also called atomic transition operators and account for atomic coherence.

2.2.1 Interaction with a two-level atom

We begin our treatment with a general description of an electromagnetic field interacting with a two-level atom. We will assume the field is monochromatic with angular frequency ω to model the laser field

$$E(t) = \hat{\epsilon} E_0 \cos(\omega t) \tag{2.60}$$

we can write the total Hamiltonian for the atom and light field as a sum of the free atomic Hamiltonian H_A and the atom-light interaction Hamiltonian H_{AL}

$$H = H_A + H_{AL}. \tag{2.61}$$

The atomic Hamiltonian in terms of spin operators is given by

$$H_A = \frac{1}{2}\hbar\omega_{ef}(|e\rangle\langle e| - |g\rangle\langle g|) = \frac{1}{2}\hbar\omega_{ef}\hat{\sigma}_z \tag{2.62}$$

where we chose halfway energy between the levels as the zero point energy (reference energy).

The atom-field interaction Hamiltonian in the dipole approximation is

$$H_{AL} = -\mu.\mathbf{E} = \hbar\Omega \tag{2.63}$$

where μ is the atomic dipole operator, given in terms of the atomic electron position r_e as $\mu = -er_e$, $\Omega = \frac{\mu.\mathbf{E}}{\hbar}$ is known as the Rabi frequency that is the frequency of population oscillation for a given atomic transition in a given light field. Since the field strength of interest is usually an order of magnitude weaker than the internal Coulomb electric field of the atom, the interaction will not change the atomic level structures in any significant way. The only part on which we will be focusing here is the interaction term $-\mu.\mathbf{E}$. In general, the atomic dipole can be written in terms of atomic spins as

$$\mu = \langle g|r_e|e\rangle(\sigma + \sigma^\dagger) \tag{2.64}$$

where $|g\rangle$ and $|e\rangle$ stand for ground and excited states of a two-level atom, respectively.

Rotating-Wave Approximation

Considering time dependencies of $\mu^\pm = \mu_0 e^{\mp i\omega_0 t}$ and $E^\pm = E_0 e^{\mp i\omega t}$ we can write

$$H_{AL} = -(\mu^+ + \mu^-).(\mathbf{E}^+ + \mathbf{E}^-) \tag{2.65}$$

Assuming that $|\omega - \omega_0| \ll \omega + \omega_0$, we can imply rotating-wave approximation (RWA). This approximation focuses on slow dynamics, replacing terms rotating at optical frequencies by their zero average value. This is reasonable since optical detectors are bandwidth limited.

Thus, the atom-field interaction Hamiltonian in the RWA becomes

$$H_{AL} = -\mu^+.\mathbf{E}^- - \mu^-.\mathbf{E}^+ \tag{2.66}$$

Moving from the Schrödinger picture into the interaction picture, we can also write the atom-light Hamiltonian for a single atom in the rotating frame using the atomic operators as

$$\hat{H}^{\mathrm{RWA}}(t) \equiv \frac{\hbar\omega_{eg}}{2}\hat{\sigma}_z - \hbar g\left(\hat{a}^\dagger\hat{\sigma}^- e^{i\Delta t} + \hat{a}\hat{\sigma}^+ e^{-i\Delta t}\right). \tag{2.67}$$

where $g = \mu\sqrt{\omega/2\epsilon_0\hbar V}$ is the atom-light coupling strength, and Δ is the frequency difference between the optical field and the atomic transition. We can also include the Hamiltonian of the light field and drop the zero-point energy term, because it does not contribute to the dynamics of the system

$$H^{\mathrm{RWA}}(t) \equiv H_L + H_A + H_{AL} \equiv \hbar\omega_0\hat{a}^\dagger\hat{a} + \frac{\hbar\omega_{eg}}{2}\hat{\sigma}_z - \hbar g\left(\hat{a}^\dagger\hat{\sigma}^- e^{i\Delta t} + \hat{a}\hat{\sigma}^+ e^{-i\Delta t}\right). \tag{2.68}$$

This Hamiltonian is also known as *Jaynes-Cummings Hamiltonian* [1] and is of great

interest in quantum optics.

2.2.2 Dressed state picture

The Jaynes-Cummings Hamiltonian in Eq. 2.68 is the entire Hamiltonian of the system, but for strong atom-field coupling the complete state of the system can no longer be described as either a state of the atom or a state of the field. Instead we should specify the system via states of both atom and field. In the energy eigenstate representation, the basis states of the optical field are $|n\rangle$ with n being a positive integer. The Jaynes-Cummings Hamiltonian couples the states $|e,n\rangle$ or $|g,n+1\rangle$ and therefore

$$\langle g,n+1|H|e,n\rangle = \hbar g\sqrt{n+1} \tag{2.69}$$

and the energies of the uncoupled system are given by

$$\begin{aligned} E_{e,n} &= \langle e,n|H|e,n\rangle = \hbar(n\omega_0 + \omega_{eg}/2) && (2.70)\\ E_{e,n+1} &= \langle g,n+1|H|g,n+1\rangle = \hbar((n+1)\omega_0 - \omega_{eg}/2) \\ &= E_{eg} + \hbar\Delta. && (2.71) \end{aligned}$$

By diagonalising the entire Hamiltonian we can find the eigenvalues of the combined system

$$E_n^{\pm} = \hbar\Delta/2 \pm \hbar\Omega_n \tag{2.72}$$

with corresponding eigenstates of

$$|\pm_n\rangle = 1/\sqrt{N_{\pm}}(\Omega_n \mp \Delta/2)|g,n+1\rangle \pm g\sqrt{n+1}|e,n\rangle \tag{2.73}$$

where $\Omega_n = \sqrt{g^2(n+1)+(\Delta/2)^2}$ is the generalised Rabi frequency, and $N_{\pm} = g^2(n+1)+(\Omega \mp \Delta/2)^2$. These are the dressed states of the atom, and the coupling to the field causes an avoided crossing in the energy level structure of the atom. This is schematically shown in Fig. 2.6.

The dressed picture of atom-field interaction has been very successful in the physical interpretation of peculiar features exhibited in resonance fluorescence and absorption spectra.

2.2.3 Bloch sphere

The Bloch sphere is a geometric representation of a two-level quantum system as points on the surface of a unit sphere. The idea behind the Bloch sphere is to use the expectation values $\langle\sigma_i\rangle$ as dynamical coordinates [2] for the evolution of a two-level atom. This concept can be applied to any other system in the quantum superposition of two states. In the case of evolution of a two-level atom, the three coordinates are defined as

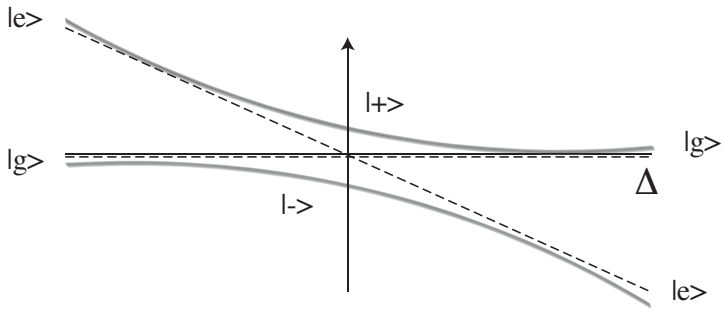

Figure 2.6: Splitting of atomic levels shown in dressed picture

$$\begin{aligned}\langle\sigma_x\rangle &= \langle\sigma\rangle + \langle\sigma^\dagger\rangle = \rho_{eg} + \rho_{ge} \\ \langle\sigma_y\rangle &= i\langle\sigma\rangle - i\langle\sigma^\dagger\rangle = i(\rho_{eg} - \rho_{ge}) \\ \langle\sigma_z\rangle &= \rho_{ee} - \rho_{gg}\end{aligned} \tag{2.74}$$

where $\langle\sigma\rangle$ and $\langle\sigma^\dagger\rangle$ are the Pauli operators and ρ is the atomic density matrix.

An arbitrary state ψ can be written in terms of probability amplitudes as

$$|\psi\rangle = \cos\theta\,|0\rangle + e^{i\phi}\sin\theta\,|1\rangle. \tag{2.75}$$

The parameters ϕ and θ uniquely specify a point on the unit sphere of Euclidean space. The measurable quantities are the probability amplitudes of the state, $\alpha = \cos\theta$ and $\beta = e^{i\phi}\sin\theta$.

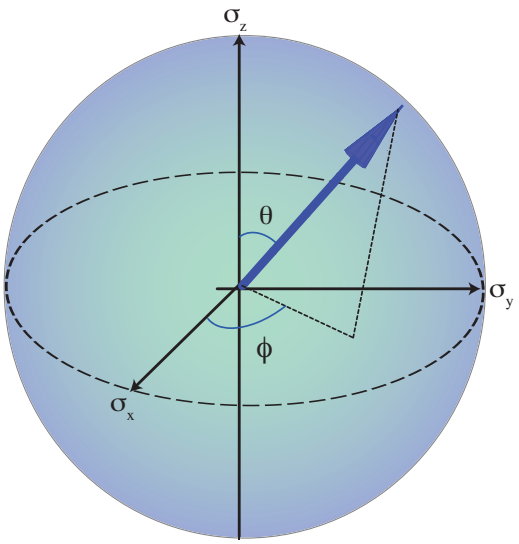

Figure 2.7: Bloch sphere representation of a two-level system on the superposition state $|\psi\rangle = \cos\theta\,|0\rangle + e^{i\phi}\sin\theta\,|1\rangle$.

The role of Pauli operators is to rotate the Bloch vector about x, y or z axes.

2.2.4 Spin and photon echo

Spin echo [2] refers to the refocusing of atomic nuclear spin precession by an electromagnetic pulse. Echo phenomena are important features of coherent spectroscopy which have been observed and used in various fields such as nuclear magnetic resonance (NMR) [31]. The photon echo phenomenon, described below, mimics the spin echo process.

To explain the photon echo phenomenon, we consider a 2-level atomic ensemble with inhomogeneous broadening, where each atom effectively has a slightly different resonance frequency, as happens with Doppler broadening in atomic vapour or in dipole-dipole interactions of ions embedded in crystal. Excitation pulses are frequently used in the observation of echoes. Such pulses change the angle of the Bloch vector by $\theta = \int_0^\tau \mathbf{d}.\mathbf{E}(\mathbf{t})/\hbar dt$. A pulse that leads to $\theta = \pi/2$ is called $\pi/2$ pulse, which elicits the largest transverse spin component. A pulse that leads to $\theta = \pi$ is called π pulse or inverse pulse, which is used to induce photon echo. In fact a π pulse inverts the population between the ground and excited states. Firstly, a $\pi/2$-pulse is sent to the atomic sample to put the atoms in a superposition of the ground and excited states. After the excitation pulse, the spin of each atom precesses at a slightly different frequency, leading to a spread in phase angles that increases with time. As shown in Fig. 2.8(a) and (b), some Bloch vectors evolve faster than others.

After the atoms have dephased, sending a π-pulse to the atoms effectively time-reverses the process and the dipoles start to rephase. Thus, the dipoles begin to come back together to the same phase. In the Fig. 2.8(c) and (d), after the π pulse, the faster dipoles are now behind the slower ones, and thus the slower ones can now "catch up". The other way to look at this is that the reflection due to the π-pulse is effectively equivalent to flipping the precession axis, and thus time-reversing the evolution. The dipoles come back to the mirror image of the original orientation. If the π-pulse is applied a time τ after the original preparation pulse, the spin echo occurs at time 2τ.

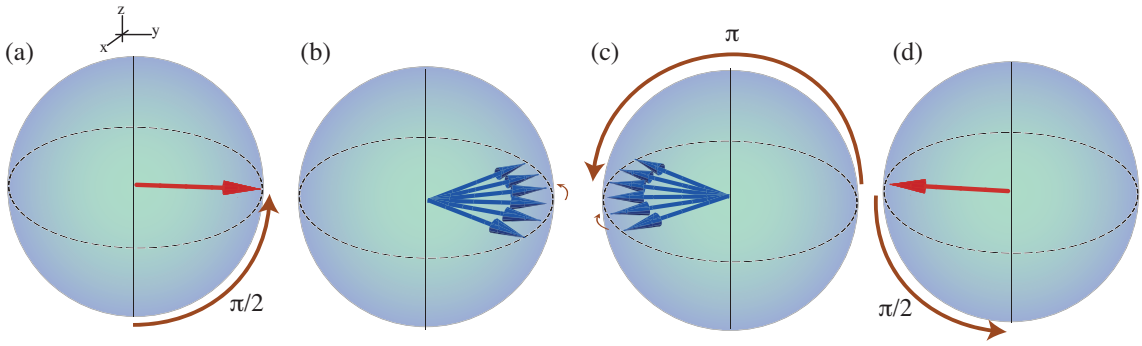

Figure 2.8: Sequences of spin echo in Bloch sphere representation: (a) A $\pi/2$ pulse excites the atoms to a superposition state; (b) and then Bloch vectors start to dephase; (c) a π pulse rephases the atomic spin; (d) when spins are phase matched a $\pi/2$ pulse is re-emitted.

The photon echo phenomena, as is discussed in the next chapter, can be used as a method of light storage. This technique also forms the basis of the storage mechanism that was used in our experiment.

2.2.5 Free induction decay

When a pulse of light excites an atomic ensemble with energy levels $|1\rangle$ and $|2\rangle$, it generates a coherence between $|1\rangle$ and $|2\rangle$ where the spins of atoms have initially the same phase. In the rotating frame, the net spin vector decays as spins lose phase coherence as shown in Fig. 2.76 (a). This is because atoms experience slightly different electric or magnetic field strengths due to interaction between spins (via their own oscillating magnetic fields). Slightly different magnetic fields mean slightly different precession (Larmor) frequencies. This causes some spins to "lag behind" the average, and some to "progress ahead" of the average. Eventually the spins point in arbitrary directions and the S_{xy} component of the net spin vector is lost. The oscillations between the $|1\rangle \rightarrow |2\rangle$ transition damp away in a drift time of order $T_2 = 1/\delta\omega_0$, where $\delta\omega_0$ measures the inhomogeneously broadened width of the atomic transition, and ω_0 is the frequency splitting between the two atomic levels, see Fig. 2.76 (b). This time constant contains information about related dipole-dipole interactions and additional loss of phase coherence due to imperfections in the external field, and to magnetic susceptibility effects. The damping of the ensemble-averaged dipole moment due to dephasing is called free-induction decay (FID).

The FID in the lab frame is described mathematically by

$$S_{xy} = S_{xy}(0)e^{-t/T_2}\cos(\omega_0 t) \tag{2.76}$$

where ω_0 is the frequency of magnetic field oscillations.

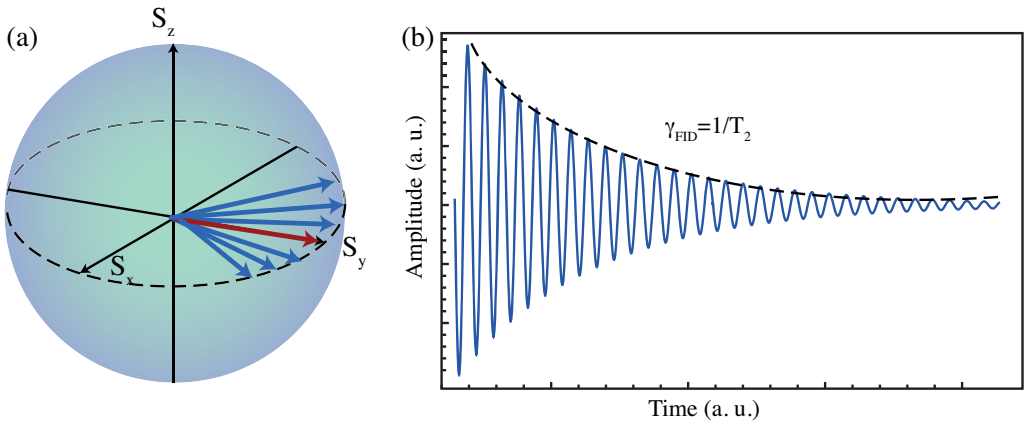

Figure 2.9: Dephasing of spins causes S_{xy} to decay away. This is shown schematically as Bloch sphere representation in (a). (b) The amplitude of the atomic coherence shows a free induction decay with a T_2 envelope.

The FID effect can be observed by using both microwave and optical signals. In both cases, the atomic sample is exposed to a short, strong resonant signal to create atomic excitations. The decay of the atomic excitation can be observed by detecting the output signal from the sample. The output signal amplitude is at its maximum when atoms are in-phase and burst a strong emission. This method is a common technique in measuring the coherence time.

2.2.6 Adiabatic following

Consider an ensemble of atoms all in the ground state of energy, so that the Bloch vector points along the z axis. By applying an intense and far-detuned field ($|\Delta| \gg \Omega$), the precession vector is aligned with the Bloch vector. The precession of the Bloch vector is very simple, since it just stays in place. Now by scanning the detuning through resonance, the precession vector moves along the x-axis and up towards the $+z$-axis. As long as we change the detuning slowly enough on the time scale of the Rabi frequency, i.e. the frequency chirp $r = d\Delta/dt \ll \Omega^2$, the Bloch vector will follow the precession vector [2]. Furthermore, the adiabatic following condition requires that the flipping time Ω/r should be much longer than the coherence lifetime T_2 and much shorter than the light pulse duration.

2.3 Optical Bloch Equations

The interaction of a two-level atom with the electric or magnetic field can be described by the Bloch equations. Using the evolution of the density operator we can write the *Schrödinger-von Neumann* equation [2] in the rotating frame

$$\partial_t \rho = -i/\hbar[H_A + H_{Al}, \rho]. \tag{2.77}$$

We can work out the equations of motion for the density matrix elements

$$\begin{aligned} \partial_t \rho_{ee} &= i\Omega/2(\rho_{eg} - \rho_{ge}) \\ \partial_t \rho_{gg} &= -i\Omega/2(\rho_{eg} - \rho_{ge}) \\ \partial_t \rho_{ge} &= -i\Delta\rho_{ge} - i\Omega/2(\rho_{ee} - \rho_{gg}) \end{aligned} \tag{2.78}$$

where Δ is detuning from excited state and Ω is the Rabi frequency. We can now include the phenomenologically damping terms with the Hamiltonian-evolution terms to obtain the optical Bloch equations:

$$\begin{aligned} \partial_t \rho_{ee} &= i\Omega/2(\rho_{eg} - \rho_{ge}) - \Gamma\rho_{ee} \\ \partial_t \rho_{gg} &= -i\Omega/2(\rho_{eg} - \rho_{ge}) + \Gamma\rho_{ee} \\ \partial_t \rho_{ge} &= -(\gamma + i\Delta)\rho_{ge} - i\Omega/2(\rho_{ee} - \rho_{gg}) \end{aligned} \tag{2.79}$$

where Γ is the excited state population decay rate. The coherence damping rate γ can be written as

$$\gamma = \Gamma/2 + \gamma_c \tag{2.80}$$

where γ_c models dephasing effects such as atom-atom collisions that do not affect the populations. We can also write the damped optical Bloch equations [2] in terms of the Bloch vector by replacing $\sigma_{ij} = \rho_{ij} e^{i\omega_{ij} t}$

$$\begin{aligned}\partial_t\hat{\sigma}_{ee} &= i\Omega/2(\hat{\sigma}_{eg} - \hat{\sigma}_{ge}) - \Gamma\hat{\sigma}_{ee}\\ \partial_t\hat{\sigma}_{gg} &= -i\Omega/2(\hat{\sigma}_{eg} - \hat{\sigma}_{ge}) + \Gamma\hat{\sigma}_{ee}\\ \partial_t\hat{\sigma}_{ge} &= -(\gamma + i\Delta)\hat{\sigma}_{ge} - i\Omega/2(\hat{\sigma}_{ee} - \hat{\sigma}_{gg})\end{aligned} \tag{2.81}$$

where $\hat{\sigma}_{ij} = \text{ı}\rangle\langle j|$ is the internal state atomic operator between the $|i\rangle$ and $|j\rangle$ states in the rotating frame.

Steady state solution

In realistic situations, due to relaxations the system eventually irreversibly relaxes to some *steady state*. The steady state solution to the Bloch equations for 2-level atoms is reached when the time derivatives vanish. For instance, solving first the equation in 2.82 in the steady state, we have

$$\sigma_{ee}(t \to \infty) = \frac{\Gamma}{4\gamma}\frac{s}{(1+s)^2} \tag{2.82}$$

where s is the saturation parameter [2] and is defined as

$$s = \frac{\Omega^2/\gamma\Gamma}{1 + \Delta^2/\gamma^2}. \tag{2.83}$$

The steady state solution is very useful in finding a simple physical picture of the combined atom-light system and will be used frequently throughout this thesis.

Mapping a single mode field into N atoms

Consider the interaction of a single mode field, $\hat{a}$, with N two-level atoms ($|1\rangle$ and $|2\rangle$) . This interaction is firstly formulated below in the dressed state picture. When all of the atoms are prepared initially in level $|1\rangle$, the only states coupled by the interaction are

$$|A\rangle = |1^N 2^0, 1_a\rangle \tag{2.84}$$

$$|B\rangle = |1^{N-1} 2^1, 0_a\rangle. \tag{2.85}$$

These states are initially degenerate, and to be clear state $|A\rangle$ represents a state with N atoms in atomic state $|1\rangle$, zero in $|2\rangle$ and one photon in mode a. The dynamics of this system is described by the interaction Hamiltonian

$$\hat{H} = \hbar g \hat{a}\hat{\sigma}_2^\dagger\hat{\sigma}_1 + H.c. \tag{2.86}$$

Given that

$$\hat{a}\hat{\sigma}_2^\dagger\hat{\sigma}_1|A\rangle = \hat{a}\hat{\sigma}_2^\dagger\hat{\sigma}_1|1^N 2^0, 1_a\rangle = \sqrt{N}|1^{N-1}2^1, 0_a\rangle \tag{2.87}$$

$$= \sqrt{N}|B\rangle. \tag{2.88}$$

The matrix elements of the Hamiltonian can be calculated as

$$\langle A|\hat{H}|B\rangle = \hbar g^* \sqrt{N} \tag{2.89}$$
$$\langle B|\hat{H}|A\rangle = \hbar g \sqrt{N} \tag{2.90}$$
$$\langle A|\hat{H}|A\rangle = 0 \tag{2.91}$$
$$\langle B|\hat{H}|B\rangle = 0. \tag{2.92}$$

The eigenvalues and eigenstates of the system can then be obtained as $\lambda = \pm\hbar g\sqrt{N}$ and $|\Psi\rangle = \frac{1}{\sqrt{2}}(|A\rangle \pm |B\rangle)$, respectively.

This is equivalent to assuming N photons interacting with a single atom in a cavity, which is a well-known cavity quantum electrodynamic (QED) problem. In this case, the states and Hamiltonian of the system can then be equivalently written as

$$|A'\rangle = |1^1 2^0, 1_a\rangle \tag{2.93}$$
$$|B'\rangle = |1^0 2^1, 0_a\rangle \tag{2.94}$$
$$\hat{H}' = \hbar g\sqrt{N}\hat{a}\hat{\sigma}_2^\dagger\hat{\sigma}_1 + H.c. \tag{2.95}$$

This Hamiltonian is essentially the single atom, Jaynes-Cummings type of Hamiltonian with $g \to g\sqrt{N}$.

Now we take an alternative approach to this problem and describe the system using the bare atomic levels. Again we will show that the effective atom-light coupling is strengthened by a factor of $\sqrt{N}$ due to N possible ways of distributing one photon among N atoms. The initial and final collective atomic states can then be written as

$$|A\rangle = |11...1\rangle \tag{2.96}$$
$$|B\rangle = \frac{1}{\sqrt{N}}\sum_i^N |11...2_i...1\rangle. \tag{2.97}$$

The $\sqrt{N}$ appears due to the permutation of a single excitation among N atoms. This factor would be different if there is more than one excitation. For instance for two excitations we would have:

$$|BB\rangle = \frac{1}{\sqrt{2N(N-1)}}\sum_{j\neq i=1}^N |11...2_i...2_j...1\rangle. \tag{2.98}$$

The Hamiltonian is given by

$$\hat{H} = \hbar g\hat{a}\sum_i^N |1\rangle_i\langle 2|_i + H.c. \tag{2.99}$$

and the elements of the Hamiltonian matrix for a single excitation are then calculated as

$$\langle A|\hat{H}|B\rangle = \hbar g\langle 11...1|\frac{\sum_{i,j}^{N}|1\rangle_i\langle 2|_i|1...2_j...1\rangle}{\sqrt{N}}$$
$$= \hbar g\frac{1}{\sqrt{N}}\sum_{i,j}^{N}\delta_{ij} = \hbar g^*\sqrt{N} \tag{2.100}$$
$$\langle B|\hat{H}|A\rangle = \hbar g\sqrt{N} \tag{2.101}$$
$$\langle A|\hat{H}|A\rangle = 0 \tag{2.102}$$
$$\langle B|\hat{H}|B\rangle = 0. \tag{2.103}$$

The eigenvalues of the system can then be obtained $\lambda = \pm\hbar g\sqrt{N}$. This treatment has been used in some literature [32, 33] to find the equations of motion, where the term $\sum_i^N |1\rangle_i\langle 2|_i$ is replaced by $\sqrt{N}\hat{S}_{12}$ and $\hat{S}_{12}$ refers to a collective atomic operator.

In order to generalise this theory to multimode fields we discuss the propagation of light in three-level media under conditions of electromagnetically-induced transparency (EIT) in the following section.

2.4 Light interaction with a Λ-atom

Consider a three-level atom interacting with two coherent light fields (probe and control fields) as shown in Fig. 2.10. The interaction Hamiltonian of this system can be written as

$$H_{\text{int}} = -\hbar/2(\Omega_p\hat{\sigma}_{31}e^{i\Delta_p t} + \Omega_c\hat{\sigma}_{32}e^{i\Delta_c t} + H.c.) \tag{2.104}$$

where Ω_p and Ω_c denote the Rabi frequency associated with the probe and control fields, respectively. The frequency detuning of the probe and control fields from the excited state are Δ_p and Δ_c, respectively.

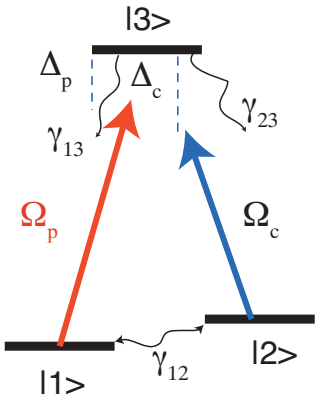

Figure 2.10: A three-level atom, with frequency spacings ω_{31} and ω_{32}, interacts with a probe field with frequency ω_p and Rabi frequency Ω_p and control field ω_c and Rabi frequency Ω_c in a Λ configuration. The ground and excited state decay rates are γ_{12} and γ_{13}. $\Delta_{p/c}$ is the detuning of the probe/control field from the excited state.

The dynamics of laser-driven atomic systems are governed by the *master equations*

[34] for the atomic density operator that can be obtained considering a small quantum system coupled to a large system with infinite states (reservoir or bath) [1]. The master equation for the system depicted in Fig. 2.10 is given by

$$\begin{aligned}\frac{d\rho}{dt} = 1/(i\hbar)[H_{\text{int}}, \rho] + \gamma_{31}/2(2\sigma_{13}\rho\sigma_{31} - \sigma_{33}\rho - \rho\sigma_{33}) \\ +\gamma_{32}/2(2\sigma_{23}\rho\sigma_{32} - \sigma_{33}\rho - \rho\sigma_{33}) \\ +\gamma_{12}/2(2\sigma_{22}\rho\sigma_{22} - \sigma_{22}\rho - \rho\sigma_{22})\end{aligned} \tag{2.105}$$

where the second and third terms on the right-hand side describe spontaneous emission (Langevin noise) from state $|3\rangle$ to states $|1\rangle$ and $|2\rangle$, with rates γ_{13} and γ_{23}, respectively. The last term describes population shuffling and dephasing between two ground states. The master equation is written in the Schrödinger picture. In the following section, however, we take an alternative approach and derive the equations of emotion in the Heisenberg picture, for simplicity.

2.4.1 Electromagnetically induced transparency

When light frequency matches energy splitting between particular atomic levels, a resonance condition occurs and the optical response of the medium is greatly enhanced. Light propagation is then accompanied by absorption and dispersion. However, in a Λ-scheme, where a strong control field (or even intra-cavity vacuum field [35]) resonantly interacting with the excited states and an auxiliary state, the optical response of the medium can be significantly altered. In this regime , known as electromagnetically induced transparency (EIT) [36, 37], the two possible pathways in which light can be absorbed by atoms undergo quantum interference. Due to destructive interference, the absorption vanishes and a narrow transparency window is opened inside the opaque medium and is accompanied by strong dispersion. The combination of these two effects stimulates the atoms into a superposition of the two ground states, which is decoupled from the excited state. The atoms are then said to be in the "dark states".

Description of slow light propagation

To mathematically describe the EIT regime, we consider the interaction of a multimode field with N three-level atoms. The Λ structure under consideration is depicted in Fig. 2.10. A quantised electromagnetic field with the positive frequency part of the electric component is defined as

$$\mathbf{E} = \sqrt{\frac{\hbar\omega}{2\epsilon_0 V}} \sum_k \epsilon_k \hat{a}_k u_k(r) e^{-i\omega t} \tag{2.106}$$

that couples the transition between the ground state $|1\rangle$ and the excited state $|3\rangle$ with Rabi frequency of $\Omega_p = \mu_{\mathbf{13}}.\mathbf{E}/\hbar$. Furthermore, the upper level $|3\rangle$ is coupled to the stable state $|2\rangle$ via a coherent control field with Rabi frequency Ω_c.

The interaction of the light with an ensemble of atoms can be described through collective atomic operators [38]. The atomic ensemble, with the total atom number N and length L, is divided into thin slices dz along the propagation axis. Each slice is assumed

thick enough to contain $N_z \gg 1$ and thin enough that the resulting collective field can be considered continuous. The slowly varying operators are introduced as

$$\hat{\tilde{\sigma}}_{\mu\nu}(t,z) = \frac{1}{N_z}\sum_{i=1}^{N_z}\hat{\sigma}^i_{\mu\nu}e^{-i\omega_{\mu\nu}(t-z_i/c)} \tag{2.107}$$

$$\hat{\tilde{\sigma}}_{\mu\mu}(t,z) = \frac{1}{N_z}\sum_{i=1}^{N_z}\hat{\sigma}^i_{\mu\mu} \tag{2.108}$$

$$\hat{\mathcal{E}}(t,z) = \sum_k \hat{a}_k e^{ikz}. \tag{2.109}$$

We assume a continuum of annihilation operators $\hat{a}_k$ for the field modes of different k that satisfy the commutation relation

$$[\hat{a}_k, \hat{a}^\dagger_{k'}] = \delta(k-k'). \tag{2.110}$$

Using the collective operators defined in Eqs. 2.107, the interaction Hamiltonian of the three-level system can be expressed in terms of the collective atomic operators [38] by replacing $\sum_{i=1}^{N_z}$ by $\frac{N}{L}\int dz$ as

$$\hat{H}_{int} = \hbar g\frac{N}{L}\int_o^L(\hat{\mathcal{E}}(t,z)\hat{\tilde{\sigma}}_{31}(t,z) + \Omega_c e^{i\Delta_c t}\tilde{\sigma}_{32} + H.c.)dz \tag{2.111}$$

where $g = \mu_{13}\sqrt{\frac{\omega}{2\hbar\epsilon_0 V}}$ is the atom-light coupling constant. We also performed a transformation into a frame that rotates with the laser frequency.

To find the equations of motion for the envelope field operator $\hat{\mathcal{E}}$ we write the Heisenberg equation of motion for a field $\hat{\mathcal{E}}(t,z)$

$$\frac{\partial}{\partial t}\hat{\mathcal{E}}(t,z) = \frac{1}{i\hbar}\int dk[\hat{a}_k, \hat{H}_{int} + \hat{H}_L]e^{ikz} \tag{2.112}$$

where $\hat{H}_L = \hbar\sum_k \hat{a}^\dagger_k\hat{a}_k\omega_k$ is the light field Hamiltonian. Using

$$\left[\hat{\mathcal{E}}(z), \hat{\mathcal{E}}^\dagger(z')\right] = L\delta(z-z') \tag{2.113}$$

$$[\hat{a}_k(t,z), H_L] = \hbar ck\hat{a}_k(t,z) \tag{2.114}$$

and the spatial Fourier transform of Eq. 2.114, we obtain an equation of motion for the collective evolution of the all optical modes

$$(\frac{\partial}{\partial t} + c\frac{\partial}{\partial z})\hat{\mathcal{E}}(t,z) = \frac{1}{i\hbar}\left[\hat{\mathcal{E}}(t,z), \hat{H}_{int}\right] \tag{2.115}$$

$$= igN\tilde{\sigma}_{13} \tag{2.116}$$

The atomic evolution is governed by a set of Heisenberg-Langevin equations. Using Eqs. 2.107 and 2.108 and considering the following relations

$$\left[\sum_{j=1}^{N_z}\sigma_{13}^{j},\sum_{i=1}^{N_z}\hat{\sigma}_{31}^{i}\right] = \sum_{j=1}^{N_z}\sigma_{11}^{j}-\sigma_{33}^{j}=N_z(\tilde{\sigma}_{11}-\tilde{\sigma}_{33}) \tag{2.117}$$

$$\left[\sum_{j=1}^{N_z}\sigma_{12}^{j},\sum_{i=1}^{N_z}\hat{\sigma}_{23}^{i}\right] = \sum_{j=1}^{N_z}\sigma_{13}^{j}=N_z\tilde{\sigma}_{13} \tag{2.118}$$

we arrive at

$$\begin{aligned}\dot{\tilde{\sigma}}_{12} &= -(\gamma_{12}-i\delta)\tilde{\sigma}_{12}+i\Omega_c^{\star}/2\tilde{\sigma}_{13}-ig\hat{\mathcal{E}}\tilde{\sigma}_{32}+\hat{F}_{12}\\ \dot{\tilde{\sigma}}_{13} &= -(\gamma_{31}-i\Delta)\tilde{\sigma}_{13}+ig\hat{\mathcal{E}}/2(\tilde{\sigma}_{11}-\tilde{\sigma}_{33})+\hat{F}_{13}\\ \dot{\tilde{\sigma}}_{32} &= -(\gamma_{32}-i\Delta)\tilde{\sigma}_{32}+i\Omega_c^{\star}/2(\tilde{\sigma}_{33}-\tilde{\sigma}_{22})-ig\hat{\mathcal{E}}^{\star}\tilde{\sigma}_{12}+\hat{F}_{32}\end{aligned} \tag{2.119}$$

where $\delta=\Delta_p-\Delta_c$ is the two-photon detuning and $\Delta=\Delta_c$ is the one photon detuning. The Langevin noise operators [1] F_{ij}, whose explicit form is not of interest here, describe the coupling of the atoms to vacuum modes of large reservoirs and include spontaneous emission noise and ground state dephasing. Solving the above equations in the steady state, assuming all population are initially pumped to state $|1\rangle$ and neglecting noise terms ($F_{ij}=0$), one can obtain an expression for the linear susceptibility of the medium [37]

$$\begin{aligned}\chi^{(1)}(\omega)=\mu_{13}^2N/\epsilon_0\hbar V[&\frac{4\delta(|\Omega_c|^2-2\delta\Delta)-4\Delta\gamma_{12}^2}{||\Omega_c|^2+(\gamma_{13}+i2\Delta)(\gamma_{12}+i2\delta)|^2}\\ &+i\frac{8\delta^2\gamma_{13}+2\gamma_{12}(|\Omega_c|^2+\gamma_{12}\gamma_{13})}{||\Omega_c|^2+(\gamma_{13}+i2\Delta)(\gamma_{12}+i2\delta)|^2}]\end{aligned} \tag{2.120}$$

This linear susceptibility contains many of the important features of EIT. The real and imaginary parts of susceptibility are plotted in Fig. 2.11 (a) and (b) respectively (solid red lines) as a function of the two-photon detuning δ assuming $\Delta=0$. Maximum transmission occurs when the two beams are on resonance.

The steep variation of the real part of susceptibility for frequencies inside the transparency window indicates a large refractive index change. This means that light with frequencies inside the transparency window propagates through the medium with a group velocity much lower than c. The imaginary part of the susceptibility describes absorptive properties of the medium (thereby modifying the signal-field intensity transmission coefficient T), whereas the real part determines the medium refractive index n:

$$\begin{aligned}T(\omega)&=e^{-\mathrm{Im}[\chi(\omega)]kL},\\ n(\omega)&=1+\mathrm{Re}[\chi(\omega)]/2.\end{aligned} \tag{2.121}$$

The associated reduced group velocity and transparency frequency bandwidth can be written as

$$v_g = \frac{d\omega_p}{dk_p}=c\Omega_c^2/(\Omega_c^2+g^2N)\simeq\frac{\Omega_cL}{d\gamma} \tag{2.122}$$

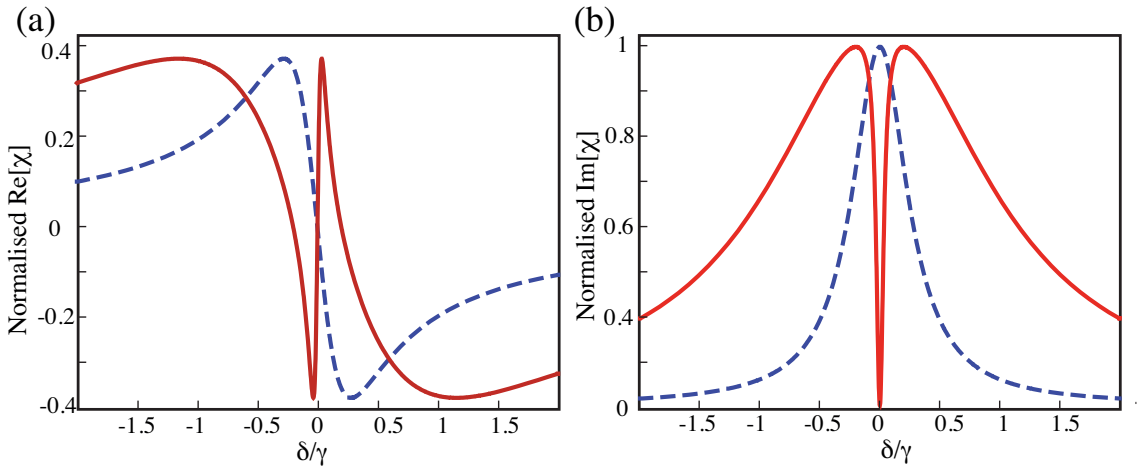

Figure 2.11: Real (a) and imaginary (b) parts of susceptibility plotted as a function of two-photon detuning. The solid line and dashed line indicate susceptibility for three- and two-level atoms, respectively.

and

$$\Delta\omega_{\text{trans}} \simeq \frac{\sqrt{d}v_g}{L} \tag{2.123}$$

respectively, where $\gamma = \gamma_{13} \simeq \gamma_{23}$ is the spontaneous emission rate from the excited state, L is the length of the atomic ensemble and $d = g^2NL/\gamma c$ is the optical depth (OD). In fact, the OD of a sample specifies the strength of atom-light interaction. Note that approximation in Eq. 2.122 is only valid at limits of large OD. From the above expressions it can be seen that the group velocity and width of the transparency window can be controlled by the control field Rabi frequency. One can reduce the group velocity of light by decreasing the control field intensity at the expense of losing the bandwidth, because the transparency window becomes narrower. Low group velocities for large-frequency bandwidth pulses of light can be simultaneously achieved only at large optical densities, $d \gg 1$. In other words, the delay-bandwidth product $\Delta\omega_{\text{trans}}\tau$ (where $\tau = L/v_g$) of EIT scales with the square root of the optical depth. Using EIT in cold atomic samples, group velocities down to 17 m/s have been achieved [39].

We note here that for a Doppler-broadened atomic ensemble (with a Doppler width of Γ_d), at low Ω_c, the EIT width is given by

$$\Delta\omega_{\text{trans}} \simeq \gamma_{12} + \frac{\Omega_c^2}{\sqrt{d}(\Gamma_d+\gamma)}. \tag{2.124}$$

Using this equation one can measure the ground state decoherence rate (γ_{12}) by varying the control field power [40] and extrapolating values to zero power.

In the next chapter, we will discuss that how the EIT phenomenon can be used to store light in an atomic memory.

2.4.2 Raman scattering

Raman scattering refers to a category of light-matter interactions during which incident photons interact with atomic energy levels of the material so that new photons with a different frequency are generated. Many different types of Raman scattering interactions [41] exist, in particular, coherent anti-Stokes Raman scattering (CARS) and stimulated as well as spontaneous Stokes Raman scattering.

Spontaneous Stokes Raman scattering is a process by which an atom in its ground state is first pumped into an excited state and then decays to a lower excited electronic state while spontaneously emitting a photon with an energy equal to the energy difference between the ground and excited states. In the case that this process continues in the presence of the first emitted photon, the newly generated photon will have the same frequency, phase and direction as the previous one. The spontaneous fluorescence process can then turn into the stimulated emission process that resembles the operation of most lasers and optical amplifiers. The schematic atomic transition schemes of Stokes and anti-Stokes Raman scattering are shown in Fig. 2.12 (a) and (b), respectively. The energy of the Stokes/anti-Stokes photon is less/more than the absorbed pump photon.

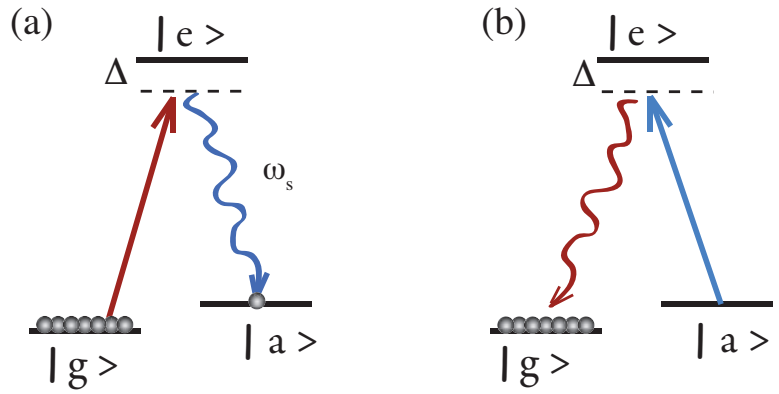

Figure 2.12: Schematic of (a) Stokes and (b) anti-Stokes Raman scattering.

The stimulated Stokes Raman scattering (SSRS) is often the most dominant non-spontaneous Raman process, however, in practice it is always accompanied by two other non-spontaneous Raman processes, namely CARS and stimulated anti-Stokes Raman scattering (SARS). Whereas SSRS generates Stokes photons with a frequency ω_s that is Raman down-shifted with respect to the pump frequency ω_p, CARS is able to generate so-called anti-Stokes photons with a frequency ω_{as} that is Raman up-shifted with respect to ω_p. CARS is generally described as a nonlinear four-wave mixing (FWM) process - an interaction involving four electromagnetic waves - that can only take place in a Raman-active medium.

2.4.3 Light shift

When light of intensity $I(r,z)$, frequency ω_l , and polarisation $q = 0, \pm 1$ [corresponding to linear, right (+) and left (-) circular polarisations, respectively] is shone onto an atom, there will be a change in the energy of the internal states. This is known as the ac Stark effect. For alkali-metal atoms, this effect can be calculated for a given ground state $|g\rangle = |1/2, F, m_F\rangle$ from second-order time-dependent perturbation theory [42] to be

$$U_{F,m_F}(\omega_l, q, I) = \frac{I(r,z)}{2c\epsilon_0\hbar} \sum_a \frac{|\langle a|e\hat{\mathbf{r}}.\epsilon_{\mathbf{q}}|g\rangle|^2}{\omega_l - \omega_{ag}} \tag{2.125}$$

where $e\hat{\mathbf{r}}$ is the electric dipole, and $|g\rangle$ and $|a\rangle$ are ground and excited atomic states with which light is interacting.

2.5 Summary

We have introduced the basic concepts and theory of atom-light interactions that can generally be applied to various systems. Most of the theory described here will be frequently used throughout this thesis to describe particular schemes.

Chapter 3

Literature Review on Optical Storage

"My journey has been as long as yours. I had to learn to hold a light, lest its brilliance destroy me."

Andromeda: Fear Burns Down to Ashes

The bandwidth and versatility of optical devices has revolutionised information technology systems and communication networks. Precise and arbitrary control of an optical field that preserves optical coherence is an important requisite for many proposed photonic technologies. For quantum information applications, a device that allows the storage and on-demand retrieval of arbitrary quantum states of light would form an ideal quantum optical memory.

An ideal quantum optical memory must be capable of coherently storing multiple quantum states of light for on-demand recall with memory fidelity beyond the classical limit. Arriving at this goal is a challenge for experimentalists and extensive research efforts have been dedicated to the development of such a quantum memory for the last decade.

In this chapter, we review different techniques proposed, to date, to coherently store optical states. In the first three sections we discuss memory schemes that do not require coherent interaction of light with atomic ensembles and are based on either free space optical loops or parametric processes. The rest of the chapter is dedicated to optical memory schemes that rely on the controlled coherent interaction of light with atoms to store, manipulate and retrieve optical pulses. These schemes can be divided into two categories: those that utilise transmissive properties of materials to slow down or store light, such as electromagnetically induced transparency (EIT), four-wave mixing (FWM), and off-resonance Faraday interaction protocols, and other schemes that rely on absorptive properties of the medium such as photon echoes and Raman processes.

3.1 Delay and storage in optical waveguides

3.1.1 Optical Fibres and Cavities

The easiest approach to delay the light is to increase the distance travelled by photons using an optical delay line, such as an optical fibre or cavity. The development of high-quality optical fibres with good transmission capabilities has significantly impacted the global communication network. The 2009 Nobel prize was awarded for work dedicated to optical fibres due to its impact on technology. The success of fibre technology is due to its wide bandwidth, its unique low-loss performance, and also its extremely low production cost.

Fibre delay lines have been used as the simplest form of quantum memory to synchronise and transform signals [43]. However, to induce a delay of 50 μs, light needs to propagate through a 15 km fibre in which, with current technology, at least 50% of the light will be lost through propagation. On the other hand, for fibres to be adapted as a coherent memory, or even as classical delay channels (used to optimise the flow of data traffic in future networks), the lack of a tuneable delay is a severe drawback of simple delay lines. Experimental demonstration of an all-optical cyclical quantum memory (CQM) [44] device based on the storage of photonic qubits in a simple free-space optical loop was performed for down-converted photons [45].

Alternatively, light can be delayed in a high-Q cavity that allows photons to transmit through the cavity with variable probability depending on the mirror separation. When the cavity is on-resonance with the incoming light, the light cycles back and forth between the reflecting mirrors, allowing it to stay inside the cavity. The light can then be retrieved by dynamically driving the cavity off-resonance. For instance, it was demonstrated in a basic experimental setup that 600 round trips between two 15 cm-diameter mirrors spaced 2.5 m apart provides ten microseconds of time delay, with an optical insertion loss of 12 dB [46]. To date, some proposals have been suggested which rely on optical cavities as a method for light storage [47, 48]. It was proposed by Lloyd et al. that quantum entanglement over long distances can be created and stored by using a single atom in a high-Q cavity [49]. Furthermore, experiments were performed to demonstrate the storage of single photons generated by parametric down conversion [50, 51]. It was recently shown that coherent light pulses (with a duration of 1.90 ns) can be stored for 1.45 ns in wavelength-scale photonic crystal cavities that have a tuneable Q factor [52]. In this experiment the dynamic Q-tuning was done using timing-controlled pump pulses, which allows control over the storage time. However, due to the short cycle time, the light must make many round trips inside the cavity to provide the minimum storage time required and this will limit the storage efficiency due to the insertion loss.

3.1.2 Stimulated Brillouin Scattering

One way to accomplish tuneable delay in optical fibres is to use the stimulated Brillouin scattering (SBS) technique. Brillouin scattering is an interaction of light waves (photons) with acoustic or vibrational waves (phonons). This interaction is an inelastic scattering process in which a phonon is either created (Stokes process) or annihilated (anti-Stokes process). The energy of the scattered light is slightly changed: the energy is decreased for a Stokes process and increased for an anti-Stokes process. Brillouin scattering is similar to Raman scattering, discussed in the previous chapter, where both phenomena represent inelastic scattering processes of light. In a Raman scattering process, the photons are usually scattered by interactions with the rotational transitions of atomic dipoles (resulting in a change of the atomic angular momentum), while in the case of Brillouin scattering the scattering of photons happens due to interactions with acoustic waves (phonons).

The electric field or light field itself can generate acoustic waves stimulated by electrostriction (elastic deformation of a dielectric induced by an electric field) in media such as optical fibre. The beam may undergo Brillouin scattering from these acoustic vibrations, usually in the opposite direction to the incoming beam. This parametric process is known as stimulated Brillouin scattering (SBS).

Phonons created using SBS can efficiently grow while having a long lifetime. SBS can be adapted to delay or store optical fields. The first experimental demonstrations of

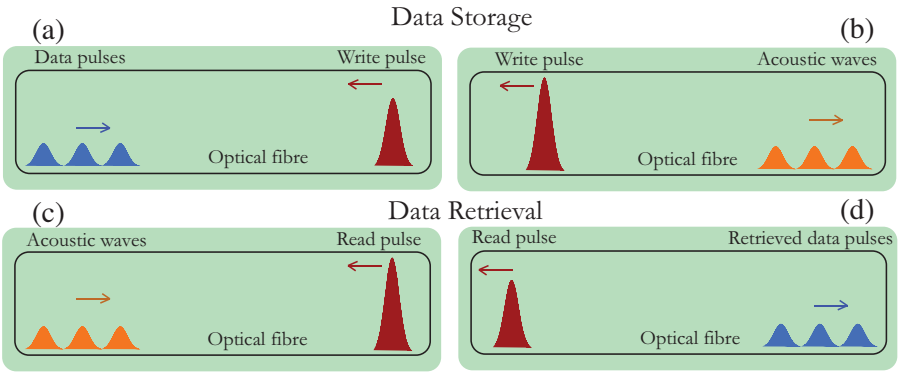

Figure 3.1: Schematic plot of the data storage sequence in an SBS scheme. A short, intense write pulse causes the data pulses to become depleted with the information being stored as an acoustic wave in the fibre (a,b). In the retrieval stage (c), a short, intense read pulse at the same frequency as the write pulse depletes the acoustic wave and converts the data back to the original optical frequency, thereby reconstructing the incident data pulses (d).

SBS-induced slow light in optical fibres were reported in 2005 [53] and independently soon after by a different group [54]. In the simplest configuration, two optical waves, an intense write field and a weak signal field, to be stored and propagating in opposite directions in a single-mode fibre, create a longitudinal acoustic wave which induces a dynamic Bragg grating in the fibre core. As a result of the slow velocity (around 5,800 m.s^{-1}) of the phonons compared with the photons in the fibre, the phase-matching criteria require that the two lightwaves must counter-propagate, and phase matching is only possible under very strict conditions. An efficient conversion to the acoustic wave is observed only if the frequency difference between the optical waves is precisely set to a value known as the Brillouin frequency shift, which is equal to the acoustic wave frequency.

Coherent large bandwidth optical storage via SBS also appears to be a promising approach [55]. In this storage process, a short, intense write pulse that is red-detuned from the signal field frequency by the Brillouin frequency shift causes the data pulses to become depleted (Fig. 3.1 a) with the information being stored as an acoustic wave in the medium (Fig. 3.1(b)). In the retrieval process (Fig. 3.1 (c)), a short intense read pulse at the same frequency as the write pulse depletes the acoustic wave and converts the data back to the original optical frequency, thereby producing a replica of the incident data pulses (Fig. 3.1(d)). The results of this experiment [55] show that stored pulses can be retrieved later, after a time interval of 12 ns which is mainly limited by the lifetime of the acoustic excitation. The results were reported for storage of a single pulse; 2 ns-long pulses are stored with a readout efficiency of 29% at 4 ns storage time and 2% at 12 nanoseconds. It is shown also that this memory is capable of storing multiple pulses of light, which indicates that this approach has the potential to be used as a broadband optical delay line.

The SBS process is described mathematically by one-dimensional coupled wave equations involving a forward data field, a backward control field, and a forward acoustic field [56]. It can be shown that complete storage of the data signal requires the fulfilment of four conditions. The first condition is that the area of the pulse should be equal to $\pi/2$ for both the write and read pulses. The second condition is that the write and read pulses must have a bandwidth larger than any data pulses to be stored. Third, the storage time

must be less than the acoustic lifetime. Finally, the spatial extent of the data packet must be less than twice the length of the storage material. Under these conditions, the entire spectrum of the data pulses can be reliably recorded and retrieved.

3.1.3 Trapped light in a metamaterial waveguide

Recently, materials with negative refractive indices have attracted attention for many applications. Probably the most important among them are so called "perfect lenses" [57], which focus all Fourier components of a 2D image, including evanescent modes, thus providing resolutions beyond the diffraction limit. Very recently Tsakmakidis et al. [58] showed theoretically that a material with a negative refractive index can be adapted to store optical data coherently. To understand this scheme, let us first look at the properties of materials with negative refractive indices.

Although there is no naturally-occurring material with a negative refractive index, methods were proposed for its practical implementation [59, 60]. Some composite materials, if built properly, show negative permeability and permittivity for microwaves. This can be attained by putting split-ring resonators and metallic wire strips together in a periodic structure inside some materials. Materials built this way are called metamaterials. It can be mathematically shown that when the permeability and permittivity of a material is negative the refractive index of the materials is negative [61] because of causality. Materials with negative refractive indices are also called left-handed materials(LHM).

Consider a light beam propagating through an optical pipe where a ray of light bounces back and forth off the walls and propagates. Due to total internal reflection, light experiences a phase shift and consequently a lateral displacement each time it strikes the interfaces of the core [62]. This displacement is called Goos-Hanchen displacement [63] which is negative for LHMs. Negative Goos-Hanchen displacement in left-handed materials seen by the light field is the key to this method of light storage. Due to the negative Goos−Hanchen displacement, the point at which the incident and reflected rays meet will sit inside the left-handed core and the effective thickness of the guide will be smaller than its physical thickness. The combined effect of the phase shifts from the walls can be such that the thickness of the waveguide core becomes effectively zero ($2\alpha + x_1 + x_2 = 0$), see Fig. 3.2. Since this displacement is frequency dependent, for some particular frequency and physical core thickness light does not propagate and is stopped in the waveguide. When the lateral displacement differs such that the effective thickness becomes larger or smaller than zero, the light field will propagate forward or backward, respectively.

Knowing this fact, one can store multifrequency optical pulses in a tapered waveguide constructed from LHM. Since the lateral displacement of the light depends on the frequency of the light, it is expected that by gradually reducing the physical core thickness along the waveguide, there would be a point for each frequency of light where the effective thickness of the guide will vanish and each frequency component of light will be stopped longitudinally at a different positions. In principle, using a tapered waveguide, it is possible to stop different frequencies of the optical data at different positions of the waveguide. In this scenario, releasing optical pulses cannot be easily achieved.

An immediate question is whether the negative index-of-refraction property can be implemented at optical frequencies. The first LHM built at the University of California [61], based on split-ring resonators and metallic wires with dimension control on a unit cell of about 3 cm, was used to show experimental scattering data at microwave frequencies

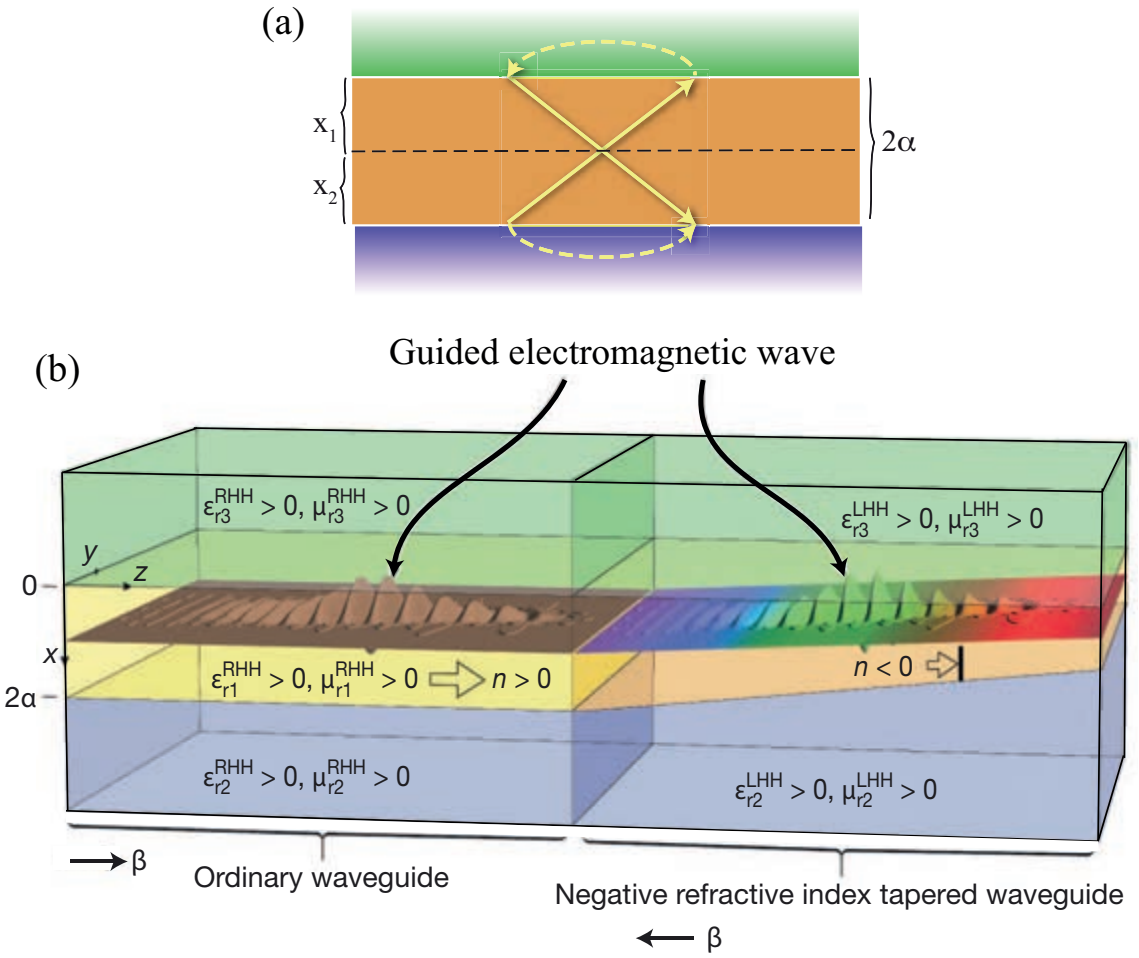

Figure 3.2: (a) Schematic demonstration of stopped light in the core waveguide. The two lateral displacements can become such that $x_{12} + x_{13} = 2\alpha$ exactly. In this case, the effective thickness, t_{eff}, vanishes and the ray becomes trapped, forming a double light cone. 2α here is the physical thickness of the waveguide core. (b) Schematic of a trapped rainbow showing different frequency components of a guided wave packet stopped at correspondingly different thicknesses inside a tapered waveguide made of left-handed materials (LHM). Figure taken from Ref. [58]

which exhibits a frequency band where the effective index of refraction is negative. Today, thanks to current technology, nanofabrication of split ring resonators to build metameta-materials in the infrared range is feasible [64, 65], which is promising for experimental implementations of this memory scheme in the near future.

3.2 Transmissive Atomic Memories

In the rest of this chapter we focus on memory schemes based on the coherent interaction of light with atomic ensembles. In this section, we consider controlling the group velocity of the light propagating through atomic ensembles as a storage mechanism.

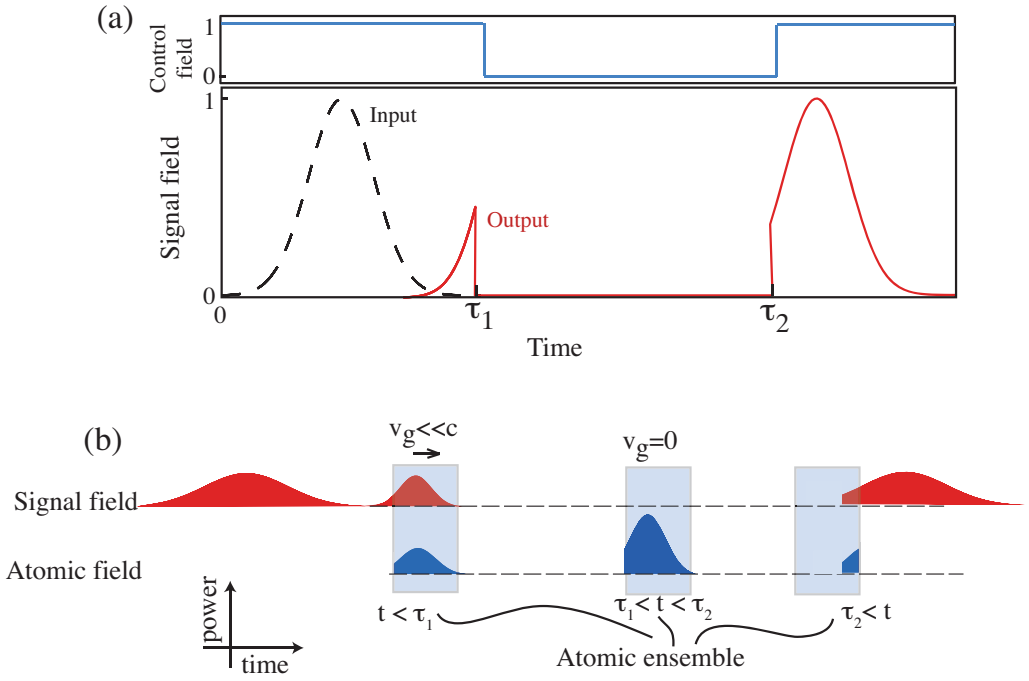

Figure 3.3: (a) Storage and recall of a pulse of light into/from the EIT medium by switching off and on the control field intensity. (b) Schematic light storage showing light and atomic fields at different times.

3.2.1 EIT light storage

The electromagnetically induced transparency (EIT) phenomenon was introduced in the previous chapter. To date, EIT has been suggested and used in various applications in optics and spectroscopy such as magnetic field imaging [66] and formation of solitons [67]. In 2000, Fleischhauer and Lukin suggested EIT as a method of coherent light storage [68]. Here we describe how this phenomenon can be used to store optical information.

To describe light-atom dynamics inside the EIT medium, let us consider the propagation of a single pulse of light in an ensemble of Λ-type atoms. Initially the pulse is outside the medium in which all atoms are in their ground states $|1\rangle$. Assuming the pulse bandwidth fits within the transparency window, after the front edge of the pulse enters the medium it is rapidly decelerated, whereas the back edge still propagates with vacuum speed c. As a result, upon entering the medium, the spatial extent of the pulse is compressed by the ratio c/v_g, while its peak amplitude remains unchanged. The energy of the light pulse is much lower when it is inside the medium compared to a freely propagating field. A small fraction of energy is expended to change the state of the atom, with any excess energy carried away by the control field. Energy is given back to the pulse from the control field as the pulse exits the medium[69, 70]. The spatial extent increases again and the atoms return to their original ground state.

Inside the medium the collective atomic excitation evolves together with the light field. The energy is exchanged back and forth between the electric field and atomic polarisation as the light pulse propagates through the medium.

After the pulse enters the medium and is spatially compressed, one can adiabatically reduce the control field intensity to zero to reduce the group velocity and map the in-

formation into the ground state atomic coherence. In this protocol the group velocity of light is tuned by the control eld intensity so that on demand recall is feasible. After a controllable time, the intensity of the control eld can be intensi ed to increase the group velocity and couple the light out of the medium. A detailed treatment of EIT can be found in Ref. [71, 72]. A schematic of this process is presented in Fig. 3.3 (b). It was shown theoretically that the control eld intensity can also be switched in a non-adiabatic manner [73].

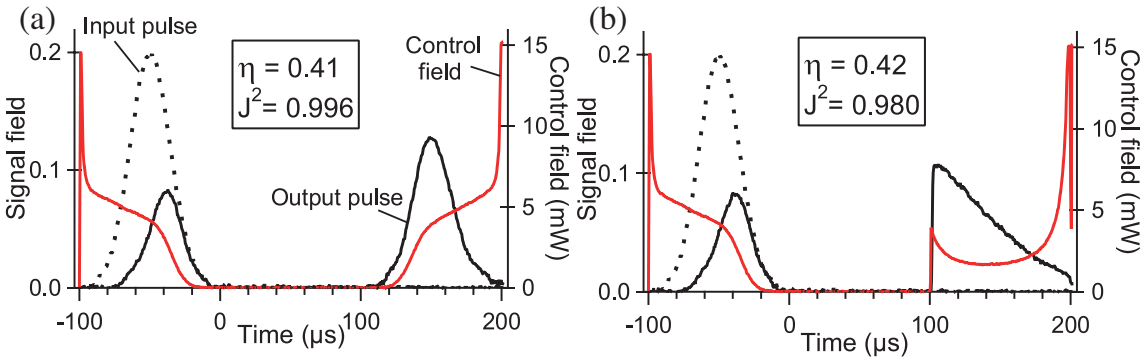

Figure 3.4: An input Gaussian pulse is stored and retrieved either into its original pulse shape (a) or into a ramp pulse shape (b). Figure taken from Ref. [74]

For the optimum storage of a data pulse, a medium is required to provide both a wide transparency window and a low group velocity in order to spatially localise the entire pulse inside the ensemble. Otherwise a fraction of data will leave the medium without interaction. This is shown in Fig. 3.3 (a) where the control eld is switched off between τ_1 and τ_2 while a part of the input pulse is transmitted without storage. It is worth noting that the stored entity is not energy but information. The energy of the probe eld is given to the control eld and leaves the medium, but information is imprinted into the atomic coherence. After the control eld is turned back on, energy is returned to the signal eld to retrieve the stored information in the form of an optical eld.

To date, various experiments have been performed to store classical light pulses as well as quantum states of light via the EIT scheme. The experimental demonstration of light storage via EIT was rst performed in 2001 independently by two different groups [75, 76] where a single pulse of coherent light was stored and recalled after 1 ms [75].

Recently, Gorshkov et al. [33] proposed an optimal control strategy for the storage and retrieval of a photon wave packet of any given shape (provided prior knowledge of the pulse shape). This strategy relies on shaping the control eld intensity in time to minimise the loss and to optimise the storage and retrieval process at a given OD. Using this approach, this group achieved efficiency of 42% in warm ^{87}Rb atoms in a glass cell mixed with 30 Torr of Ne buffer gas [77, 74]. Furthermore, it was experimentally demonstrated that using this method, one can shape the output pulse by choosing the correct control eld shape; see Fig. 3.4. One of the limitations of this method of light storage is that prior knowledge of the input light pulse is required. Achieving a higher memory efficiency with EIT in warm atomic ensembles is currently limited by four-wave mixing processes, where a generated Stokes eld contaminates the output signal eld [77].

The temporal multimode capacity of an optical memory is a crucial requirement for many optical communication applications. This is measured as a quantity which is nor-

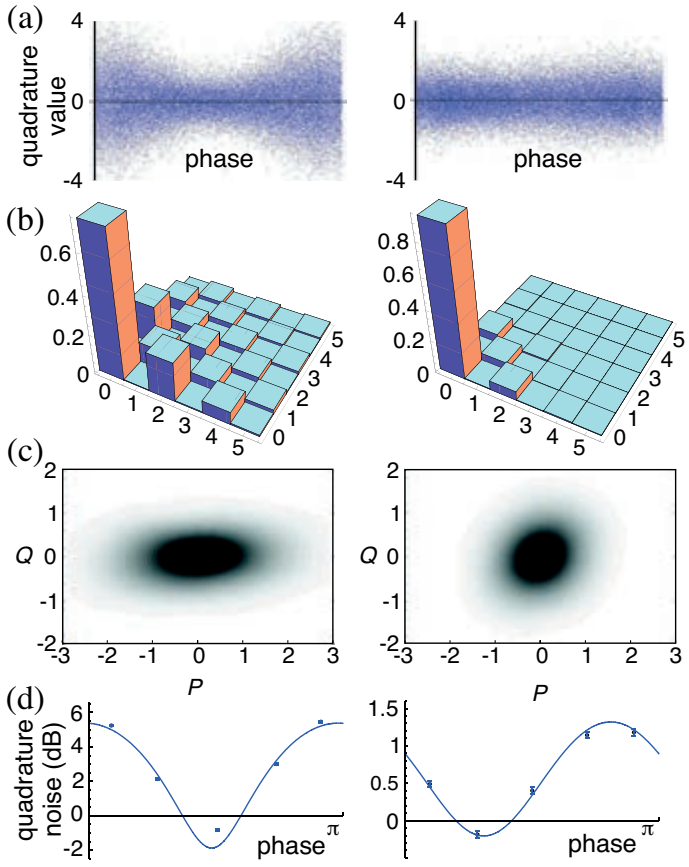

Figure 3.5: Optical squeezed state of the input (left column) and retrieved (right column) states. (a) Data of quadrature noise as a function of phase of the LO. (b) The density matrices obtained using maximum-probability reconstruction in the Fock basis (absolute values), Wigner functions (c) and quadrature noise variances (d) are displayed, [78]. Figure taken from Ref. [78].

mally referred to as the delay-bandwidth product (DBP) (product of data pulse rate and delay). In most EIT experiments the DBP is found to be on the order of one or even less. As mentioned before, the DBP of an EIT system is scaled by the square of the optical depth. The maximum DBP achieved, to date, with slow light is roughly 140, corresponding to a 50-pulse delay, in a hot rubidium experiment using two absorption resonances [79]. There are two effects that limit the bandwidth of EIT: frequency-dependent group velocity that broadens the pulse as it propagates, and also a frequency-dependent transmission that spectrally narrows a pulse [80]. Very recently, the group at University of Calgary experimentally demonstrated that a comb-shaped transparency spectrum enhances the delay-bandwidth product and the light storage capacity for a probe pulse by a factor of about 50 compared to a single EIT line [81]. Furthermore, using EIT arbitrary two-dimensional images have been slowed and stored in warm atomic vapour for up to 30 μs [82].

In principle, EIT can be used for storage of quantum states of light and it can be shown that it does not add extra noise to the output state [83, 84]. Several experiments have been performed to prove that EIT is capable of storage and retrieval of quantum states of light such as a squeezed vacuum state [85, 78]. In 2008, J. Appel et. al. experimentally presented storage and retrieval of a squeezed state of light [78] and measured a fidelity of

$F = 0.89$, which is significantly higher than the classical fidelity of 0.74. The results are presented in Fig. 3.5, where the properties of the input and recalled light are shown on the left and right of the figure, respectively.

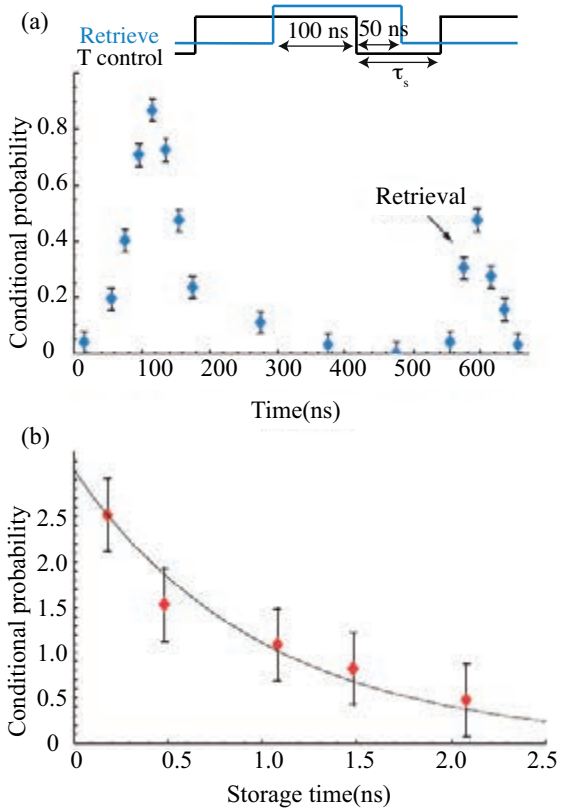

Figure 3.6: Time-resolved measurements of single-photon pulse delay and storage using the EIT technique. (a) Storage and retrieval of a single photon anti-Stokes pulse. The EIT control field is turned off 100 ns after the retrieval from the source ensemble begins; after waiting for a storage time of $t_s = 460ns$, the control field is turned back on, resulting in the retrieved pulse centred at 600 ns. The control field switching dynamics is depicted above. (b) Conditional probability (per 300 ns) of detecting a photon retrieved from the target ensemble for different storage times. The decay of probability is fitted by an exponential with a 1/e characteristic time of about 1 ms; this is consistent with the diffusion of atoms from the interaction volume [86]. Figure taken from Ref. [87].

M. D. Eisaman et. al. in 2005 [87] performed an experiment to measure the time delay associated with the reduced group velocity of single-photon pulses and reported observation of the storage and retrieval of single photons (Fig. 3.6). In this experiment, single photons are created via Stokes and anti-Stokes scattering. The direction, bandwidth, and central frequency of the single-photon anti-Stokes pulse is determined by the direction, intensity and frequency of the retrieving laser beam [88].

Furthermore, Choi et al. [89] demonstrated the creation of entanglement between two atomic ensembles by the coherent mapping of an entangled state of light (generated by splitting a single photon). They showed that entanglement can be reconstructed after a programmable delay with an overall efficiency of 17%. To date, the largest storage time using EIT was achieved by the team at the Australian National University, where

coherence times of seconds have been demonstrated for hyperfine transitions of rare earth ions doped in crystal at cryogenic temperatures [90].

Using the EIT technique, a group in China observed reversible mapping of entangled photons into and out of a remote optically thick cold atomic memory [91]. The entangled photons were generated by building a 5 MHz frequency-uncorrelated double cavity source. The storage of a triggered single photon with arbitrary polarisation is shown to reach an average fidelity of 92% for 200 ns storage time. Also in this experiment, polarisation-entangled photon pairs are prepared, and one of the photons is stored in the atomic memory with the other photon freely propagating. Violation of Bell's inequality was observed for storage time up to 1 μs. This demonstrates that entanglement is stored and survives during storage.

Very recently, it was shown that a single photon created in the atom-cavity system is transported to a Bose-Einstein condensate (BEC) and stored into a collective excitation in the BEC, thus establishing entanglement between the atom inside the optical cavity and the BEC [92]. After a variable delay, this entanglement is converted into photon-photon entanglement. The total fidelity of all concatenated operations was shown to be 95%. This hybrid system could be extremely useful in the field of quantum information.

3.2.2 Light storage using four wave mixing

Four-wave mixing (FWM) refers to a process where three wavelengths interact in a nonlinear medium, and give rise to a fourth wavelength (conjugate beam) which is formed by the scattering of the incident photons. CARS is the most common of all the FWM processes. In this process two photons of frequency ω_1 interact in a nonlinear medium with a single photon of frequency ω_2 to create an output field with a frequency of $\omega_s = 2\omega_1 - \omega_2$. The two input frequencies are chosen so that $\omega_1 - \omega_2$ is near a transition of the medium; this is a coherent version of Raman scattering. The sharp gain feature obtained with four-wave mixing in a double-lambda system [93] leads to a large dispersion over a small frequency range and therefore a large reduction in group velocity.

The ultraslow propagation of matched pulses in nondegenerate four-wave mixing in a hot atomic vapour were observed by a group at NIST in Maryland [93] where probe pulses as short as 70 ns were delayed by a tuneable time of up to 40 ns with little broadening or distortion. Very recently the same group at NIST [94] showed that a four-wave mixing process based on a double-Λ scheme in hot ^{85}Rb vapour allows one to obtain an optically tuneable delay for EPR entangled beams of light. In this experiment a significant delay, on the order of the width of the cross-correlation function, is achieved. The delay can be controlled by changing the value and bandwidth of the gain, which in the case of a gas medium can be done by changing the temperature and pump power used for the four-wave mixing. In principle, it is possible to combine both the temperature and pump power tuning capabilities of the system to obtain even greater delays. However, reducing the pump power decreases the bandwidth of the memory. On the other hand, the gain, associated with the four-wave mixing process itself is the main source of excess noise responsible for the degradation of the output quantum state. It was also shown [94] that FWM can preserve the quantum spatial correlations of entangled beams, see Fig. 3.7.

Recently, a group at the University of Rochester in New York [95] reported an experiment on pulse storage in hot atomic rubidium vapour, in which a four-wave-mixing normal mode is stored using a double-Λ configuration. In this work, the entire waveform of the input signal is recovered after about 120 μs, and a new optical mode (idler) is generated

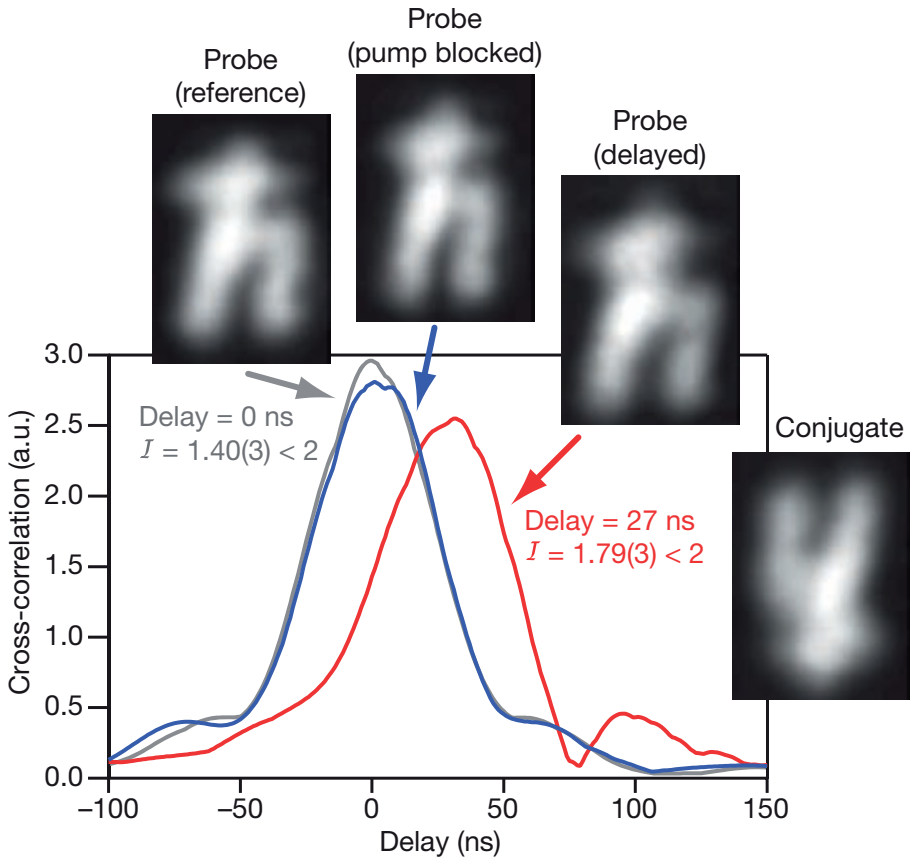

Figure 3.7: Tuneable relative delay of up to 27 ns for entangled images between the probe and the conjugate via FWM. This corresponds to a delay-bandwidth product of 0.45. The spatial pattern for the conjugate is shown on the right side of the figure. The grey curve shows the cross-correlation between probe and conjugate when there is no delay. The red curve shows the cross-correlation at the point where only a small degree of entanglement, $1.79 < 2$, is left between the delayed probe and the conjugate. Figure taken from Ref. [94].

by the four-wave-mixing process.

3.2.3 Off-resonant Faraday interaction

Faraday interaction between light and atomic spin can also be used to map information into atomic spin. In this scheme, coherent storage of light is achieved in three steps: first an interaction of off-resonance photons with atoms; second, a subsequent polarisation measurement of the transmitted light; and third, feedback onto the atoms conditional on the measurement result. The proof of principle experiment performed on warm Cs atoms shows mapping of quantum information to/from an atomic spin wave [96].

In this experiment, initially the atomic ensemble is prepared by optical pumping where the quantisation is defined by a magnetic field along the x axis; hence all the atomic spins will be along the x axis. Whereas, due to the quantum uncertainty principle, the other two projections of spin angular momentum are not zero:$\langle \delta J_y^2 \rangle = \langle \delta J_z^2 \rangle = 1/2J_x$. Consider a light pulse detuned from atomic transition and polarised along y axis interacting with this atomic ensemble. The z component of angular momentum will cause Faraday rotation of the optical field. This rotation can be measured after the atomic ensemble and results

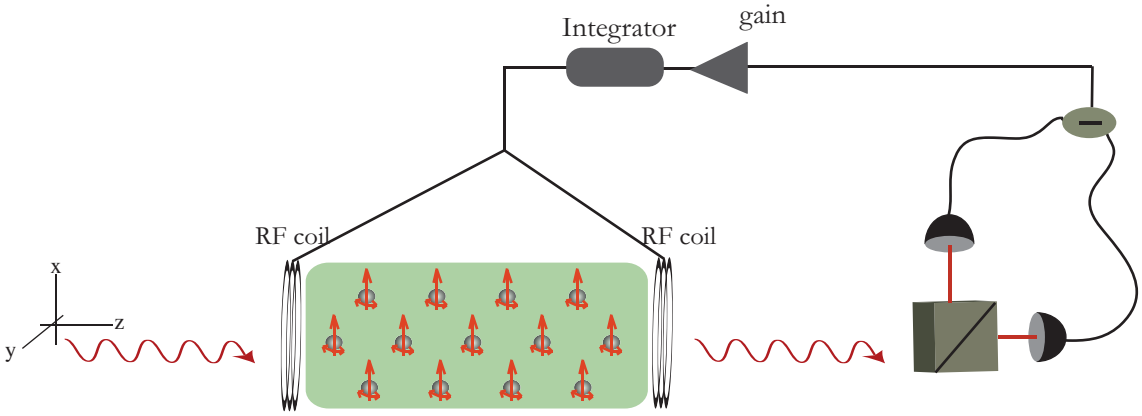

Figure 3.8: Schematic experimental setup for quantum memory based on the off-resonant Faraday interaction between light and atoms. Here, quantum information is encoded in the polarisation of photons. After propagating through the cell, the pulse is subjected to a polarisation measurement, the result of which is then fed back to the atoms by applying a magnetic field pulse of a known magnitude and duration

are fed back by a feedback gain to the atomic spins through an RF signal. A schematic of the experiment setup is shown in Fig. 3.8. In the ideal case, where gain and atom-light interaction are maximum, the mapping of light into the atomic spins is perfect. In the read out stage, a $\pi/2$ RF pulse is followed by a read pulse to reconstruct the input state. It has been demonstrated in this work that fidelity of the output state stays above the best classical recording for up to 4 ms storage. For instance, after storage of a 1 ms pulse containing an average photon number of n= 4, for 0.7 ms, the fidelity of the output state was measured to be about 70%, which is better than its classical limit (54%). The uncertainty in the y component of the angular momentum will limit the fidelity and can be overcome by initially preparing the atoms in the spin-squeezed state [97]. It was also theoretically demonstrated that by directing the light through the atomic sample such that it crosses the medium twice under an angle of 90° in the plane orthogonal to the axis of the magnetic field, it is possible to avoid measurement and feedback to the atomic ensemble [98]. Furthermore, utilising Faraday interaction, a quantum state encoded in a light pulse has been teleported to an atomic ensemble containing caesium atoms [99]. In this experiment deterministic teleportation is achieved for coherent states for mean photon number $n = 20$ with fidelities of 0.58 and for $n = 5$ with a fidelity of 0.60, higher than classical state transfer.

Very recently, the same group succeeded in demonstrating a quantum memory for continuous variable entangled states [100]. It was shown that various two-mode 6.0 dB squeezed states obtained by varying the orientation of squeezing and the displacement of the states can be stored in an ensemble of caesium atoms. The two components of the entangled state are stored in two room-temperature cells separated by 0.5 m, one for each mode, with a memory time of 1 ms. These multi-photon states are two-mode squeezed by 6.0 dB with a variable orientation of squeezing and displaced by a few vacuum units. The true quantum character of the memory is proved by showing that the experimental memory fidelity 0.52 ± 0.02 exceeds the best possible classical memory. The schematic of the experimental setup is shown in Fig. 3.9.

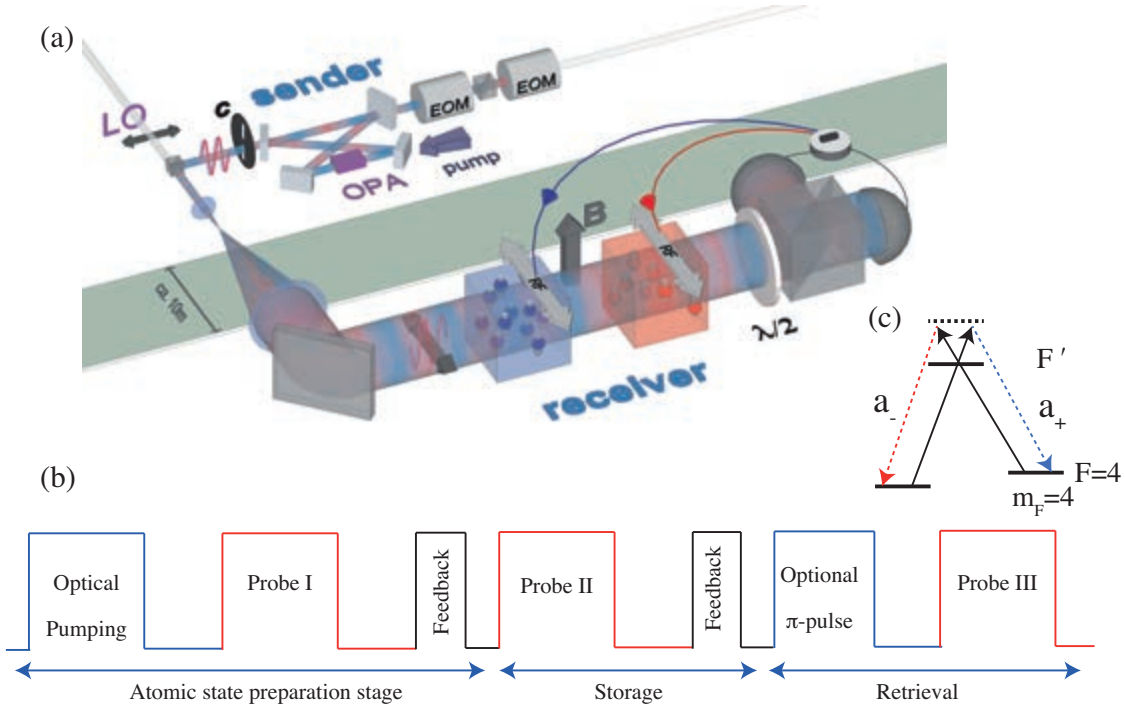

Figure 3.9: (a) Schematic setup of the experiment. At the sender station two-mode entangled (squeezed) light is generated by the OPA. A variable displacement of the state is achieved by injecting a coherent input into the OPA modulated by EOMs. The output of the OPA is shaped by a chopper, and combined on a polarising beam splitter with the local oscillator (LO) beam, such that the squeezed light is on only during the input pulse. The light is then sent to the receiver (memory) consisting of two oppositely oriented ensembles of spin-polarised caesium vapour in paraffin-coated cells and a homodyne detector. The detector signal is processed electronically and used as feedback onto the spins obtained using radio-frequency magnetic field pulses. Figure taken from Ref. [100] (b), Pulse sequence for the preparation of the memory, storage and verification. RF feedback pulses are 0.15 ms long. (c), Atomic-level structure illustrating interaction of quantum (dashed lines) and classical (solid lines) modes with the memory. Two modes drive two Raman lines and information is mapped into one atomic coherence.

3.3 Absorptive Atomic Memories

In comparison with the EIT technique, coherent optical memory schemes discussed in the following sections utilise full absorption in an optically dense medium. Two and three-pulse photon echo, an off-resonance Raman memory, controlled reversible inhomogeneous broadening (CRIB), and atomic frequency comb (AFC) are four memory schemes that are discussed in the following sections.

3.3.1 Off-resonance Raman memory

We start by introducing a memory scheme based on a simple Raman transition between two ground states. The signal field and the control field create a Raman transition via a virtual state. This far-detuned Raman transition provides absorption of broadband pulses. In the Raman memory, the bandwidth is generated dynamically by off-resonance write/read control pulses. Furthermore, off-resonance Raman memory guarantees that any

unstored light is transmitted with small attenuation and there is also a small probability of spontaneous emission. In the experiment performed by Reim et al. [101] a strong write pulse and a weak signal pulse are overlapped and sent together into a caesium vapour cell where the Raman interaction with the storage medium takes place. The signal pulse is mapped via a two-photon transition with the write pulse into a collective atomic excitation. At a later time a strong read pulse converts back the atomic excitations into an optical output signal.

The storage and retrieval of weak coherent light pulses at the single-photon level in warm atomic Cs vapour with an efficiency of 30% has recently been demonstrated [102]. Furthermore, it was shown that noise introduced from the memory to the recalled state is sufficiently low.

The off-resonance Raman memory can, in principle, provide 100% efficiency only if stored data is recalled in the backward direction. Although this type of memory is capable of storage of large bandwidth pulses (GHz), it would be difficult to store and recall multi-pulses of data. If multiple pulses are stored in the ensemble, in the reading stage, most of the information will be recalled with the first read pulse. This will limit the multimode capacity of the memory.

3.3.2 Pulse photon echo storage

The phenomenon of spin echo [103] introduced more than half a century ago is used extensively in material sciences and especially in nuclear magnetic resonance (NMR). This concept was discussed in the previous chapter. The corresponding phenomenon in photonic systems is called the photon echo, first introduced as two-pulse [104, 105] and then three-pulse photon echoes [106, 107, 108].

The two-pulse photon echo is carried out by two off-resonance pulses interacting with an ensemble of two-level atoms. The first pulse with an area of $\pi/2$ creates a coherent superposition between the ground and excited atomic states. As a result, the coherence between the oscillating dipoles decays with a rate corresponding to the homogeneous linewidth of the excited state. The second pulse, of area π, exchanges the population between the ground and excited levels in the coherent superposition, therefore the sign of the phase is reversed for each atom. After an additional evolution time, equal to the time delay between the first and second pulses, the phase shift for each atom would be zero, which leads to a rephasing of the coherence and an intense burst of coherent emission, known as the photon echo. This process can be elegantly described by Bloch vector evolution inside the Bloch sphere (see Fig. 2.8).

While two-pulse photon echoes are very good at storing classical information they are incapable of storing quantum information. The reason is that the rephasing optical π pulses are applied to transitions that are populated; therefore this type of photon echo is accompanied by spontaneous emission from the excited state. On the other hand, if one wants to completely store the input data, an optically thick atomic ensemble is required, however in the regime of high OD there is a chance of absorption of the π pulse. This will cause the π pulse to be partially absorbed which means not all the atoms will see a perfect π pulse and therefore the efficiency would never be perfect [109]. Further discussion on this subject is provided in Ref. [110].

A similar idea can be used in order to store optical data using a different pulse sequence. In this case, a preparation pulse is first applied with a bandwidth equal to or larger than the maximum data rate. This pulse creates a spectral absorption grating that will cause

absorption of the data input pulse sent later to the medium. The amplitude and phase of the input pulse is imprinted onto the frequency modulated atomic sample. After a wait of τ, applying another $\pi/2$ pulse (read pulse) negates the relative phase of the precessing dipoles which then rephase. After a further wait of τ the sample produces a photon echo. This phenomenon is known as three-pulse echo or stimulated echo (see Fig. 3.10). Photon echo based experiments, in rare-earth doped materials, have demonstrated the ability to store thousands of pulses per optical spot [111] and perform signal processing at gigahertz bandwidths [112]. For the same reason as in the case of the two-pulse echo, the traditional three-pulse echo is not appropriate for storing quantum information.

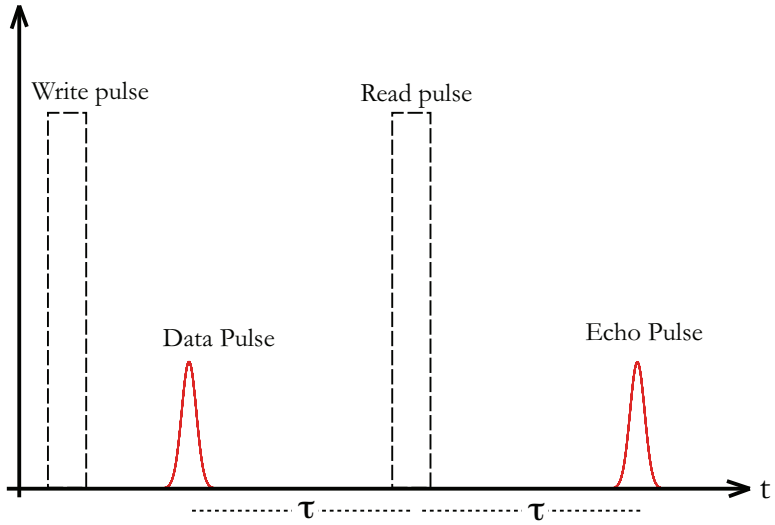

Figure 3.10: Extension of three-pulse photon echo for data light storage.

An experiment performed by a group in Switzerland on two $LiNbO_3$ waveguides, doped with erbium ions with absorption frequency of 1.53 μm, demonstrated storage of optical states of light in several temporal modes and retrieved from the optical memories using two-pulse photon echoes [113]. The stored and retrieved optical pulses, when combined at a beam splitter, showed almost perfect interference, which demonstrates both phase preserving storage and indistinguishability of photon echoes from separate optical memories. Setup and result of interference is shown in Fig. 3.11 (a), (b) and (c).

In a different experiment by the same group, using the stimulated photon echo technique, interfering photon echoes produced in a single-mode $Ti{:}Er{:}LiNbO_3$ waveguide were observed [114]. Because the efficiency of the memory is at best a few percent, most of the stored excitation is left in the atomic ensemble after the read pulse. Therefore, more echoes can be produced by sending in several read pulses. In this experiment, two subsequent read pulses were used to produce two copies of the data pulse and make them interfere. Even though the probability of retrieval from the memory is only a few percent, limited by the efficiency of the photon echo process and by decoherence processes in the storage material, close to 100% visibility was measured. The interference between the echoes shows that the memory preserves the phase of the input states.

A modified version of three-pulse photon echo was also suggested [115] for quantum applications where the information is transferred to the long-lived ground state coherence and recalled later using additional pulses. Very recently, by applying this technique, more than 50% retrieval efficiency was experimentally measured by Ham and Hahn [116].

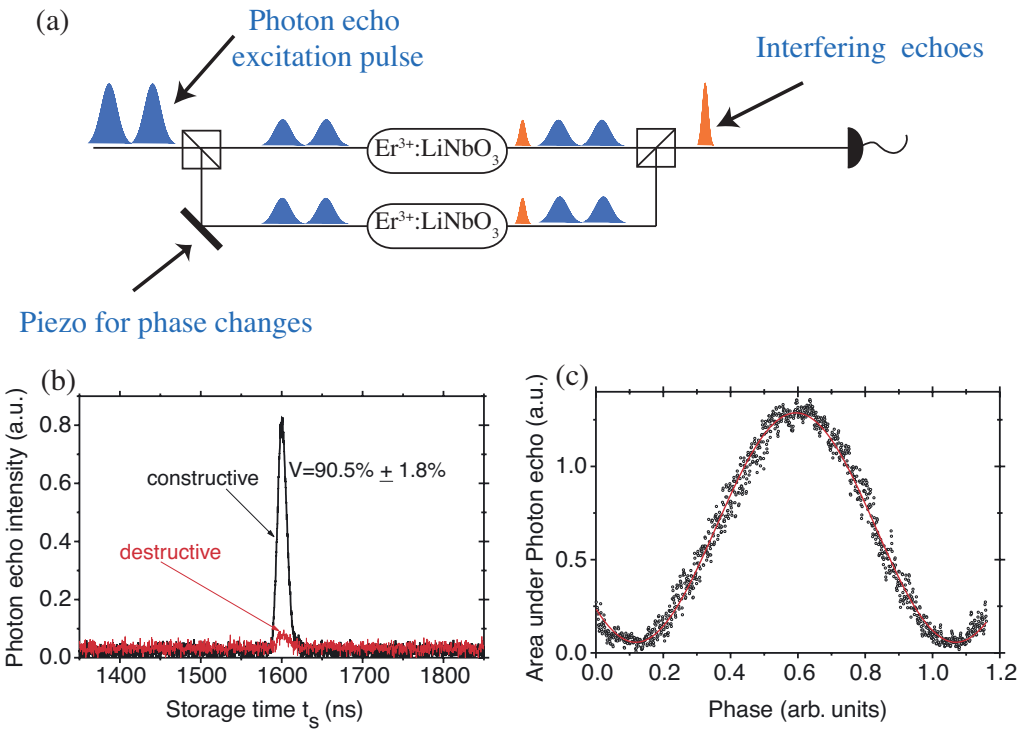

Figure 3.11: (a) Experimental setup: two Er^{+3} doped $LiNbO_3$ wave guides are placed in the arms of an interferometer at 4 K. In one arm, a piezoelectric element allows for controlled phase shifts. The generated echoes interfere at the second coupler. (b) Destructive and constructive echo signals. (c) Interference fringe: The area under the interfering photon echoes generated in two spatially separated memories is shown as a function of phase difference. For this particular fringe, a visibility of 91.5% is reached (averaging over many measurements this gives a visibility of 90.5%), limited by phase noise caused by vibrations in the cooling system. (b) and (c) taken from Ref. [113].

3.3.3 Controlled Reversible Inhomogeneous Broadening

Besides the recently modified stimulated echo procedure that makes the photon echo suitable for quantum applications, other ideas have also been proposed for the implementation of quantum memory techniques by modifying the original photon echo procedure [117, 118, 119, 120]. It was suggested that an approach to time reverse the storage process can overcome difficulties associated with the storage of quantum information using a photon echo scheme in gaseous and solid state media. An ideal photon echo quantum memory utilises full absorption in an optically dense medium and a completely reversible reconstruction process between the light and medium. Such reversibility is realised by the control of atomic coherence dephasing in an inhomogeneously broadened system. This scheme is known as controlled reversible inhomogeneous broadening (CRIB). CRIB uses a non-optical method to time-reverse the absorption process due to the inhomogeneous broadening of the transition. The photon echo memory on the other hand uses an optical pulse to reverse the dephasing of the Bloch vectors that is accompanied by spontaneous emission. To realise CRIB, the atomic coherence dephasing is reversed by switching atomic

detuning from Δ to $-\Delta$. In the simplest form, the retrieval efficiency of an ideal system using the above method is limited to 54% in the forward direction retrieval [121] due to the reabsorption of the pulse by the atoms as it leaves the ensemble. However, it has been proved theoretically [117, 122] that using Raman-coupled hyperfine states, it is possible to avoid reabsorption in the forward direction and therefore an efficient quantum memory can be constructed.

A Doppler-broadened atomic gas was initially suggested [117] for the realisation of the CRIB procedure as opposite Doppler shifts automatically occur for the counter-propagating light fields. The information is mapped by a "write" pulse which follows the input pulse and drives the atoms to an auxiliary ground state. Here the information is stored in the ground state coherence. To retrieve the information a counter-propagating "read" pulse drives the atoms back to the excited state causing the re-excited atomic dipoles to rephase. The medium can then irradiate the photons of the data signal as an echo pulse in the opposite direction. Two pulses can be separated in time, and between them the coherence is stored in the ground state transitions.

A similar procedure can be applied to a solid state sample where the inhomogeneous broadening is provided by dipole-dipole interactions in the solid [119]. It was initially suggested that the frequency inversion can be performed by applying an additional radio frequency (RF) π-pulse. This pulse inverts the states of all atoms, which changes the interatomic interactions.

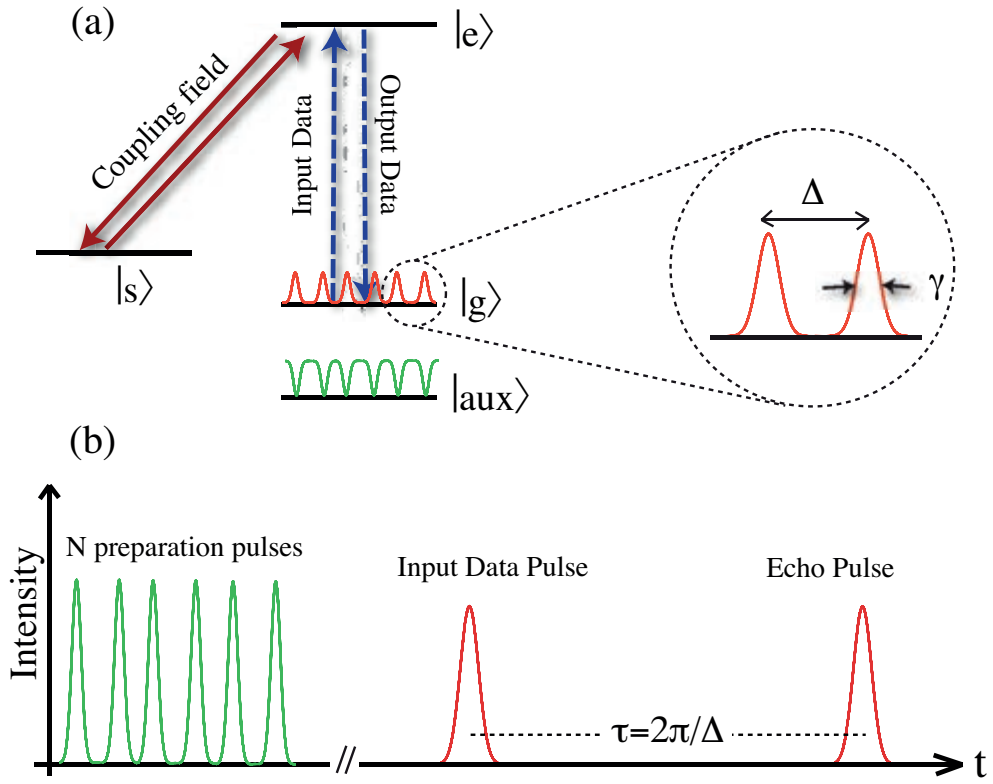

Figure 3.12: The principles of the proposed AFC quantum memory. (a) Schematic atomic level structure showing created AFC in the inhomogeneously broadened transition. Information can be transferred to a metastable state $|s\rangle$ using a coupling field for longer coherence time. (b) A set of N preparation pulses with linewidth γ and peak separation, Δ.

3.3.4 Atomic frequency comb

Similar to CRIB memory, a photon echo type QM based on an atomic frequency comb (AFC) was proposed by Afzelius *et al.* [123] and since then many light storage experiments have been performed based on this protocol. In the simplest case where an ensemble of two-level atoms is used, the basic requirement is that the transition between ground state and excited state needs to be inhomogeneously broadened. To produce narrow absorbing peaks (a frequency comb), a large number of preparation pulses with linewidth γ and peak separation Δ are sent to the sample, see Fig. 3.12. If the ensemble is initially prepared in state $|aux\rangle$, for instance a third hyperfine state, the preparation pulses can frequency-selectively transfer populations to ground state $|g\rangle$ and therefore create narrow absorbing peaks. Provided the input data bandwidth is larger than Δ, data can be uniformly absorbed through the entire spectrum. This is due to the fact that absorption is localised in time. This method, to some extent, is analogous to three-pulse photon echo.

A photon-echo type emission couples the stored light out of the atomic ensemble after a pre-determined time of $T + 2\pi/\Delta$. To control the storage time one can use a pair of control pulses resonantly interacting with the excited state and another metastable state $|s\rangle$. The first control pulse is sent to the medium right after the input modes to transfer the excitations to the metastable state. The second control pulse is sent after a controllable time to transfer the excitations back to the excited state. Eventually the photon echo is emitted after an extra wait of $2\pi/\Delta$. The effective optical depth of the AFC system is defined as $d' = d/F$ where d is the optical depth of atomic ensemble and $F = \Delta/\gamma$ is AFC finesse. To obtain maximum absorption, high finesse and as high optical depth are required. In principle, AFC efficiencies close to 100% in the backward direction can be obtained in regimes of high optical depths.

The number of modes that can be stored in an AFC medium is independent of optical depth, therefore an AFC memory has the potential for providing multimode storage capacity [124, 123]. The multimode capability of AFC was experimentally demonstrated by a group at the University of Geneva [125]. In this experiment interference of multiple optical bits was also investigated. Optical bits with different phases are stored and analysed after interfering two partial readouts. The measured net visibilities were observed to be above 95% for various values of n between 0.4 and 1.7, which demonstrates the high coherence of the storage process, even at the single-photon level. This phase preservation results from the collective enhancement and the almost complete suppression of background noise. Several other experiments have been performed using the AFC protocol by different groups around the world [126, 127] with the aim of storing optical quantum states and, to date, a maximum efficiency of 35% has been achieved [128].

Very recently, storage of entanglement using the AFC protocol has been demonstrated by two different groups separately. In the first experiment [129], one photon from an energy time entangled pair (down conversion) is mapped onto the crystal and then released into a well-defined spatial mode after a predetermined storage time. The other photon (at telecommunication wavelength) is sent directly through a 50-metre fibre link to an analyser. This experiment illustrated that non-classical intensity correlations between the two photons still exist after storage and retrieval. The classical efficiency of this memory was measured to be about 20%. In the second experiment [130], a thulium-doped lithium

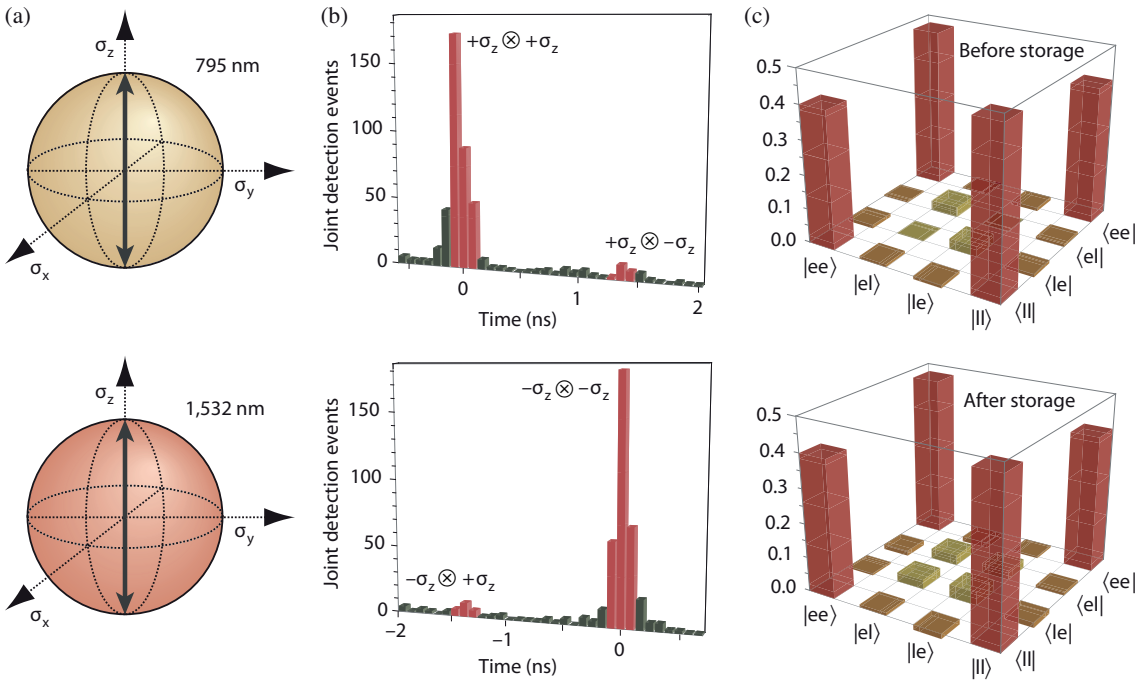

Figure 3.13: (a) Bloch sphere representation of projection measurements. The measurement settings for the 795-nm (or 1,532-nm) analyser are depicted on the upper (or lower) Bloch sphere. (b), Results for joint projection measurement after storage. The top (bottom) histogram displays joint detection events for the projection onto $\sigma_z \otimes \sigma_z$ and $\sigma_z \otimes -\sigma_z$ ($-\sigma_z \otimes \sigma_z$ and $-\sigma_z \otimes -\sigma_z$) as a function of the time difference between detections of the 795-nm and the 1,532-nm photons. The red-highlighted windows are the desired events. (c), Density matrices calculated using a maximum-likelihood estimation for the two-photon states before and after storage. Figure taken from Ref. [130]

niobate waveguide is used with a bandwidth of 5 GHz. The entanglement preserving nature of storage through Bell inequality violations has been assessed by comparing the amount of entanglement contained in the photon pairs before and after storage. The density matrices ρ_{in} and ρ_{out}, depicted in Fig. 3.13 , were obtained using a maximum likelihood reconstruction method. The storage, in this experiment, yielded a conditional input-output fidelity of 95.4 % and it has been shown that the storage process preserves the entanglement without significant degradation. The classical efficiency of the system is measured to be about 15%.

Although AFC offers extremely large memory bandwidth, efficient retrieval is only possible in the backward direction. The efficient retrieval in the backward direction is not even possible when the memory spectral width is limited. In this regime, the dispersive part of the susceptibility no longer vanishes, and the retrieved signal is no longer spatially phase-matched to the atomic coherences. This will have a negative impact on AFC quantum efficiency and fidelity [131].

A modified AFC scheme that restores spatial phase matching and its reversibility has been recently proposed [131] that uses absorption lines on the sides of the AFC. This scheme can potentially enhance the efficiency and fidelity of the AFC memories.

In this thesis, we focus on a similar photon echo based light storage technique known as the Gradient Echo Memory (GEM). The GEM scheme is a variant of CRIB that uses

an external gradient field to prevent the re-absorption of light by atoms at the recall stage.

3.4 Optomechanical light storage

Optomechanical resonators, in which optical fields couple to mechanical oscillations (phonons) via radiation pressure, provide another potential avenue for light storage. This novel approach to light storage involves an optical waveguide coupled to one or an array of mechanical oscillators, where light in the waveguide can be dynamically and coherently transferred into long-lived mechanical vibrations of the system [132].

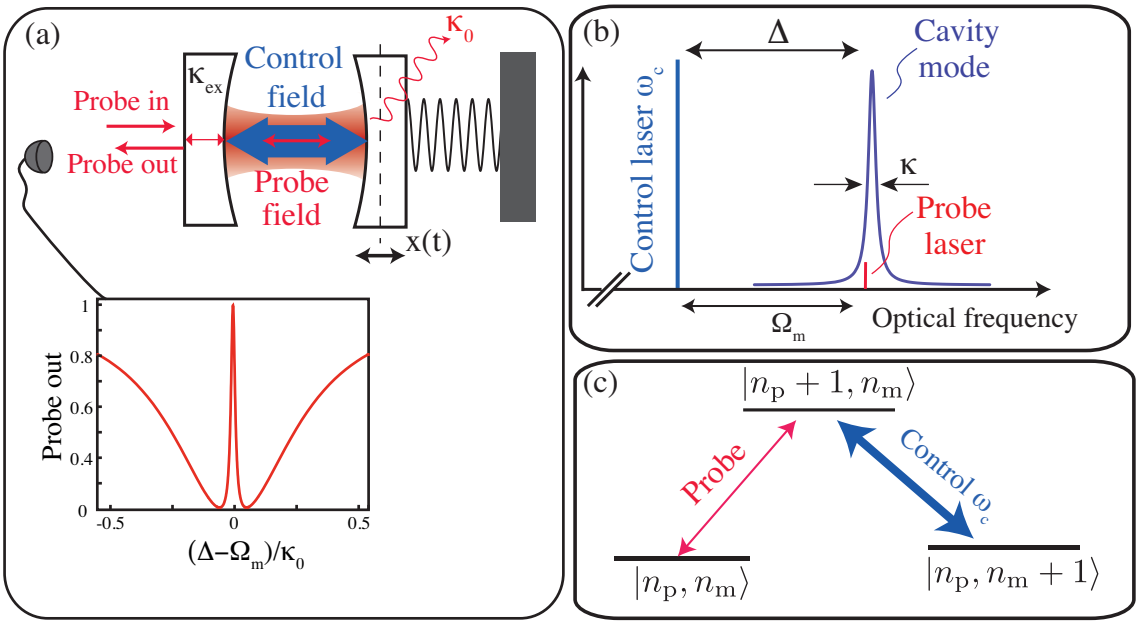

Figure 3.14: (a) A simplified optomechanical system consists of a Fabry-Perottype cavity with a movable boundary. The cavity has an intrinsic photon loss rate κ and is coupled to an external optical mode at the rate κ_{ex}. The response of this driven optomechanical system is probed by a weak probe field sent toward the cavity. The inset shows the probe power reflected from the resonator as a function of the control field detuning. (b) The control field is detuned from the cavity resonance frequency by $\Delta \simeq -\omega_m$. The probe laser's frequency is offset by a tuneable frequency from the control laser. The cavity has a linewidth of $\kappa = \kappa_0 + \kappa_{ex}$. (c) The equivalent level scheme of the optomechanical system. The control field is tuned close to red-sideband transitions, in which a mechanical excitation quantum is annihilated (mechanical occupation $n_m \rightarrow n_m - 1$) when a photon is added to the cavity (optical occupation $n_p \rightarrow n_p + 1$), thereby coupling the corresponding energy eigenstates. The probe field probes transitions in which the phonon occupation is unchanged.

A generic optomechanical system is shown in Fig. 3.14 (a). The radiation pressure interaction between a near-resonant cavity light field and mechanical motion results in the shift of the optical mode's frequency. By driving the system with an intense red-detuned optical "control" beam at frequency ω_c, as shown in Fig. 3.14 (b), the form of the effective interaction changes. In phonon-photon interactions, a photon maybe scattered into the Stokes or anti-Stokes sidebands, heating or cooling the system, respectively. The control beam induces anti-Stokes scattering that cools the mechanical motion and allows for quantum state transfer between motion and light. This beam is also responsible for weaker, off-resonant heating via Stokes scattering. The energy level structure of the

simplified system is shown in Fig. 3.14 (c). The number of photons and phonons are denoted by n_p and n_m, respectively. The optomechanical driving amplitude ω_c couples states $|n_m + 1, n_p\rangle \leftrightarrow |n_m, n_p + 1\rangle$, while the probe light couples states $|n_m, n_p\rangle \leftrightarrow |n_m, n_p + 1\rangle$. The two couplings create a set of Λ-type transitions. With the control beam detuning from the optical cavity resonance (Δ) set equal to the mechanical frequency ω_m, the light scattered from the control field (Stokes field) is frequency shifted and matches the frequency of the probe field. The intra-cavity mode will then destructively interfere with the probe field via the phononic excitations causing a transparency window to appear on the reflected light. This phenomenon is known as optomechanically induced transparency and is analogous to EIT in atomic systems.

The probe light travelling through the OMIT window experiences a steep variation in the refractive index and its group velocity consequently decreases. Experimental demonstrations of OMIT have been provided both in a defect cavity photonic crystal [133] and a toroidal microcavity [134]. In theory, the delay-bandwidth product of a single mechanical oscillator is limited to 2. However, undistorted pulse propagation is only possible by fabricating a cascade of near identical oscillators in order to achieve large delay-bandwidth products. This is analogous to using an ensemble of atoms instead of only one.

Another limiting factor for quantum applications of optomechanical systems is the re-thermalisation time of the mechanical resonator, defined as $\tau_{th} = \hbar Q_m / kT$, where Q_m is the mechanical Q-factor of the resonator. Reducing the temperature of the system to a value below 100 mK (routinely attained in a dilution refrigerator) can potentially increase the re-thermalization time and should also result in a significant increase in the mechanical Q-factor. At these temperatures, it is likely that one could achieve storage times on the order of 100 ms [133].

Very recently, an experimental demonstration of storing optical information as a mechanical excitation in a silica optomechanical resonator has been demonstrated [135]. The technique used in this experiment was analogous to the Raman storage method discussed in Sec. 3.3.1. The storage lifetime of 3.5 μs was determined by the relatively long damping time of the mechanical excitation at room temperature.

3.5 DLCZ protocol

Finally in this chapter, we review a scheme proposed by Duan, Lukin, Cirac and Zoller (DLCZ) in 2001 for creating long-lived, long-distance entanglement between atomic ensembles [136]. An elementary step towards the realisation of the DLCZ protocol is to create a stored collective excitation in an ensemble of Λ-type atoms. In contrast to other optical memory schemes, this excitation is produced not by an external photon entering an ensemble but by the ensemble itself interacting with an off-resonance classical (write) optical field, and is heralded by the emission of a Stokes photon. This excitation can be retrieved later in the form of a signal photon (anti-Stokes photon) by applying a control (read) field to the ensemble.

Initially, all the atoms are prepared in the ground state. A sample is illuminated by a short, off-resonant laser pulse that induces Raman transitions into the states $|a\rangle$, see Fig. 3.15. The off-resonant classical laser pulse couples the transition $|g\rangle$ to $|e\rangle$, resulting in the forward-scattered Stokes light comes from the transition $|e\rangle$ to $|a\rangle$, which has a different polarisation and frequency to the write beam. This emission is a result of spontaneous Raman scattering collectively from the atomic ensemble. To ensure that atoms emit one photon at a time, we assume off-resonant coupling with a large detuning Δ. The mode

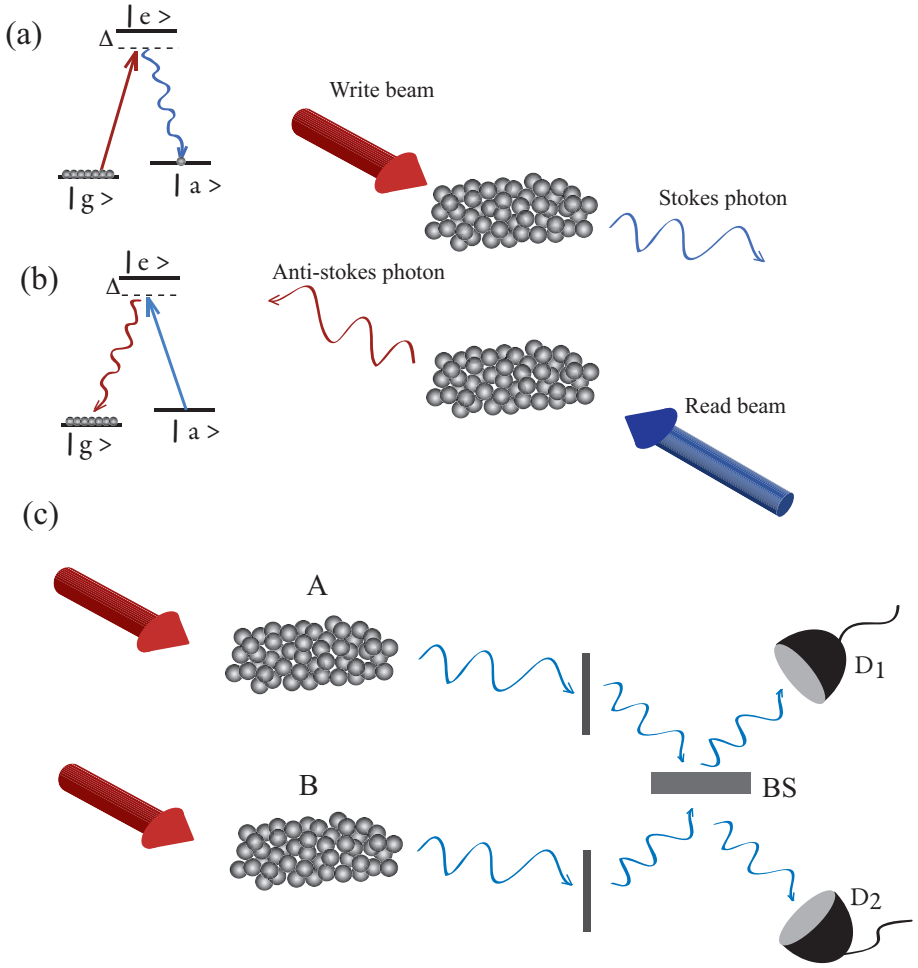

Figure 3.15: Schematic set-up for entanglement generation. (a) Generation of a Stokes photon by applying an off-resonance classical beam with relevant level structure of the atoms in the ensemble shown on the left. (b) Retrieval of anti-Stokes photon from stored excitations again with the relevant atomic level structure on the left, where $|g\rangle$, the ground state, $|a\rangle$ the auxiliary state for storing a qubit, and $|e\rangle$, the excited state. (c) Schematic demonstration of DLCZ for generating entanglement between the two atomic ensembles, A and B.

in which the single photon is detected defines the mode in which the collective atomic excitations emit the photon. Once the photon is emitted, the single photon and the collective atomic excitations are in an entangled state. To generate entanglement between two atomic ensembles, the forward-scattered Stokes photons from the two ensembles are collected separately via polarisation and frequency-selective channels to filter the classical light. The two Stokes fields interfere at a 50-50 beam splitter, with the outputs detected respectively by two single-photon detectors D1 and D2. If there is a click in D1 or D2, the process is finished and the entanglement between the ensembles is successfully generated. This is because a click in one of the detectors registers a photon from one of the ensembles and it is impossible to tell which one. If the process fails, a repumping laser pulse is applied to the ensembles, to set the state of the ensembles back to the ground state. The same process is repeated until finally we have a click in the D1 or the D2 detector. The entanglement can be stored in the ground state coherence, and then be recalled on-demand after applying a read pulse in the backward direction.

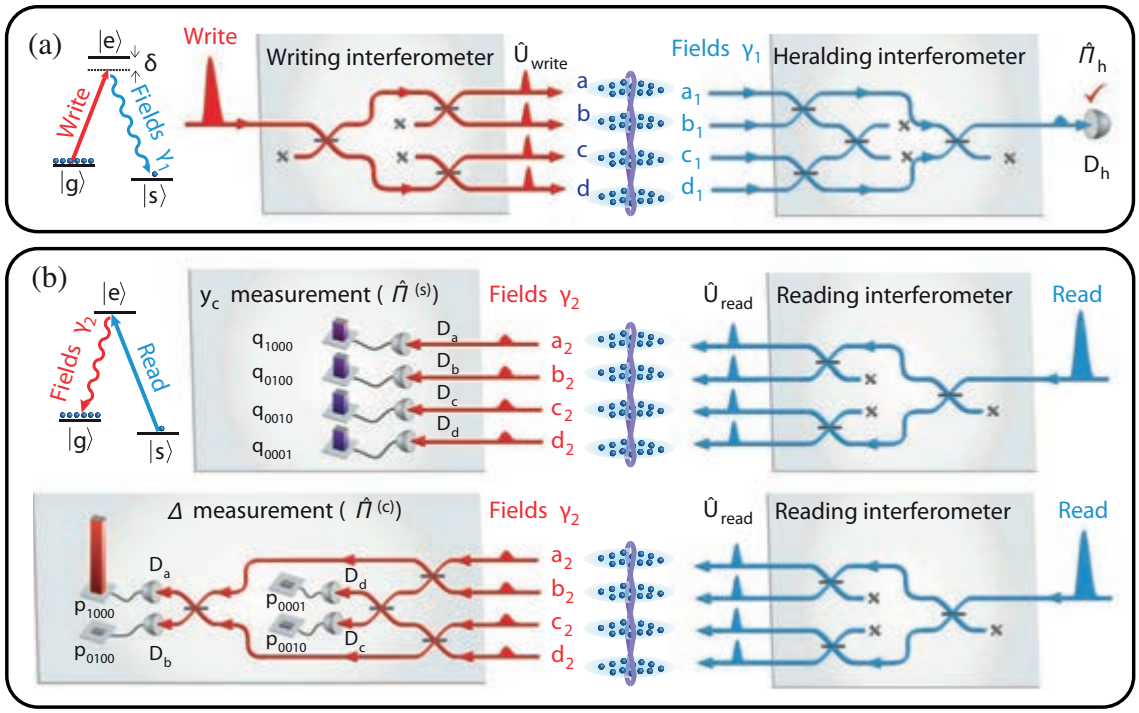

Figure 3.16: (a) Entanglement generation. A single Raman scattered photon for four fields is emitted by the ensembles, after a weak write laser excites atomic ensembles, and detected by a projective measurement at detector D_h. (b) Entanglement verification. A strong read pulse is sent into the four atomic ensembles, and the atomic state is mapped to an entangled state of light for four fields. This entangled field state then propagates to the entanglement verification ports. The upper panel shows the measurement of quantum statistics with the modes projected on detectors $D_{a,b,c,d}$. The lower panel shows the measurement performed by rerouting the relevant fibre-optical connections. Figure modified from Ref. [137]

The DLCZ scheme is ideally suited for quantum communication applications, but can not be directly applied to information encoded in arbitrary optical states. There has been a significant amount of work done on applying the DLCZ protocol to various quantum optics experiments [138, 87, 139, 140]. Storage of a collective excitation left in the atomic ensemble after emission of the Stokes photon was demonstrated for a few milliseconds using the magnetically insensitive clock transition of atoms [141, 142].

Taking full advantage of the DLCZ idea, a memory-built-in teleportation experiment for an unknown polarisation state of a single photon was performed over 7 m onto a remote atomic quantum bit that also serves as a quantum memory [143]. In this experiment the teleported state was stored and successfully read out up to 8 μs later.

Very recently Choi *et al.* succeeded in demonstrating measurement-induced entanglement stored in four atomic memories using the DLCZ scheme [137]. The schematic experimental setup is shown in Fig. 3.16. In this experiment, a coherent transfer of the atomic entanglement to four optical channels and characterisation of the quadripartite entanglement was fully investigated. The measurement results revealed high-fidelity measurement-induced entanglement between modes stored among the four laser cooled atomic memories.

3.6 Summary

The emiclassical and quantum storage of optical states have come a long way in a short time, as the history outlined in this chapter has demonstrated. With this context in mind, in the next chapter, I introduce the gradient echo memory scheme as an alternative method for light storage, which is the core of this thesis.

Part II
Semiclassical light storage using GEM

Chapter 4

Gradient Echo Memory; Theory and Experimental Techniques

"With the magnificence of eternity before us, let time, with all its fluctuations, dwindle into its own littleness."

Thomas Chalmers

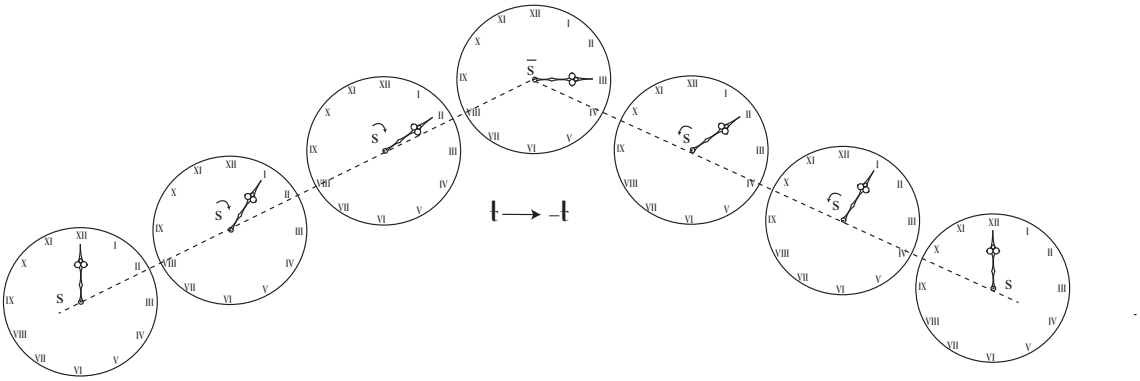

Figure 4.1: The evolution of the collective atomic spin created after storage of light can be time reversed.

In the previous chapter, we provided an overview of various optical storage techniques such as the photon echo approach. In this chapter we introduce a memory scheme known as the gradient echo memory (GEM). This is a photon echo based memory and can be applied to two- or three-level atomic media. The GEM scheme is a particular form of CRIB where the inhomogeneous broadening is controlled by an external field gradient. In this chapter, we discuss the theoretical concepts and the experimental techniques used to implement this type of memory.

The relevant publication for this chapter is

Photon echoes generated by reversing magnetic field gradients in a rubidium vapour G. Hétet, M. Hosseini B. M. Sparkes, D. Oblak, P. K. Lam, and B. C. Buchler, Opt. Lett. 33 No.20, 2323 (2008).

4.1 Theoretical description of GEM

The principle behind CRIB is to construct a reversible absorption process. After absorption in an inhomogenously broadened atomic medium, some mechanisms can be used to invert the detunings of the individual absorbers that are spatially distributed in the medium. This reversal in detuning gives rise to a photon echo and thus the retrieval of stored optical information. CRIB was proposed in gas cells [144] and solids [145, 146], and was first demonstrated in 2006 using a cryogenic ensemble of two-level rare-earth ions [147]. It was then realised in 2008 that the application of a detuning gradient longitudinally along the length of the storage medium allowed for high recall efficiencies in the forward direction [148] by preventing reabsorption of the light. This overcame the limit of 54% recall efficiency that had previously been determined [121]. The use of a longitudinal gradient to control the broadening of the atomic ensemble is referred to as longitudinal-CRIB or gradient echo memory (GEM). In 2010, ensembles of cryogenic rare-earth ions were used in a GEM system to demonstrate the first unconditional quantum memory with 69% recall efficiency [149].

In this chapter we review the basics of the GEM scheme. We discuss the particular issues that relate to the gaseous rubidium vapour that is the basis of our experiments. We also present the first experimental results of light storage in a warm Rb vapour cell.

4.1.1 Basic concepts

The GEM is a variant of CRIB that relies on inhomogeneous broadening being introduced as an atomic frequency gradient along the length of the storage medium. In theory, GEM is ideally 100% efficient [148, 150].

The GEM protocol works without any need for π-pulses, as opposed to traditional photon echo techniques. Rephasing is controlled by the linear atomic frequency spectrum, $\delta(z,t) = \eta(t)z$, that is induced along the length of the storage medium. $\eta(t)$ is the slope of the gradient, that can change in time, and z is the position along the propagation axis. Consider, for example, an ensemble of two-level atoms as shown in Fig. 4.2(a). Each frequency of the probe optical pulse is absorbed by the ensemble at a different point along its length and stored in the atomic polarisation. The atomic polarisation in the z direction is thus proportional to the Fourier spectrum of the electromagnetic field as shown in Fig. 4.2(b). To release the stored light, the gradient η is simply inverted at time τ and the optical field is regenerated as a photon echo at time 2τ, as shown in Fig. 4.2(c). In this most basic two-level scheme the input pulses emerge in the forward direction but shape-reversed [151].

The Bloch sphere representation of light storage with GEM is shown in Fig. 4.3. After the light pulse is absorbed by the atomic medium, it drives the atomic spin to a particular point on the sphere. Different atoms then start to dephase with a rate corresponding to their detuning from the unperturbed transition frequency. Rephasing of atomic spins, caused by inverting the sign of the detuning, generates a photon echo, ideally identical to the input light pulse.

4.1.2 Model

We start by deriving the equations of motion for the two-level GEM. We then show that a Λ-system driven off-resonance by a strong coupling beam and a weak probe is equivalent

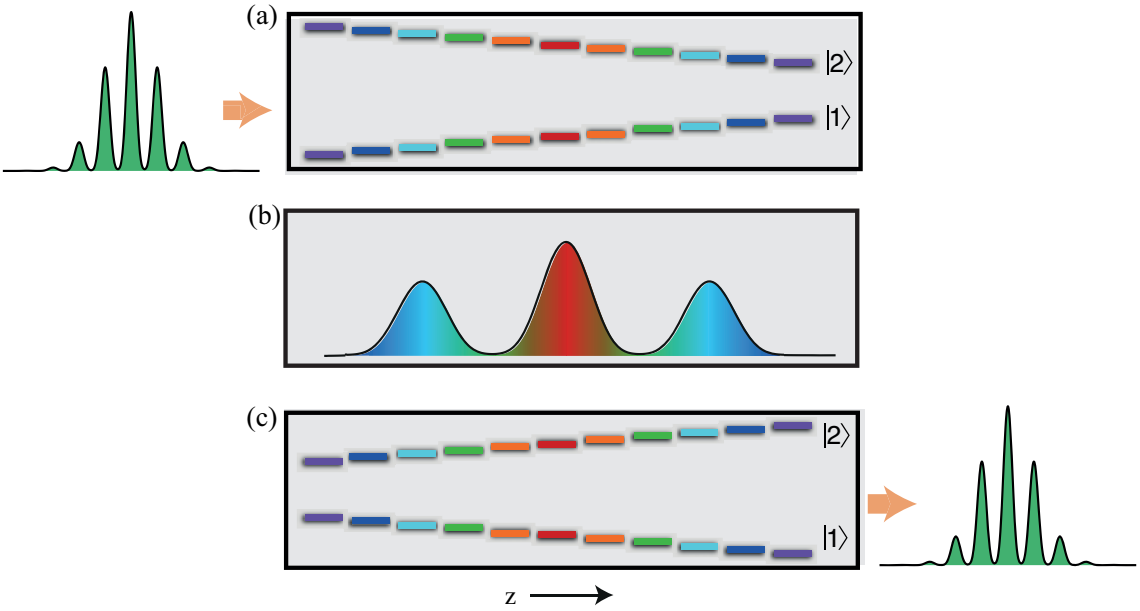

Figure 4.2: (a) The atomic storage medium with an atomic frequency spectrum (ηz). The bandwidth of the atomic broadening covers the input modulated pulse spectrum. (b) Fourier spectrum of the input pulse is absorbed and stored as an atomic polarisation. (c) To release the pulse, the atomic detuning (η) sign is inverted ($-\eta$) at time τ and the stored light emerges at time 2τ.

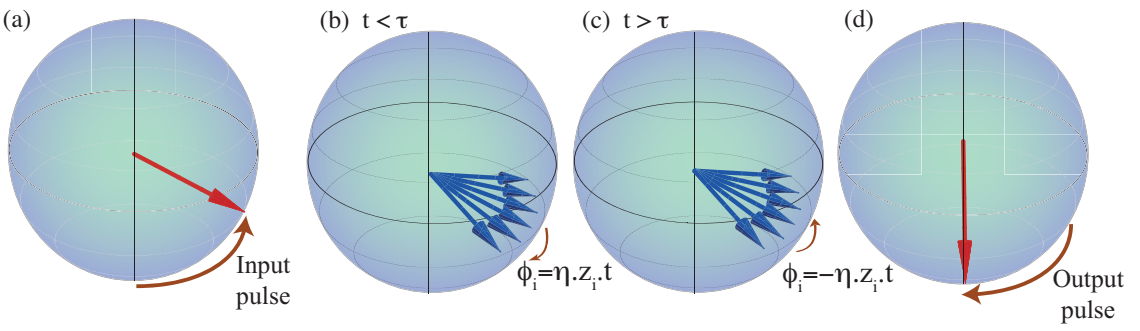

Figure 4.3: Bloch sphere representation of the gradient echo technique in light storage. (a) A light pulse interacts with an inhomogeneously broadened atomic sample (with gradient slope η) and creates a collective atomic excitation. The angle of the Bloch vector is shown nearly as $\pi/2$ for clarity, but in fact the stored pulses are very weak and excitation angle is very small. (b) Atoms at different positions of the memory (z_i) dephase at different rates controlled by the field gradient. (c) When the gradient sign is flipped at $t = \tau$, atomic spins start to rephase causing time-reversal of the absorption process. (d) A photon echo is emitted at $t = 2\tau$ when phase matching is satisfied.

to a two-level system driven by the weak probe and therefore the same storage protocol can be used.

Two-level atoms

We use an ideal two-level system to model the storage and retrieval dynamics. We consider the interaction between a collection of two-level atoms with total number of atoms N inside the quantisation volume V and a quantum optical field with slowly varying envelope $\hat{\mathcal{E}}(t,z) = \int \hat{a}_k e^{ik.r} dk$.

The interaction Hamiltonian which is the two-level atom Jaynes-Cummings Hamiltonian can then be written as

$$\hat{H} = -\hbar \frac{N}{L} \int [\delta(z,t)\sigma_{22} + g(\hat{\mathcal{E}}^{\dagger}\hat{\sigma}_{12} + H.c)]dz \tag{4.1}$$

Here σ_{ij} is the collective atomic operator. Assuming that all of the atoms are initially in the ground state $|1\rangle$ we describe the system evolution by the following Heisenberg/Maxwell equations

$$\dot{\hat{\sigma}}_{12}(t,z) = -(\gamma + i\delta(z,t))\hat{\sigma}_{12}(t,z) + ig\ \hat{\mathcal{E}}(t,z) + \hat{F}_{12} \tag{4.2}$$

$$\frac{\partial}{\partial z}\hat{\mathcal{E}}(t,z) = i\mathcal{N}\hat{\sigma}_{12}(t,z) \tag{4.3}$$

with atom-light coupling constant g, and effective linear atomic density $\mathcal{N} = gN/c$. The atomic polarisation $\hat{\sigma}_{12}(t,z)$ and the electric field $\hat{\mathcal{E}}(t,z)$ are found by numerically solving of Eqs. 4.2 and 4.3. The two-photon detuning $\delta(z,t)$ can be varied in time and be made linear with a magnetic or electric field $\delta(z,t) = \eta(t)z$, i.e. the linearly varying detuning from resonance. We also introduced γ as a decay rate from the excited state and the corresponding Langevin operator ($\hat{F}_{12}$) that accounts for noise arising from spontaneous emission.

To calculate the dispersion relation associated with the two-level atoms, one can take the Fourier transform of the Eqs. 4.2 and 4.3 and finds $\omega = -g\mathcal{N}/k_0$ assuming $\gamma = 0$. This solution is only true assuming $\eta \to 0$ after the pulse enters the medium and k_0 is the value of the spatial frequency at the time that the gradient is switched off. Therefore, the group velocity of the light can be written as $v_g = \frac{gN}{k_0^2}$. This is the group velocity of the light inside the medium given that the intensity of light also scales linearly with N.

Efficiency of 2-level GEM

To find the efficiency of the 2-level GEM, one needs to calculate the transmission factor of the medium during the writing and reading stage. By solving Eqs. 4.2 and 4.3 in the Fourier domain and integrating along the z axis [152], $-z_0 \to z$, one arrives at

$$\mathcal{E}(z,\omega) = \zeta(z,\omega)\mathcal{E}(-z_0,\omega) \tag{4.4}$$

where $\mathcal{E}$ is the electric field inside the medium and

$$\zeta(z) = \left(\frac{\gamma - i(\eta z + \omega)}{\gamma - i(-\eta z_0 + \omega)}\right)^{-i\beta} \tag{4.5}$$

is the transmission factor of the medium; further, $\beta = g\mathcal{N}/\eta$ is the optical depth of the atomic sample. Substituting $z = z_0$ and assuming $\gamma = 0$ in the above equation for each spectral component of the input light after propagating through the memory, but before

switching the field,

$$\ln \frac{\mathcal{E}(z_0, t)}{\mathcal{E}(-z_0, t)} = \beta \ln [-1]^i = -\pi\beta. \tag{4.6}$$

This means that the input pulse is attenuated by a factor of $e^{-\pi\beta}$, which means $(1-e^{-\pi\beta})$ part of the light is stored in the memory. The total efficiency after rephasing (after switching the electric field) can also be evaluated by considering a light field propagating backwards and using auxiliary light pulses [152]. Therefore, the intensity efficiency can be written as $\epsilon = (1-e^{-2\pi\beta})^2$. Fig. 4.4 shows the efficiency of a 2-level GEM system as a function of the optical depth. We note here that in the above calculations it is assumed that the bandwidth of the memory is much greater than the atomic linewidth, i.e. $\eta L \gg \gamma$.

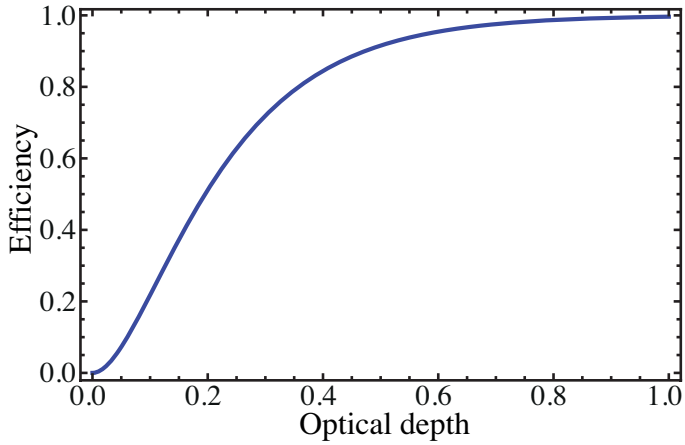

Figure 4.4: Efficiency plot of a two-level GEM system against OD of atomic medium.

4.1.3 Three-level atoms

Let's now consider the simplified level structure depicted in Fig. 4.5 (a) where the coupling and probe fields, with Rabi frequencies of $\Omega_c = \mathbf{d}.\mathbf{E_c}(\mathbf{t})/\hbar$ and $\Omega_p = g|\hat{\mathcal{E}}|$ are interacting with a three-level atom. The coupling field amplitude is assumed to be a strong classical field and defined as

$$E_c(t) = \epsilon_c \mathcal{E}(t) \cos \omega_c t \tag{4.7}$$

where ϵ_c is the polarisation vector.

The normalised transmission of the probe field is depicted in Fig. 4.5 (b) for different coupling field detuning as a function of probe field detunings. When the two-photon detuning is zero, a transparency window is opened inside the medium on two-photon resonance and outside the EIT window incoherent absorption occurs. As the coupling field detuning is increased, instead of transmission, we move to a Raman absorption line centred around two-photon resonance. If the ground state decoherence, γ_0, is very small then by increasing the one-photon detuning, Δ_p, the Raman line becomes more and more symmetric and absorption does not decrease significantly. This suggests that in cold atomic ensembles, where the decoherence between $|1\rangle$ and $|2\rangle$ is small, a Raman line can be far-detuned to avoid scattering whilst maintaining large absorption. If $\gamma_0 \neq 0$, increasing the

detuning will cause a reduction of the Raman absorption. This effect is apparent in warm vapour cells where the ground state decoherence is larger due to inelastic collisions.

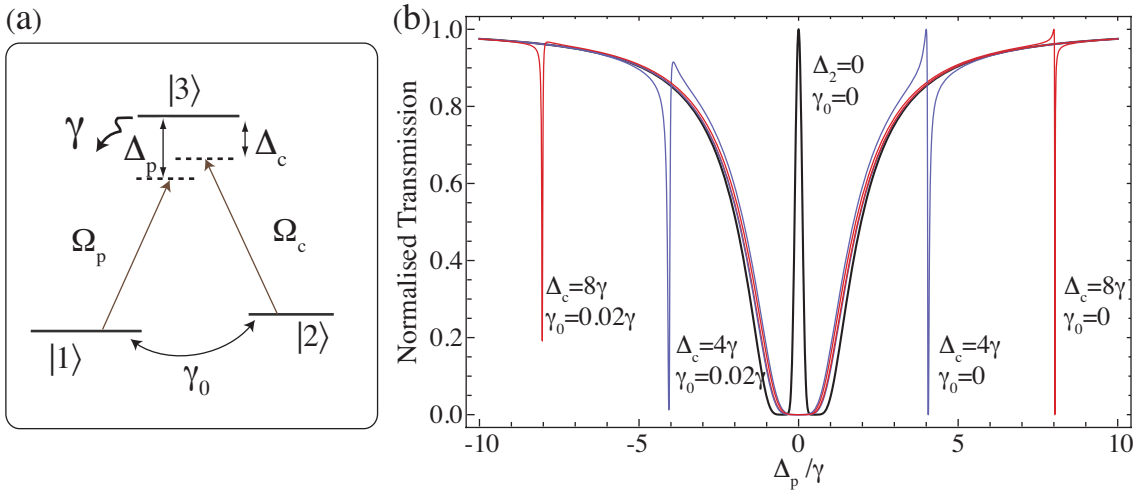

Figure 4.5: (a) Schematic level structure of a Λ atom interacting with two laser fields (probe and coupling fields) with Rabi frequency of Ω_c and Ω_p, respectively. The $|1\rangle \rightarrow |2\rangle$ decoherence rate is γ_0, detunings of the two fields from the excited state are Δ_p and Δ_c. The excited state linewidth is γ. (b) Normalised transmission of the probe signal as a function of its detuning from the excited state for different coupling field detunings. When both fields are on resonance with the excited state, the EIT transparency window is apparent in the middle of the plot. Raman lines on the right side of the EIT window are plotted assuming zero decoherence. The Raman lines on the left side of the EIT window correspond to the non-zero decoherence rate.

Weak probe approximation

We consider the three-level system depicted in Fig. 4.6 (a) with a one photon detuning Δ, a classical coupling beam Ω_c, and a weak quantum field $\hat{\mathcal{E}}$. One difference between the off-resonance Raman scheme and EIT is that in the steady state and under normal experimental conditions, the atoms are not fully pumped by the coupling field to the level $|1\rangle$. To ensure that this is the case, an initial pumping step is required. Here we suppose that this has been performed, and assume all the population to be in state $|1\rangle$ initially.

The system Hamiltonian is given by

$$\hat{H} = -\hbar \frac{N}{L} \int [g\hat{\mathcal{E}}\hat{\sigma}_{31} + \Omega_c \hat{\sigma}_{32} + h.c] dz. \tag{4.8}$$

From this interaction Hamiltonian, we can obtain a set of Heisenberg-Langevin equations (see Sec. 2.4.1)

$$\dot{\hat{\sigma}}_{11} = \gamma\hat{\sigma}_{33} - ig\hat{\mathcal{E}}\hat{\sigma}_{31} + ig\hat{\mathcal{E}}^{\dagger}\hat{\sigma}_{13} + \hat{F}_{11} \tag{4.9}$$

$$\dot{\hat{\sigma}}_{22} = \gamma\hat{\sigma}_{33} - i\Omega_c\hat{\sigma}_{32} + i\Omega_c^*\hat{\sigma}_{23} + \hat{F}_{22} \tag{4.10}$$

$$\dot{\hat{\sigma}}_{13} = -(\gamma + \gamma_0/2 + i\Delta)\hat{\sigma}_{13} + ig\hat{\mathcal{E}}(\hat{\sigma}_{11} - \hat{\sigma}_{22}) + i\Omega_c\hat{\sigma}_{12} + \hat{F}_{13} \tag{4.11}$$

$$\dot{\hat{\sigma}}_{32} = -(\gamma + \gamma_0/2 + i\Delta)\hat{\sigma}_{32} - ig\hat{\mathcal{E}}^{\dagger}\hat{\sigma}_{12} + i\Omega_c^*(\hat{\sigma}_{33} - \hat{\sigma}_{22}) + \hat{F}_{32} \tag{4.12}$$

$$\dot{\hat{\sigma}}_{12} = -(\gamma_0 + i\delta(z,t))\hat{\sigma}_{12} + i\Omega_c^*\hat{\sigma}_{13} - ig\hat{\mathcal{E}}\hat{\sigma}_{32} + \hat{F}_{12} \tag{4.13}$$

$$\dot{\hat{\sigma}}_{33} = -(\dot{\hat{\sigma}}_{11} + \dot{\hat{\sigma}}_{22}) \tag{4.14}$$

$$(\frac{\partial}{c\partial t} + \frac{\partial}{\partial z})\hat{\mathcal{E}} = i\mathcal{N}\hat{\sigma}_{13}. \tag{4.15}$$

The Langevin operators $\hat{F}_{ij}$ account for noise arising from the coupling of the atoms to vacuum modes of large reservoirs. It has been demonstrated that no significant excess noise is generated from these processes [83]. In this thesis we ignore the Langevin terms in our analysis and assume that their impact on the output field is small. We also ignore population redistribution terms for simplicity, in order to ensure that once the atoms are prepared in state $|1\rangle$ they stay there.

Using the the steady-state solution for σ_{32}

$$\hat{\sigma}_{32} \simeq \frac{-ig\hat{\mathcal{E}}^{\dagger}\hat{\sigma}_{12}}{\gamma + i\Delta}, \tag{4.16}$$

and the population preservation relation to the first order in the weak probe approximation

$$\hat{\sigma}_{11} = 1 \tag{4.17}$$

$$\hat{\sigma}_{33} = \hat{\sigma}_{22} = 0, \tag{4.18}$$

we obtain the following approximated equations

$$\dot{\hat{\sigma}}_{13} = -(\gamma + \gamma_0/2 + i\Delta)\hat{\sigma}_{13} + ig\hat{\mathcal{E}} + i\Omega_c\hat{\sigma}_{12} + \hat{F}_{13} \tag{4.19}$$

$$\dot{\hat{\sigma}}_{12} = -(\gamma_0 + i\delta(z,t) + \phi)\hat{\sigma}_{12} + i\Omega_c^*\hat{\sigma}_{13} + \hat{F}_{12} \tag{4.20}$$

$$(\frac{\partial}{c\partial t} + \frac{\partial}{\partial z})\hat{\mathcal{E}} = i\mathcal{N}\hat{\sigma}_{13} \tag{4.21}$$

where $\phi = \frac{g|\hat{\mathcal{E}}|^2}{\gamma + i\Delta}$ is small in the weak probe regime and with large detuning, and so can be neglected.

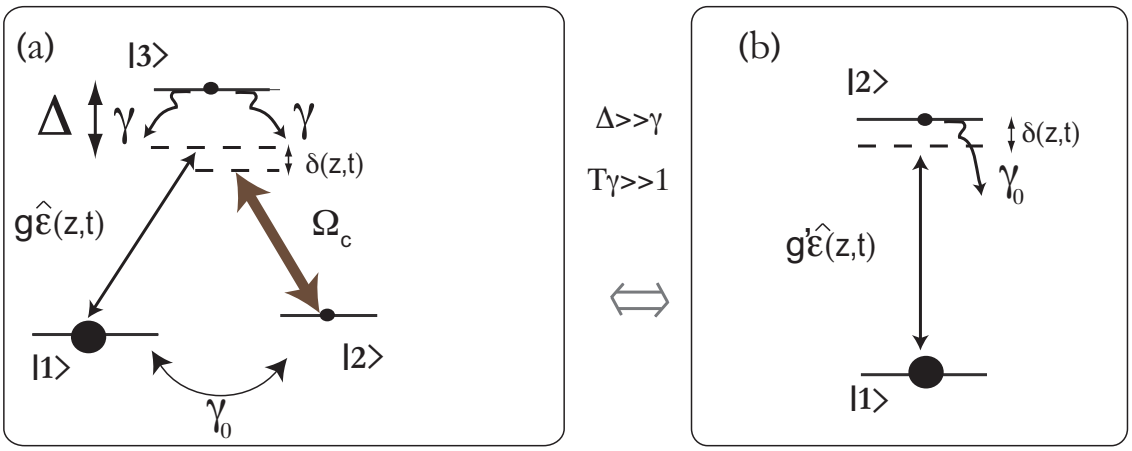

Figure 4.6: (a) Level structure of the three-level atom. (b) Quasi-two-level atom.

Using Eqs. 4.20-4.21, the susceptibility of the medium can be written [37] as

$$\chi = \frac{g\mathcal{N}}{k}[i\frac{(8\delta^2\gamma + 2\gamma_0(\Omega^2 + \gamma_0\gamma)}{|\Omega^2 + (\gamma + 2i\Delta)(\gamma_0 + 2i\delta)|^2} + \frac{(4\delta(\Omega^2 - 4\delta\Delta) - 4\Delta\gamma_0^2}{|\Omega^2 + (\gamma + 2i\Delta)(\gamma_0 + 2i\delta)|^2}]. \tag{4.22}$$

The real and imaginary parts of susceptibility are important quantities in understanding absorption and dispersion properties of Raman memories. This expression will be used in Sec. 4.3.3 to describe dispersion effects of the Raman line. We now simplify the equations further by performing an adiabatic elimination of the excited state, and using a far off-resonance approximation.

Adiabatic elimination and far off-resonance approximation

We adiabatically eliminate fast excited state fluctuations [153] by assuming $\frac{\partial}{\partial t}\hat{\sigma}_{13} \ll \Delta\sigma_{13}$, or equivalently $1/T \ll \Delta$, where T is the fastest time-scale of the system. We also assume a large detuning compared to the spontaneous emission rate ($\Delta \gg \gamma$). By solving the Maxwell equation for the probe field and substituting it back into the equations of motion for $\hat{\sigma}_{13}$ we can show that $1/dT \ll \gamma$ and $\Delta \gg \gamma$, are sufficient conditions for elimination of the exited state. This is due to the collective coupling between the optical modes and the many atom state. Assuming the coupling beam to be real, combining the above three equations yields

$$\dot{\hat{\sigma}}_{12} = (-\gamma_0 + i\delta(z,t) - i\frac{\Omega_c^2}{\Delta})\hat{\sigma}_{12} - i\frac{g\Omega_c}{\Delta}\hat{\mathcal{E}} \tag{4.23}$$

$$(\frac{\partial}{c\partial t} + \frac{\partial}{\partial z})\hat{\mathcal{E}} = \frac{ig\mathcal{N}}{\Delta}\hat{\mathcal{E}} + i\frac{\mathcal{N}\Omega_c}{\Delta}\hat{\sigma}_{12}. \tag{4.24}$$

The term Ω_c^2/Δ is the ac-Stark frequency shift caused by the coupling field and can be cancelled by changing the coupling field frequency. Performing the transformations $\mathcal{E} \to \mathcal{E}e^{i\frac{ig\mathcal{N}c}{\Delta}t}$ and $\Omega_c \to \Omega_c e^{-i\frac{ig\mathcal{N}c}{\Delta}t}$ we can remove the first term on the right hand side of the Maxwell equation. We also perform the transformation $z' = z + ct$, i.e. moving to a frame with speed of light, to reach

$$\dot{\hat{\sigma}}_{12} = -(\gamma_0 + i\delta(z' - ct, t))\hat{\sigma}_{12} - i\frac{g\Omega_c}{\Delta}\hat{\mathcal{E}} \tag{4.25}$$

$$\frac{\partial}{\partial z'}\hat{\mathcal{E}} = i\frac{g\mathcal{N}\Omega_c}{\Delta}\hat{\sigma}_{12}. \tag{4.26}$$

The equations for two-level GEM are [154]

$$\dot{\hat{\sigma}}_{12} = -(\gamma_{12} + i\delta(z,t))\hat{\sigma}_{12} - ig\hat{\mathcal{E}} \tag{4.27}$$

$$\frac{\partial}{\partial z}\hat{\mathcal{E}} = i\mathcal{N}\hat{\sigma}_{12} \tag{4.28}$$

which are formally equivalent to the above Raman situation if we set $\mathcal{N} \to \frac{\mathcal{N}\Omega_c}{\Delta}$, $g \to \frac{g\Omega_c}{\Delta}$ and $\gamma_{12} \to \gamma_0$. Therefore, one can see that the GEM storage mechanism described above for two-level atoms is also a good description for the 3-level system in certain regimes.

Efficiency of Λ-GEM

The effective optical depth of Λ-GEM is defined as $\beta' = \frac{g\mathcal{N}}{\eta}(\frac{\Omega_c}{\Delta})^2$,with the coupling field Rabi frequency Ω_c and the one photon detuning Δ contributing to the optical depth of the memory. Therefore to achieve the same efficiency as a 2-level system one needs to increase the OD of a three-level system by a factor of $\frac{\Delta^2}{\Omega_c^2}$ compared to the two-level system.

Since the excited state linewidth of Λ-type atoms is large compared to the typical memory bandwidth, the assumption that we used previously, i.e. $\eta L \gg \gamma$, is not always valid. Thus, we generally write the efficiency of a Λ system as

$$\epsilon = (1 - e^{-\beta'(2\pi + \frac{4\gamma\eta L}{\gamma^2 + (\eta L)^2})})^2. \tag{4.29}$$

In the limit of large broadening, $\eta L \gg \gamma$, the efficiency is simply given by: $\epsilon = (1 - e^{-2\pi\beta'})^2$. The theoretical plot of efficiency as a function of optical depth,β', and also the $(\Omega_c/\Delta)^2$, is shown in Fig. 4.7 (a). In Fig. 4.7 (b), the coupling field-induced scattering is included in the model as an extra loss term for efficiency. As can be seen, the loss due to the scattering can be significant at large OD or large Ω_c/Δ and dominates the efficiency. This is further discussed in the following section.

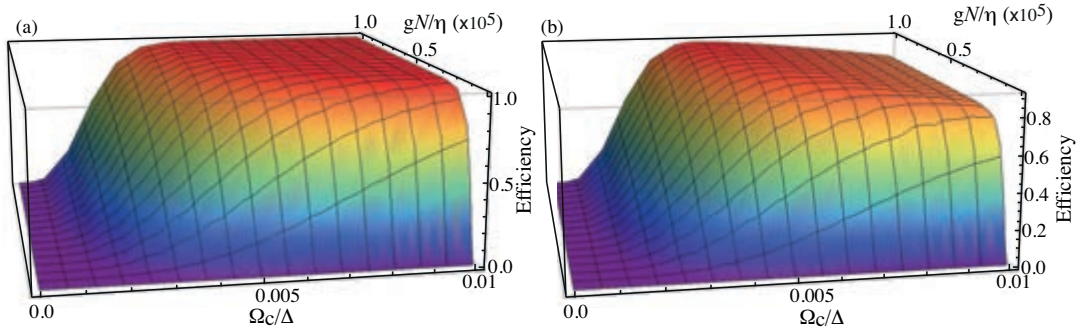

Figure 4.7: Efficiency plot of a Λ-GEM scheme vs. optical depth, $g\mathcal{N}/\eta$ and Ω_c/Δ (a) without and (b) with scattering loss taken into account. The loss due to the scattering was estimated for storage time equal to one pulse duration of 4 μs.

4.2 Atomic vapour properties

In our experiment, we used an ^{87}Rb vapour cell above room temperature as the memory medium. Before we explain the experimental setup, here we provide an overview of the Rb atomic structure and its properties.

4.2.1 ^{87}Rb Atomic level structure

^{87}Rb has 37 electrons, only one of which is in the outermost shell. The $5^2S_{1/2} \rightarrow 5^2P_{1/2}$ (D1 line) and $5^2S_{1/2} \rightarrow 5^2P_{3/2}$ (D2 line) transitions are the components of a fine-structure doublet. The D1 line transition of ^{87}Rb has a wavelength of 795 nm and is shown in Fig. 4.8 (a). The saturation absorption lines of Rb are shown in Fig. 4.8 (b), (i) trace. The corresponding transitions in (a) and (b) are shown by (a, b, c, d). The D2 line has a wavelength of about 780 nm and the excited state contains 4 hyperfine levels.

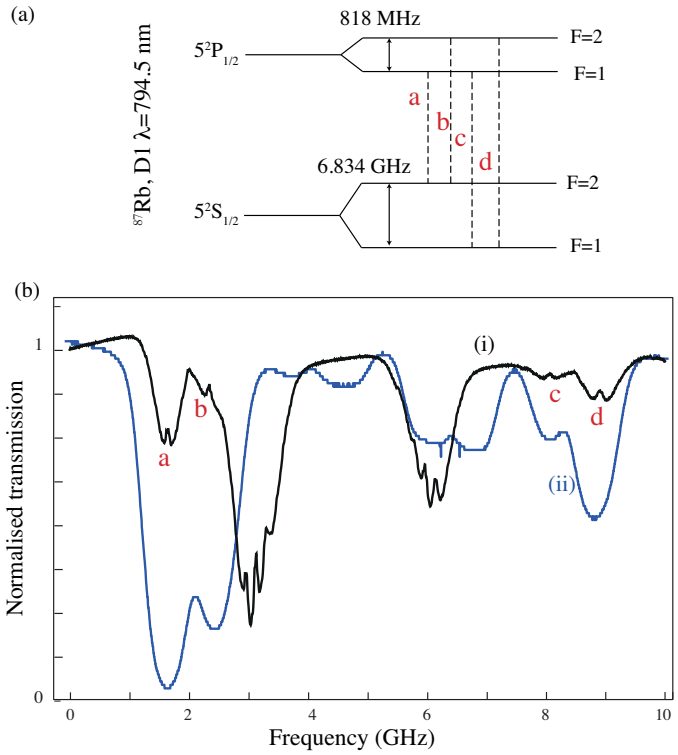

Figure 4.8: (a) Atomic level structure for D_1 line of ^{87}Rb. (b) (i) Saturation absorption trace for a natural mixture of Rb as a function of detuning frequency, (ii) Absorption trace of ^{87}Rb with 0.5 Torr Kr buffer gas. The features in the middle of the trace (ii) (between b and c transitions) are due to the mode hopping of the diode laser.

4.2.2 Broadening phenomena in atomic vapour

In far-detuned Raman absorption situations, where the different frequencies of the two lasers coincides with the energy spacing of the ground states, the two ground states do not take part in fluorescence cycles. The linewidth of the Raman line is governed by the ground-state relaxation rate. In a warm vapour cell there are some other phenomena such as diffusion, collisional decoherence, and power broadening that can affect the total linewidth and therefore the ground state coherence. The crossing angle between the probe and control beams can also affect the linewidth of both EIT and Raman lines. In the following sections we discuss these phenomena in more detail.

Coupling field-induced power broadening and scattering

If the Raman detuning is not large enough, the coupling field can drive the population in the levels $|1\rangle$ or $|2\rangle$ and cause spontaneous Raman scattering (SRS). This can reduce the coherence time of the memory after the light is stored. The scattering of light with frequency ω_l in a multi-level atom can be written [155] as

$$\Gamma_{F,m_F}(\omega_l, p, I) = \frac{I(r,z)}{6\pi\epsilon_0^2\hbar^3c^4}\sum_j(\omega_l-\omega_{ji})^3\times|\sum_{k,p}\frac{\mu_{jk}\mu_{ki}}{\omega_{ki}-\omega_l}|^2 \tag{4.30}$$

where μ_{ij} is the dipole moment for transition $i \to j$, ω_{ij} is the frequency of the transition $i \to j$ and p is the polarisation of the scattered photon.

At large detuning, the scattering rate or the FWHM of the Raman line asymptotically follows the laser power, $\Gamma_{scatt} = \gamma\Omega^2/(\gamma^2 + \Delta^2)$. At low coupling field powers the FWHM of the Raman line is the ground state linewidth γ_0. In order to reduce the coupling field induced scattering, we typically switch off the coupling field during the storage time. This will increase the coherence time by almost an order of magnitude [156].

Doppler broadening

In order to describe the properties of warm vapour cells used in our experiment, we need to consider Doppler effects caused by the thermal motion of Λ systems. Taking into account the Doppler shifted frequencies of a Λ atom, which moves at velocity v with respect to the propagation direction of the two laser beams [157], for the position of the single-frequency Raman absorption line we have

$$\omega_R \simeq \omega_{12}(1 + v/c). \tag{4.31}$$

The velocity spread of the contributing velocity class can be roughly determined by taking into account the resonant absorption linewidth of the excited stated. The velocity spread leads to a Doppler broadening of the observed Raman line in the laboratory frame. This width at $T \simeq 70°$ C is around 500 MHz and can be estimated from the linewidth of the one-photon absorption lines in Fig. 4.8 (b), (i) trace. Far-detuned two-photon absorption would be insensitive to the Doppler broadening of the excited state as long as the two fields are co-propagating. The angular dependency in the presence of Doppler broadening is discussed in the next section.

The effect of Doppler-broadening of a medium on the EIT linewidth has been theoretically investigated by A. Javan et al. [158]. An explicit expression for the FWHM of an EIT resonance in a Doppler-broadened medium can be found

$$\Gamma_{EIT}^2 = \frac{\gamma_0}{\gamma}\Omega^2(1+x)[1 + (1 + \frac{4x}{(1+x)^2})^{1/2}] \tag{4.32}$$

where $x = \frac{\gamma}{2\gamma_0}\Omega^2/W_D^2$ and W_D is the FWHM of the Doppler-broadened resonance. This equation is plotted for two different Doppler broadenings in Fig. 4.9 (a). As it is apparent from Eq. 4.32, in the regimes where $x \gg 1$ the linewidth shows a quadratic dependence on the coupling field Rabi frequency, Ω. In the regimes where $x \ll 1$, linewidth increases linearly with Ω.

In most light storage experiments, the ground state decoherence rate (γ_0) is low, and the Doppler broadening is on the order of 50γ; therefore a quadratic dependence is expected for the EIT linewidth as a function of Ω.

The Raman line shows similar behaviour as a function of Ω. We follow a similar method to the one described in Ref. [158] and solved the integrals numerically to calculate the FWHM of the Raman line for different coupling field Rabi frequencies. The results of numerical calculations of the Raman linewidth for two different detunings as functions of Ω are depicted in Fig. 4.9 (b).

It is worth mentioning that the presence of a buffer gas leads to completely different physics from the usual Doppler approach to hot gases, due to the velocity-changing

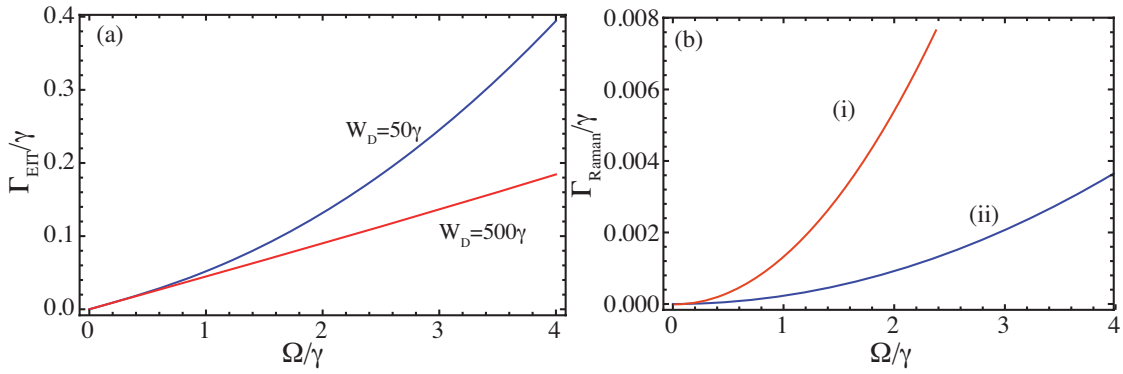

Figure 4.9: (a) FWHM of the EIT line plotted using Eq. 4.32 for two different Doppler broadenings, $W_D = 50\gamma$ (blue line) and $W_D = 500\gamma$ (ref line). Parameters used for this calculation are: $\Delta = 0$, $\gamma_0 = 10^{-3}\gamma$ and $\gamma = 2\pi 5.6 \times 10^6$. (b) FWHM of the Raman line plotted using numerical integration. Parameters used for this calculation are: $\Delta = 100\gamma$ (i), $\Delta = 300\gamma$ (ii), $\gamma_0 = 0$ and $T = 350k$.

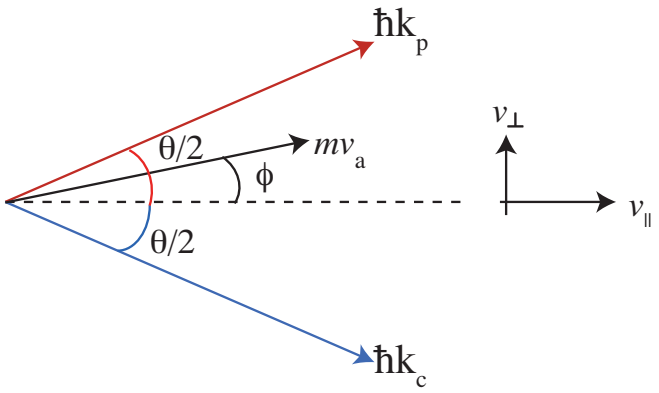

Figure 4.10: Schematic diagram showing the crossing angle between optical and atomic beams. The reference coordinates are $V_{||}$ and $V_{\perp}$, representing the quantisation axis and its perpendicular, respectively. V_a is the velocity of the atom.

collisions.

Angular dependency of absorption and transmission lines

The mode-matching and crossing angle between the control and probe beams are crucial for the performance of both EIT- and Raman-based memories. To determine the proper orientation between the two beams the following analysis is required.

Consider the angular configuration of optical and atomic beams shown in Fig. 4.10, where the angle between the control and probe is shown as θ and the atomic velocity makes an angle α with the quantisation axis.

In a vapour cell, due to the non-zero crossing angle between the beams, the one-photon and two-photon detunings have to be modified to include the extra frequency shift [159] in order to describe the physics of the system more accurately. The change in the detuning of the probe and coupling fields as a function of their wave vectors, k_p and k_c, can be

written as

$$\begin{aligned} \delta &\rightarrow \delta - \mathbf{k_p}.\mathbf{v} \\ \Delta &\rightarrow \Delta + (\mathbf{k_p} - \mathbf{k_c}).\mathbf{v} \end{aligned} \tag{4.33}$$

where

$$\begin{aligned} -\mathbf{k_p}.\mathbf{v} &= -k_p v_a cos(\theta/2 + \alpha) = -k_p v_p \\ (\mathbf{k_p} - \mathbf{k_c}).\mathbf{v} &= 2k_p v_\perp sin(\theta/2) \end{aligned} \tag{4.34}$$

and bold letters represent vectors. The velocity v_p is the component of atomic velocity along the probe beam and $v_\perp$ is the component of atomic velocity perpendicular to the quantisation axis. Taking these frequency shifts into account, Eq. 4.22 for one atom can be rewritten as

$$Im[\chi] = \frac{(8(\delta - k_p v_p)^2\gamma + 2\gamma_0(\Omega^2 + \gamma_0\gamma)}{|\Omega^2 + (\gamma + 2i(\Delta + k_p v_\perp sin(\theta/2)))(\gamma_0 + 2i(\delta - k_p v_p))|^2} \tag{4.35}$$

The atomic velocity in each direction is defined by the Maxwell-Boltzman distribution

$$N(v_z)dz = N\sqrt{\frac{m}{\pi 2k_B T}} exp^{-\frac{mv_z^2}{2k_B T}} dv_z \tag{4.36}$$

where N is the number of atoms, m is atomic mass, k_B is the Boltzman constant, and v_z is the velocity in one dimension. We assume that the velocity is isotropic in the vapour cell, such that the distribution of v_z is the same as the distribution of $v_\perp$ and v_p. Therefore, the absorption coefficient of the medium is given by

$$\alpha \propto \int_{-\infty}^{\infty}\int_{-\infty}^{\infty} Im[\chi](v_p, v_\perp)N(v_p)N(v_\perp)dv_p dv_\perp \tag{4.37}$$

This integral can be numerically solved at $T > 0$ to find the absorption coefficient and FWHM of Lorentzian-shaped EIT or Raman lines. The results of numerical calculations for the absorption coefficient and width of the transparency window of an EIT line are shown in Fig. 4.11 (a) and (b), respectively. As can be seen in Fig. 4.11 (a), the EIT resonance decreases rapidly as the crossing angle between the control and probe increases. As the temperature of the ensemble increases, the EIT resonance dies away at a non-zero crossing angle. Also the linewidth of the EIT resonance (see Fig. 4.11 (b)) is quadratically increasing with the crossing angle. These behaviours have been experimentally investigated in Ref. [160].

Similar numerical results for Raman absorption are shown in Fig. 4.12. The absorption of the Raman line has a maximum value that approaches the zero crossing angle at $\Delta/\Omega \gg 1$. The absorption coefficient for two different values of Ω as a function of the crossing angle is plotted in Fig. 4.12 (a). The Raman linewidth relationship with the crossing angle is linear, as shown in Fig. 4.12 (b), as opposed to that in EIT which is quadratic.

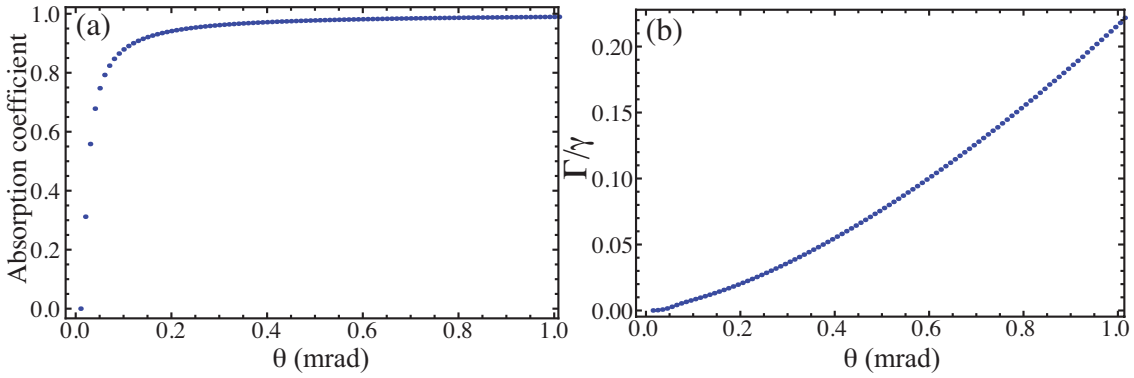

Figure 4.11: (a) Normalised absorption coefficient calculated by the numerical integration of Eq. 4.37 for different crossing angles of the control and probe beams. (b) FWHM of the Lorentzian transmission line calculated again using Eq. 4.37. Parameters used for this calculation are: $\Delta = 0$, $\Omega = 0.2\gamma$, $\gamma_0 = 0$, and T=350 K.

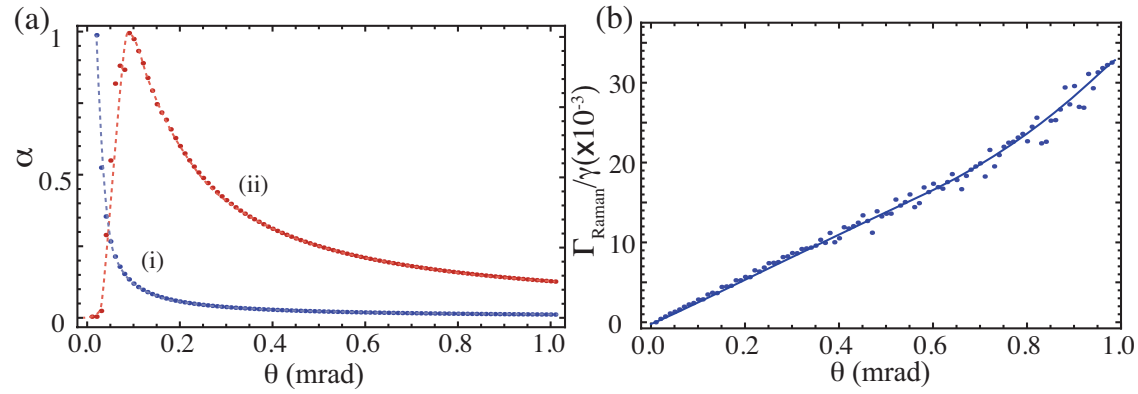

Figure 4.12: (a) Normalised absorption coefficient calculated for detuned light by numerical integration of Eq. 4.37 for different crossing angles of the control and probe beams. Red (i) and blue (ii) data show the absorption coefficient for $\Omega = 1.0\gamma$ and $\Omega = 2.0\gamma$ respectively. The rest of the parameters used for this calculation are: $\Delta = 300$, $\gamma_0 = 0$, and $T = 350$ K. (b) FWHM of Lorentzian Raman absorption line calculated again using Eq. 4.37. Parameters used for this calculation are: $\Delta = 300$, $\Omega = 1.0\gamma$, $\gamma_0 = 0$, and $T = 350$ K.

Buffer gas in vapour cells

In most light storage experiments that have been performed on warm Rb vapour cell, inert gases (buffer gases) such as Ne, Kr, He etc. have been used to increase the time of flight of atoms inside the laser beams due to velocity-changing collisions. However, the collisions with buffer gas will shuffle the population in the excited state and can cause collisional broadening [157] of the excited state. The collision rate is given by

$$\Gamma_{col} = \frac{p}{k_B T}\sigma_k \bar{v} \tag{4.38}$$

where p is the gas pressure, T is the temperature and $\bar{v}$ is the average velocity of the atoms. σ_k is the kinetic cross section; and is around 4×10^{-15} cm^2 for Rb-Ne. At room

temperatures, the collisional broadening for Rb-Kr is $\Gamma_{col}^{Rb-Kr} = 17.1$ MHz/Torr and for Rb-Ne is $\Gamma_{col}^{Rb-Ne} = 9.84$ MHz/Torr [161].

Apart from broadening of the excited state of atoms due to collisions with the buffer gas, the hyperfine atomic energy level also shifts due to the inelastic collisional process. The frequency shift of the ^{87}Rb ground-state hyperfine levels for different buffer gases are given in Table 4.1.

Buffer gas	Frequency shift (Hz/Torr)
He	720
Ne	392
Ar	-52
Kr	-580
H_2	660
N_2	520

Table 4.1: Buffer gas-induced frequency shift of ^{87}Rb ground-state hyperfine levels in Hz/Torr for different buffer gases [162].

At zero crossing angle between probe and coupling beams, the two-photon detuning of Raman transition in a Doppler broadened medium is given by

$$\delta' \rightarrow \delta(1 - v_n/c). \tag{4.39}$$

where δ is two-photon detuning between two Raman fields.

To study the effect of collisional broadening [157] on the atomic coherence, one can use the Liouville-von Neumann equations of motion

$$\frac{d\rho_n}{dt} = \frac{1}{i\hbar}[\hat{H}, \rho_n] + \sum_{m=1}^{N_v} W_{nm}\rho_m \tag{4.40}$$

where W_{nm} is called the collision kernel and represents the population losses and dephasing of atoms with the velocity classes n. N_v is the number of atoms moving with velocity v_j for $j \in [1, ..., n]$. The collision kernel is simplified [157] by neglecting the velocity dependency of the collision rate as

$$\begin{aligned} W_{nm} &= \Gamma_{col} P_n \qquad n \neq m \\ W_{nm} &= \Gamma_{col}(P_n - 1) \qquad n = m \end{aligned} \tag{4.41}$$

where $P_n = \frac{e^{-(v_n/v_w)^2}}{\sum_{n=1}^{N_v} e^{-(v_n/v_w)^2}}$ indicates the probability of finding the atom in the velocity classes n. Here, $v_w = \sqrt{2k_BT/m}$ is the most probable velocity. This equation can be solved numerically in order to see the effect of the buffer gas on the coherence of atoms in a warm vapour cell.

We note here that, in our experimental regime, collision rate between Rb atoms is much smaller than collision rate between Rb and buffer gas atoms. This is because, the

Rb pressure is at least 3 orders of magnitude smaller than the buffer gas pressure.

Dicke narrowing

If the collision rate between the Rb atoms and the buffer gas is much higher than the optical decay rate, $\Gamma_{col} \gg \gamma$, a Doppler-broadened spectrum can be dramatically narrowed due to frequent velocity-changing collisions. This regime is known as *Dicke narrowing* [163]. The narrowing factor, known as the Dicke parameter, is proportional to the ratio between the mean free path, $D = v_{th}/\Gamma_{col}$. In the Raman transition scenario, the wave vector to be considered is $\mathbf{k_p} - \mathbf{k_c}$. Dicke narrowing occurs when collisional velocity changes hinder the buildup of the Doppler phase $\int_0^t (\mathbf{k_p} - \mathbf{k_c}).\mathbf{v}(\mathbf{t}')\mathbf{dt}'$. The Doppler phase builds up coherently during the time interval Γ_{coll}^{-1}. Hence Dicke narrowing occurs if $|\mathbf{k_p} - \mathbf{k_c}|\mathbf{v_w}/\mathbf{\Gamma_{col}} \ll \pi$.

Dicke narrowing was previously observed for optical transitions [164]. A narrowing of the expected Doppler width for two-photon transitions, such as coherent population trapping (CPT) was also observed and was attributed to a Dicke-like narrowing [165, 166].

Atomic diffusion in a gas cell

A major relaxation process appears due to spatial diffusion out of the laser beams. In our case, we use a cylindrical geometry with a transverse diameter of a few millimetres, and a length of 7-20 cm. We are interested in how long it takes for an atom to diffuse out of the transverse cross-section (i.e. the interaction volume). In two dimensions, the standard deviation in position σ_r (defined such that approximately 32% of atoms have moved a distance greater than σ_r) is given by [167]

$$\sigma_r = 2\sqrt{2Dt} \tag{4.42}$$

where D is a diffusion coefficient with units of cm^2/s that is defined as

$$D = D_0(\frac{P_0}{P}) \tag{4.43}$$

Here $P_0 = 760$ Torr, P is the buffer-gas pressure in Torr, and t is the time. The diffusion constant D_0 for Rb-Kr is calculated at the temperature of 45° to be about 0.16 $\mathrm{cm}^2/\mathrm{sec}$ [162]. The diffusion constant above room temperature also scales with $T^{3/2}$ [162].

Furthermore, if an atom moves longitudinally by a distance δz during the storage time, it will experience a frequency shift of $\eta\delta z$ at read out due to the applied atomic frequency gradient. The random frequency shift of atoms might result in the frequency blurring of the output spectrum. The effect of longitudinal motion in our experiment is negligible because $\eta\delta z$ is small compared to the unbroadened Raman linewidth.

Collisions with walls

The decay rate of atomic coherences (dark states) in a gas cell is related to depolarisation. In the presence of a buffer gas the decay rate is mainly a function of collisions with the cell walls and collisions with buffer gas atoms. Alkali atom vapour cells with anti-relaxation coatings are used in many experiments in quantum optics [96] to provide long relaxation times of atomic polarisation. This is necessary for these types of experiments, and new

coating materials can improve the spin relaxation time due to wall collisions in the absence of optical pumping.

The traditional paraffin coated cells show a large improvement in the atomic coherence time. It was shown very recently that cells prepared with a single compound alkene-based coating show a spin relaxation times [99, 168] a few order of magnitude longer than the paraffin-coated ones. Using this alkene coating, minute long spin relaxation has been observed [169].

The transverse beam profile effect on transmission and absorption

In a Rb vapour cell or any other thermal gas of free particles, the translational motion of atoms plays an important role and can affect the resonance line shape. This occurs primarily through the Doppler shift of the resonance frequency, as discussed in Sec. 4.2.2, or transit-time effects due to the finite interaction time of the atoms with the laser beam. In the transit-time regime, it has been shown [170] that the power-broadening contribution to the linewidth is at a minimum when the beam radius is approximately equal to the mean free path. The other factor that can influence the interaction is the intensity profile of the laser beam.

The transverse profile of both the probe and control beams is crucial in optimising the absorption (in the case of Raman) or transmission (in the case of EIT). Depending on the type of buffer gases and pressure, temperature, wall coating and scheme (EIT or Raman) used, there exists an optimum beam profile. This can be different for the probe and the control beams.

The dependency of the EIT line shape on the transverse intensity distribution has been studied by A. V. Taichenachev et. al [171], where a dramatic difference in the resonance line shape was found when comparing a beam with a top-hat profile to a beam with a Gaussian profile. This important factor leads to significant changes in the resonance as well as the off-resonace shape and width of the absorption line.

We assume that atoms have a large relaxation rate of Γ_r, i.e. the rate of redistribution of atoms among internal degrees of freedom, so that for a vapour cell with buffer

$$\Gamma_r \gg D/r_0^2 \tag{4.44}$$

and with no buffer gas

$$\Gamma_r \gg v/r_0 \tag{4.45}$$

where D is the diffusion constant, r_0 is the radius at $1/e$ of the maximum intensity and v is the root-mean-square thermal velocity of the atoms. Using this assumption, the excess linewidth for a beam with a Gaussian profile can be written as

$$\Gamma_G \simeq 0.86\frac{\Omega_p^2 + \Omega_c^2}{\gamma} \tag{4.46}$$

and for a beam with a top-hat profile

$$\Gamma_{TH} \simeq 2\frac{\Omega_p^2 + \Omega_c^2}{\gamma} \tag{4.47}$$

where Ω_p and Ω_c are the Rabi frequencies of the probe and coupling fields, respectively, and γ is the excited state linewidth. The linewidth of a top-hat beam is larger than that of a Gaussian beam. Moreover, a top-hat beam profile leads to a more standard Lorentzian line shape while a Gaussian profile has a more complicated line shapes.

In our experiment, we work in an off-resonance Raman regime where a large coupling field is used to enhance the absorption. In this regime the power broadening is significant and similar behaviour to that described for EIT is expected.

4.2.3 Interaction of Rb with external magnetic fields

Each of the hyperfine (F) energy levels contains $2F+1$ magnetic sub-levels that determine the angular distribution of the electronic wave function. In the absence of external magnetic fields, these sub-levels are degenerate. However, when an external magnetic field is applied, their degeneracy is broken. For weak magnetic fields, the interaction Hamiltonian perturbs the zero-field eigenstates. To the lowest order, the levels split linearly according to

$$\Delta E_{|Fm_f\rangle} = \mu_B g_F m_f B z \tag{4.48}$$

where the Lande factor g_F is given by

$$g_F \simeq g_J \frac{F(F+1) - I(I+1) + J(J+1)}{2F(F+1)} \tag{4.49}$$

and g_J is defined as

$$g_J \simeq 1 + \frac{J(J+1) + S(S+1) - L(L+1)}{2J(J+1)} \tag{4.50}$$

Here, μ_B is the Bohr Magneton, J and F are the total electron angular momentum and the total atomic angular momentum, respectively, and m_f is the Zeeman sub level. The coefficient m_f determines the Zeeman sub-level. This implies that, for instance, the splitting between the ground state of ^{87}Rb is $\Delta E/B_{F=2,1} \simeq \pm 1.4/2$ MHz/G. For the excited state , $5^2P_{1/2}$ this splitting is less; approximately $\pm 1.4/3$ MHz/G [172].

4.3 Experimental techniques

In this section we discuss experimental elements and techniques used to implement the gradient echo memory. The experimental setup is explained in Sec. 4.3.1 and experimental evidence of photon echoes generated using this scheme is presented in Sec. 4.3.2.

4.3.1 Experimental setup

The first photon echo generated via the gradient echo technique in a warm vapour cell was observed using the experimental setup shown in Fig. 4.13 (a) and (b). The vapour cell (length and diameter of 75 mm and 22 mm, respectively) contains isotopically enhanced ^{87}Rb and helium buffer gas at a pressure of 5 Torr. An arrangement of 4 coils, shown in Fig. 4.13(a) is used to generate the required magnetic fields. There is a small gap between each pair of coils with the same diameter to allow a gradient to be created. The ratio of

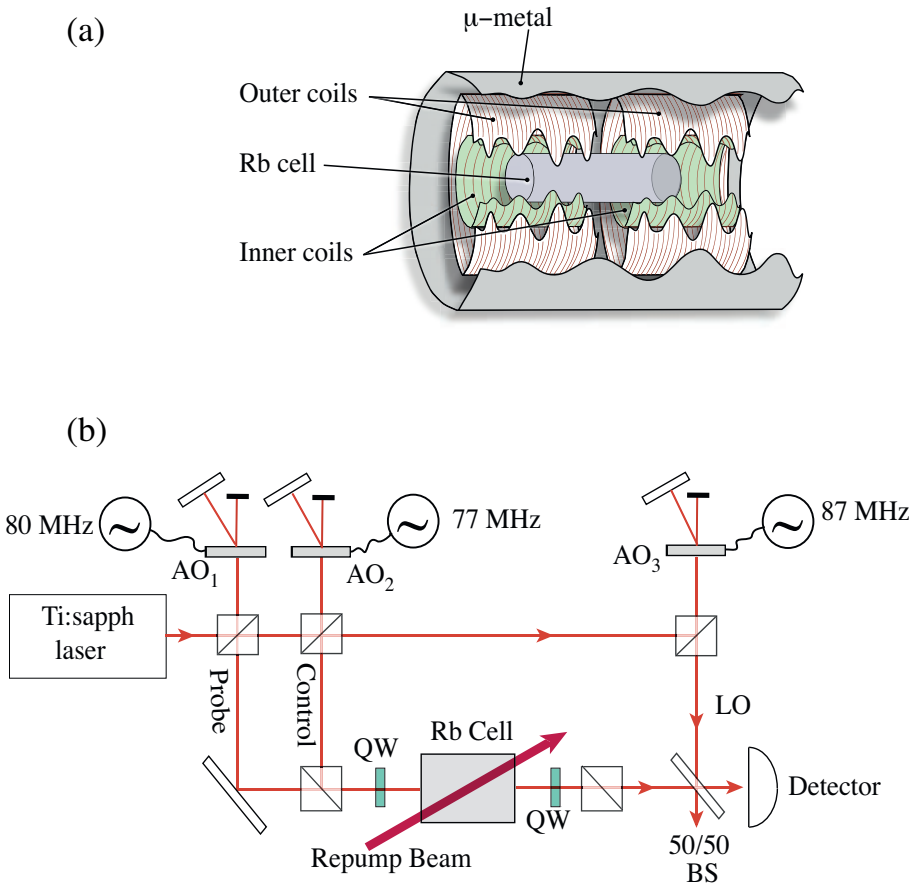

Figure 4.13: (a) Cross-section of the magnetic coil configuration around the Rb cell. (b) Diagram of the optical layout $AO_{1,2,3}$ are acousto-optic modulators, and QW are quarter-waveplates.

current between the two coils defines the strength of the gradient. The outer coils are used to generate a B-field with an average of 3.4 G at the centre of the gas cell and a slope that could be tuned to accommodate the Fourier width of the light pulse to be stored. The inner coils are switchable and allows us to reverse the sign of the B-field gradient over a period of 1 μs.

A schematic of the optical set-up is shown in Fig. 4.13(b). The Ti:sapph laser was red detuned by 600 MHz from the hyperfine transition $F_g = 2 \rightarrow F_e = 1$ of the ^{87}Rb D_1 line. The two Zeeman sub-levels of $F_g = 2$, $m_f = 0, 2$, were Raman coupled. The frequency of the control and the probe could be tuned to match the two-photon detuning introduced by the constant magnetic field offset (3.4 G) and the light shift (50 kHz). The two beams had opposite circular polarisation creating a Λ-transition between two Zeeman sub-levels ($m_f = 0, 2$) of the $F_g = 2$ hyperfine state. The control and probe beams had diameters of 2 and 0.3 cm respectively. An external cavity diode laser could be used to pump atoms from the $F_g = 1$ to the $F_e = 2$ hyperfine levels.

To observe the Raman absorption line, shown in Fig. 4.14(a) (i), the control beam frequency was scanned and the probe absorption was monitored. The width of the absorption line was observed to be 170 kHz. Compared to the transmission without the control beam (iii) we have about 75% absorption at the line centre. Trace (ii) shows the Raman line after Zeeman broadening is applied using the spatially varying B field. Even with the laser

600 MHz detuned from the Doppler-free transition frequency, the background absorption present in trace (iii) is 50%.

One of the first steps towards generating photon echoes is observing free induction decay (FID) [2]. After exciting the atoms participating in the Raman absorption by a pulse shorter than the inverse of the linewidth, the atomic macroscopic coherence will cause coherent light re-radiation. A long FID signal indicates a long macroscopic coherence time and therefore a small ensemble linewidth. To observe the FID, we use heterodyne detection and excite the atoms with a short weak pulse of 250 ns. Fig. 4.14(b) (i) shows an FID observed without applying a broadening magnetic field. Oscillations of the amplitude are observed for about 2.5 μs. The decay time of the intensity of the signal is then about 1.2 μs, consistent with the width of the unbroadened Raman feature ($1/(2\pi 170\text{ kHz}) \approx 1\ \mu s$). Trace (ii) shows the result of the same experiment but with the Raman feature broadened by the chirped Zeeman shift. The FID then decays much faster and the oscillations are almost completely eliminated.

The decay of the unbroadened FID depends mainly on the time-of-flight of the atoms in the beam. In an EIT experiment, the probe and control beams are resonant with the upper atomic level so that only atoms of a single velocity class can contribute. In a Raman system, atoms of any velocity class can absorb. This means the optical depth could potentially be larger but on the other hand the decoherence due to the atomic motion is likely to be more severe. To observe the Raman line, we scan the control beam frequency (δ) and monitor the probe absorption. Fig. 4.14 (c) shows the evolution of the absorption profile for different values of one-photon detuning (Δ) and a constant coupling field (Ω_c).

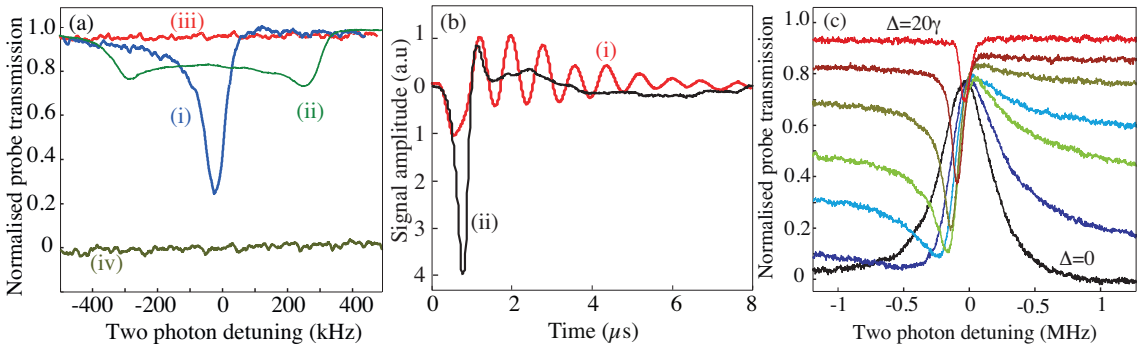

Figure 4.14: (a) The Raman absorption is shown in (i). The broadening of the Raman line induced by the magnetic field is shown in (ii). (iii) was obtained with the control beam blocked and (iv) shows the level when the probe light is blocked. Experimental parameters were: $\Delta = 600$ MHz, control and probe beam powers of 40 mW and 1 μW respectively, and a cell temperature of 60°C. (b) The FID shown in (i) has an amplitude decay time of about 2.5 μs. With a linearly varying B-field, the FID decay is much faster, as can be seen in (ii). (c) The transition between the EIT or Raman absorption profile is evident when the one-photon detuning Δ is scanned from 0 to 20γ.

When one-photon resonance, $\Delta = 0$, we find the EIT profile with a Lorentzian shape. By increasing the detuning, the transparency window becomes more and more asymmetric. For detunings larger than the Doppler width [173], the transparency window vanishes and a Raman absorption profile appears. No parameters, other than the laser frequency, were changed for this measurement. The absorption efficiency of the Raman process is not optimised here. In practice, the Faraday polarisation self-rotation effect [174] depends on

the one photon detuning; for a given laser frequency the power of the coupling field and the polarising optics ($\lambda/4$ plates) have to be re-optimised. Such a self-rotation mechanism comes from ac-Stark shifts induced by the off-resonant atomic levels. The magnitude of the self-rotation depends on the amount of population in the two ground states situated in the middle of the manifolds. As the optical pumping to the $m_F = -2$ state reduces with one photon detuning, the ground state population becomes evenly distributed across the manifolds. This causes the off-resonant levels to disturb the dark-state preparation and also causes a significant rotation of the light polarisation. See, for example, Ref. [175]. In the following section we present the first proof of principle demonstration of light storage using the GEM in a warm vapour cell.

4.3.2 First observation of echo in warm vapour

A narrow Raman absorption line was prepared and broadened using monotonically varying and reversible magnetic fields. The first observation of a photon echo generated by reversing the magnetic field gradients in a rubidium vapour is shown in Fig. 4.15 (a) [176]. Trace (i) shows an input pulse, of around 1 μs long, being measured by blocking the coupling field. Trace (ii) shows the amount of light that is being transmitted through the cell without being absorbed. The shape of the transmitted pulse is a consequence of the filtering of high-frequency components of the input by the Zeeman-shifted medium. We indeed notice that the fast variations of the pulse are not absorbed as efficiently. Using a broader Zeeman shift reduced the strength of these fast variations, but also the total efficiency, as the optical depth for each spectral component decreased[154].

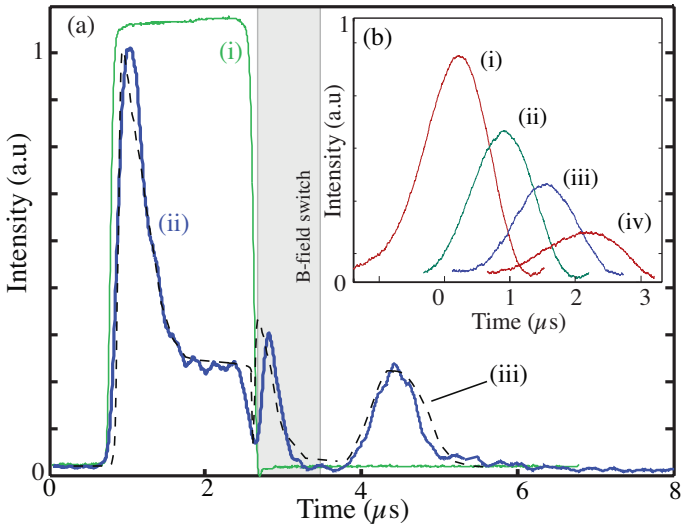

Figure 4.15: (a) The input pulse (i) is shown without Raman absorption, although its height is reduced by a factor of 2 due to the residual loss in the gas cell. The absorption is strongly enhanced by the Raman beam, as shown by the left-hand side of (ii). After switching the B-field, an echo emerges as seen on the right-hand side of (ii). (iii) The model shows good agreement with the experiment. Parameters used in the model are γ_0=500 kHz, η=0.2 G/cm and a B-field switching time of 300 ns. (b) As the B-field switch was delayed in steps of 200ns, we observe a corresponding delay in the echo.

After flipping the magnetic field slope at $t = 3.5$ μs we retrieved part of the stored excitation. This is shown on the right-hand side of trace (ii). About 30% of coherently

absorbed light was retrieved as an echo. This result was well predicted by numerical simulations using the two-level atom model[154]. Trace (iii) shows the result of the simulations, using a decay time of 500 ns, an optical depth of 0.4, and magnetic field gradient of 0.2 G/cm and accounting for the finite switching rate of the current. The main features of the experiment are reproduced by the model. The reason that the shape of the unabsorbed pulse is different from the input is due to low frequency absorption of the input pulse. The memory bandwidth, in this case, is not large enough to encompass the entire input pulse and therefore high-frequency components will leave the medium without absorption. To enlarge the bandwidth of the memory, one should increase the gradient field as well as the vapour density. In principle, large-memory bandwidth can be achieved, provided that the memory bandwidth is much smaller than the one-photon detuning of the Raman transition. In practice, the main limitation of increasing the memory bandwidth is increasing the optical density of the memory.

It is important to point out that the efficiency of the whole storage process cannot be assessed from the present results only. As the laser was operated close to the Doppler profile, there was about 50% absorption of the input beam when the control beam was off. Moving further off resonance reduced this incoherent absorption (thereby making the Raman feature more symmetric) but also reduced the depth of the Raman absorption.

To characterise the light storage mechanism further we measured the evolution of the efficiency as a function of storage time. Fig.4.15 (b) shows the echo output as a function of time, as the input pulse was shifted further away from the switching point. The input pulse was moved backwards by steps of 200 ns. The echo emerges further away from the magnetic field switching, as expected from the dipoles' time-reversed evolutions. The decay time constant of the echoes, determined using an exponential decay function, was found to be 600ns.

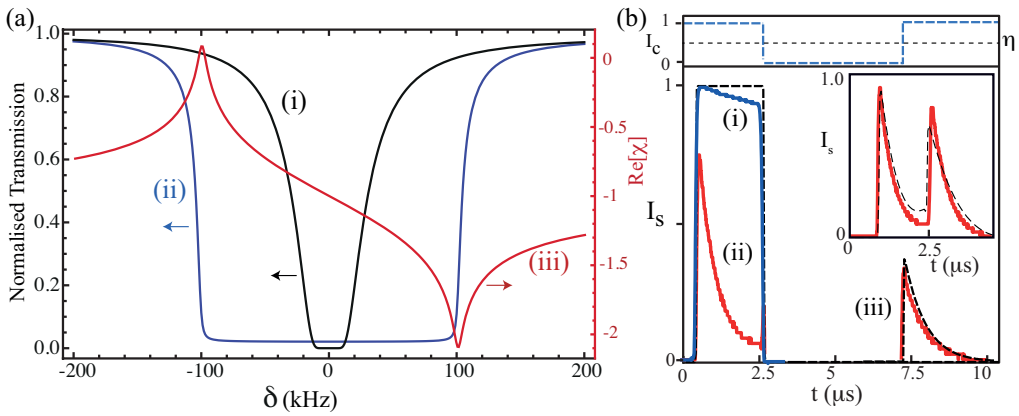

Figure 4.16: (a) Normalised transmission of the probe signal as a function of two-photon detuning for unbroadened (i) and broadened (ii) Raman lines as well as the real part of susceptibility corresponding to the broadened line (iii). Parameters used to obtain susceptibility are: $\Omega_c = 20MHz$, $\gamma_0 = 5kHz$, $\Delta = 2GHz$, and $\eta L = 200kHz$ for the broadened line. (b) Storage of slow light. (i) Input pulse (ii) unabsorbed transmitted pulse, (iii) recalled light. Inset shows the transmitted light when the coupling field stays on. The top section of the figure shows the switching protocols for the coupling and magnetic fields. Dashed lines show the corresponding curve obtained from numerical simulation.

4.3.3 Slow light contribution

The normalised transmission of the probe field and the real part of the susceptibility is depicted in Fig. 4.16 (a) as a function of two-photon detuning, δ. The absorption of the unbroadened line (trace (i)) is significant due to the large OD, and applying a broadening of 200 kHz does not noticeably alter the maximum absorption (trace (ii)). The susceptibility shown as trace (iii) indicates the group velocity of the light for different frequency components. From this plot, it can be seen that the frequency components of the light outside the edge of the Raman line, which are not absorbed, propagate with a slow group velocity due to the steep variation of susceptibility.

As discussed earlier in this chapter, for a medium with a small number of atoms the effective optical depth of the memory is inversely proportional to the frequency gradient η. So using a decoherence-free medium, pulses with smaller frequency bandwidths can be stored more efficiently. However, a pulse with a small frequency bandwidth corresponds to a long duration pulse, which requires a system with long-lived coherence for photon echoes to be efficiently recalled. In the case of a pulse that has a frequency bandwidth slightly larger than the memory bandwidth, part of the input pulse is slowed down as mentioned above. This slow light, similar to EIT, can be stored in spin-state coherence by adiabatically switching the coupling field intensity to zero, and recalled later on by increasing the coupling field intensity.

The slow light observed in the experiment is shown in Fig. 4.16 (b). The inset is obtained by keeping the coupling field on all the time. This will cause part of the input pulse, i.e. frequency components near the outer edge of the Raman line, to be delayed. The slow light can be mapped onto the atomic excitations by turning off the coupling field after the pulse enters the medium. Increasing the coupling field intensity again, after a few μs, causes the stored slow light to be coupled out (shown in trace (iii)).

4.3.4 Summary

In summary, we described the theory of GEM in two- and three-level atomic systems. In particular, we considered the practical implementation of such a memory scheme in an ensemble of warm Rb atoms in a vapour cell. We also studied different phenomena expected from interactions between a laser beam and Rb atoms in a warm vapour cell. Furthermore, we provided the first experimental results of light storage in a warm Rb cell by means of the GEM technique.

Chapter 5

Light Storage in the Polariton Picture

"I believe neither in what I touch nor what I see. I only believe in what I do not see, and solely in what I feel."

Gustave Moreau

Quasi-particles are a particular class of mathematical objects formed by a superposition of two disparate quantised fields. Their main purpose is to predict the physical behaviour of complex systems. There are many quasi-particles associated with various physical systems and they prove to be successful in explaining physical mechanisms. For instance, an *exciton* is a superposition of an electron and hole, or a *Plasmon* is a quasiparticle resulting from the quantisation of plasma oscillations (oscillation of free electron density).

The surface plasmons (plasmons that are confined to surfaces) interact strongly with light resulting in a polariton. The *polariton* is a form of quasi-particle that results from the coupling of the electromagnetic field with atomic excitations. The frequency of the surface plasmons is blue-shifted compared to thefrequency in the bulk. Gerard Milburn pointed out that this is illustrated by The Lycurgus Cup in the British Museum (see Fig. 5.1). Also, Mark Stockman states in Physics Today (issued on February 2011, page 39):"The resonant properties of plasmonic metal nanoparticles are readily apparent to the naked eye because the excitations absorb and scatter light at optical frequencies. The most ancient example is the famous fourth-century CE Lycurgus cup from the British museum, whose glass looks green in reflected light but ruby red in transmitted light. Those colors are complementary, evidence that there is little optical loss inside the glass. Investigation has shown that the dichroic glass contains nanocrystals of a gold-silver alloy at a fraction of less than 1%" [177].

A similar effect can be seen in the stained glass used in the windows of Sainte-Chapelle and rose window of Notre-Dame de Paris. In Sainte-Chapelle at sunset, the scattering of light by gold nanoparticles in the windows creates a pronounced red glow that appears to slowly move downward. This is because the intensity of the red light strongly depends on the incident and viewing angles. However, the intensities of blue tints from ions of copper or cobalt remain the same. "The artistic impression, probably intended, suggests a stream of blood slowly flowing downward" [177].

Quasi-particles, like real particles, can have bosonic or fermionic statistics. Polaritons, like photons, have bosonic statistics [178] and, in fact, Bose-Einstein condensation of exciton polaritons has been observed in a microcavity [178]. For instance, a polariton can also be associated with a light field propagating through a medium with a group velocity less than c to provide an intuitive picture of the atom-light interactions. Particularly,

Figure 5.1: The Lycurgus cup from the British museum, whose glass looks green (on the left) in reflected light but ruby red in transmitted light (on the right).

theoretical models for light storage based on polariton evolution can provide a powerful tool for understanding the physics of such systems and this information can then be used to manipulate the system's properties.

In this chapter, we introduce a polaritonic description of light storage in an atomic medium. We start by describing the polariton associated with an electromagnetically induced transparency (EIT) medium and then compare it with its counterpart in a gradient echo memory (GEM) system. We show how some of the detailed physical phenomena behind these light storage techniques can be precisely described using this theoretical picture.

5.1 The EIT dark-state polariton

Employing an EIT mechanism, one can change the response of a medium for a weak resonant field using a strong resonant control field, thanks to quantum interference between the two absorption paths. In that case, the system is said to be in the *dark state* [68] and is decoupled from the excited state. As long as the pulse is inside the medium, the information remains as a form of a partial electromagnetic field and partial atomic coherence. The latter term refers to an excitation of the atomic spin state, $|1\rangle$ and $|2\rangle$, coherence. In this interaction regime, the system cannot be described by the individual atomic or electric fields and it is possible to associate a quasi-particle with its propagation. This quasi-particle is called a dark-state polariton [68]. The adiabatic dark state polariton can be written as

$$\hat{\Psi}(z,t) = \cos\theta\hat{\mathcal{E}} - \sqrt{N}\sin\theta\sigma_{12} \tag{5.1}$$

where

$$\cos\theta = \Omega_c/\sqrt{\Omega_c^2 + g^2N}$$

$$\sin\theta = g^2 N/\sqrt{\Omega_c^2 + g^2 N} \tag{5.2}$$

Here, we dropped the operator sign for atomic operators for simplicity. The state $\hat{\Psi}(z,t)$

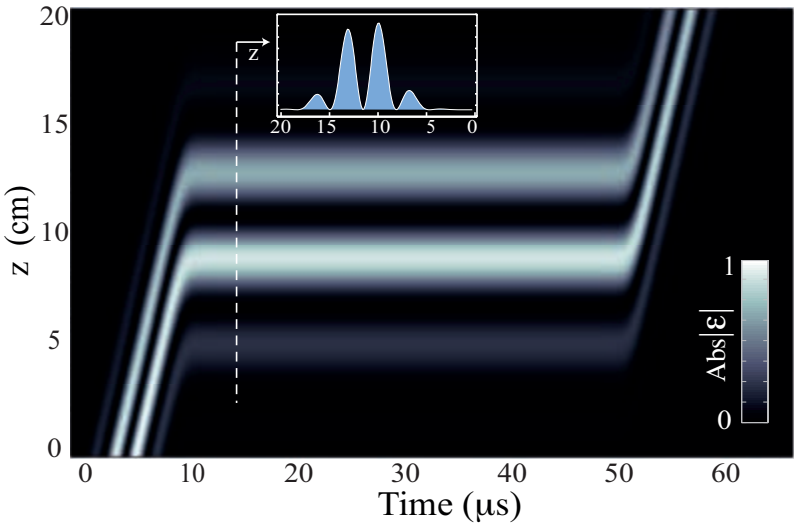

Figure 5.2: Absolute value of the EIT normal mode presentation in $z-t$ plane. The temporal profile of the input modulated pulse is obtained by taking cross sections along the z axis and is shown in the inset. The control field is turned off during t =15-50 μs. In this time window the polariton is entirely atomic ($\cos\theta = 0$ and $\sin\theta \neq 0$).

obeys the following equation of motion

$$[\partial/\partial t + v_g \partial/\partial z]\hat{\Psi}(z,t) = 0 \tag{5.3}$$

which describes shape-preserving propagation of the polariton with velocity $v_g = c\cos^2\theta$. Using this picture we can describe propagation and storage of a light pulse through an EIT medium as evolution of the dark-state polariton: As the light pulse enters the medium, the combined atom-light system is gradually driven from entirely photonic to a superposition of photonic and atomic modes. The ratio between the these modes is defined by the Rabi frequency of the control field, Ω_c, and atom-light coupling, $g\sqrt{N}$. This is one of the most interesting aspects of dark-state polariton that allows one to coherently control and manipulate atom-light interference coupling properties by changing Ω_c. Thus one can drive the system from all-photonic to all-atomic by reducing the control field power to zero. In this case the amplitude and phase information of the light pulse is mapped into the atomic coherences and so the light field is stored coherently. By increasing the control field power, the system can be driven back to the superposition state and the polariton can be reaccelerated and eventually becomes all photonic as the light pulse leaves the medium with the vacuum speed c. The EIT normal mode (polariton) is depicted in Fig. 5.2 in $z-t$ plane for a modulated input pulse. Before the control field is adiabatically switched to zero (t <15 μs), the system is in a superposition of the atomic and photonic fields, where the light field is propagating with a group velocity ($v_g \ll c$). After the control field is switched to zero, the information is mapped into the atomic coherence and the polariton becomes all-atomic. As it is shown in the inset, the temporal profile of the input pulse is obtained by taking cross section along the propagation axis. By turning back on the

control field, the light field is regenerated and eventually released at the end of the sample and propagates with vacuum speed, $v_g = c$.

5.2 GEM Normal mode

Similarly to EIT, one can associate a quasi-particle (polariton) with the light field and spin wave inside the GEM system. The evolution of the polaritonic mode inside the GEM system yields a clear insight to the physical picture of the system.

To obtain a mathematical description of a polariton in a GEM system we solve Eqs. 4.2 and 4.3 while making a plane-wave decomposition of the optical and atomic fields via a spatial Fourier transform. Neglecting the decoherence and taking the spatial Fourier transform of Eqs. 4.2 and 4.3 we arrive at

$$\frac{\partial}{\partial t}\sigma_{12}(t,k) = -\eta\frac{\partial}{\partial k}\sigma_{12}(t,k) + ig\hat{\mathcal{E}}(t,k) \tag{5.4}$$

$$k\hat{\mathcal{E}}(t,k) = \mathcal{N}\sigma_{12}(t,k) \tag{5.5}$$

and therefore

$$(\frac{\partial}{\partial t} + \eta_{(t)}\frac{\partial}{\partial k} - i\frac{g\mathcal{N}}{k})\sigma_{12}(t,k) = 0 \tag{5.6}$$

A similar equation can be written for the electric field ($\mathcal{E}$). Thus, a single mode polariton-like operator in time and k space for two-level atoms is obtained [151], $\hat{\psi}(k,t) = k\hat{\mathcal{E}}(k,t) + \mathcal{N}\hat{\alpha}(k,t)$, which has the following equation of motion

$$(\frac{\partial}{\partial t} + \eta_{(t)}\frac{\partial}{\partial k} - i\frac{g\mathcal{N}}{k})\hat{\psi}(k,t) \quad = \quad 0 \tag{5.7}$$

k here is the spatial frequency component of the joint system.

One can write another solution for the above equation of motion as $\hat{\psi}(k,t) = k\hat{\mathcal{E}}(k,t) - \mathcal{N}\hat{\sigma}(k,t)$. It can be shown, however, using the Maxwell equation that $k\hat{\mathcal{E}}(k,t)$ is equal to $\mathcal{N}\hat{\sigma}(k,t)$ and therefore this mode will never be excited. The normal mode equation of motion (Eqn. 5.7) indicates that $\psi(k,t)$ propagates in the k-axis with a speed defined by the slope of the gradient. As the polariton reaches higher k values the electric field amplitude gradually decreases in time. As each frequency component of light propagates through the medium and gets absorbed by resonant atoms, dispersion due to the neighbouring atoms having slightly different resonant frequencies will affect propagation and absorption. This is, in fact, the origin of the photonic part of the polariton and also the phase shift of the echo [179]. The intensity of the atomic excitation, created after the input light enters the medium, remains unchanged during the storage time. Flipping the gradient (i.e. $\eta \to -\eta$) time reverses the absorption process so that when the polariton reaches $k = 0$ (the phase matching condition) photon-echo emerges from the ensemble in the forward direction. We note here that at each particular time, the system is described by a normal mode with different amplitudes for optical and atomic fields; therefore it makes more sense to picture the GEM storage as a continuum of evolving polaritons and not just a single polariton.

In a three-level atomic ensemble, in the far-detuned and adiabatic regime, using Eqs. 4.25and 4.26 a similar polaritonic mode can be described as $\hat{\psi}(k,t) = k\hat{\mathcal{E}}(k,t) + \mathcal{N}'\hat{\sigma}(k,t)$, where $\mathcal{N}' = \mathcal{N}\Omega/\Delta$. The second term in this equation necessarily goes to zero

if the coupling field is switched off during storage. Therefore, as it is still the case that $k\mathcal{E} = \mathcal{N}'\sigma$, the slowly propagating electric field vanishes and the polariton becomes all atomic.

The real parts of the electric field and atomic polarisation, for a modulated input pulse, are plotted in Fig. 5.3 (a) and (b), respectively, using XMDS [180] numerical simulation of Eqs. 4.27 and 4.28. It can be seen that the light is nearly stopped at the centre of the ensemble after the pulse enters the medium and its intensity gradually decreases. The atomic field is quickly generated after the pulse enters the memory. We also see that as time progresses the spatial structure of the atomic and electric fields becomes increasingly fine before gradient switching. Fig. 5.3 (c) represents the polariton evolution of a two-level atomic sample in the $k-t$ plane. The atomic excitations emit a burst of light (echo) when the polariton returns to $k = 0$ (i.e. when the phase matching condition is satisfied).

The group velocity of the light field propagating inside the medium is given by $v_g = g\mathcal{N}/k^2$. The further away the polariton is from $k = 0$, the less intense the electric field and also the smaller the group velocity. The group velocity and amplitude of light inside the medium can be controllably tuned by varying the coupling field intensity. In a Λ-GEM scheme, however, the group velocity and light amplitude can be controlled by both the coupling field and the detuning of the gradient fields. This extra control over the information provides a fertile ground for data manipulation.

The spatial cross section of the atomic polarisation at any time during the storage is the Fourier spectrum of the input pulse. This explicitly demonstrates the frequency-encoding nature of GEM. Inversely, any cross section of the polariton, $\hat{\psi}(k,t)$, along the k axis (see Fig. 5.3 (c)) shows the temporal profile of the pulse [151] as a second Fourier transform into k-space returns the original pulse shape, i.e. $\sigma(z,t) \rightarrow \sigma(k,t)$. This is shown in Fig. 5.3 (c) where the normal mode for a modulated pulse is plotted. The cross section of the normal mode at the switching time is also shown in the inset.

5.2.1 Steering of the GEM polariton

The microscopic dynamic characteristics of the GEM polariton allow one to precisely control and manipulate the state of the system in time. This control is even more versatile in Λ-GEM thanks to the contribution of the coupling field and detuning gradient in determining the state of the system.

Atomic detuning

The detuning gradient causes the different frequency components of the light to be absorbed spatially along the atomic memory. In the polaritonic picture, the rephasing condition is equivalent to $k = 0$. After the light is stored, η can be switched to any arbitrary shape in time. However, the photon echo is only emitted when the atoms are rephased and the coupling field is on (in the case of Λ-GEM). The shape of the frequency detuning is chosen to be monotonic in order to avoid any re-absorption. Obviously, one can use other forms of frequency detuning to avoid reabsorption, but a linearly shaped detuning is practically easier to implement.

The shape of the detuning can be engineered in such a way as to optimise storage of a light pulse with a particular frequency spectrum. The size of the frequency gradient determines the bandwidth of the memory and by applying a larger gradient field the storage bandwidth increases. On the other hand, for a simple linear gradient, the efficiency of GEM is inversely proportional to the size of the gradient. Therefore there is always a

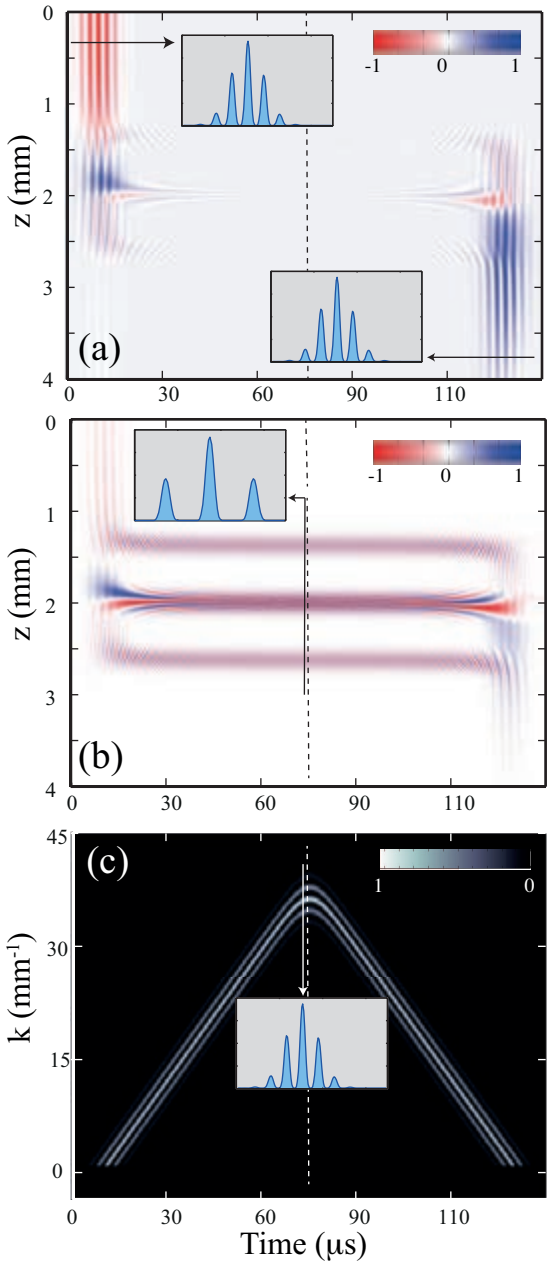

Figure 5.3: Numerical simulation of the storage of an intensity-modulated pulse. (a) The real part of the electric field in $z-t$ plane. Inset shows the temporal shape of the pulse at the input and at the output. The electric field decreases in strength until the atomic frequency gradient is switched at $t = 75\ \mu s$. It then increases and eventually an echo is emitted. (b) The real part of the atomic polarisation in the $z-t$ plane. A cross-section of the atomic polarisation along the z-axis reveals the Fourier spectrum of the input probe light. The inset shows the absolute value of the polarisation at the indicated position. (c) Absolute value of the polaritonic excitations in the $k-t$ plane. $k = 0$ indicates that the rephasing of the atomic spin is completed to produce a coherent emission. A cross section of the polariton along k reveals the temporal shape of the stored pulse (as shown in the inset). Parameters used for this simulations are: $g\mathcal{N}/\eta = 1.74$, $\eta L = 16\gamma$, and $\gamma_0 = 0$.

trade-off between the bandwidth and storage efficiency. For efficient storage of broadband information, a large OD is required.

The frequency gradient can be switched to higher or lower values or even to zero during the storage time without affecting the storage protocol. In Fig. 5.4 we show the numerical simulation for the evolution of the normal mode in the $k-t$ plane where η is switched to different values. Firstly, a recall gradient four times larger than the input gradient is introduced and therefore the atomic field evolves four times faster towards the origin. Shortly after, before the polariton reaches $k=0$, η is switched to zero which stops the evolution and freezes the polarisation at a constant k value. In other words, the system can be described as a single polariton. Eventually, after $\eta{=}{-}\eta_0$, light is emitted after atomic excitations are phase-matched at $k=0$.

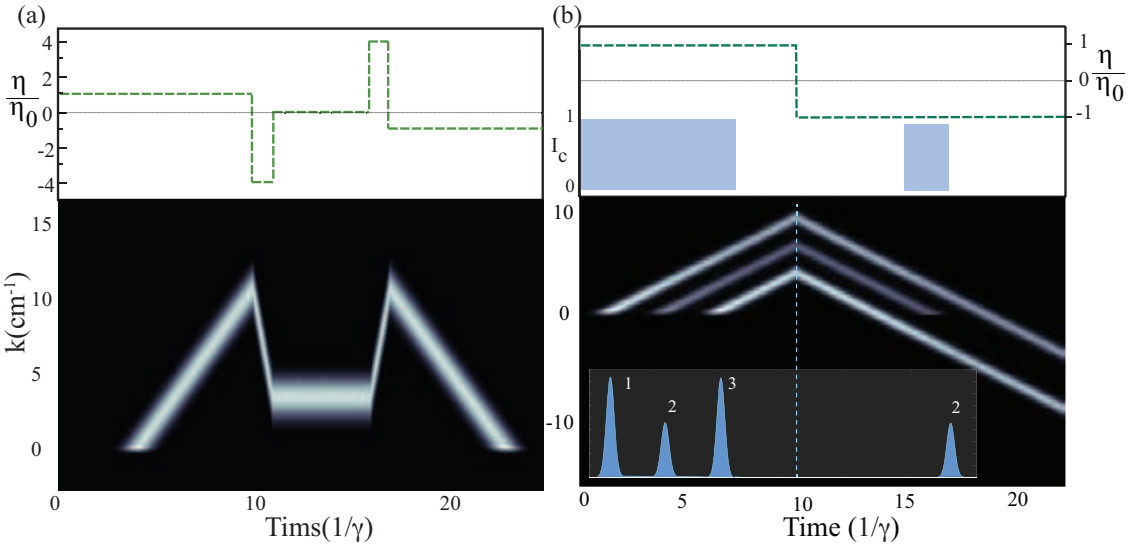

Figure 5.4: Numerical simulation of GEM showing the absolute value of the polaritonic excitation in $k-t$ plane. (a) Multiple switches of the atomic gradient field. The switching protocol of the gradient detuning is depicted on top where η is switched to $\eta=-4\eta_0$, then $\eta=0$, $\eta=4\eta$ and finally to $\eta=-\eta_0$. (b) Arbitrary probe retrieval. The coupling field is turned on during the writing stage and only for a short period during the reading stage when the condition $k=0$ for the middle pulse is satisfied. This guarantees that only the second pulse is recalled. The top part of the figure shows the switching protocols for coupling field intensity , I_c, and detuning gradient, η. The inset shows the temporal profiles of the input and echo pulses.

Tuneable coupling strength in Λ-GEM

The role of the classical coupling field in Λ-GEM is to couple the weak probe light via Raman transition to the ground states.

The coupling field is also required at the reading stage when the photon echo is emitted to transfer the energy from the atomic field back to the light field. In an ideal system, the dynamics of the coupling field during the storage time would not affect the storage process, but practically it is beneficial to turn off the coupling field during the storage time to reduce scattering and therefore loss. The scattering process is further discussed in the experiment section.

The coupling field intensity determines the effective atom-light coupling and therefore the optical density. Decreasing the coupling field intensity at the writing stage will reduce the recall efficiency. At the reading stage this can result in partial retrieval. In other

words, the intensity of the coupling field when the normal mode reaches $k = 0$ determines how much stored excitation is converted to the electric field and how much is left inside the memory.

Fig. 5.4(b) shows a simulation of the atomic polarisation evolution in the $k - t$ plane in the Λ-GEM system. The coupling field intensity is switched to zero shortly after the three light pulses enter the medium and their information is transferred into the atomic excitations. After the gradient is flipped and the excitations reach $k = 0$, the coupling field is turned back on only for the time window of $t = 16 - 18$ in order to couple out only the second pulse. In this case, the information imprinted into the atomic ensemble from the two other pulses will remain inside the memory.

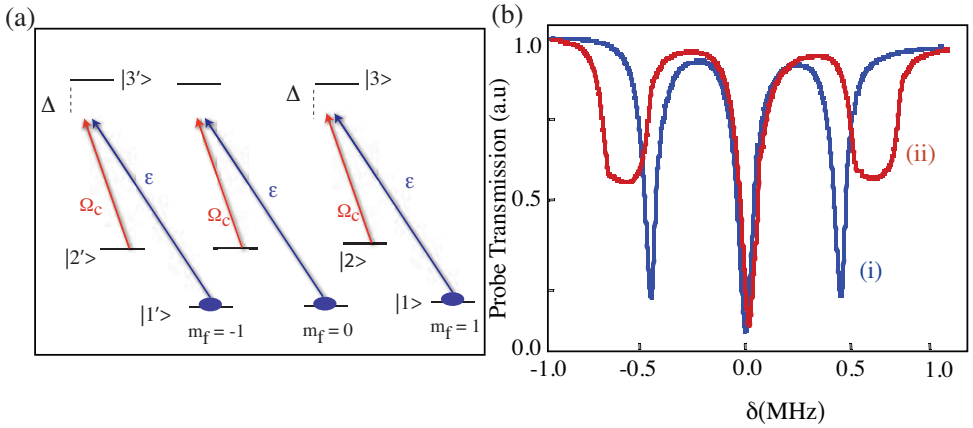

Figure 5.5: (a) Schematic optical transition and level structure required for generating two polaritons. (b) Un-broadened (i) and broadened (ii) Raman lines of non-degenerate ground state $F = 1$ of ^{87}Rb.

5.2.2 Polariton-Polariton interaction

Let's now consider the interaction of a probe field with all Zeeman sub-levels of the $F = 1$ hyperfine ground state of ^{87}Rb atoms. Interaction of the probe and coupling fields with three sets of Zeeman sub-levels is shown in Fig. 5.5 (a). The unbroadened and broadened probe absorption lines are shown in Fig. 5.5 (b) (i) and (ii), respectively. These lines have been experimentally observed by scanning the coupling field frequency in the presence of a uniform magnetic field parallel to the propagation axis. Since the $m_f = 0$ level is insensitive to the magnetic field, the $m_f = \pm 1$ of the $F = 1, 2$ hyperfine ground state levels can simultaneously be used for storage of light.

Applying a positive magnetic field gradient in the z direction will lead to a positive frequency gradient to the $m_f = +1$ and a negative frequency gradient to the $m_f = -1$ Zeeman sublevel. In this manner, two detuning gradients with opposite signs will be introduced to the ensemble. The two frequency gradients are not centred around the same frequency. The magnitude of the frequency shift per Gauss of magnetic field is the same for the both $m_f = \pm 1$ states. Using a phase-modulated, or dual-frequency, coupling field it is then possible to map the light into the left, $\sigma_{1'2'}$, and right, σ_{12}, atomic coherences, simultaneously.

The polariton picture for this storage scenario is shown in Fig. 5.6 (a) in the $k - t$ plane where two frequency gradients with opposite signs create two polaritons propagating

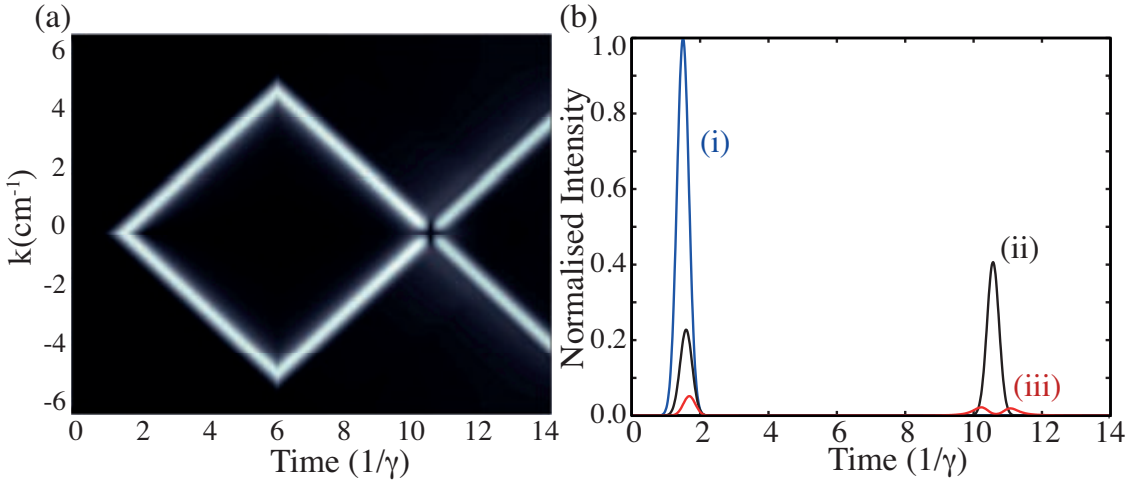

Figure 5.6: (a) Absolute value of normal mode plotted in the $k-t$ plane for a light pulse stored simultaneously in two Zeeman sub-levels ($m_f = \pm 1$) of an atomic ensemble. (b), (i) Electric field intensity at the the beginning of the memory. The output field corresponding to storage in $m_f = 1$ state and both $m_f = \pm 1$ states are shown in trace (ii) and (iii), respectively.

in opposite k directions. For this reason, the two atomic fields are out of phase considering the Maxwell equation $k\mathcal{E}(t,k) = \mathcal{N}\sigma_{12}(t,k)$. From this equation, it can be seen that for positive k values the electric field amplitude and atomic field have the same phase, but for negative k values they are out of phase. This results in suppression of the echo signals at the recall stage. This effect has been demonstrated using numerical simulation in Fig. 5.6 (b). The echo intensity is much smaller when two set of Zeeman sub-levels $m_f = \pm 1$ are used compared to the case of storage using only one set of m_f states. The phase of the interference can be controlled using the relative phase between the two coupling fields during the recall stage.

Chapter 6

Spectral Processing of Stored Light

The frequency-encoding nature of GEM provides us with knowledge about the position of the stored frequency components of a light field. One can take advantage of this fact to manoeuvre the bandwidth of the retrieved light and also selectively address different stored spectral components.

In this chapter we first study the inherent linear and nonlinear frequency shift that a GEM, and in general a CRIB, system can exhibit. We then discuss the spectral properties of the memory in detail and consider manipulation of the atomic frequency gradient to allow fine control of the optical field recalled. To simulate the system, we use a decoherence-free atomic system as considered in Ref. [151] to model the storage and retrieval dynamics.

The relevant publication for this chapter is

Precision spectral manipulation of optical pulses using a coherent photon echo memory B. C. Buchler, M. Hosseini, G. Hétet, B. M. Sparkes, P. K. Lam, Opt. Lett. 35, 1091 (2010).

6.0.3 Self-induced frequency shift

The frequency shift in the two and three-level CRIB systems has been theoretically studied in Ref. [179]. It was shown that a three-level CRIB system can show frequency shift and frequency chirp in the echo field, particularly at short interaction times ($\tau_{storage} < 10\ \delta t_{duration}$), high optical densities, and large memory bandwidth. In this regime, the non-linear phase shift can potentially reduce the fidelity of the memory. In this section, we investigate the phase shift induced to the recalled light in a GEM scheme.

To understand the reason for the phase shift, we consider the schematic light storage picture in Fig. 6.1 where the absorption lines of a few atoms are shown along the propagation axis z. Consider a single frequency component ω_0 of the input light, resonant with the blue atom, traveling from the left to the right. The neighbouring atoms have different resonance frequencies due to the applied gradient. The dispersion and absorption caused by neighbouring atoms will affect the amplitude and group velocity of light, as it travels towards the blue atom. If the interaction time is long enough compared to the pulse duration, the field will eventually reach the blue atom and be totally absorbed by the atom. However, if the gradient is switched before the field is completely absorbed, a

frequency shift will be induced to the echo field due to the incomplete time reversal. If the interaction time (storage time) is long or the field gradient η is large, the light field will be rapidly absorbed. Therefore, when the gradient is flipped, the echo process is time symmetric and the frequency shift effect will be negligible. If, on the other hand, the gradient is flipped before full absorption, the process is not time symmetric and the gradient flip will lead to a frequency shift of the photons that are yet to be absorbed.

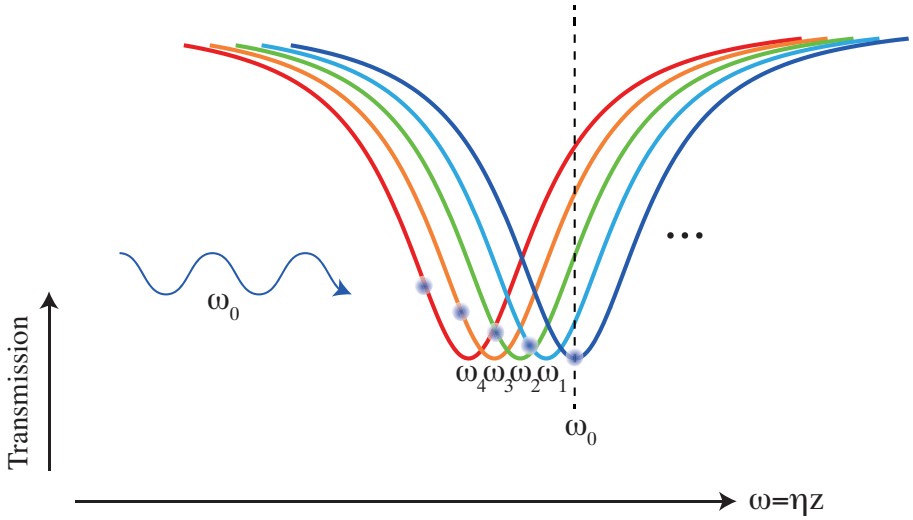

Figure 6.1: Schematic representation of light storage at the microscopic level. A single frequency field component resonant with the blue atom which is traveling from the left will experience a phase delay due to dispersion from neighbouring atoms.

Numerical simulations of the GEM in this regime reveals a clear k dependent frequency shift. These results are plotted in Fig. 6.2. The observed frequency shift here is linearly dependent on the inverse of $k = \eta t$ (see Chap. 5) so that the longer the storage time is, or the larger the atomic frequency gradient is, the smaller the linear frequency shift will be. We note here that for large values of $\eta\tau$, the remaining electric field amplitude inside the memory will be small.

To find a theoretical description of the phase shift that the memory induces on the echo signal we first need to obtain an expression for the spatial shape of the atomic excitation that reproduces the data pulse spectrum. This can be obtained through the susceptibility equation [179, 152]

$$\chi(z) = \left(\frac{\gamma - i(\eta z + \omega)}{\gamma - i(-\eta L/2 + \omega)}\right)^{-i\beta} \tag{6.1}$$

where $\beta = \frac{g\mathcal{N}}{\eta}$ is the optical depth of the atomic sample extended from $-L/2$ to $L/2$. Using this expression, Moiseev et al. [179] showed that the echo signal gains a phase shift expressed as

$$\delta\phi(t) \quad = \quad \beta \ln\left[\frac{\eta L}{2}(t + \tau_\beta - \tau_s)\right] \tag{6.2}$$

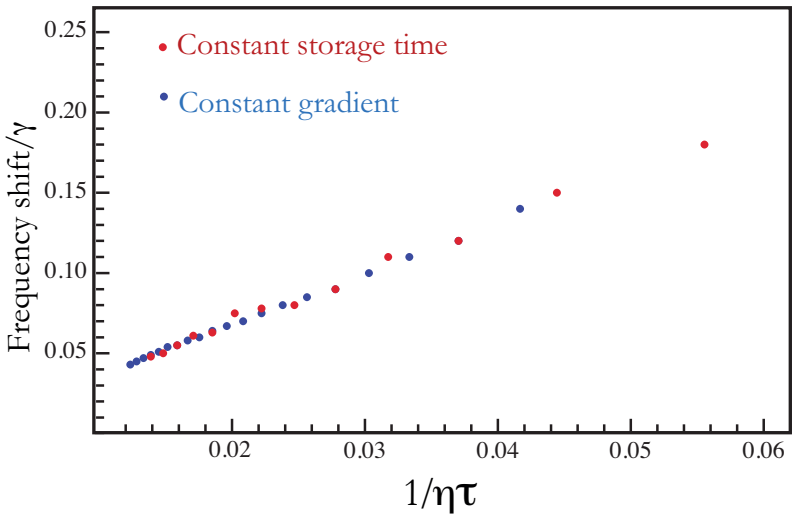

Figure 6.2: Numerical simulation showing the frequency shift of the output field for various values of $1/\eta t$. The frequency shift is shown for two cases. The red points correspond to a constant storage time (τ) while varying η, and blue points are corresponding to constant η while varying τ. The rate γ is the excited state linewidth.

where τ_s is the storage time and $\tau_\beta = \frac{2\beta}{\eta L}$. It was shown that this phase shift can be decomposed into three terms: a constant phase shift, a constant frequency shift and a frequency chirp term [179]. The total phase shift for different sets of parameters is plotted in Fig. 6.3 (a)-(d). It can be seen that for a large optical depth β and a short storage time (τ_s), a frequency chirp can be observed across the pulse envelope. One should notice that the frequency chirp for interaction times longer than the pulse duration (minimum possible storage time) is important. The effective optical depth in our experiment is around $\beta \simeq 1$ and pulse duration is around 2-3 μs. Under these conditions, the effect of the frequency chirp is almost negligible as observed in our experiment.

Along with the non-linear phase shift mentioned above, the storage process in a two-level or three-level GEM system can induce a constant phase shift and frequency shift to the output light [181, 179].

Now we investigate the frequency shift under various circumstances by monitoring the electric field at the output. Fig. 6.4 (a) shows the real part of the light field inside the atomic sample, presented in the time-space domain, where the interaction time is 10 times the length of the input pulse. As depicted in Fig. 6.4 (b) and (c), increasing the interaction time [154] or applying a larger field gradient can significantly reduce the frequency shift. The amount of the frequency shift of the light can be estimated by the angle of the wave front near the end of the memory.

An alternative method involves applying a DC detuning offset to actively cancel out the above-mentioned frequency shift of the output echo. Fig. 6.4 (d), shows the real part of the light field inside the two-level atomic sample where a DC detuning is applied after flipping. The frequency shift is completely removed by choosing the right DC offset.

Fig. 6.4 (e) and (f) show the real part of the electric field inside a three-level atomic ensemble when the coupling field is on and off during the storage time, respectively. By switching off the coupling field during the storage time (see Fig. 6.4 (f)), the light field is mapped into the atomic excitations before it gets fully absorbed by resonant atoms.

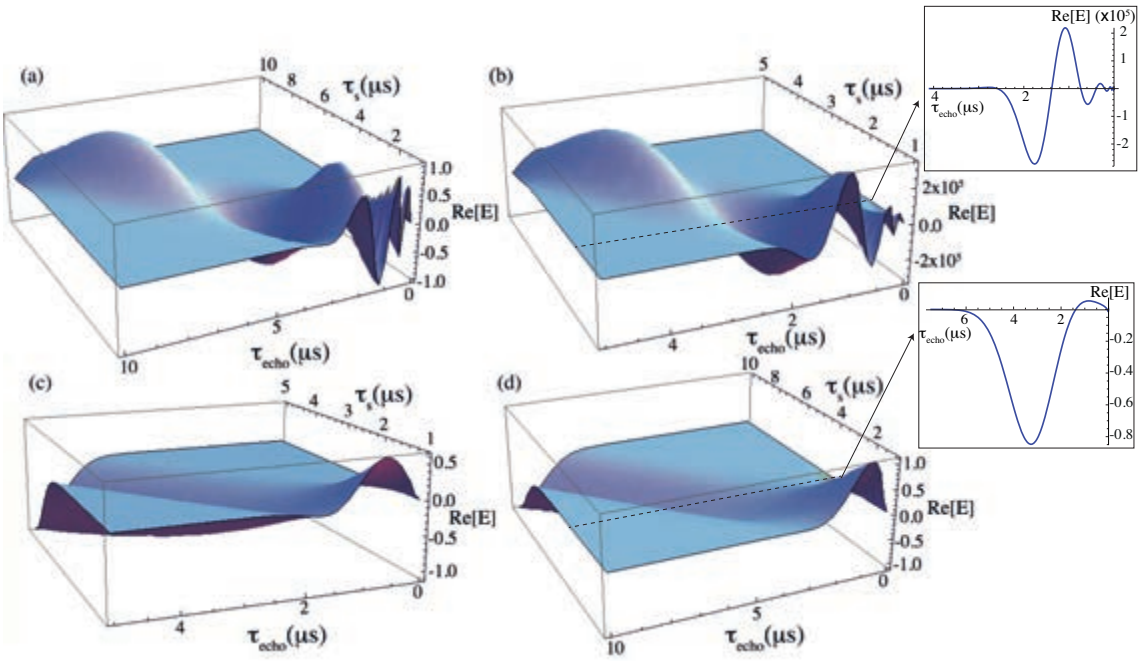

Figure 6.3: The real part of the echo signal plotted for a Gaussian pulse using the expression 6.2 as a function of interaction time and echo time τ_{echo} for (a) $\beta = 5$, $\eta L = 2$MHz, pulse width of 1 μs, (b) $\beta = 5$, $\eta L = 2$MHz, pulse width of 0.5 μs, (c) $\beta = 1$, $\eta L = 2$MHz, pulse width of 0.5 μs, and (d) $\beta = 1$, $\eta L = 2$MHz, pulse width of 1 μs. The insets in (b) and (d) show the corresponding echo amplitude for storage time of 1.5 μs and 3 μs, respectively.

This effectively reduces the interaction time of unabsorbed light with atoms and therefore induces a larger frequency shift to the recalled light.

6.1 Controlled frequency shifting

A simple frequency shift of the retrieved light can be achieved by adding/subtracting energy to/from light while it is stored into the atomic coherence. An offset (δ) can be added to the atomic frequency spectrum as it is inverted so that $\eta(z,t)L \rightarrow -\eta(z,t)L + \delta$. In this way every frequency component in the pulse is shifted by δ on retrieval. An example is shown in Fig. 6.5. Panels (a) and (b) show the real part of the optical field during storage with $\delta = 0$ and $\delta = 0.5$ MHz respectively. The rapid phase rotation of the output in Fig. 6.5(b) indicates a shift of the output frequency relative to the frame of the simulation that is rotating at the input optical frequency. Fig. 6.5(c) shows the Fourier spectra of the output pulses correspondingly shifted for five values of δ between -1 and 1 MHz. Apart from being an interesting processing capability, being able to frequency shift in this way enables compensation of inherent frequency shifts that can occur in GEM under conditions of short storage time [154] (this is discussed in Sec. 6.0.3). In the case of three-level GEM a frequency shift can be introduced by changing the frequency of the coupling field that controls the connection between the two atomic ground states. This may be easier in practice since a precise frequency shift could be dialled up by using an acousto-optic modulator to control the coupling beam frequency in a similar manner to EIT experiments that show frequency shifts [182].

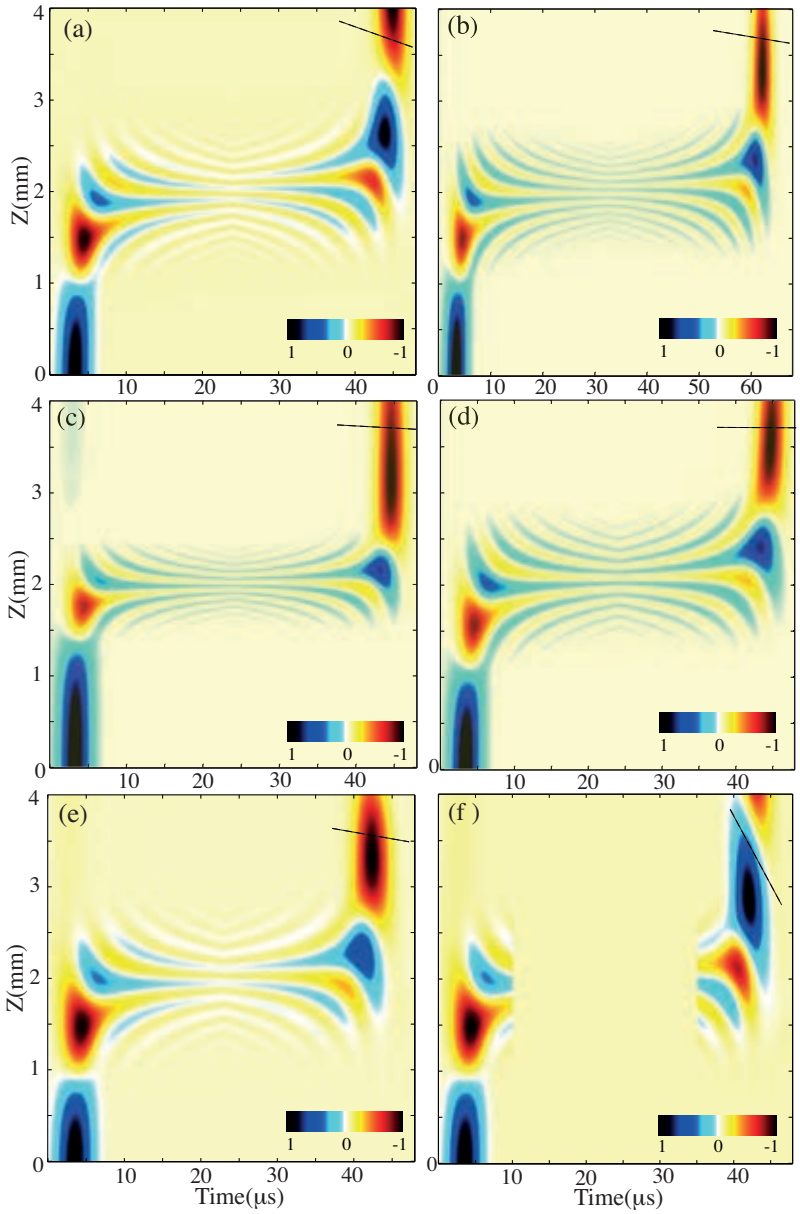

Figure 6.4: Numerical plot of the real part of the electric field inside a two-level atomic ensemble indicating the frequency shift of the echo for, (a) a short interaction time, (b) a long interaction time. Parameters used for this plots are: $\eta L = 8$ MHz, $g\mathcal{N}/\eta = 2.2$. (c) A steeper detuning gradient ($\eta L = 14$ MHz) is applied for a short interaction time to reduce the frequency shift. (d) A constant detuning offset of 100 kHz is applied after flipping the gradient field to cancel the frequency shift, with other parameters the same as (a). (e) The real part of the electric field inside a three-level atomic sample when the coupling field is on during the storage time. (f) the coupling field is switched off during the time window $t = 10 - 35\mu$s. The frequency shift from each plot can be estimated by the angle of the dashed line along which the phase is constant.

6.1.1 Experimental observation of frequency shift

As mentioned above, the frequency shift is experimentally observable by applying various techniques. One way to achieve this is to vary the frequency of the coupling field used at

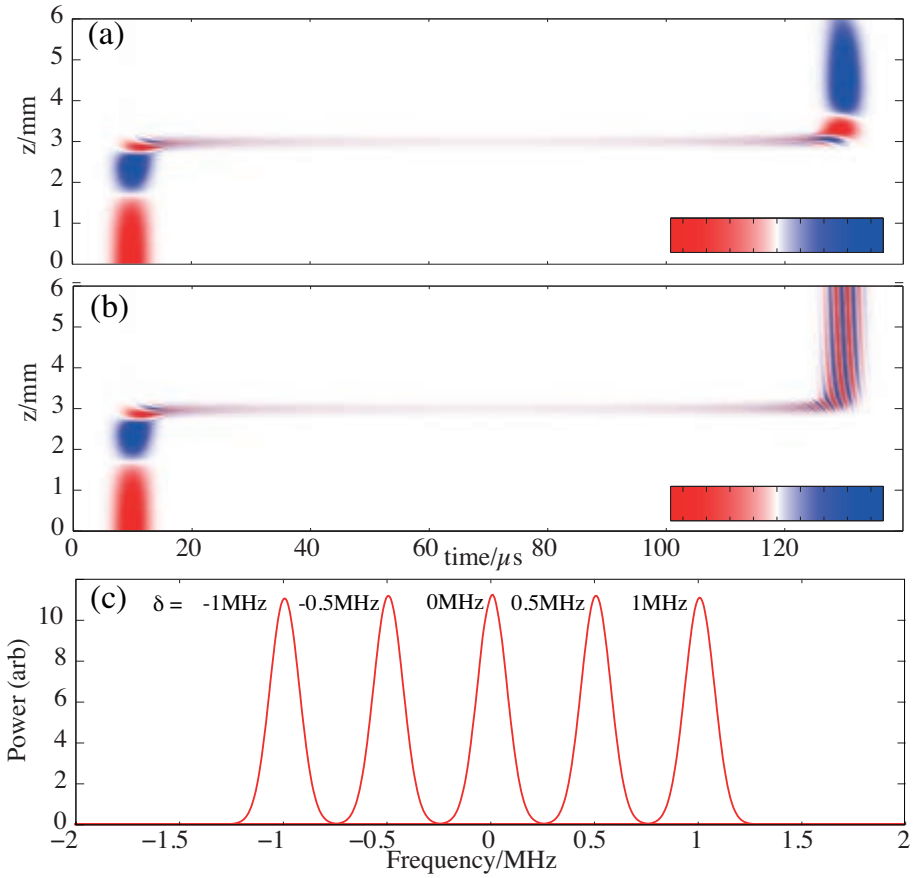

Figure 6.5: The real part of the optical field when (a): $\delta = 0$ MHz. (b): $\delta = 0.5$ MHz. (c): Fourier spectra of the output with δ=-1,-0.5, 0, 0.5 and 1 MHz for Gaussian input pulses . The effective optical depth in these simulations is $gN/\eta = 3.75$.

the recall stage. One can store the light with a coupling field on the Raman resonance with the input light field, and then change the frequency of the control field at the reading stage only before the echo is emitted. The other method is to apply a DC magnetic field after the gradient is flipped. This will change the two-photon detuning and as a result it causes the output light frequency to change.

The experimental result of a frequency-shifted echo pulse is shown in Fig. 6.6. This was achieved by applying an offset magnetic field after the magnetic field gradient was flipped to increase the splitting of the atomic ground states. On the recall stage, the pulse is shifted by the added splitting, which in this case is 600 kHz, as seen by the interference fringes in the heterodyne signal.

6.2 Bandwidth manipulation

Since the storage bandwidth of GEM is determined by the size of the gradient applied along the memory, one can coherently alter the bandwidth of the recalled light, to some extent, by changing the read gradient. This will allow time-compression and -decompression of the input pulse after recall. For instance, applying a steeper gradient after flipping the detuning forces all the Bloch vectors to rotate backward faster and this causes the time

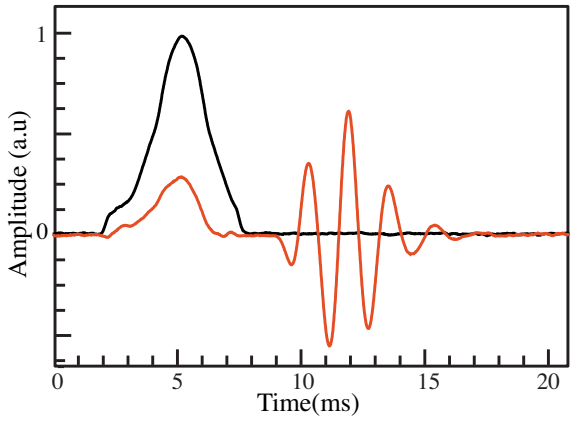

Figure 6.6: The input pulse (black) is stored and recalled with an introduced offset to the magnetic field gradient. The red curve denotes the straight transmitted pulse and the recall pulse. The interference pattern shows that the pulse is coherent with the original light field and is shifted by 600 kHz.

compression of the echo. Similarly, decompression of the pulse can be obtained when a shallower gradient is applied at the reading stage compared to the initial gradient. Fig. 6.7 (a) and (b) show numerical results for (i) compression and (ii) decompression of light pulses. The recall gradient is 5 times steeper than the input gradient. The atomic polarisation evolves faster towards $k = 0$, and the second pulse leaves the memory compressed in time. Immediately following the first echo the gradient is changed to 5 times smaller than the input gradient so that the excitations evolve very slowly towards $k = 0$, and a time-stretched echo is emitted.

An experimental demonstration of time-compressed and stretched echoes are provided in Fig. 6.7 (c). In principle, the ability to coherently control the bandwidth of the output light can ultimately be used for generating on-demand, tuneable-bandwidth single photons. Fig. 6.7 (d) shows the amplitude of a retrieved modulated pulse in the frequency domain (with a carrier and 4 sidebands) when the bandwidth of the memory is tuned by altering the slope of the recall gradient to 4 times larger, or smaller, than the input gradient.

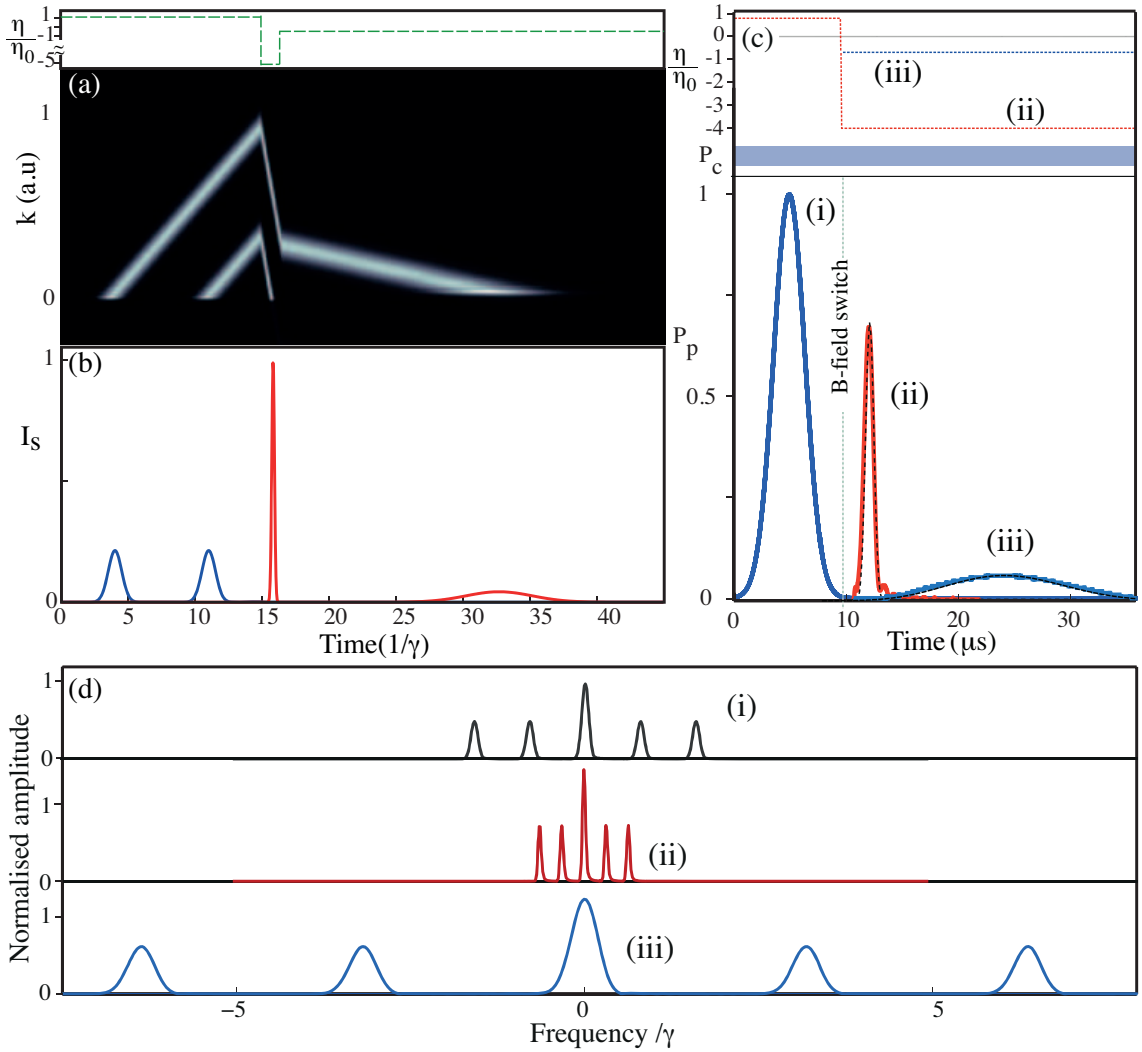

Figure 6.7: (a) Numerical simulation plotted for polariton evolution in k-t plane. (b) The temporal shape of the input pulses (blue trace) and time-compressed and time-stretched echoes (red trace) retrieved in the FIFO manner. Switching algorithms are shown on the top panel. (c) Compression and expansion: Separate experiments show; (i) time-compressed retrieval with $\eta = -4\eta_0$. and (ii) time-stretched retrieval with $-0.6\eta_0$. Data shown without magnification and the top part of the figure shows the corresponding switching protocol of the gradient field. The numerical simulation is shown as dashed lines on the pulses. (d) Amplitude of a retrieved modulated light pulse shown in the frequency domain when the ratio between input and output bandwidth of the memory is 1(i), 0.25 (ii), 4 (ii).

Chapter 7

Arbitrary Manipulation of Optical Bits

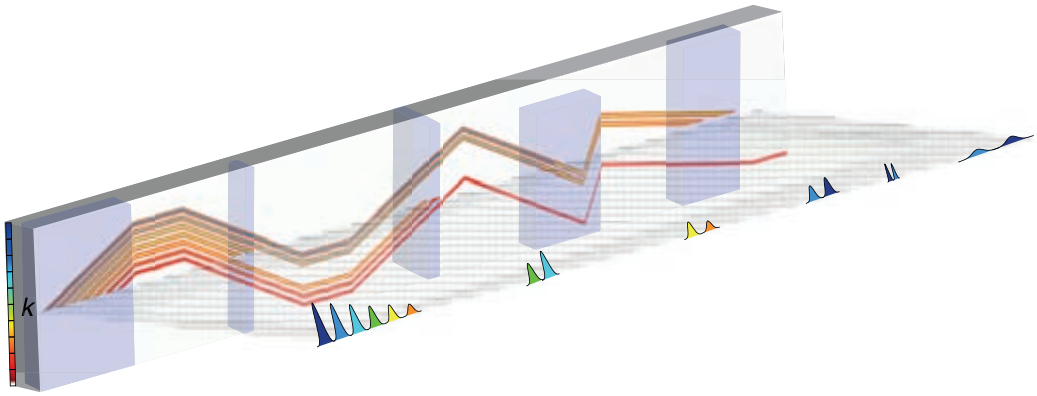

Figure 7.1: A conveyor belt for optical pulses

The bandwidth and versatility of optical devices has revolutionised information technology systems and communication networks. Precise and arbitrary control of an optical field that preserves optical coherence is a requisite for many proposed photonic technologies. In this chapter we present storage of multiple pulses of light within a chosen frequency bandwidth. Stored pulses can be recalled in arbitrary order with any chosen delay between each recalled pulse. Furthermore, we show that pulses can be split into multiple smaller pulses and recalled in several pieces at chosen times. This memory can play the role of a random access memory for optical bits.

The relevant publication for this chapter is

Coherent optical pulse sequencer for quantum applications M. Hosseini, et al. Nature 46, 241-245 (2009).

7.1 Time sequencing

Using the polariton description introduced in Chap. 5, we show how optical information can be coherently manipulated in an arbitrary manner. We discuss the possibility of coherent pulse sequencing, first-in-last-out (FILO) , first-in-first-out (FIFO), arbitrary recall and backward retrieval of information using Λ-GEM.

One of the intrinsic properties of GEM, as we have discussed it so far, is that the photon echo is a time-reversed copy of the input pulse. When the optical field frequencies are stored spatially along the z-axis, flipping the gradient triggers the time-reversal process so that the pulse sequence is reversed. This process is well understood using the normal mode picture.

Fig. 7.2 (a) shows the numerical simulation of a polariton for first-in-last-out (FILO) storage of four input pulses, depicted in $k-t$ plane. The evolution "speed" of the normal mode in the k-direction is given by the frequency gradient $\eta(t)$. Using the normal mode picture discussed in Chap. 5, the reason for the pulse sequence reversal is made clear: the last pulse to enter the system returns to $k=0$ first, and is thus re-emitted first.

A natural question is whether it is possible to avoid reversing the pulse shape. One approach is to use two memories and do FILO storage twice. This will introduce more loss to the light and more complexity to the storage protocol.

Shape-preserving storage in a single-memory device would require that the normal mode returns to $k=0$ travelling in the positive k direction. The last pulse in would then be the last pulse out. With a two-level system this would seem impossible without loss: after reversing the frequency gradient there is no way to suppress the emission when the normal mode returns to $k=0$. FIFO storage can be achieved in a single memory operation based on two-level GEM, but for the expense of loss. This can be done by switching the gradient to a very steep value and the opposite sign after storage as shown in Fig. 7.2 (b). This will effectively reduce the optical depth (OD) of the system (see Sec. 4.1.2) at the first reading stage and therefore most of the excitation will remain inside the memory. The left-over excitations, which contain most of the information, can be recalled later by applying a gradient similar to the one at the writing stage. In principle, $\exp(-2\beta L\pi)[1-\exp(-2\beta L\pi)]$ part of the light field, where L is the length of the atomic sample, remains inside the sample [152] after the echo is emitted as leftover excitations. These decay over time due to the decoherence. Provided the coherence time of the atoms is long enough, part of the leftover excitations can be converted back to the light field by flipping the field gradient multiple times. In fact, multiple switching of the gradient allows atomic excitations to travel back and forth in k space and each time they pass through $k=0$, a fraction of the excitations will contribute to the photon echo emission until, eventually, all the leftover excitations become depleted. Ignoring decoherence, the fraction of the input light released in the n^{th} echo is $[1-\exp(-2\beta L\pi)]^2\exp[-2\beta L\pi(n-1)]$.

With a three-level system, however, we are free to turn off the coupling beam. In this case, although the dipoles will rephase when the normal mode reaches $k=0$, no light can be emitted. This is seen in Fig. 7.2 (c), which shows $|\psi(t,k)|^2$ for the switching scheme shown above the figure. With the coupling beam off, the normal mode passes straight through $k=0$ to negative k values. We can then switch the frequency gradient again to obtain a normal mode travelling in the positive k-direction. Now with the coupling field back on, the normal mode is converted into a photon echo at $k=0$ without pulse shape reversal. In this way we can construct a first-in-first-out (FIFO) memory.

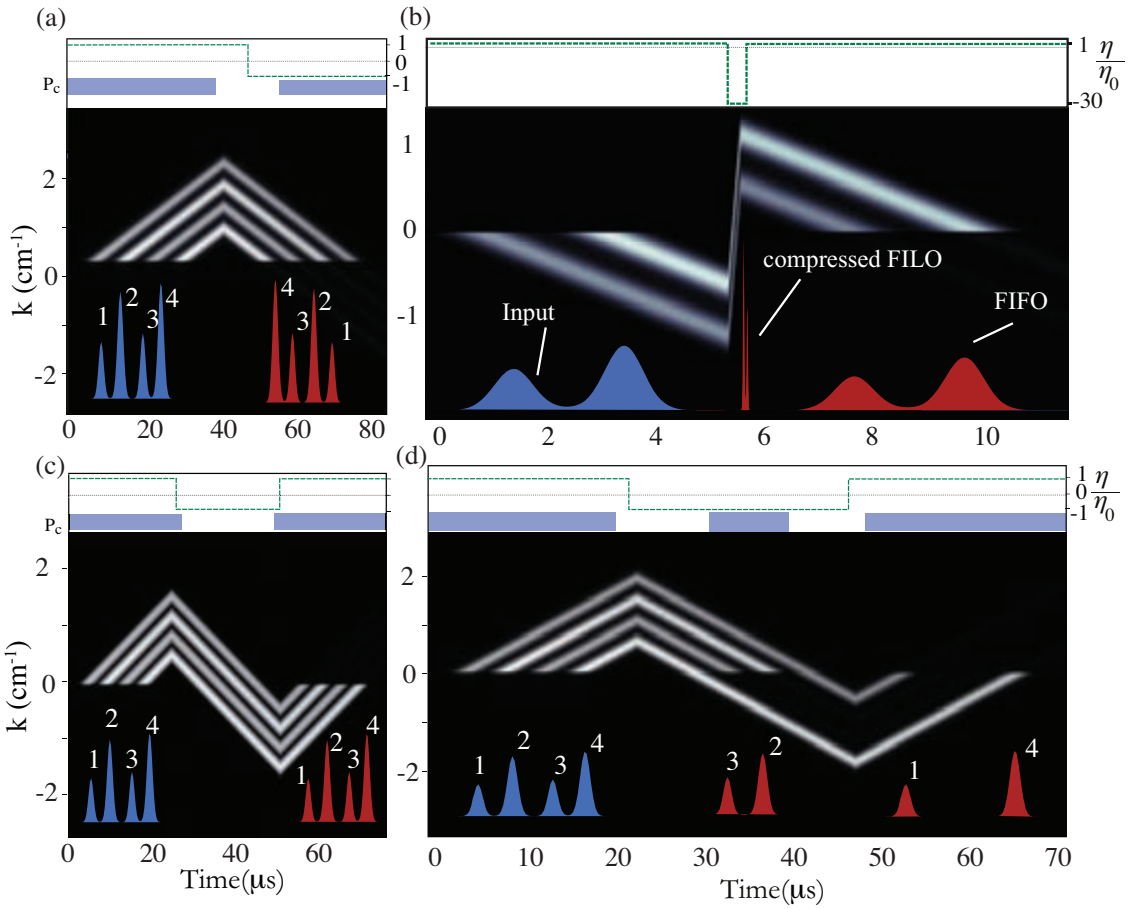

Figure 7.2: Numerical simulation of the polaritonic excitations showing, (a) first-in-last-out and (b) first-in-first-out in a three-level system of four input pulses in $k-t$ plane. (c) FIFO memory in a two-level system. The original gradient is switched to a much steeper negative gradient to reduce the effective OD of the memory. The two pulses are retrieved in FIFO manner after switching the gradient once more to its original slope. In this case, around 7% of the light is retrieved as FILO at the first readout stage. (d) Storage of a train of four pulses in 1,2,3,4 order and recalled in 3,2,1,4 order. The switching scheme of the coupling field intensity and gradient detuning is plotted on top of each part. Insets show the temporal shape of input (blue) and echo (red) pulses.

7.1.1 Arbitrary retrieval

Combining the FIFO and FILO techniques, our system can be thought of as a k-space conveyer belt for the stored light pulses. The normal mode can be moved back-and-forth along the k-axis by controlling the frequency gradient, η. Furthermore, we are able to push pulses off the conveyer belt whenever they pass through $k = 0$ by turning on the coupling beam. In this way we are able to construct a system that can recall the pulses in any order we choose. A decoherence-free model of the on-demand retrieval is shown in Fig. 7.2 (d), where 4 pulses are stored in the memory, and after the first field switch, pulses 3 and 2 are recalled by turning the coupling field on, only during the time window that these two pulses cross $k = 0$. The other two pulses are recalled later after the second field switch. One can choose any other combination in the reading stage by controlling the detuning gradient and also the coupling field switching.

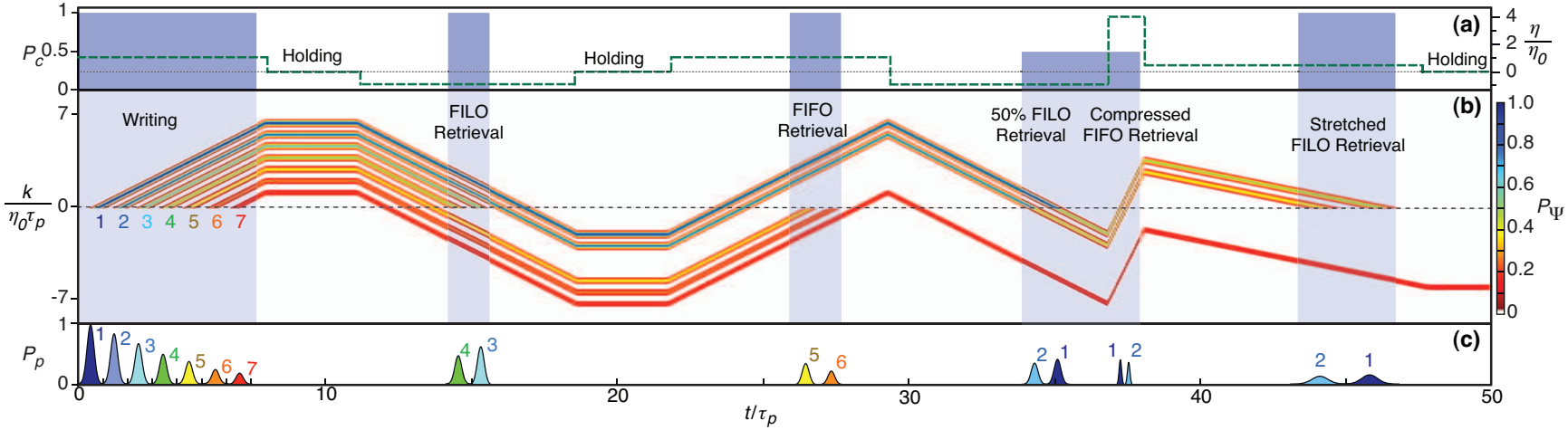

Figure 7.3: The quantum optical pulse sequencer. (a) Switching algorithm for the frequency gradient η and optical coupling field P_c. (b) Evolution of the k-space normal mode power $P_\psi = |\psi(t,k)|^2$ for seven input pulses. (c) Temporal profile for the input and recalled pulses. All quantities plotted are normalised units. Writing of the pulses occurs with the frequency gradient and coupling field on. The normal modes can be kept in a holding pattern by turning both fields off. Optical pulses are retrieved by turning on the coupling field when the normal mode crosses $k = 0$. FILO retrieval of pulses (4,3) is achieved with a negative frequency gradient. FIFO retrieval of pulses (5,6) is achieved with a positive frequency gradient. Partial retrieval of pulses (2,1) is realised with reduced coupling power. A variation of the frequency gradient is used to stretch or compress pulses (1) and (2) in further recall events. Parameters used are: $\eta L_0 = 48\gamma$; $\Omega_c = 35\gamma$; $g = 3\gamma$; $P_{p,\max} = 2.5 \times 10^{-7} P_c$; $\Delta = 1000\gamma$; $\gamma_0 = 0$;$\gamma = 1$; and optical depth $g\mathcal{N}L/\gamma = 600$.

7.1.2 Optical conveyor belt

Fig. 7.3 shows the various types of manipulation that can be done on the optical data using abovementioned protocols [183]. This figure demonstrates not just arbitrary recovery of pulses, but also methods for manipulating the pulses during storage. We start with seven pulses of different size. The pulses are first read into the memory with $\eta = \eta_0$, then held in a steady state with $\eta = 0$. Reversing the motion in k-space with $\eta = -\eta_0$ allows us to couple out some pulses in reverse order as they pass through $k = 0$. By timing the coupling field correctly we recover pulses (3) and (4) at $t = 15\tau_p$, where τ_p is the width of a single pulse. Next we hold the normal mode for some time at negative k-values, before switching to a positive velocity on the k-axis. Again choosing the coupling beam timing correctly, we recover pulses (5) and (6) without reversal at $t = 27\tau_p$. The remaining pulses move to positive k. On the next pass through $k = 0$, we reduce the power of the coupling beam by a factor of 2. This allows us to couple out half the power of pulses (1) and (2) in reverse order at $t = 34\tau_p$. This system amounts to a beamsplitter with a variable time delay on one port since we are free to recover the rest of these pulses at a later time. We now switch back to a positive slope, but this time with a higher frequency gradient, $\eta = 4\eta_0$. As explained in the previous chapter, this causes pulse compression because increasing η expands the range of frequencies covered by the atomic ensemble and a wider Fourier width leads to shorter pulses. This is seen intuitively in k-space since the normal mode moves faster through $k = 0$, leading to faster pulse recovery. In this way, half of what remains of pulses (1) and (2) is compressed and released from the memory in their original order at $t = 37\tau_p$. In the last stage, we reduce η to achieve pulse stretching. The expanded remains of pulse (1) and (2) are thus released from the memory in reverse order at $t = 45\tau_p$. The last pulse (7) is left in the atomic medium.

7.2 Experimental Implementation

The experiment has been performed using a cylindrical (length and diameter were 75 mm and 25 mm, respectively) cell containing ^{87}Rb atoms mixed with 1Torr Kr buffer gas in order to increase time of flight of atoms inside the beam. The optical layout of the experiment is shown in Fig. 7.4 (a). The previous experimental setup [151] was based on the coherence built on Zeeman sub-level ground states of $F = 2$ of Rb atoms, where the signal and the coupling field with orthogonal circular polarisation were detuned from $F' = 1$ so that coherence is built between $m_f = 2$ and $m_f = 0$ of F=2 ground state. However, in thermal equilibrium and after repumping, more population is expected in $F = 1$ ground state [184] than $F = 2$. For this reason, we used a 6.8 GHz frequency shifted signal beam, generated using fibre-coupled EOM (FC-EOM), to address $F = 1$ to $F' = 2$ transition with higher coupling strength compared to the previous setup. We split the Ti:Sapph laser beam, red detuned by ∼2 GHz from the transition $F_g = 2$ to $F_e = 1$ of the ^{87}Rb D1 line, into two beams. The signal beam after FC-EOM goes through the cavity on resonance with +6.8 GHz sideband to filter out carrier and -1 sideband. The second laser beam was used as the coupling beam. Both the coupling and the signal fields pass separately through AOMs which frequency-shift the fields by 80 MHz and 85 MHz, respectively, to match the splitting between the ground state levels. Finally the coupling and signal beams were collimated to 7 mm and 15 mm respectively with orthogonal linear polarisation and were mixed in a polarising beam splitter before the cell. The typical peak coupling field and signal field powers were 200 mW and 50 μW, respectively.

The temperature of the cell was controllably tuned around 75^{o}C using a bifilar resistive heater wound around the cell. At 65^{o}C, for instance, Rb vapour has a density of 3×10^{11} cm^{-3}. However, at the maximum case only 60% of these atoms are in $F = 1, m_F = 1$ state due to the corresponding Clebsch-Gordan coefficient. An initial repumping using a resonant beam with a circular polarisation can place most of the atoms in the desired atomic state.

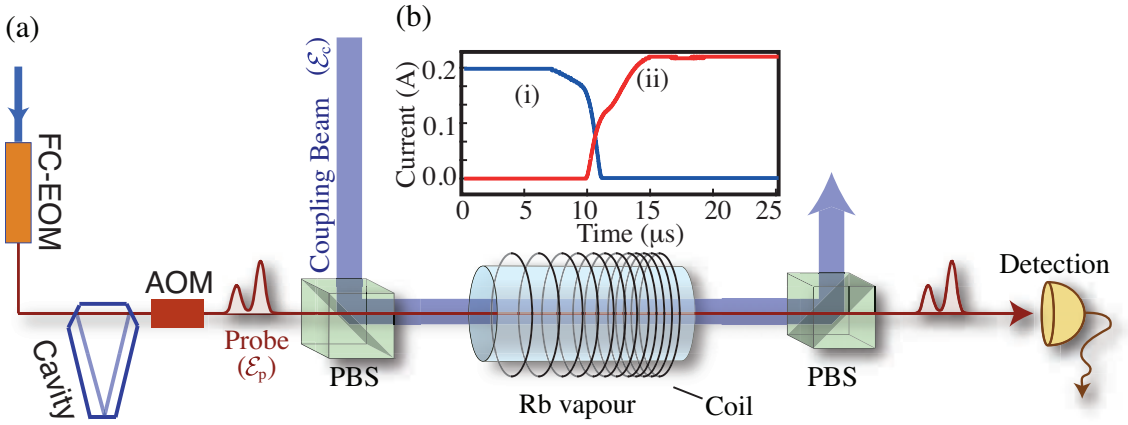

Figure 7.4: (a) The optical layout. Orthogonal linearly polarised coupling and probe fields were sent through a warm Rb^{87} enhanced cell with 1 Torr of Kr buffer gas. The double layer μ-metal shielded gas cell was surrounded by two variable pitch coils that were used to apply magnetic field gradients in opposing directions. The D1 $|\mathrm{F_g} = 2 > \rightarrow |\mathrm{F_e} = 2 >$ transition was used for the probe beam, while the D1 $|\mathrm{F_g} = 1 > \rightarrow |\mathrm{F_e} = 2 >$ was used for the coupling beam. (b) Current flowing through the two coils during the gradient switching time. Trace (i) and (ii) show the current flowing through the inner coil (being switched off) and outer coils (being switched on), respectively.

The Raman absorption of the probe typically had a visibility of 85% and a width of 120 kHz. To create the atomic frequency gradient (η) we used a solenoid with variable winding pitch to create a linearly varying magnetic field. For photon echo recall, a second variable-pitch solenoid with opposing current was used to invert η. In this setup, the magnetically broadened ensemble had Raman absorption widths up to 1 MHz. The current flowing in two coils during the switching time period is shown in Fig. 7.4 (b). The magnetic broadening decreases the effective optical depth so that the absorption was reduced to ~60%. Resistive bifilar wires were used to heat up the two end-sides of the gas cell more than the middle in order to prevent Rb from condensing on the sides.

We have observed the FID (see Sec. 2.2.5) from our Rb vapour cell under the Raman absorption situation. A coupling beam with power of 10 mW was used on Raman resonance with the probe pulse and 1 GHz detuned from the excited state. The Raman absorption line in the CW regime is shown in Fig. 7.5 (a) suggesting a linewidth of 6 KHz. At such a low coupling field power, where the effect of power broadening is negligible, this width is close to the ground state decoherence rate. Fig. 7.5 (b) shows the FID decay of atoms after the probe pulse is being absorbed while the coupling field is on during the entire time. The plot in Fig. 7.5 (c) shows the Raman linewidth as a function of the coupling field power and as can be seen the linewidth linearly increases with the coupling field power. The linear fit returns a 3.1 kHz intercept that corresponds to a ground state decoherence rate.

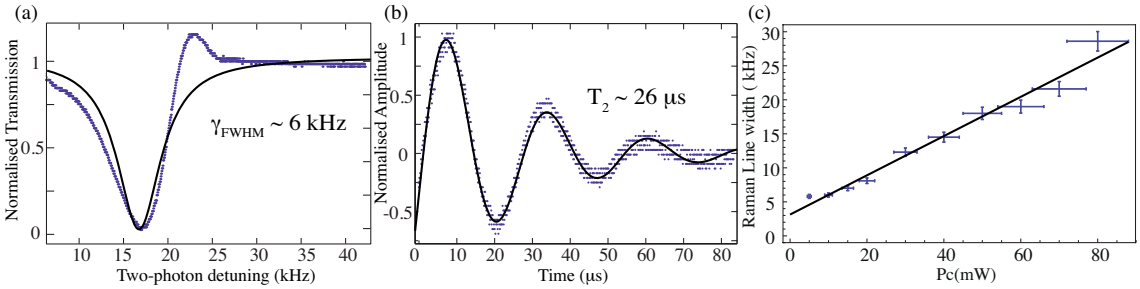

Figure 7.5: (a) The Raman absorption line for a coupling field power of 10 mW and a detuning of 1 GHz. The solid line is the Lorentzian fit to the Raman line. The asymmetry of the experimental line is due to having relatively small one-photon detuning. (b) FID oscillation together with the prediction (solid line) corresponding to Raman situation in (a). Both the Raman Linewidth and FID decay rate is about 6 kHz. (c) FWHM of Raman line as a function of the coupling field power. The solid line is a linear fit with intercept of 3.1 kHz.

7.2.1 Experimental results

FILO and FIFO storage

To use our system as a coherent optical memory in its simplest form, a coupling beam and atomic frequency gradient were applied using the pattern shown in Fig. 7.6 (a) to store a train of four pulses. It is not a requirement that $\mathcal{E}_c$ is switched off during the storage phase, but it is beneficial in practice since it eliminates spontaneous emission from the excited state. The experimental data is shown in Fig. 7.6 (c). The most striking feature of this result is that the shape of the input pulse train is reversed in time, as predicted previously [185]. In this scenario, GEM is a first-in-last-out (FILO) memory. A train of four pulses enters the cell, which spans the length of the z-axis, and is absorbed. The pulse train emerges in the forward direction symmetrically about the point of frequency gradient switching. The inset of Fig. 7.6 (c) shows the evolution of $|\psi(t,k)|^2$ for the real space data of Fig. 7.6 (d). The mode starts at $k = 0$ and evolves to higher k at a rate determined by $\eta(t)$ until the frequency gradient is switched, leading to a reversal in propagation direction. The pulse is re-emitted when the mode returns to $k = 0$. A cross section through $|\psi(t,k)|^2$ at any time is proportional to the temporal profile of the input optical field intensity. Including ground state decoherence (γ_0) and $\mathcal{N}$ as free parameters in our numerical model, we could fit the data in Fig. 7.6 (c) with excellent agreement, as shown by the dashed lines.

The numerical simulation of FIFO storage can be seen in Fig. 7.6(f), which shows $|\psi(t,k)|^2$ for the switching scheme in Fig. 7.6 (b). With the coupling beam off, the normal mode passes straight through $k = 0$ to negative k values. We can then switch the frequency gradient again to obtain a normal mode travelling in the positive k-direction. Now with the coupling field back on, the normal mode is converted into a photon echo at $k = 0$ without pulse shape reversal. This is demonstrated experimentally in Fig. 7.6(e). In this way we have constructed a first-in-first-out (FIFO) memory. As with the case of FILO memory, our numerical model (dashed curve) shows excellent agreement.

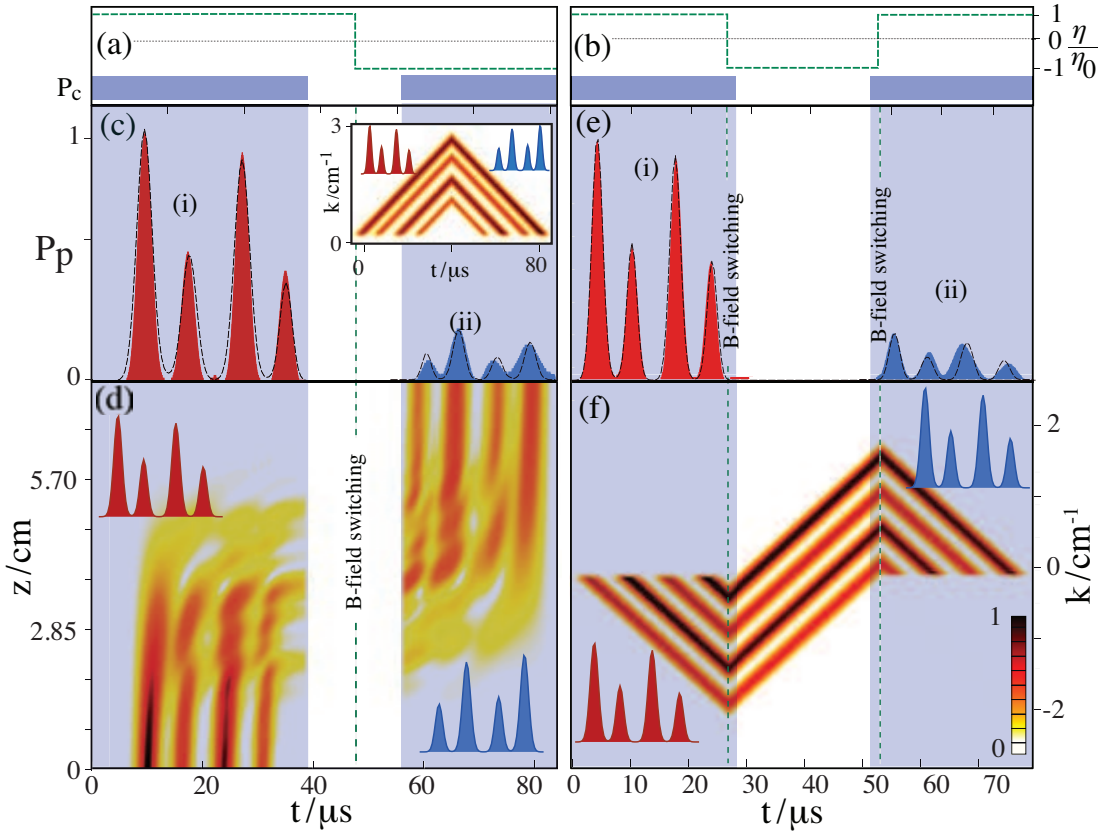

Figure 7.6: FILO and FIFO memory. Switching scheme for (a) FILO and (b) FIFO storage showing the frequency gradient (η) denoted by dashed lines and the presence of the coupling field (P_c) denoted by grey shading. (c) Experimental observation of FILO storage. (i) The input pulses and (ii) the photon echo showing order reversal. The frequency gradient was flipped at $t = 30$ μs. Dashed lines show a numerical simulation using the parameters $\Delta = 320\gamma$, $\eta L = 0.08\gamma$, $\gamma_0 = 4$ kHz and optical depth $g\mathcal{N}L/\gamma = 1.5$. The output echo and simulation are magnified 10×. The inset shows the the dynamics of $|\psi(t,k)|^2$ for this storage scenario. (d) A decoherence-free numerical simulation showing the power of the optical excitation, P_p, in the (t,z) plane for FILO memory. The input pulse sequence (red) is reversed at the output (blue). (e) Experimental observation of FIFO retrieval. (i) The input pulses and (ii) the photon echo showing order preservation. The dashed line shows numerical modelling with the same parameters as the FILO retrieval except with $\gamma_0 = 3$ kHz. The output echo and simulation are magnified 10×. P_p, P_c and η are plotted with normalised units. (f) A decoherence-free numerical simulation of $|\psi(t,k)|^2$ for FIFO storage. In this case, the coupling beam is off when the normal mode crosses $k = 0$.

Arbitrary recall and pulse splitting

Fig. 7.7 (a) and (b) shows pulse reordering and splitting of a pair of pulses over two recall events, respectively. Beam splitting can be achieved by reducing the coupling beam power at reading stage. In our experiment, however, we find that we can split pulses with constant $\mathcal{E}_c$. This is due to the low optical depth in our system, which limits both the writing and readout stages of the photon echo. Inefficient recall allows us to simply read out twice without changing $\mathcal{E}_c$, as discussed in Sec. 7.1. Numerical modelling again shows excellent agreement with our experimental data. The numerical simulations performed for Gaussian pulses with (a) $\gamma_0 = 5$ kHz, $\eta L = 0.06\gamma$, (b) $\gamma_0 = 1$ kHz, $\eta L = 0.08\gamma$, and in

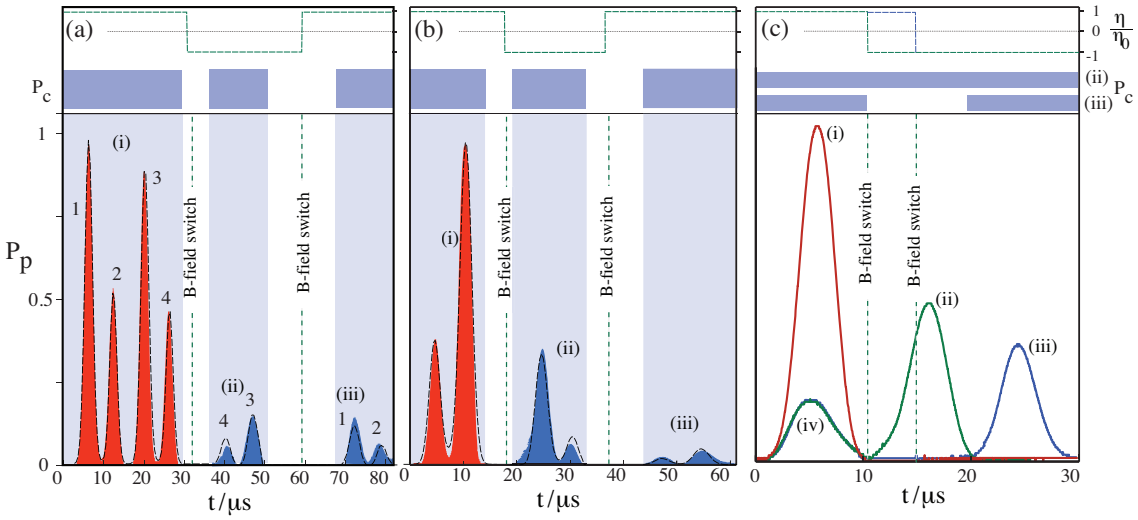

Figure 7.7: Flexible pulse recall. The switching patterns are shown at the top of each panel with the frequency gradient (η) denoted by dashed lines and presence of the control beam (P_c) shown by grey shading. (a) Pulse reordering: (i) Four input pulses are written into the memory. (ii) After the first frequency gradient switch FILO retrieval of pulses 4 and 3 is observed. (iii) A second frequency gradient switch produces FIFO retrieval of pulses 1 and 2. The output echo and simulation are magnified 10×. (b) Pulse splitting: (i) Two input pulses are written into the memory. (ii) Partial FILO retrieval of the input follows immediately. (iii) A second partial FIFO retrieval of the input follows at later time. The output echo and simulation are magnified 10×. (c) High efficiency single pulse storage: (i) is the the input pulse, (ii) shows 42% recall efficiency and (iii) 31% recall efficiency. (iv) 20% of the input leaks through the cell due to limited optical depth. The dashed lines show numerical simulations of Gaussian pulses.

all cases the optical depth was $g\mathcal{N}L/\gamma = 1.5$ and detuning $\Delta = 320\gamma$. Fig. 7.7 (c) shows single pulse storage with 42% efficiency.

Shape mirroring

One of the intrinsic properties of GEM is that the recalled photon echo has the same shape as the input signal, but it is time reversed. Fig. 7.8 shows the experimental proof of the shape preservation for a double Gaussian and ramp shape input pulse, respectively. Output echoes are indeed a mirror-image copy of the input pulses due to the time-reversed nature of the process.

7.3 Backward retrieval and stationary light

Light stored using the EIT method can be retrieved in forward or backward direction by applying forward or backward control field after storage, respectively. Simultaneous retrieval with forward and backward control fields, however, suppresses emission of the recalled signal from the memory. This is because the standing light wave created by the two control fields modulates the refractive index and effectively creates a Bragg grating that traps the light. Andre and Lukin in 2002 [186] showed that dynamic control of such a band gap can be used to coherently convert a propagating light pulse into a stationary excitation with a nonvanishing photonic component. When two counter-propagating control fields

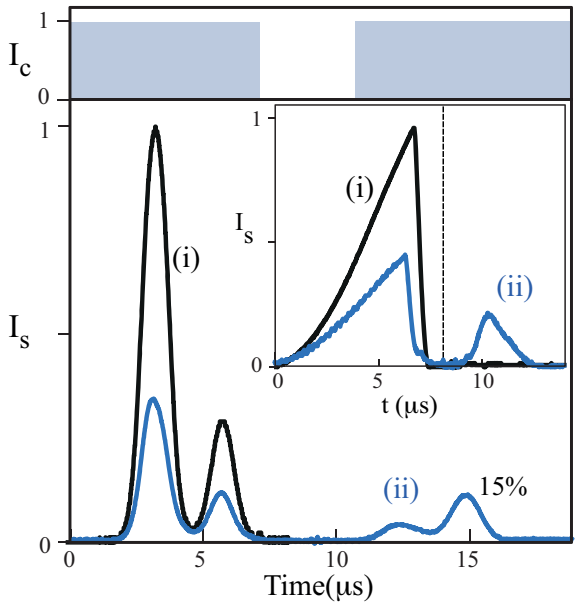

Figure 7.8: The shape mirrored photon-echo for a train of two pulses with different amplitude ratio. inset shows a ramp shape pulse showing (i) input pulse intensity and (ii) shape mirrored photon echo. Top section shows the switching protocol for the coupling fields.

are applied, signal light propagating near atomic resonance in the forward direction can undergo Bragg scattering into the backward propagating mode. Therefore, a range of frequencies (photonic band gap) can appear for which light propagation is forbidden. The photonic band structure of the medium can be written using the Blochs theorem [186], $E(z+a) = E(z)e^{iKa}$, as

$$\cos(Ka) = -\cosh[a/v_g\sqrt{\Omega^2/\Delta - (\delta_1 - \frac{v_g}{c}\delta_2)^2}] \tag{7.1}$$

where Δ is the control field detuning from the excited state, δ_1 is detuning of the probe from the centre frequency, δ_2 is detuning of the probe centre frequency from the excited state, K is the Bloch wave vector and $a = \lambda/2$ is the periodicity. If the light shift term, Ω^2/Δ, is larger than the effective two-photon detuning, $\delta_1 - \frac{v_g}{c}\delta_2$, the Bloch wave vector acquires an imaginary part and the propagation of waves inside the medium is impossible. This effect has also been experimentally demonstrated [187, 188]. The results of numerical simulation, shown in Fig. 7.9 (a) and (b), represent the forward , $\hat{\mathcal{E}}_+$, and backward , $\hat{\mathcal{E}}_i$, probe field inside the medium where counter-propagating control fields were used at the retrieval stage.

Furthermore, it has been shown [188] that even if the counter-propagating fields have totally different wavelengths (795nm and 780 nm) a stationary light is still achievable. This can be explained in terms of balanced multi-wave mixing (MWM) processes [189, 190] without the need for introducing standing wave fields.

Photon echoes created using two-level GEM always co-propagate with the input pulse and there seems to be no way to recall information propagating in a backward direction. However, similar to EIT [187], Λ-GEM is capable of recalling stored information in both backward and forward directions. Writing the equations of motion for forward and back-

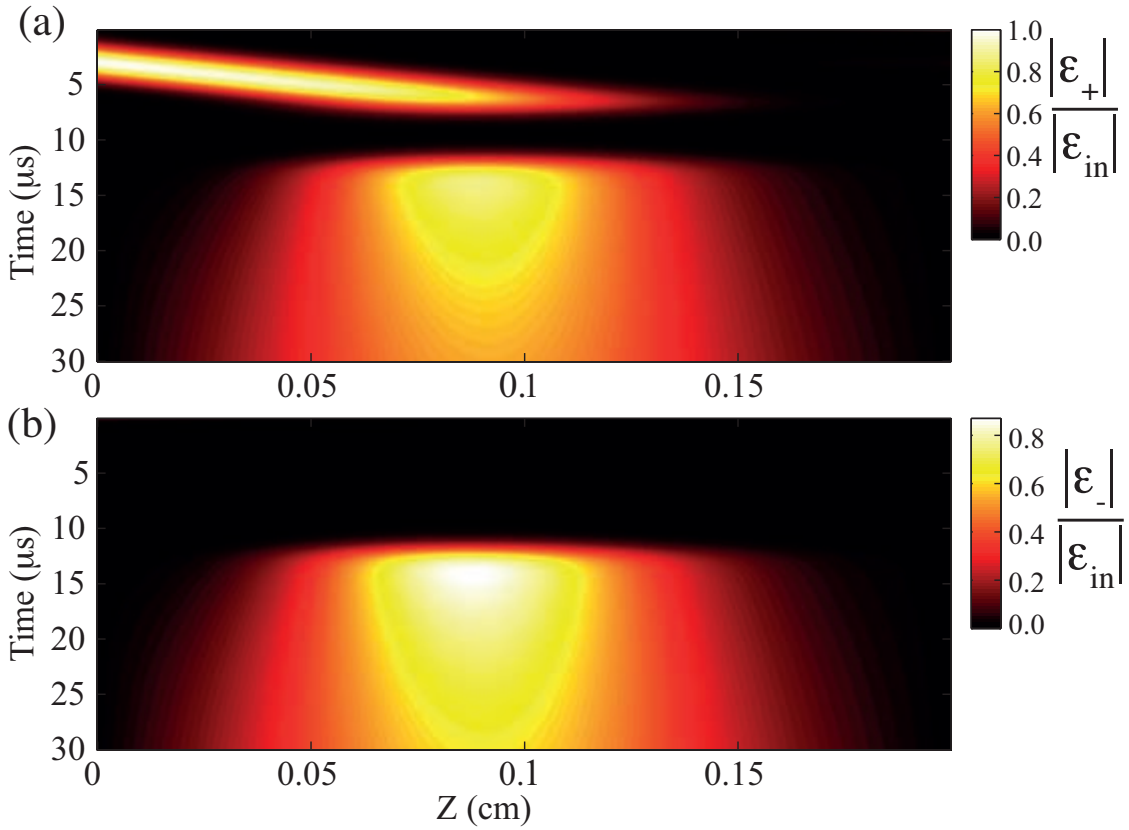

Figure 7.9: (a) Forward and (b) backward propagating probe fields inside the EIT medium. The forward propagating probe signal is slowed down using the co-propagating control field which is on during the time $t = 0 - 7\mu s$. The forward propagating control field is adiabatically switched to zero to store the optical pulse inside the medium. At time $t = 12\mu s$ both forward and backward-propagating control fields are switched on to generate a Bragg grating and therefore stationary light. In this case, a backward propagating field is generated inside the medium as shown in (b) that has the same amplitude as the forward-propagating component. The overall effect thus prohibits the probe light from propagation.

ward propagation, one can arrive at two sets of coupled equations with the same phase shift induced on the excitations owing to counter-propagating coupling fields. When the forward coupling field is turned off, the slow light vanishes, and a collective spin excitation is created. Finally, when the coupling beam is turned back on, the signal pulse is recreated propagating with the coupling field.

To mathematically describe the system we write the Maxwell-Bloch equations of motion for pair of counter-propagating fields. Assuming $\Omega_c = \Omega_+ e^{-ikz} + \Omega_- e^{ikz}$ and $\hat{\mathcal{E}} = \hat{\mathcal{E}}_+ e^{-ikz} + \hat{\mathcal{E}}_- e^{ikz}$, we arrive at the following equation for the atomic fields [191]

$$\begin{aligned} \frac{\partial \sigma_{12}}{\partial t} &= -(\gamma_0 + i\eta z)\sigma_{12} + i\Omega_+ \sigma_{13}^+ + i\Omega_- \sigma_{13}^- \\ \frac{\partial \sigma_{13}^+}{\partial t} &= -(\gamma + \gamma_0/2 + i\Delta)\sigma_{13}^+ + ig\hat{\mathcal{E}}_+ + i\Omega_+ \sigma_{12} \\ \frac{\partial \sigma_{13}^-}{\partial t} &= -(\gamma + \gamma_0/2 + i\Delta)\sigma_{13}^- + ig\hat{\mathcal{E}}_- + i\Omega_- \sigma_{12} \end{aligned} \tag{7.2}$$

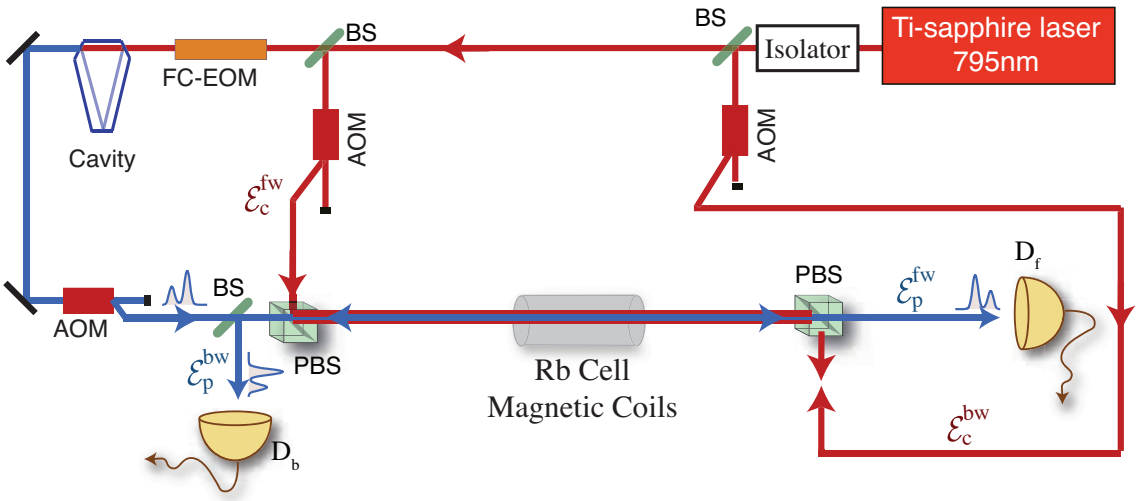

Figure 7.10: Schematic experimental setup for forward and backward retrieval of the echo signal from the memory. The probe field is shifted by 6.8 GHz using a fibre-coupled electro-optic modulator (FC-EOM) to match the frequency splitting between the hyperfine ground states of ^{87}Rb. A cavity was then used to separate the carrier and -6.8 GHz sideband from the probe field after the FC-EOM. BS: beam splitter, PBS: polarising beamsplitter, AOM: acousto-optic modulator, $\mathcal{E}_p^{bw}$: backward-propagating probe field, $\mathcal{E}_p^{fw}$: forward-propagating probe field, $\mathcal{E}_c^{bw}$: backward-propagating coupling field, $\mathcal{E}_c^{fw}$: forward-propagating coupling field, $D_{b/f}$: detectors for the forward and backward-propagating modes.

whereas the Maxwell equations for the electric fields are given by

$$\frac{\partial \hat{\mathcal{E}}_+}{\partial t} = i\mathcal{N}\sigma_{13}^+ \tag{7.3}$$
$$\frac{\partial \hat{\mathcal{E}}_-}{\partial t} = i\mathcal{N}\sigma_{13}^-$$

In regimes of large detunings, $\Delta \gg \gamma$, one can adiabatically eliminate the excited state and reduce the above equations to

$$\frac{\partial \sigma_{12}}{\partial t} = -(\gamma_0 + i\eta z + i\delta_{LS})\sigma_{12} + ig\frac{\Omega_+}{\Delta}\hat{\mathcal{E}}_+ + ig\frac{\Omega_-}{\Delta}\hat{\mathcal{E}}_- \tag{7.4}$$
$$\tag{7.5}$$

whereas the Maxwell equations for the electric fields are given by

$$\frac{\partial \hat{\mathcal{E}}_+}{\partial z} = i\mathcal{N}\frac{\Omega_+}{\Delta}\sigma_{13}^+ \tag{7.6}$$
$$\frac{\partial \hat{\mathcal{E}}_-}{\partial z'} = -i\mathcal{N}\frac{\Omega_-}{\Delta}\sigma_{13}^-$$

where $z' = z - ct$ and light shift term $\delta_{LS} = i\frac{|\Omega_+|^2+|\Omega_-|^2}{\Delta}$. Use of a pair of counter-propagating coupling fields allows us to excite the coherence term σ_{13}^- which is also coupled to the long-lived coherence σ_{12} and therefore results in retrieval of stored light in the backward direction.

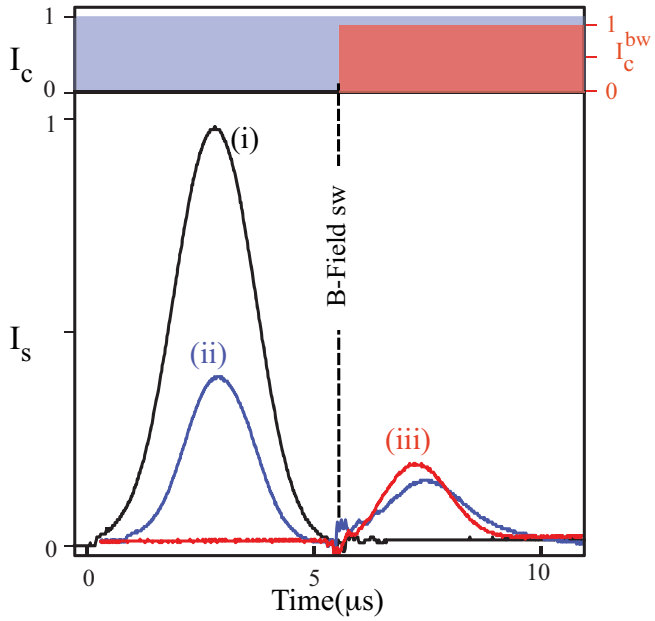

Figure 7.11: Forward and backward retrieval of echo. (i) the input pulse, (ii) forward-propagating signal light at the output of the memory when the coupling and signal beams are co-propagating. (iii) backward propagating light at the output of the memory when a coupling field, counter-propagating with respect to input light, is applied at the retrieval stage. Backward propagating light is measured using a 50/50 beam splitter before the memory, for this reason traces (iii) are amplified by a factor of 2. The top section shows the switching protocol for the forward (blue) and backward (red) propagating coupling fields. Due to the low OD, part of the input light leaks from the memory without absorption.

To experimentally demonstrate backward retrieval of the echo, we used a coupling field propagating in the opposite direction with respect to the input pulse. Initially, the input pulse was stored with a co-propagating coupling field. At the read-out stage the photon echo was retrieved either in the forward or the backward direction by means of forward or backward coupling field after the gradient flip, we observed counter-propagating photon echoes recalled from the memory. The results are shown in Fig. 7.11 where photon echoes were retrieved in the forward (trace (ii)) or backward (trace (iii)) directions.

When two counter-propagating coupling fields are applied, the echo signal propagating in the forward direction can undergo Bragg scattering into the backward propagating mode. The physics of trapping the light in this case is similar to the stationary light generated in an EIT medium as discussed in the previous section.

Fig. 7.12 shows results of the numerical simulation using XMDS [180] for forward and backward propagating probe fields. When the gradient is switched to zero just before the echo is emitted, the system polariton is very close to $k = 0$. At this point most of the polariton is in the photonic mode and the light field is propagating with a group velocity $v_g = g\mathcal{N}/k^2$. Due to the non-zero group velocity, the light field eventually leaves the memory in the presence of the coupling field. This is shown in Fig 7.12 (a), where the coupling field co-propagating with the probe is on and the gradient is switched off. This leads to the retrieval of the echo in the forward direction. However, if the counter-propagating coupling fields are switched on after the gradient is turned off, a stationary

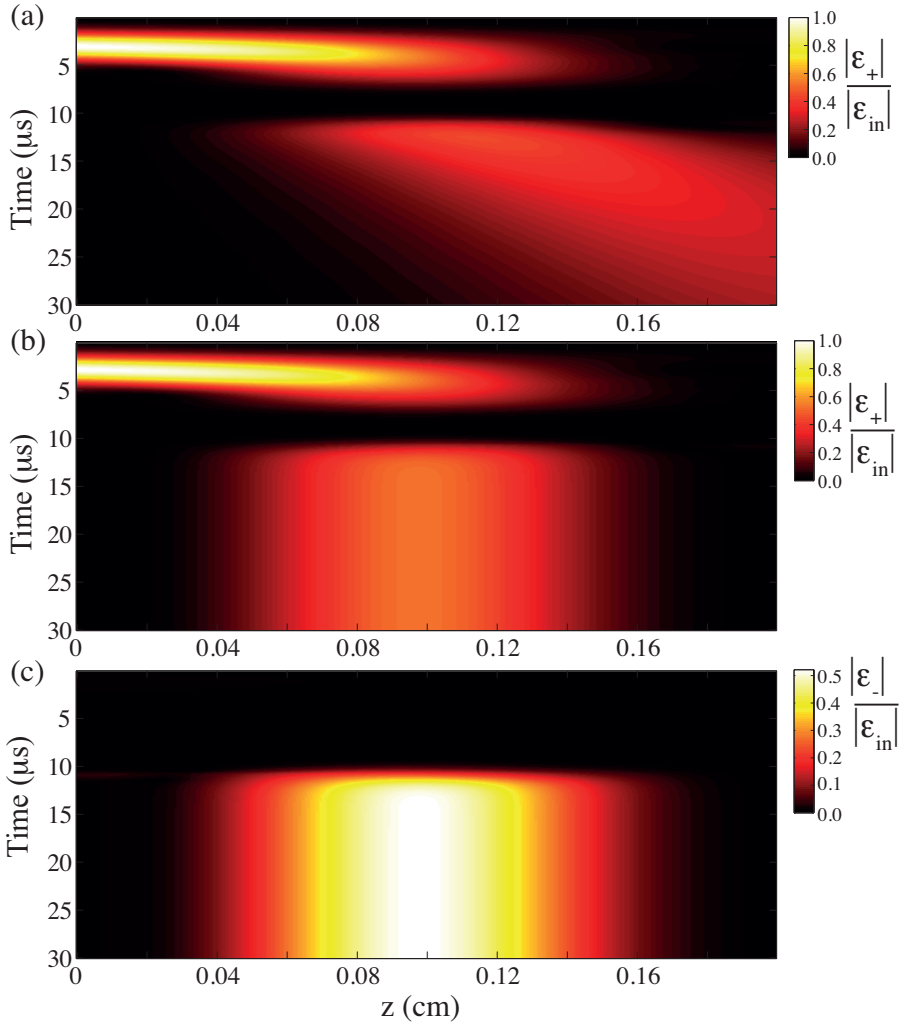

Figure 7.12: (a) Forward propagating probe signal in the presence of forward-propagating coupling field. The frequency gradient is switched off before the phase matching condition ($k = 0$) is satisfied. The photonic part of the polariton is propagating with a non-zero group velocity and eventually leaves the memory. (b) and (c): forward and backward-propagating probe signals, respectively, when the counter-propagating coupling fields are switched on after switching off the gradient field. The light propagation is then forbidden and stationary light is generated.

light pulse which remains inside the memory is generated. The amplitude of the forward and backward propagating probe field are shown in Fig. 7.12 (a) and (b), respectively. The physics of the trapping light in this case is similar to the stationary light generated in an EIT medium.

It is worth mentioning that by applying the counter-propagating coupling fields during the writing stage we observed that the probe absorption on the Raman resonance was suppressed. Instead we observed that the probe signal was divided in half, propagating with the two coupling fields. The technique can potentially be used as an all-optical switch [192, 193, 194] where the direction of the fields can be switched optically with a tuneable delay.

7.4 Conclusion

We presented storage of multiple pulses of light within a chosen frequency bandwidth, and stored pulses can be recalled in arbitrary order with any chosen delay between each recalled pulse. Furthermore, we show that pulses can be time-compressed, time-stretched or split into multiple smaller pulses and recalled in several pieces at chosen times.

Although our experimental results are, so far, limited to classical light pulses, our technique should enable the construction of an optical random-access memory for time-bin quantum information, and have potential applications in quantum information processing.

Chapter 8

High Efficiency Light Storage

One of the key requirements of a practical optical memory that can also be used for quantum applications is high-efficiency storage of optical information. The minimum efficiency required for any unconditional quantum memory is 50%. Using other storage techniques, the most impressive efficiencies so far attained are 43% using EIT[195] and 35% using AFC[128].

Using GEM based on two-level praseodymium ions, recall efficiencies of 69% have been experimentally demonstrated [149]. In this solid state system, the frequency gradient is applied using an electric field to induce a Stark shift. In this chapter we discuss the construction of a high efficiency 3-level GEM memory. In the previous chapter the best efficiency achieved was 42%. Through modifications to the experiment, we show how it is possible to increase the efficiency to 87%, which is so far the highest recorded efficiency for a quantum memory prototype.

The relevant published paper to this chapter is

"**High efficiency coherent optical memory with warm rubidium vapour** M. Hosseini, B. M. Sparkes, G. Campbell, B. C. Buchler, P. K. Lam, Nat. Commun. 2, 174 (2011)."

8.1 Experimental arrangement

In theory, as described in Chap. 4, the efficiency of gradient echo memory can reach unity at large optical depths. To reach the unity efficiency limit in the lab, one needs to increase optical depth of the memory. This was achieved in our experiment by using a long Rb vapour cell and increasing the temperature of the cell.

The experimental setup is similar to what was described in the previous chapter (Sec. 7.2) with a few modifications as is shown in Fig. 8.1 (a). In this setup we have used a long cell with a length and diameter of 20 cm and 25 mm, respectively, to increase the OD of the memory. To determine the optimum buffer gas pressure we examined gas cells with various Kr and Ne pressures ranging from 0-100 Torr. We have observed the maximum absorption in the vapour cell with 0.5 Torr Kr buffer gas. At buffer gas pressures higher that 5 Torr (Ne or Kr) we observed enhanced incoherent absorption of the probe and the coupling field limiting the absorption efficiency. This can be attributed to the collisional broadening of the excited state. Although large buffer gas pressures can potentially provide longer storage times as demonstrated in EIT storage schemes [196, 195], the amount of loss introduced to both beams at large buffer gas pressures could not be

tolerated, in our scheme, in order to obtain high efficiency storage.

The temperature of the cell was controllably tuned to an average temperature of ∼80^{o}C using a bifilar resistive heater wound around the cell. At this temperature a Rb atomic density of $\simeq 10^{12}$ cm^{-3} was expected. The heater was designed so that the cell windows become warmer than the middle of the cell in order to prevent Rb from condensing on the windows. This caused a 5-10 ^{o}C temperature difference between the middle and ends of the cell.

The signal beam, as described in Sec. 7.2, was prepared using a FC-EOM and the sideband was extracted using a ring cavity. Signal pulses were prepared with a peak power of < 2 μW. The signal pulses and coupling beam were then combined with the same linear polarisation, but different mode size, using another cavity (also finesse=100) resonant with the signal field. Using the same polarisation for two beams is crucial for the observation of high-efficiency echoes and reducing the FWM processes (this is explained further in Chap. 10). Using the cavity is the most efficient way of combining two beams with the same polarisation. The coupling and signal fields were converted to circular polarisation and sent into the gas cell. The signal beam was collimated to a diameter of 6 mm while the coupling field covered almost the entire cell cross section. This arrangement of beam sizes was chosen through various iterations to optimise the absorption of the probe beam. After the cell, the signal field was coupled to a single-mode fibre and sent to a heterodyne detection system. The coupling field was mostly rejected from the fibre due to its larger mode diameter. We found the polarisation and alignment of the two beams crucial to observation of high efficiency storage.

The magnetic coil arrangement was similar to what was described in the previous chapter. The switching times were 0.5 and 2.5 μs, respectively. The DC magnetic field was set to 6 G and the typical value of the gradient field is 20 mG/cm. The cell and coils were surrounded by double μ−metal shielding to reduce the influence of the Earth's magnetic field. The coils were designed to be more than twice the length of the cell. This provides enough distance (>10 cm) between ends of the cell and coils. For this reason we found the effect of μ-metal end-caps, on the background magnetic field, to be negligible.

Fig. 8.1 (b) shows the magnetic field created by one of the coils measured in three dimensions along the propagation axes, in the middle of the vapour cell. As can be seen, the field variation is quite linear along the length of the memory and contribution of transverse fields in the middle of coils is negligible. Fig. 8.1 (c) shows the current flowing through the two coils during the time period when the fields are being switched.

8.2 High efficiency storage results

Figure 8.2 (a), shows the Raman absorption line as a function of two-photon detuning (detuning from the Raman resonance) (i) with and (ii) without the applied magnetic field gradient. The absorption is sensitive to alignment, which in this case was optimised for the broadened feature. This is the reason for the larger absorption seen by the broadened Raman line compared to the unbroadened one. Furthermore, these Raman lines are results of heterodyne detection averaged over 10 traces and the signal-to-noise ratio of the absorbed signal is not high enough to accurately measure the maximum absorption point. With the applied broadening the absorption is ∼99%. This limits the maximum possible recall efficiency of our memory[152] to 0.99^2=98%. As mentioned previously, the shape of the Raman line is very sensitive to the polarisation and alignment of the beams. For orthogonal linear polarisation of the beams, we observed amplification of the signal

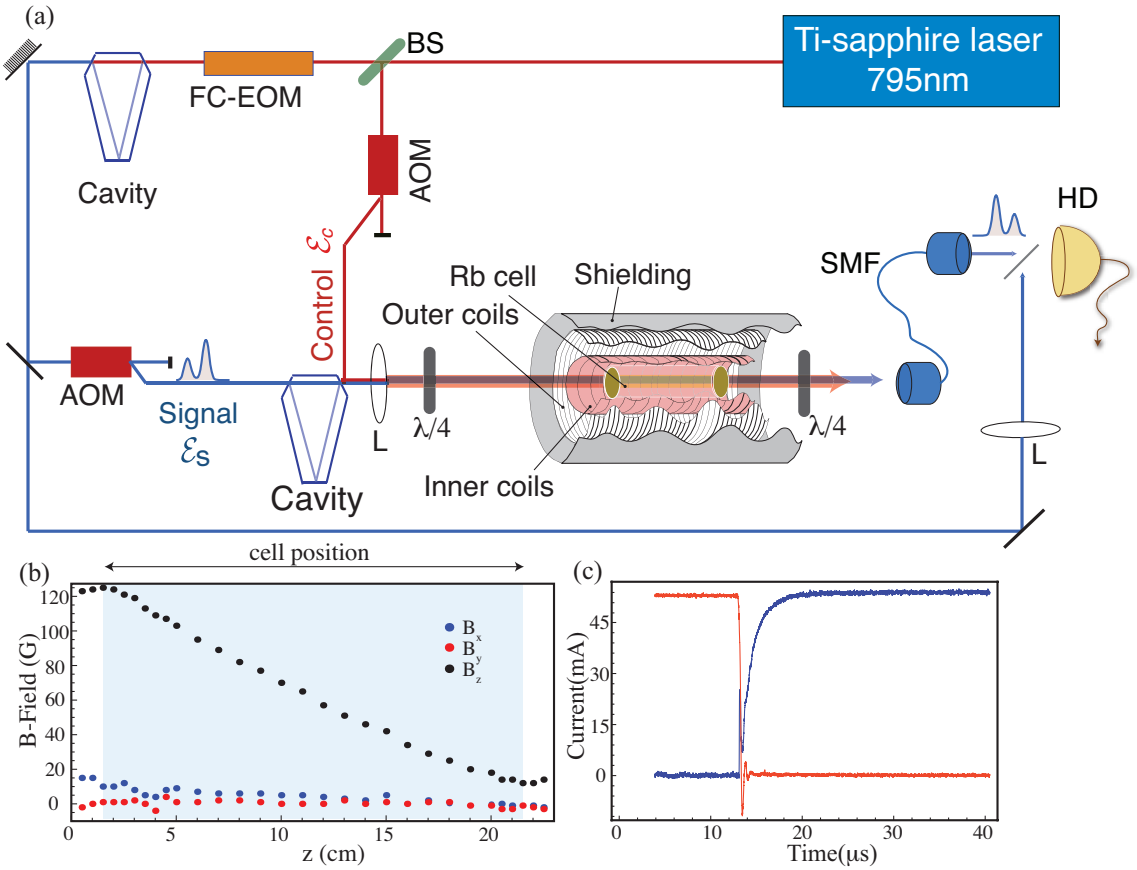

Figure 8.1: (a) **Schematic view of the experiment.** Experimental setup showing the coupling (red) and signal (blue) beams with 6.8 GHz frequency difference, collimated at different sizes and of identical circular polarisation when they go through the cell. Heterodyne measurement is performed after the memory on the signal field. BS: Beam Splitter, HD: Heterodyne Detection, SMF: Single Mode Fibre, AOM: Acousto-Optic Modulator, FC-EOM: Fibre-Coupled Electro-Optic Modulator, $\mathcal{E}_s$ and $\mathcal{E}_c$: signal and coupling field amplitudes, respectively. (b) Measurement of the 3-D magnetic field along the propagation axis, z. (c) Current flowing into the coils during the switching period

beam for gas temperatures between 80-90 ^{o}C. This is discussed in more detail in Chap. 10. For co-circular (or co-elliptical) polarisation this effect observed to be negligible. Slightly different polarisation and alignment can distort the Raman line shape and can result in unpredicted absorption spectra. This high degree of sensitivity was only observed in a 20 cm cell at high temperatures. The absorption line was optimised by firstly selecting circular polarisation for both beams. The alignment was then optimised for the broadened line at low coupling field powers. The cell positioning was then adjusted to make sure the two gradients overlapped and the broadened Raman line was symmetric.

The results of storage and recall experiments are shown in Fig. 8.2 (b). The input pulse, shown in black, has a $1/e^2$ width of 2 μs. We measure the power in this input pulse by recording the far off-resonance transmission through the gas cell without the coupling field. We measured no noticeable absorption from the atomic ensemble under these conditions and we can use the total energy in this pulse (the area under the curve) to normalise the recall efficiency of our storage experiments.

In Fig. 8.2 (b) after flipping the magnetic field gradient we recall the signal light with a

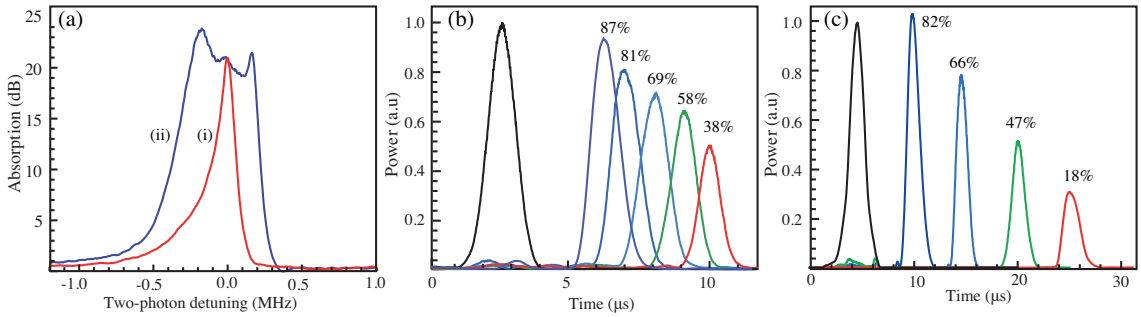

Figure 8.2: Raman Absorption line and input-echo pulses. (a) (i) The Raman absorption line before broadening. (ii) The Raman absorption line after application of the magnetic field gradient. This was observed with a single frequency cw signal beam, while the frequency of the coupling beam was scanned. (b) Storage and recall data with an input pulse duration of 2 μs. (c) Storage and recall data with an input pulse duration of 3 μs and the coupling field is turned off during storage time to reduce the decay rate of the storage. For both (b) and (c) the far off-resonant transmitted input pulse, which is used to normalise our recall efficiency, is shown in black. The coupling field power was 370 mW.

maximum efficiency of 87%. The storage time in this case is 3.7 μs peak-to-peak, or exactly one pulse width between the $1/e^2$ points power levels to ensure complete separation of the input and recalled pulses. The recall efficiency drops rapidly for longer storage times, although for these data the coupling field was on at all times. In Fig. 8.2 (c) we show the results of recall experiments where the coupling field was switched off during the storage phase of the experiment. In this case we find slower decay of the recalled pulse since we have now reduced the decoherence caused by the coupling field. The pulses in these data are slightly compressed on recall due to a higher magnetic field gradient used to recall the signal light, which is the reason for the peak recalled power exceeding the input peak power. We can achieve slightly higher efficiency using compressed pulses since the total storage time in the medium is reduced.

8.2.1 Atomic decoherence

Fig. 8.3(a) (i) shows the efficiency as a function of storage time when the coupling field is on. Taking into account the signal beam radius of 3 mm and 0.5 Torr Kr buffer gas, one can calculate the diffusion time of the atoms, defined as the time that a fraction $1/e^2$ of atoms have moved a distance greater than the radius of the signal beam, to be $\tau_d = 22$ μs. This value was fixed in our model allowing us to fit only the ground state decay time, which was determined to be $\tau_0 = 4$ μs corresponding to a decay rate of $2\pi 40$ kHz. This is consistent with the scattering rate of $2\pi \times 30$ kHz calculated above, from which we conclude that our system is limited in this regime by coupling beam-induced scattering.

One would expect the same decay rate for the atomic coherence as the FWHM of the unbroadened Raman line. This is only true if the Raman line is Lorentzian (not saturated) and unbroadened. In situations where the two beams are not spatially mode-matched or are slightly angled with respect to each other, the absorption line could be inhomogeneously broadened due to the Doppler effect. The excess broadening was shown quadratic in the angular deviation for an EIT scheme [160]. The angular dependency of the Raman line is discussed further in Chap. 10. Also, in presence of background magnetic

field, the absorption line could be inhomogeneously broadened. For very low coupling field powers and in the absence of a background magnetic field, the width of the Raman line directly reflects the ground state decoherence. At high coupling field powers, however, power broadening or scattering introduces extra loss to the atomic coherence. In our system, this scattering rate is calculated to be $2\pi \times 30$ kHz.

This scattering effect results in an exponential decay of atomic coherence after light is stored. We note, however, that this may not be the case for very short storage times where the decay is not exponential and does not agree with our simple model. This effect can be attributed to the highly photonic nature of the memory for short storage times. The pulse, in this case, has yet to be fully mapped into the atomic spin wave. The impact of the scattering, collisional and diffusion decay terms will vary as the light is absorbed into the atomic ensemble leading to decay of the memory that differs from the model at short times.

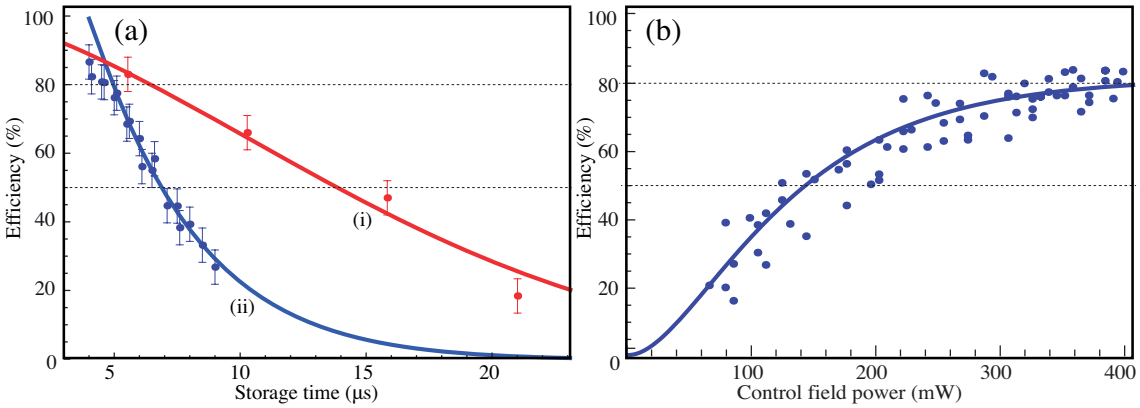

Figure 8.3: coupling field effect on efficiency and noise. (a) Echo efficiency as a function of storage time. (i, red) Data taken for a 3 μs pulse while the coupling field with power of 380 mW was switched off during the storage time. (ii, blue) Data taken for a 2 μs pulse while the coupling field with power of 290 mW was kept on during the storage time. Error bars indicate the detection error derived from fluctuation of the amplitudes of pulses. (b) Efficiency of photon echoes of a 3 μs pulse as a function of coupling field power. The solid line is the theoretical predictions taking into account diffusion time of 22 μs, coupling field induced scattering and ground state decoherence rate of $2\pi \times 3.5$ kHz.

To understand the contribution of the coupling field-induced scattering we investigated memory behaviour both in the presence and absence of the coupling field during the storage time. We can gain some insight into our system by considering a simple model that includes an atomic diffusion time, τ_d, a total ground state decoherence rate, τ_0, and a maximum possible memory efficiency, η_0, limited by the optical depth. The efficiency η_m will then be given by

$$\eta_m = \eta_0 e^{-(t/\tau_d)^2} e^{-t/\tau_0}. \tag{8.1}$$

The scattering rate can be minimised by switching off the coupling field during the storage time. Atomic diffusion then becomes the dominant decay mechanism; hence a more Gaussian-like decay is expected. The curve in Fig. 8.3 (a) (i) is the result of a convolution of a Gaussian decay function ($\tau_d = 22$ μs) due to diffusion and an exponential decay function due to the ground-state decoherence. The fitted exponential decay time in this

case is $\tau_0 = 60$ µs, giving a decay rate of $2\pi \times 2.6$ kHz. This is still much higher than the collision-limited ground-state dephasing time, but this is expected because the decay rate in this case varies as the coupling beam is switched on and off over the course of the experiment.
We also studied the effect of the coupling field power on the memory efficiency for storage times of one-pulse width. As can be seen in Fig. 8.3 (b), the recall efficiency saturates with increasing coupling field power. This is because increasing Ω_c can effectively provide a higher optical depth as long as $\Delta \gg \Omega_c$. In this case the effective atom-light coupling strength can be described as $g\prime = g\Omega_c/\Delta$. If Ω_c is further increased beyond this limit, the system can no longer be described by a simple quasi two-level atomic ensemble and there is no further improvement in optical depth.

Based on our experimental conditions, the rate of spontaneous emission due to the signal beam is found to be $2\pi \times 1$ Hz at pulse peak intensity. The scattering rate due to the coupling field, on the other hand, is found to be $\sim 2\pi \times 30$ kHz at power of 370 mW.

8.3 Multi-pulse storage

Multimode storage of photonic information is crucial for optical communication as well as quantum information technology. To date, various techniques have been proposed for the implementation of an optical memory that satisfies this requirement [197, 198, 199, 124, 185]. Among these proposals the atomic frequency comb (AFC) has been proven to have high multimode capability regardless of the ensemble's OD [200, 201]. The GEM technique has also multimode storage capacity [151]. Similar to AFC, GEM can store wide input spectra regardless of OD, although with small efficiencies at low OD. Below, we present experimental results for storage of multiple optical pulses inside warm atomic vapour using GEM technique.

In Fig. 8.4 we show the storage and recall of 20 Gaussian pulses with an overall efficiency of 2%. For this experiment the coupling field power was reduced from 370 mW to 64 mW to reduce the decay rate of the memory. The lower optical depth in this case limits the efficiency of the storage and recall. From this data we can infer a delay-bandwidth product (DBP)[202] of ∼40 for the our memory. The highest multimode capacity demonstration was achieved using AFC where 1064 pulses were delayed [201].

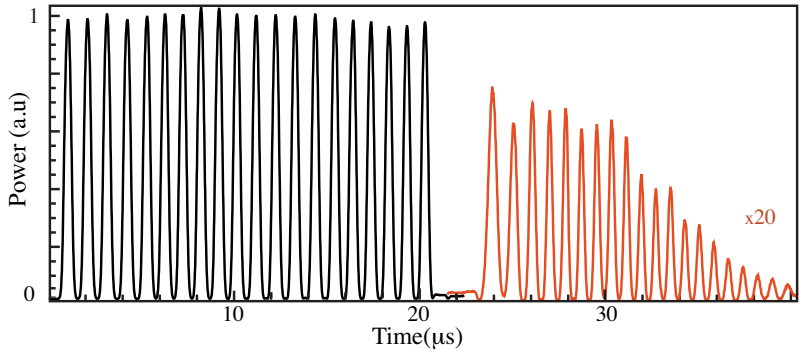

Figure 8.4: Results of 20 pulse storage Amplitude of 20 Gaussian input (black) and echo pulses (red) with total recall efficiency of 2 %.

It can be seen that the amplitude of the echo pulses decays differently in time for short

and long storage times. This is in agreement with the abovementioned discussion about diffusion and scattering effects resulting in different decoherence mechanisms. One can obtain echoes with constant amplitude by flipping the gradient twice and retrieving it in the first-in-first-out manner. This way, all of the pulses will experience the same decay time inside the memory.

The maximum number of pulses that can be stored, in this case, is limited by the decoherence rate of the memory. The bandwidth of the memory can be increased by applying large detuning gradient η as long as $\Delta \gg \eta L$.

8.3.1 A pillar that pacifies the oceans

In free space, the 20 optical pulses shown in Fig. 8.4 occupy more than 6000 meters of the space that during storage are squeezed in a few-cm-long memory. This is equivalent to a medium with a refractive index of approximately 60000! This ability to control light by tuning its group velocity is unique to the atomic-based memories.

Figure 8.5: The "Monkey King" is the main character of a classical Chinese novel dating back some four hundred years ago. Image from: Jon Sigurdsons Collection (http://chinaposters.org)

There is a veiled analogy between a multimode optical memory and a character in a classical Chinese epic novel that I would like, if I may, to draw here. Sun Wukong, also known as the Monkey King is the main character in the Chinese novel "Journey to the West". In the novel, he was a monkey born from a stone who possessed an immense amount of power. In search of a weapon, Sun Wukong gain the Golden-banded staff, which could change its size and multiply itself. A poster of him by Jon Sigurdson is shown in Fig. 8.5. The staff was originally used to measure ocean depth and later became the

"Pillar that pacifies the oceans". It weighed 8.1 tons and he could wield it as a staff and keep it inside his ear as a sewing needle.

A long-lived optical memory is able to do a similar trick by squeezing kilometres of light in a centimetre-long medium. At the recall stage, light can be compressed or stretched ondemand depending on the application.

8.4 Conclusion

In conclusion, we have shown light storage in warm vapour gas up to 87% memory efficiency using $\Lambda-$GEM technique. All measurements were performed using coherent heterodyne detection. We have demonstrated a time-bandwidth product of ~ 40. The decay rate of our memory can be controlled, to some degree, by minimising the use of the coupling beam to the extent that for longer storage times we become limited by atomic diffusion.

Chapter 9

Atom-Light Interference

"Constantly regard the universe as one living being, having one substance and one soul; and observe how all things have reference to one perception... observe too the continuous spinning of the thread and the contexture of the web."

Marcus Aurelius

In this chapter we present experimental observation of interference between an atomic spin coherence and an optical field in a Λ-type gradient echo memory. The interference is mediated by a strong classical field that couples a weak probe field to the atomic spin coherence through a resonant Raman transition. Interference can be observed between a prepared spin coherence and another propagating optical field, or between multiple Λ transitions driving a single spin coherence. In principle, the interference in each scheme can yield a near unity visibility and could be used as a coherent all-optical switch.

The relevant published paper to this chapter is

"**Time and frequency domain polariton interference** G. Campbell, M. Hosseini, B. C. Buchler, P. K. Lam, Submitted to New J. Phys. (2011)."

9.1 Introduction

Coherent manipulation of atomic systems using photons is a key element of many quantum atom-optics experiments. The ability to controllably tune atom-light interactions while preserving the quantum properties of a system has also great potential with regard to the development of quantum information technology. Many of the techniques employed in quantum atom-optics involve the interaction of light with ensembles of atoms that have long-lived coherences between hyperfine energy levels. In such systems, a two-photon transition between hyperfine states can be used to manipulate the atomic state in a coherent manner. Examples of this include stimulated Raman adiabatic passage (STIRAP) [203], electromagnetically induced transparency (EIT) [204] and photon echoes [205], all of which have been proposed as central elements in a range of protocols for storing and processing optical quantum information.

Within the range of schemes that exploit light-atom interactions, a number of them, particularly photon echo schemes, pertain to interference effects between the quantum modes. A time-delayed quantum interferometer has previously been proposed as a method for quantum interference between two single photons [206]. Experimental observation of interference between backward-propagating stimulated photon echoes has also been reported [205], where two echoes have been selectively chosen in time to destructively

interfere while the information contained in the suppressed echo was not recovered from the sample. Furthermore, the phase-preserving nature of storage was previously investigated by interfering echoes generated from separate optical memories [207].

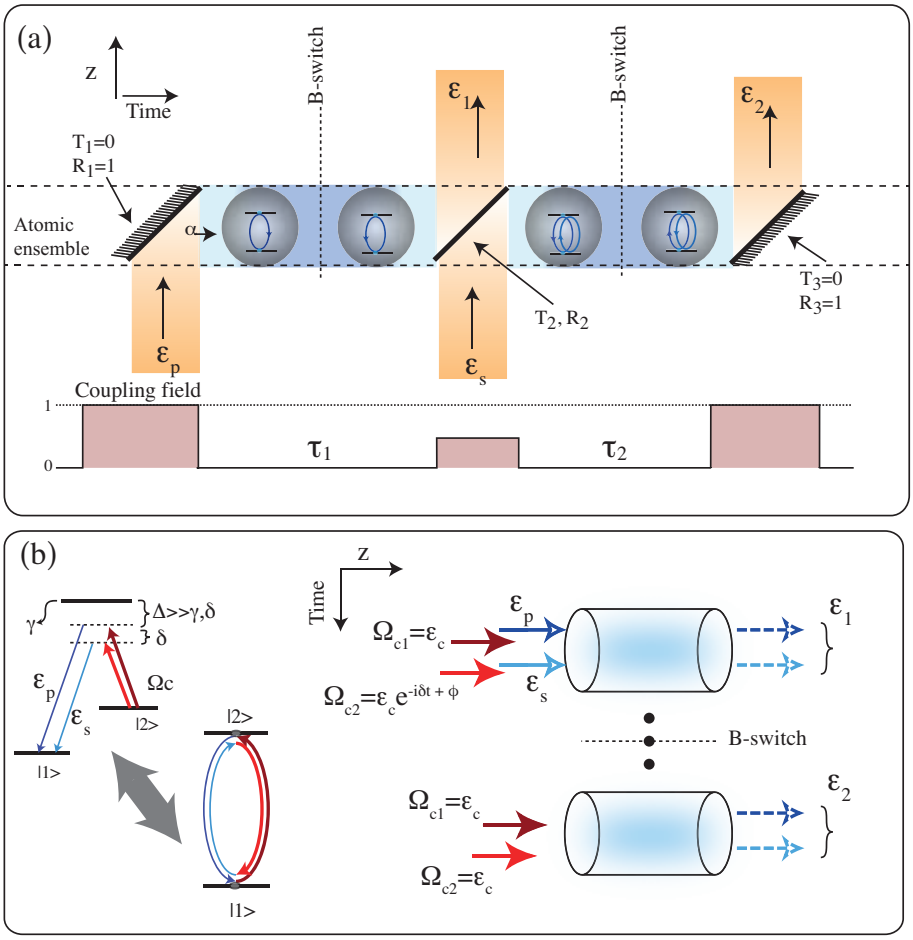

Figure 9.1: (a) Schematic representation of atom-light interference in the memory. The probe pulse, $\mathcal{E}_p$, is fully absorbed in the atomic spin coherence (α). The second steering pulse, $\mathcal{E}_s$, enters the memory at the precise time that the first echo is being emitted so that it can interfere with the recalled light. The interference is determined by the relative phase of the pulses and the effective beamsplitter (T_2, R_2), which is controlled by the strength of the Raman coupling field. The remaining atomic coherence can be recalled later as $\mathcal{E}_2$. (b) Left: Double-Λ level structure and optical fields used for interference of two Raman absorption paths of signal fields (probe and steering) with different frequencies. Both Λ transitions drive the same coherence. Right: The procedure used for observing double-Raman interference. The probe and steering pulses are sent into the memory each with a corresponding coupling field. Interference between the unabsorbed probe pulses, $\mathcal{E}_1$, and the atomic coherence, which is recalled from the memory as $\mathcal{E}_2$, can be observed by varying the relative phase of the two Λ transitions.

In the following sections, we investigate the coherent interference of atomic polarisation and an optical field using the three-level gradient echo memory. We treat the read and write stages of the memory as being analogous to a beam-splitting operation acting between an optical mode and an atomic spin coherence. Both the splitting ratio and the interference phase are controlled optically via the strength of the Raman coupling field.

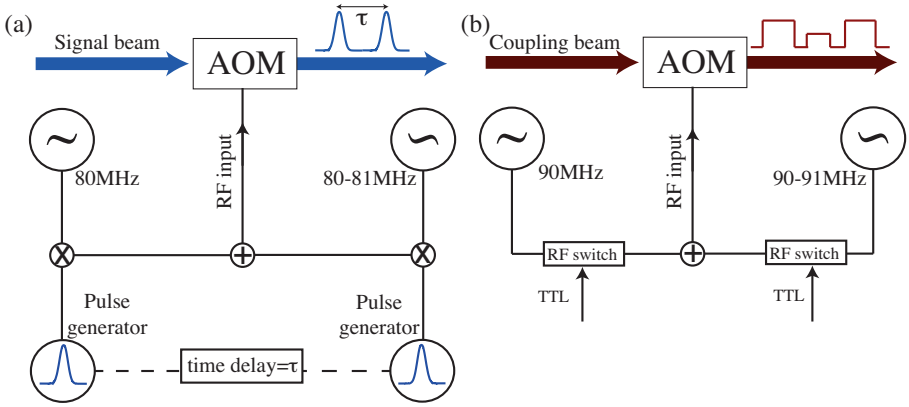

Figure 9.2: (a) Schematic representation of signal pulse preparation using two pulse generators and two function generators to control phase, frequency and amplitude of the two pulses individually. (b) Schematic representation of RF signal preparation for the coupling field using two function generators and RF switches to control the relative phase, frequency, power and shape of the coupling field in time.

9.2 Method

We explore the nature of atom-light coupling through two separate mechanisms. The first scheme (Fig. 9.1(a)) is a time-domain interferometer. We prepare the atomic polarisation by storing a pulse of light in the atomic memory. A second steering pulse is sent into the memory just as the stored field is being recalled. The two pulses are observed to interfere as polaritonic modes. The second scheme (Fig. 9.1(b)) is a frequency domain interferometer. In this case the atomic coherence is simultaneously driven via two distinct Raman transitions. Interference is then produced between the two nondegenerate absorption paths. We first briefly introduce the storage technique in general and then explain each scheme in more detail.

Similar to our previous setup as described in Sec. 8.1, our experiment was performed using a 20 cm long vapour cell of warm Rb atoms and a linear switchable varying magnetic field. The coupling and probe fields are passed through acousto-optic modulators (AOMs) which allow us to create the required pulse sequences by driving them with appropriate RF signals. To generate the probe and steering pulses, the RF signals were created using separate, but phase-locked, arbitrary waveform generators and were combined together before the AOM (details are in the supplementary material). In this manner, the frequency, phase and amplitude of the coupling, probe and steering fields can be independently controlled. The coupling field power used for maximum coupling between the optical and atomic modes was 330 mW and was adjusted to control the coupling. The probe and steering pulses were on the order of few μW. In order to generate and control the phase, timing, and amplitude of the signal and coupling fields, the method shown in Fig. 9.2 (a) and (b) respectively was used.

9.2.1 Time-domain interference

Our first experiment investigates interference of light pulses with a mode stored in the atomic memory. Following on from Ref. [152], this effect can be thought of as a time-delayed beamsplitter system. The effective optical depth (OD) of a Λ-GEM is defined

as

$$\beta = \frac{gN}{\eta}(\frac{\Omega_c}{\Delta})^2. \tag{9.1}$$

For the writing stage the transmissivity, $T(\beta)$, of the effective beamsplitter is the fraction of the input light field that is leaked through the memory so that $T(\beta) = e^{-2\pi\beta}$, while the fraction of the light written into the memory is given by the reflectivity $R(\beta) = 1 - T(\beta)$. For the reading stage, the $R(\beta)$ will be the fraction of the polariton that is converted into a recalled optical field, while $T(\beta)$ will be the fraction that remains in the memory. Since $T(\beta)$ and $R(\beta)$ are defined by the strength of the coupling field, one can tune the transmissivity of the beam-splitting through the power of the coupling field. A series of reading and writing events, as shown in Fig. 9.1(a), can then be described using appropriate reflectivities. The amount of light recalled in the first echo is given by $\mathcal{E}_1 = \sqrt{R_1 R_2}e^{-\gamma_0\tau}\mathcal{E}_p + e^{i\theta}\sqrt{T_2}\mathcal{E}_s$, where $\mathcal{E}_p$ is an initial probe pulse and $\mathcal{E}_s$ is a second pulse, which we label the steering pulse, that enters the medium at the time that the probe pulse is recalled. The exponential term arises from the decay of $\mathcal{E}_p$, at a rate γ_0, during the storage time τ. The phase θ can be chosen at will. This equation shows that interference can arise between recalled fractions of $\mathcal{E}_p$ and $\mathcal{E}_s$ and, in particular, if $\sqrt{R_1 R_2}e^{-\gamma_0\tau} = \sqrt{T_2}$ and $\theta = \pi$ then $\mathcal{E}_1$ can be fully suppressed. This simple analysis ignores other details such as the matching of the temporal modes of the pulses. Other factors that limit ideal interference will be discussed later when we analyse the results of our experiments.

We use the polariton picture to visualise the dynamics of the time-domain beamsplitting operation. Figure 9.3 shows a numerical simulation of this interference scheme. The simulation shows the evolution of the electric field in real space (the $z - t$ plane) and the atomic spin coherence in Fourier-space (the $k - t$ plane). In this numerical simulation the atomic and electric fields are out of phase. This results in a suppression of the echo from the first pulse. The constructively interfered atomic polarisation is recalled in field $\mathcal{E}_2$ after the second gradient switch.

The result of the interference is observed as either an atomic or an optical field. The interference happens through the entire atomic medium and results in transfer of amplitude and phase information between the atomic coherence and the optical field. The simplified picture provided above using the beam splitter analogy misses some physical details about the interference processes which happen at the microscopic level. From the Maxwell equation, one can find that $k\mathcal{E}(t,k) = \mathcal{N}\alpha(t,k)$ and it suggests that when $k < 0$ the electric field and atomic field are out of phase. Here, $\mathcal{N}$ in the effective linear atomic density. The extra π phase shift between the atomic and electric field at $k < 0$ agrees with the conservation of energy principle expected from such unitary operation similar to a beam splitter. This effect is demonstrated by numerical simulation of the amplitude of the electric field and atomic polarisation plotted in the $z - t$ plane in Fig. 9.4 (a) and (b), respectively. The amplitude of the electric and atomic fields, which is plotted in time at the beginning of the memory ($z = 0$) on the top of the figure, shows the phase difference between the steering pulse and the atomic field.

We stored a 4 μs probe pulse in the memory and recalled it after a storage time of $\tau_1 = 10$ μs. The steering pulse was injected just as the atomic coherence excited by the probe returned to $k = 0$. We label the light detected at this time as $\mathcal{E}_1$, and integrate the detector signal over the pulse duration to obtain a value for the pulse energy. The polariton that remains in the atomic medium after the first recall is itself recalled after storage time

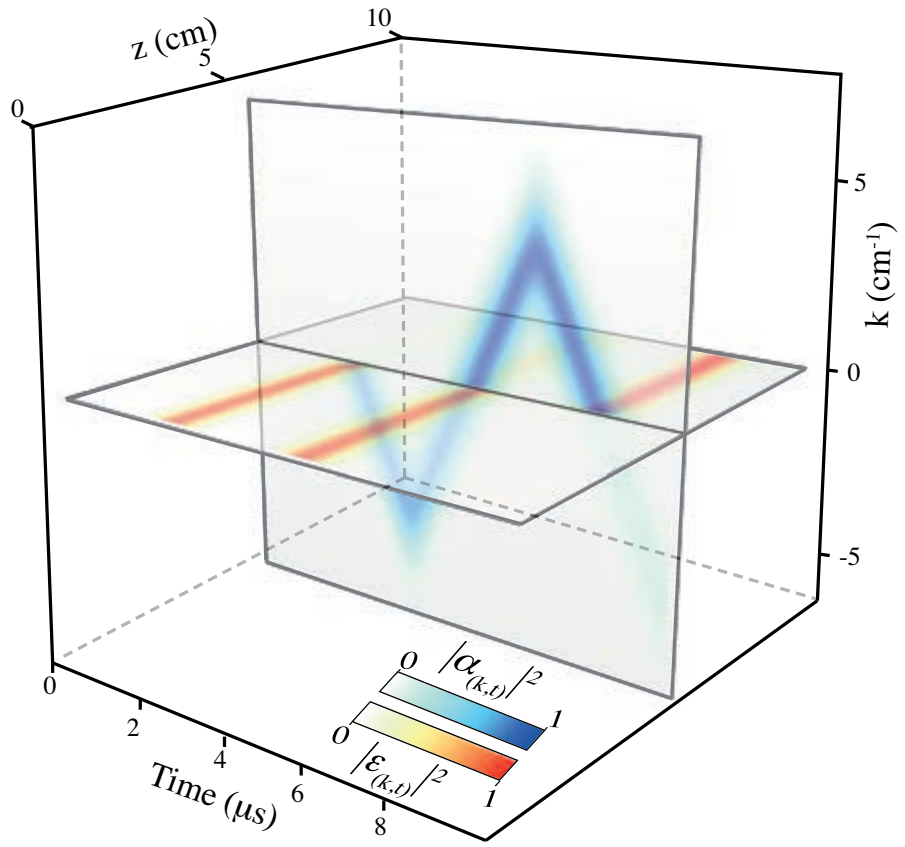

Figure 9.3: Numerical simulation showing interference between the electric field, plotted on the z-t plane, and atomic excitations, plotted on the k-t plane, where the second light pulse is out of phase with the first echo field. The parameters used in the simulations are: $gNL/\gamma = 40$, $\Omega_c/\Delta = 0.75$, $\Omega_c(t = 4\ \mu s) = 0.7\Omega_c(t = 2\ \mu s)$ and $\phi_{\mathcal{E}_s} - \phi_{\mathcal{E}_p} = \pi$

$\tau_2 = 10$ μs. We detect it in the same manner as $\mathcal{E}_1$ and label it $\mathcal{E}_2$. Figure 9.1(a) shows the sequence of pulses that are stored, interfered and retrieved along with the coupling field intensity for each step.

The energies of the recalled pulses, $\mathcal{E}_1$ and $\mathcal{E}_2$, were measured as a function of the relative phase of the probe and steering pulses. The phase of the atomic coherence depends on the relative phase of the coupling and probe fields. It is therefore possible to control the phase of the interference by scanning the phase of either the steering pulse or the corresponding coupling field. Fig. 9.5(a) shows interference fringes for $\mathcal{E}_1$ (blue, dashed line) and $\mathcal{E}_2$ (red, solid line) obtained by varying the phase of the coupling field corresponding to the steering pulse. This was accomplished by varying the phase of the RF signal that drives the coupling field AOM during the interference event relative to its phase during the storage of the probe pulse. For this data, the powers of $\mathcal{E}_p$ and $\mathcal{E}_s$ were equal and the coupling field power during the interference event was tuned to find the maximum fringe visibility on $\mathcal{E}_2$, which was found to be 68%. The visibility of $\mathcal{E}_1$ echo, 23%, is substantially lower due to the power mismatch of the steering pulse and the recalled atomic coherence required to optimise the interference in $\mathcal{E}_2$. The reflectivity corresponding to the recall of $\mathcal{E}_1$ is 37%.

Control over the effective beamsplitter ratio is demonstrated in Fig. 9.5 (b). It can

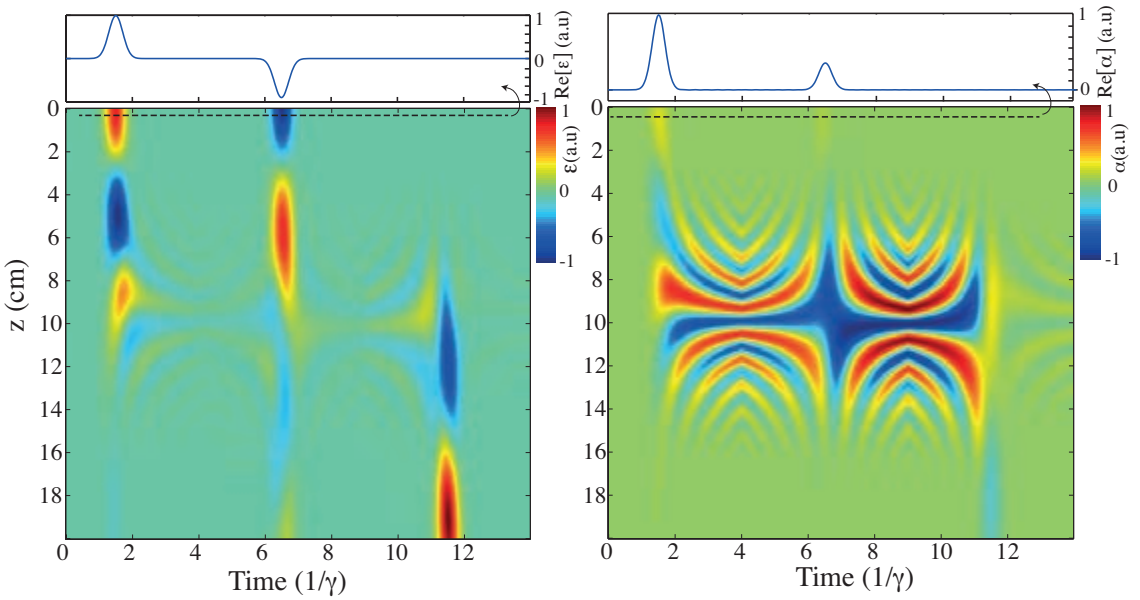

Figure 9.4: Numerical simulation showing (a) amplitude of the probe and steering pulses and (b) amplitude of the atomic coherence in the $z-t$ plane. The top sections of (a) and (b) show the real part of the electric field and atomic coherence as a function of time at the beginning of the memory.

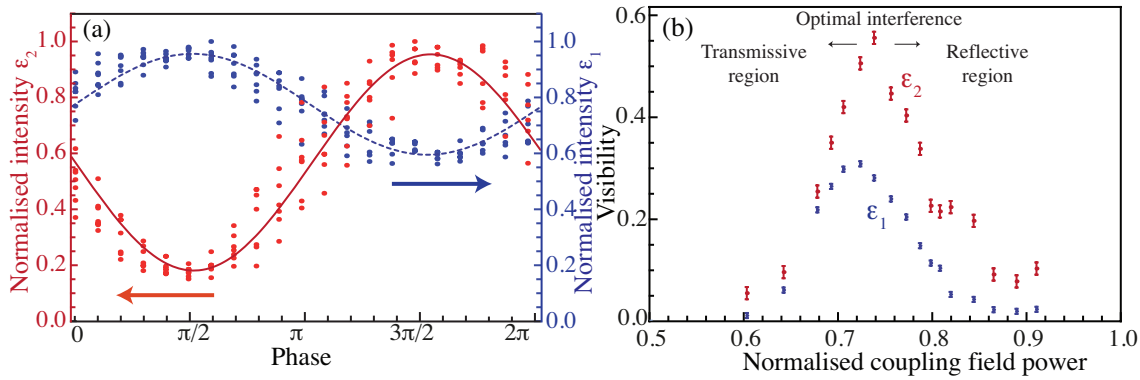

Figure 9.5: (a) Atom-light interference fringes at different times resulted from interaction of the steering pulse with echo generated from the probe pulse. The first arm of the interferometer which is in the optical mode leaves the memory(blue data) and the second arm is stored as an atomic coherence that is transformed back to the light field after re-switching the B-field (red data). These data were taken by optimising experimental parameters such as efficiency. The dashed blue and solid red lines are sinusoidal fits to the corresponding data. The red and blue data yield a fringe visibility of 68% and 23%, respectively. (b) Visibility of fringes for two pulses separated in time at the first (blue points) and second (red points) reading stage as a function of the normalised coupling field power.

be seen that by varying the coupling field power the effective splitting ratio can be tuned to find a maximum in the interference. For this data, the power contained in the steering pulse was adjusted to provide good visibility for both $\mathcal{E}_1$ and $\mathcal{E}_2$. It is interesting to note that for strong coupling fields, one optical pulse is written into the memory while another

is being recalled with little interference between the two, analogous to a high-reflectivity beamsplitter. For a weak coupling field, on the other hand, the effective beamsplitter becomes fully transmissive, again meaning no interference between the pulses as the steering pulse passes straight through without storage and the probe pulse remains trapped in the atomic coherence.

9.2.2 Frequency-domain interference

Now we consider the second experiment, in which the interference results from driving a single atomic coherence with multiple two-photon transitions as depicted in Fig. 9.1(b). In this case, the probe and steering pulses are co-propagating and enter the medium simultaneously but are separated in frequency by more than the memory bandwidth. In the far-detuning and adiabatic regimes, this double-Λ system is equivalent to a quasi-two-level system interacting with two fields of different Rabi frequencies (see Fig. 9.1 (b)). The interference between the two Λ transitions will change the response of the medium to the probe and steering pulses. When they interfere destructively, the absorption of the probe and steering fields is suppressed and both pulses are transmitted through the medium. When the two Λ transitions are in-phase, both pulses are coherently absorbed and can be recalled later ondemand.

As with our first experiment, the properties of the interference can be controlled through the coupling fields. The relative intensity and phase of the two coupling fields control the superposition of the probe and steering pulses that is transferred to the atomic coherence. This effect has been explored in EIT experiments [208, 209]. Unlike EIT, however, the optical modes that are not coupled to the atomic coherence in the Λ-GEM scheme propagate through the atomic medium with little loss.

The frequency difference between the probe and steering fields was set to 1 MHz, which was greater than the memory bandwidth of 300 kHz to avoid overlap between two broadened Raman lines. Each of the probe and steering fields has a corresponding coupling field which is tuned to the Raman resonance. The pulse length, 4 μs, was chosen to give a slightly smaller bandwidth than the memory bandwidth. Fig. 9.6 shows the interference fringe obtained by varying the relative phase between the two Raman absorption lines. This was done by sweeping the phase of one of the coupling fields. The powers of the coupling fields are equal, 160 mW each, and remain constant throughout the storage and retrieval process. $\mathcal{E}_1$ is the portion of the probe and steering pulses that does not get stored in the memory and $\mathcal{E}_2$ is the portion that is retrieved from the memory after a 10 μs storage period. The energies of $\mathcal{E}_1$ and $\mathcal{E}_2$ are measured by integrating the detector signal over the pulse period.

From an operational standpoint, this second experiment can be thought of as the frequency-domain counterpart to the first. While the first experiment demonstrated a beamsplitting operation between two pulses separated by time, the second demonstrates a beamsplitting operation between simultaneous pulses separated by frequency.

In both the time and frequency-domain interference experiments we attribute the less-than-unity fringe visibility primarily to a spatial and temporal mode mismatch between the probe polariton and the steering pulse. We believe that this is mainly due to the atomic motion and non-zero transverse magnetic field, which affects the echo signal for long storage times. This can be justified by the larger visibility measured in the frequency-domain interference scheme, where interference occurs between pulses that simultaneously interact with the atomic coherence. During the storage time, atomic diffusion can change

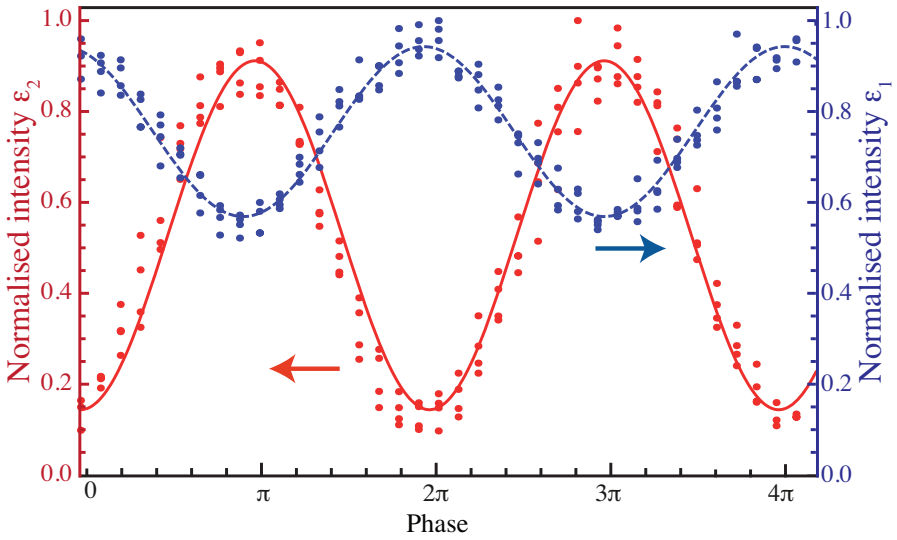

Figure 9.6: Interference fringes from transmitted (blue) and absorbed (red) part of light resulting from interference between double-Λ transitions created by the probe and steering pulses of different frequency stored simultaneously in the memory. The dashed blue and solid red lines are sinusoidal fits to the corresponding data. The red and blue data yield a fringe visibility of 73% and 25%, respectively.

the spatial mode of the coherence and as a result, the echo signal will have a slightly different mode compared to the input signal. This effect is negligible for shorter storage times. The presence of a transverse magnetic field can induce an extra spatial frequency (k_x and k_y) during storage. The transverse k vector is imprinted to the echo signal at readout, diverting the output optical field slightly from the steering pulse. In the beamsplitter analogy, this amounts to a poorly aligned interferometer. An inhomogeneous longitudinal magnetic field can alter the shape of the echo signal compared to its input leading to temporal mode mismatch. We anticipate, therefore, that visibility could be improved by increasing the buffer gas pressure or using a cold atomic sample in order to increase the time of flight of the atoms and taking extra care with the magnetic environment to prevent pulse deflection and distortion. For the time-domain interference, numerical simulations (see supplementary material) reveal that, in the limit of large OD, the interference visibility of the system can approach unity for both interfereometer outputs.

9.3 Summary

In summary, we have demonstrated interference effects between propagating optical fields and a collective atomic spin coherence. Fringe visibilities of 68% and 73% were observed for time-domain and frequency-domain interference schemes, respectively. These schemes may have relevance to manipulating optical quantum information. Unlike previous schemes, interference in a gradient echo memory could offer dynamic, optically addressable linear operations on optical qubits with little loss. These gates could operate on either time-bin or frequency multiplexed qubits or even a combination thereof. The time-delayed beamsplitter scheme can also be used for optical quantum state engineering [210, 211] and also for optimal Gaussian purification of coherent states from several imperfect copies [212]. The ability to construct this type of interferometer is also of interest in building a

coherent all-optical switch [213, 214, 215].

Chapter 10

Four-wave mixing in a double-Λ system under the GEM condition

Four-wave mixing (FWM) is a phenomenon in which interactions between three laser beams with different frequencies (non-degenerate FWM) results in the production of a fourth wavelength (conjugate), i. e. $\nu_4 = \nu_1 + \nu_2 - \nu_3$. FWM can also happen between three frequencies, i.e. $\nu_3 = \nu_1 + \nu_1 - \nu_2$. The latter phenomenon is called degenerate FWM.

Consider, for example, the double-Λ interaction scheme shown in Fig. 10.1 (a). With the pump interacting with $|1\rangle$ and the probe interacting with $|2\rangle$, a Raman transition is created. The pump field can also interact with $|1\rangle$ and as a result a Stokes field (conjugate beam) is produced to close the transition loop. The conjugate field is generated with the same polarisation as the probe. If the probe and pump enter the Λ-atomic system with a non-zero crossing angle, the conjugate beam will be spatially separated from the probe as is shown in Fig 10.1 (b). The output probe field is consequently amplified through the FWM process. It has been shown that the intensity difference between the probe and the conjugate is less noisy than the vacuum fluctuations [216]. To date more than 9 dB of relative intensity squeezing has been observed using the FWM process in a hot Rb vapour cell [217].

The presence of gain in the system causes a steep variation of the real part of susceptibility that modifies the group velocity of the probe propagating through the gain window. This makes it, in principle, possible to create delay lines and achieve fractional delays limited only by pulse broadening. The group velocity reduction effect due to nondegenerate four-wave mixing (FWM) in hot rubidium vapour has been studied previously [218]. Using this delay process, a tuneable delay of EPR entangled beams and images has been experimentally demonstrated [94].

In this chapter we investigate the interplay between the FWM coupling of the probe/conjugate and the Raman or EIT coupling of the probe/pump in a warm vapour cell.

10.1 FWM in double-Λ systems

Consider the interaction scheme depicted in Fig. 10.1 (a) where the pump Ω and probe $\mathcal{E}$ interact with the ground state $|1\rangle$ and metastable state $|2\rangle$ of an atom with hyperfine splitting Δ_{hf}. Both fields are on Raman resonance and are detuned from the excited states $|3\rangle$ by Δ. The pump also interacts with the other ground state and generates the Stokes field, $\mathcal{E}_s$. The second Λ transition is detuned from the excited state $|4\rangle$ by $\Delta' = \Delta + \Delta_{hf}$.

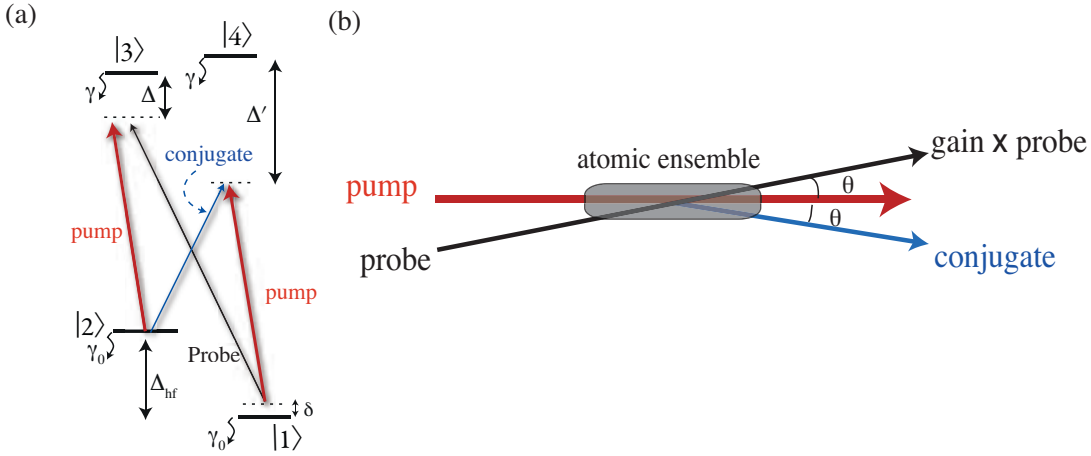

Figure 10.1: (a) Schematic interaction scheme of degenerate FWM in a double-Λ configuration. (b) Schematic setup showing propagation of the pump, probe and conjugate to/from the atomic ensemble.

The coupling strength for the latter interaction can be different from the former, due to different Clebsch-Gordan coefficients for different transitions. The interaction Hamiltonian of the system in a rotating frame is given by

$$\begin{aligned}\hat{H}/\hbar = &-(\delta+\delta_{ac})|2\rangle\langle 2| - (\delta+2\delta_{ac})|3\rangle\langle 3| - (\delta+2\delta_{ac})|4\rangle\langle 4| \\ &-[g\mathcal{E}|3\rangle\langle 1| + \Omega|3\rangle\langle 2| + g'\mathcal{E}_s|4\rangle\langle 2| + \Omega'|4\rangle\langle 1| + H.c.]\end{aligned} \tag{10.1}$$

The Maxwell-Bloch equations can therefore be written as follows

$$\frac{d\sigma_{21}}{dt} = (-\gamma_0 - i(\delta+\delta_{ac}))\sigma_{21} + i\sigma_{31}\Omega + i\sigma_{42}g'\mathcal{E}' \tag{10.2}$$

$$\frac{d\sigma_{31}}{dt} = (-\gamma - i\Delta - i(\delta+2\delta_{ac})\sigma_{31} + ig\mathcal{E} + i\Omega\sigma_{21} \tag{10.3}$$

$$\frac{d\sigma_{42}}{dt} = (-\gamma - i\Delta' - i(\delta+2\delta_{ac})\sigma_{41} + i\Omega' + ig'\mathcal{E}'\sigma_{21} \tag{10.4}$$

$$\frac{d\mathcal{E}}{dz} = i\frac{gN}{c}\sigma_{31} \tag{10.5}$$

$$\frac{d\mathcal{E}_s}{dz} = i\frac{g'N}{c}\sigma_{42} \tag{10.6}$$

where δ is the two-photon detuning between the pump and probe and the Stokes fields, $\delta_{ac} = \frac{\Omega^2}{\Delta}$ is the light shift (or ac Stark shift) induced by the pump field, and Ω' and $g'\mathcal{E}_s$ are the Rabi frequencies of the pump and Stokes fields interacting with the ground states $|1\rangle$ and $|2\rangle$, respectively. γ_0 and γ are the ground- and excited-state decay rates, respectively. In the regimes that we are studying here we can safely assume that $\Delta' \gg \gamma$, therefore we can adiabatically eliminate the excited state $|4\rangle$. This can be done by solving Eq. 10.4 in the steady state and replacing σ_{42} in Eq. 10.2.

Similar results can be obtained using the Floquet theory [219] to eliminate the fast oscillation of the system. Thus, the interaction Hamiltonian of the system in the rotating-frame [220] is given by

$$\hat{H}/\hbar = -(\delta+\delta_{ac})|2\rangle\langle 2| - (\delta+2\delta_{ac})|3\rangle\langle 3| \\ -[g\mathcal{E}|3\rangle\langle 1| + \Omega|3\rangle\langle 2| + \frac{g'\Omega'}{\Delta'}\mathcal{E}_s|2\rangle\langle 1| + H.c.] \tag{10.7}$$

The Maxwell-Bloch equations of motion in both cases can be simplified as

$$\begin{aligned} \frac{d\sigma_{21}}{dt} &= -\Gamma_0\sigma_{21} + i\sigma_{31}\Omega + i\frac{g'\Omega'}{\Delta'}\mathcal{E}_s\sigma_{14} \\ \frac{d\sigma_{31}}{dt} &= -\Gamma\sigma_{31} + ig\mathcal{E} + i\Omega\sigma_{21} \\ \frac{d\mathcal{E}}{dz} &= i\frac{gN}{c}\sigma_{31} \\ \frac{d\mathcal{E}_s}{dz} &= i\frac{g'\Omega'}{\Delta'}\frac{N}{c}\sigma_{21} \end{aligned} \tag{10.8}$$

where

$$\Gamma_0 = (\gamma_0 + i(\delta+\delta_{ac})) \tag{10.9}$$

$$\Gamma = (\gamma + i(\Delta+\delta+2\delta_{ac})). \tag{10.10}$$

In the following section we solve Eqs. 10.8 and analyse the behaviour in EIT and Raman echo systems.

10.2 FWM and EIT in a dense atomic sample

When the Λ transition created by the probe and pump is resonant with the excited state, $\Delta = 0$, the system undergoes electromagnetically induced transparency where the probe beam is transmitted through the EIT window with a reduced group velocity. In high optical density regimes, EIT can be accompanied by FWM of the pump and the Stokes field that will strongly affect the probe pulse propagation. The FWM phenomenon in EIT systems was first studied in Ref. [221] and experimentally observed later in cold [222] and warm [195, 223] atomic samples. It was shown that FWM in EIT can limit the storage efficiency at higher optical depths [224]. While non-classical correlations between the signal and Stokes fields can individually carry quantum information [225] and produce entangled images, it was shown that any information originally encoded in a seeded Stokes field is not independently preserved during the storage process [220]. The conversion of the signal field into the Stokes field may reduce the read-out efficiency [226]. However, under certain conditions, FWM may lead to gain in both the signal and Stokes fields, which could compensate for any optical losses [227] that can also result in excess noise.

To investigate the problem quantitatively, we consider the interaction of σ^+ polarised light (for the probe and pump) with the D1 transition line of an ensemble of ^{87}Rb atoms. In this case, $\Omega' = -\sqrt{3}\Omega$, $g' = -1/\sqrt{3}g$ due to the Clebsch-Gordan coefficient and $\Delta_{hf} = 2\pi 6.8$ GHz. Under EIT conditions, Eqs. 10.8 can be analytically solved [223, 228] and the amplitude of the probe and Stokes fields at the output of the medium, when the two-photon detuning is chosen such that the light shift is canceled, can be approximately written as

$$|\mathcal{E}| = \mathcal{E}(z=0)|e^{2i\alpha L} - r\frac{\Omega^2}{\Delta_{hf}\delta}(1-e^{2i\alpha L})|$$
$$|\mathcal{E}'| = \mathcal{E}(z=0)|\frac{\Omega^2}{\Delta_{hf}\delta}(1-e^{2i\alpha L}) - r| \tag{10.11}$$

where $\alpha = \frac{d\gamma\Gamma_0}{\Omega^2+\Gamma\Gamma_0}$ is the absorption coefficient, $d = \frac{g^2N}{\gamma c}$ is the linear optical density of the medium, and $r = \frac{\mathcal{E}_s(z=0)}{\mathcal{E}(z=0)}$ is the ratio of the seeded signal field to the probe field.

The presence of the Stokes field strongly affects the signal pulse propagation, and the propagation of both the signal and the Stokes fields is determined by the interplay of EIT and FWM processes.

We note here that the amplification observed in EIT systems is further enhanced due to the additional seeded Stokes field. In this case, it is the Stokes field generated via stimulated emission that results in the amplification of the signal field. This effect is shown in Fig. 10.2 where the amplitude of the probe and Stokes fields for different optical densities , $OD = g^2NL/\gamma c$, and input seed signals is plotted. For large OD (Fig. 10.2(b) and (c)) the interference and amplification of the EIT line is apparent. To precisely calculate the EIT lines, we numerically solve Eqs. 10.8 assuming a pressure broadening of $\Gamma_p = 290$ MHz that can be induced by 30 Torr of Ne buffer gas (consistent with the experimental condition in Ref. [195]). It is worth emphasising that gain due to FWM in an EIT medium is significant because the probe transmission is enhanced on two-photon resonance, where the maximum gain occurs.

10.3 FWM and Raman absorption in a dense atomic sample

With high OD, FWM phenomenon can also be observed in a GEM. We consider the level scheme shown in Fig. 10.1 (a) to derive the equations of motion. Assuming a linearly varying two-photon detuning $\delta(z) = \eta z$ and a far-detuned Raman transition, $\Delta \gg \gamma$, we can arrive at the following equation for the probe ($\mathcal{E}$) and Stokes ($\mathcal{E}_s$) fields at the centre frequency

$$\frac{\partial}{\partial z}\begin{pmatrix}\mathcal{E}(z)\\ \mathcal{E}_s^*(z)\end{pmatrix} = ia_0\begin{pmatrix}a_{11} & a_{12}\\ a_{21} & a_{22}\end{pmatrix}\begin{pmatrix}\mathcal{E}(z)\\ \mathcal{E}_s^*(z)\end{pmatrix} \tag{10.12}$$

where

$$\begin{aligned} a_0 &= \frac{N}{\gamma c(\Omega^2+\Gamma\Gamma_0)}\\ a_{11} &= ig\Gamma_0\\ a_{12} &= a_{21} = -\frac{g'\Omega\Omega'}{\Delta'}\\ a_{22} &= -i\Gamma\frac{g'\Omega'^2}{\Delta'^2} \end{aligned} \tag{10.13}$$

and

$$\begin{aligned} \Gamma_0 &= (\gamma_0 + i\delta)\\ \Gamma &= (\gamma + i(\Delta+\delta)) \end{aligned} \tag{10.14}$$

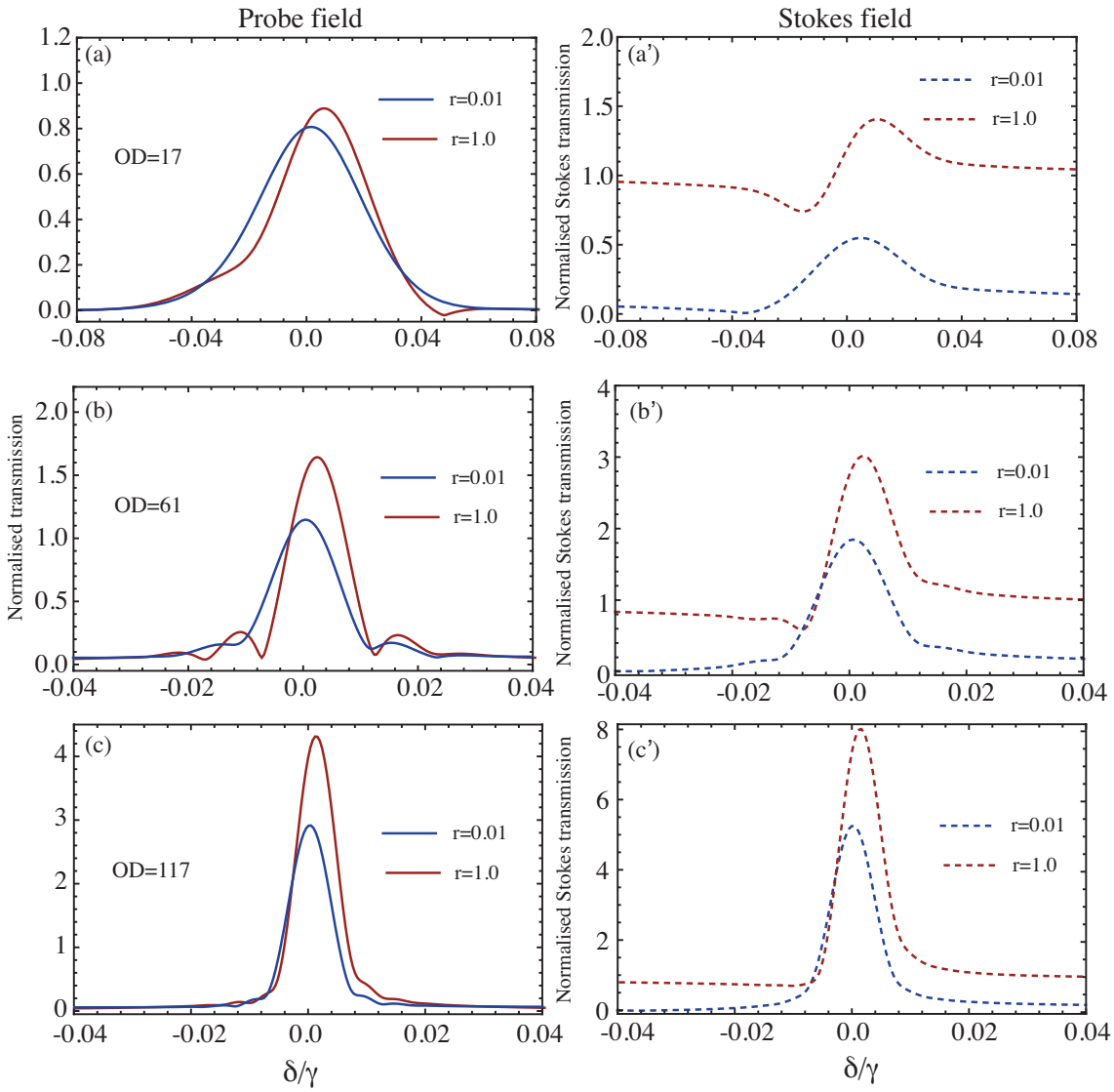

Figure 10.2: Transmitted amplitude of the probe and Stokes fields normalised to the input probe amplitude for OD=17, (a) and (a′), OD=61, (b) and (b′) and OD=117, (c) and (c′) . Parameters used for these numerical simulations are: $\Gamma_p = 25\gamma$, $\gamma_0 = 0.002\gamma$, $\Omega = 1.6\gamma$, $r = 1, 0.01$.

The susceptibility matrix elements $a_0 a_{ij}$ were obtained by solving Eqs. 10.8 in steady state. We solve these equations numerically in different regimes to understand the contribution of the FWM process in a Raman absorptive medium.

We first consider an atomic system similar to what was described above for an EIT scheme, i.e. a warm ^{87}Rb vapour cell mixed with 30 Torr of Ne buffer gas. In such high buffer gas pressures, one can neglect the Doppler effect due to Dicke narrowing [229, 160, 160]. At room temperatures, the collisional broadening for Rb-Ne is $\Gamma_{col}^{Rb-Ne} =$ 9.84 MHz/Torr [161] and, therefore, one must take into account the buffer gas-induced pressure broadening instead.

Figure 10.3 shows the calculated transmission of the probe and Stokes fields for two different values of resonant OD= $g^2 NL/\gamma c$ and two different values of the initial Stokes field amplitude, parameterized by $r = \mathcal{E}_s(z = 0)/\mathcal{E}(z = 0)$. In our experiment, a non-

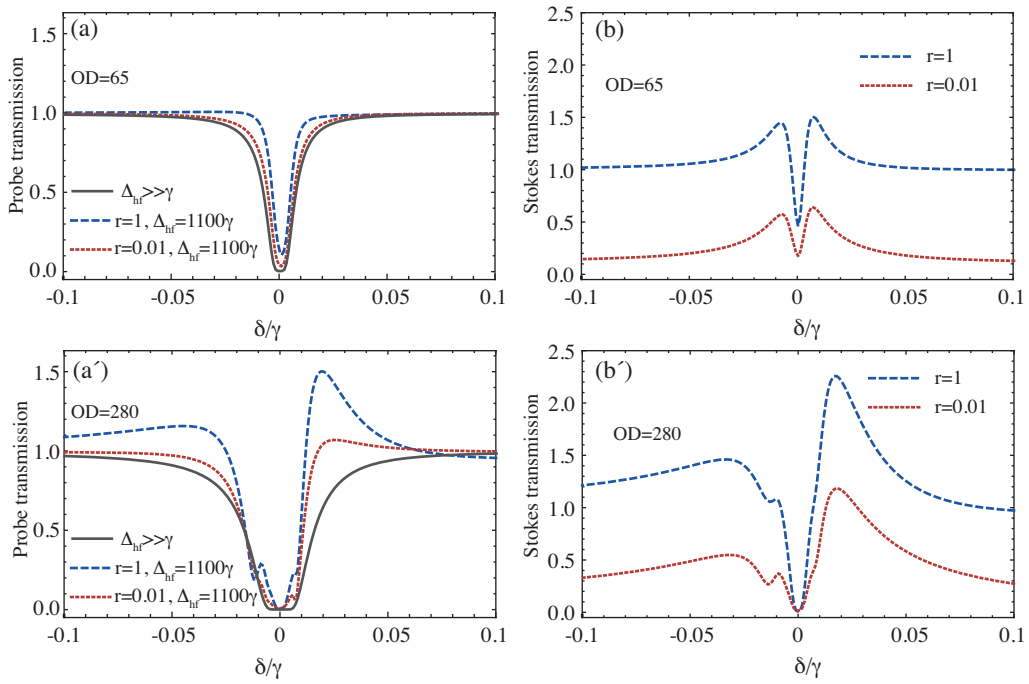

Figure 10.3: Transmitted amplitude of the probe, (a) and (b), and Stokes fields, (a′) and (b′), normalised to the input probe amplitude. Parameters used for this numerical simulation are: $\Gamma_p = 4\gamma$, $\gamma_0 = 0.002\gamma$, $\Omega = 3\gamma$, $OD = g^2NL/\gamma c = 65, 280$, $r = \frac{\mathcal{E}_s(z=0)}{\mathcal{E}(z=0)} = 1.0, 0.01$ and $\Delta = 200\gamma$.. By assuming $\Delta_{hf} \gg 1$ we can effectively switch off the FWM process.

zero Stokes seed is a possibility. The probe field is formed by one sideband of a phase modulation that is filtered by one or more resonant cavities. If the leakage of these cavities is too high, the other sideband of the phase modulation can form a Stokes seed. It can be seen that for large OD, probe amplification occurs around the edges of the Raman line. The results show that 4WM amplification of the probe can be suppressed by minimizing the seed light of the Stokes field (making r small) and by using an atomic system where $\Delta_{\mathrm{hf}} \gg \gamma$. The amplitude of the Stokes field, as well as the gain, is also substantially reduced at the point of maximum probe absorption. The Stokes field is also absorbed around two-photon resonance. FWM inside a vapor cell at 140°C has been experimentally investigated in a detuned double-Λ configuration (with $\Delta = 150\gamma$) [218], where the maximum gain was observed 20 MHz away from the Raman resonance. In a dense atomic medium and at Raman resonance, the competition between large amplification and large absorption leads to complex dynamics which can result in a breakup of the probe pulse. The interference between the probe and Stokes transition can be seen in Fig. 10.3(b)

10.3.1 Polarisation effects on FWM

Using linear polarisation instead of $\sigma^{\pm}$ polarisation can significantly enhance the FWM process in a Rb vapour cell. Linear polarisation is treated by the atoms as a superposition of left and right circular polarisation and will therefore interact with multiple excited state sublevels, as shown in Fig. 10.4. This will effectively increase the atom-light coupling that enhances the non-linear process of FWM. Fig. 10.5 (a) shows the results of numerical calculations for the transmitted probe and Stokes signals for two different ODs at a buffer

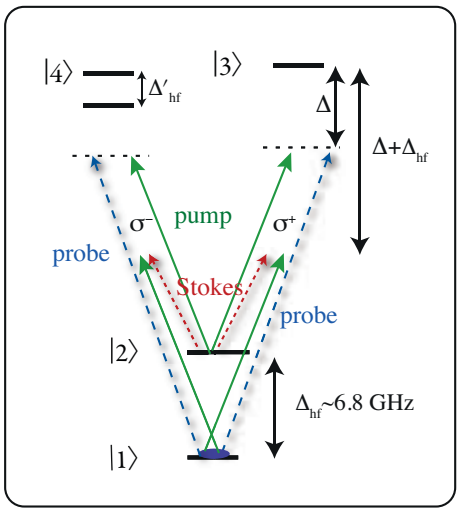

Figure 10.4: Schematic picture of the Rb level structure and possible optical transitions that can result into FWM. Blue arrows represent the signal field with a Rabi frequency of Ω_p and green arrows represent coupling field beams with a Rabi frequency of Ω_c. The red dashed arrows are Stokes photons generated via the FWM process (Ω_s). Right and left circular polarisations are show as σ^+ and σ^-. The two lower and upper hyperfine states are shown as F_g and F_e, respectively.

gas pressure of 0.5 Torr. The experimental results of broadened Raman lines for various coupling field powers and temperatures have also been shown in Fig. 10.5 (b). We note here that, in the experiment configuration, all of the beams are co-propagating together and therefore the phase matching condition is satisfied for FWM process. However, the Raman gain can be suppressed if the two Λ transitions destructively interfere. The phase of the seeded Stokes field in the experiment is not controlled and we believe that the observed gain is largely due to the vacuum seed. In our model, however, we consider phase of the seeded Stokes field such that the gain is maximal.

These experimental results were obtained using a 20 cm gas cell containing ^{87}Rb and 0.5 Torr of Kr buffer gas, while the coupling and probe signal fields have orthogonal linear polarisations. A mode cleaner cavity (with a finesse of ∼100) was used after a fibre-coupled EOM to reject the seed Stokes field. The measurement was performed using heterodyne detection. The results calculated in Fig. 10.5 (a) are obtained assuming a zero crossing angle between the pump and probe.

Using circular polarisation, however, we observed maximal absorption of the probe while the gain was negligible. Fig.10.6 shows the heterodyne signal for the broadened Raman line and, as can be seen, significant absorption without gain can be obtained in this regime. This result was obtained by using two mode-cleaner cavities for the probe beam that suppress the seed signal by a factor of 10^4 ($r = 0.01$). Using a similar setup we demonstrate in Chap. 12 that storage can be noiseless and efficient [230]. In the following section we discuss the angular dependency of the FWM process.

10.3.2 Angular dependency of FWM in a Doppler broadened medium

To include the Doppler effect in our model, similar to what was described in Chap. 4, we have numerically integrated Eqs. 10.12 over different atomic velocity classes, by utilising Eqs. 4.33-4.37.

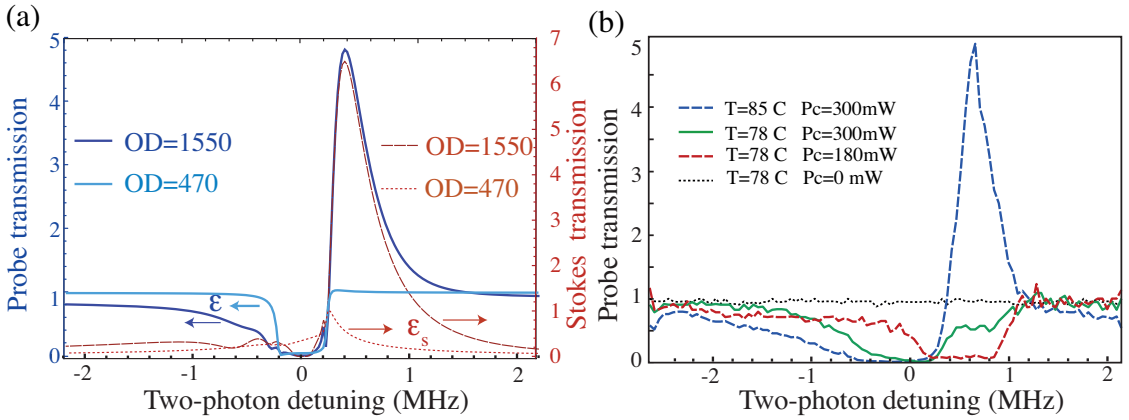

Figure 10.5: (a) Transmitted amplitude of the probe and Stokes fields normalised to the input probe amplitude. Parameters used for these numerical simulations are: $\gamma_0 = 0.002\gamma$, $\Omega = 3$ and 5.2γ, $g^2NL/\gamma c = 470, 1550$, $r = 0.01$, $\Delta = 200\gamma$ and $\eta L = 0.08\gamma$, $T = 85^o$ C. (b) Experimental measurements of the probe transmission for various temperatures and coupling field powers obtained using linear polarisation. Absorption is maximum at a non-zero two-photon detuning because of the DC offset magnetic field.

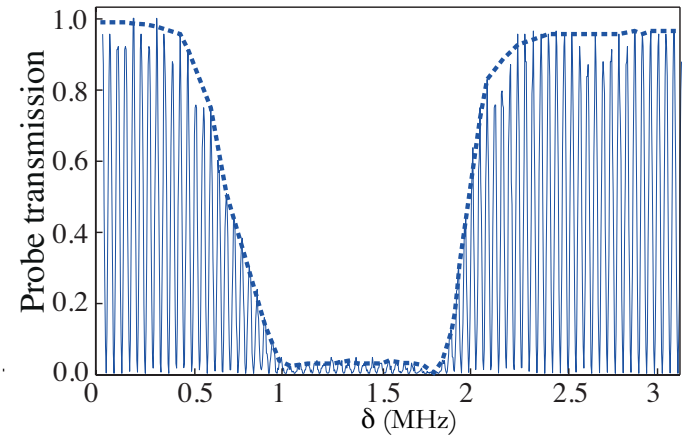

Figure 10.6: The heterodyne signal showing the broadened Raman absorption line for the same circular polarisation of the pump and probe fields with pump power of 350mW. The probe power in all cases was ∼1 μW. The envelope shown is a visual guide.

Increasing the angle between the pump and probe field increases the residual Doppler broadening in a warm atomic medium.We numerically calculate the probe and Stokes field amplitude for a non-zero crossing angle using Eqs. 4.33-4.37. Fig. 10.7 (a) and (b) shows the transmitted amplitude of the probe and Stokes field, respectively, for three different crossing angles. As can be seen, the amplification is substantially reduced after a 0.5 mrad misalignment between the probe and pump.

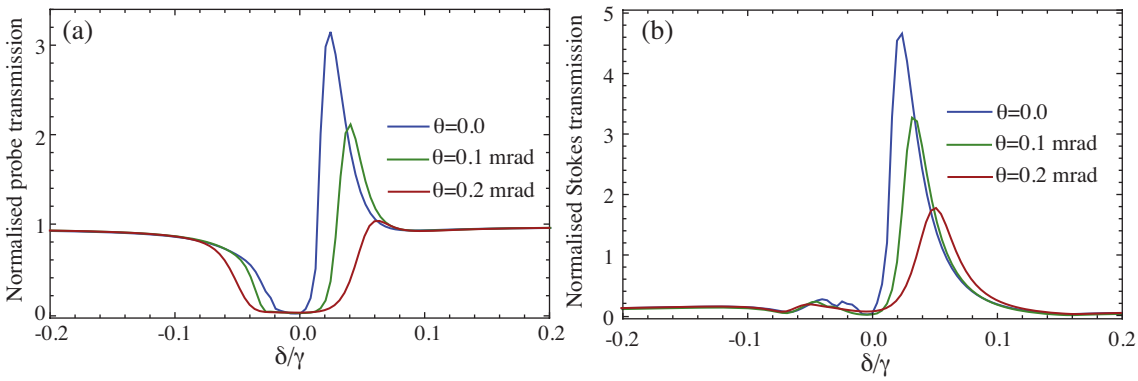

Figure 10.7: Transmitted amplitude of (a) the probe and (b) Stokes fields, normalised to the input probe amplitude for different angles between the pump and probe. Parameters used for this numerical simulations are: $\gamma_0 = 0.002\gamma$, $\Omega = 4\gamma$, $g^2NL/\gamma c = 1547$, $r = 0.01$, $\Delta = 200\gamma$, $\eta = 0$ and $T = 85^oC$

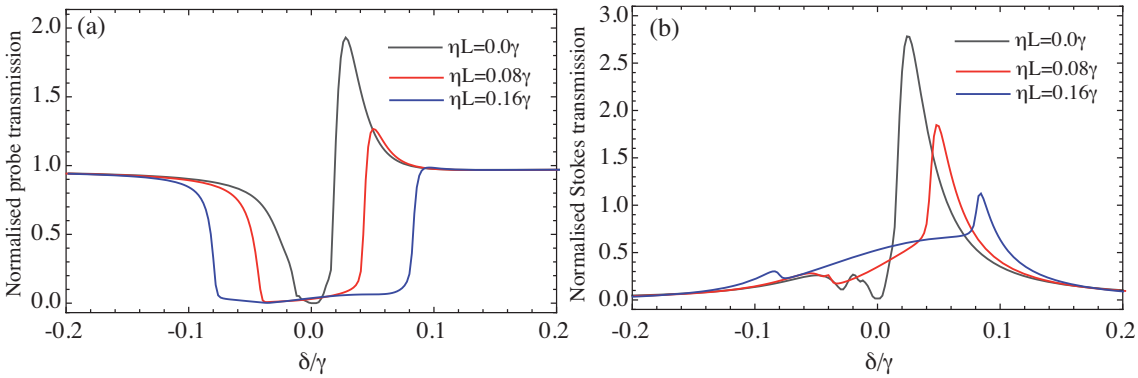

Figure 10.8: Transmitted amplitude of (a) the probe and (b) Stokes fields, normalised to the input probe amplitude for different broadening. Parameters used for this numerical simulations are: $\gamma_0 = 0.002\gamma$, $\Omega = 2\gamma$, $OD = 1114$, $\Delta = 200\gamma$, $r = 0.01$, $\eta L = 0, 0.08\gamma, 0.16\gamma$ and $T = 80^oC$

10.3.3 The effect of inhomogenous broadening on FWM

As previously stated, strong absorption of the probe signal close to the two-photon resonance at high ODs significantly reduces the gain and the generated Stokes field. In a GEM system, applying inhomogenous broadening is necessary for the storage and recall of light. Applying the detuning gradient increases the absorption bandwidth for the probe and therefore widens the region around the two-photon resonance in which gain is substantially suppressed and the memory can operate noiselessly [230]. Fig. 10.8 shows the results of numerical calculations for the transmitted probe and stokes fields in an inhomogenously broadened medium with various broadening. In regimes with large ODs, applying a gradient does not noticeably reduce the maximum absorption of the probe. The broadening does, however, strongly suppress the gain and generated Stokes field.

One signature of the Raman gain mechanism is that gain for negative pump detuning ($\Delta < 0$) is obtained for a signal frequency below the pump frequency ($\delta < 0$) and vice vera. This is explained by the fact that the Zeeman sublevel most shifted by light is also the most populated [231, 232].

We calculate the total amplitude of the Stokes field around the two-photon resonance and 0.04γ from the resonance (where the amplification is maximum) for different optical depths in an inhomogenously broadened medium. As can be seen in Fig. 10.9(a) and (b), the amplitude of the probe and of the Stokes field around the two-photon resonance, $\xi(\omega_0 = 0) = \int_{-\delta}^{\delta} \mathcal{E}(\omega - \omega_0)d\omega$, rapidly decreases as the optical depth of the medium is increased. However, 0.04γ away from the resonance the probe and Stokes amplitude, $\xi(\omega_0 = 0.04\gamma) = \int_{-\delta}^{\delta} \mathcal{E}(\omega - \omega_0)d\omega$, increase with OD.

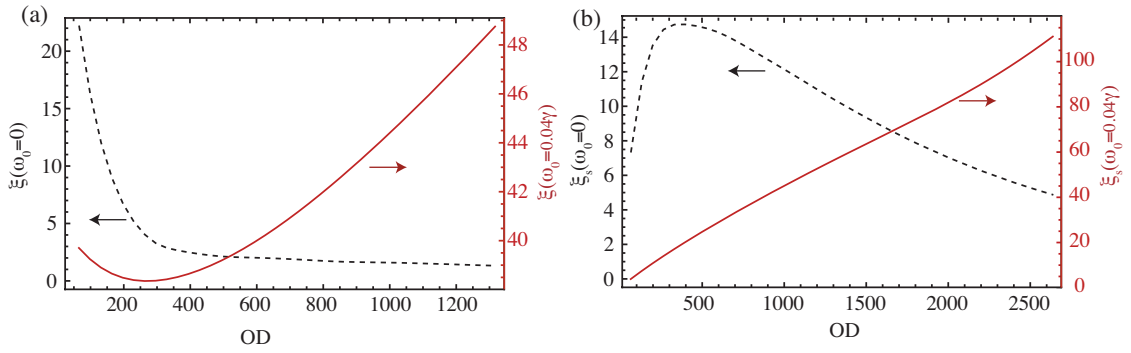

Figure 10.9: Total (a) probe and (b) Stokes amplitude within a frequency window of $2\delta = 0.04\gamma$ around zero two-photon detuning (dashed black line) and $\omega_0 = 0.04\gamma$ away from the two-photon resonance (solid red line) calculated for different ODs. Both axes are normalised to the input probe amplitude. Parameters used for this numerical simulation are: $\gamma_0 = 0.002\gamma$, $\Delta = 200\gamma$, $\Omega = 3\gamma$, $r = 0.01$, $\eta L = 0.08\gamma$.

The significant reduction of the Stokes field around the centre of the Raman line (Fig. 10.9 (b), black dashed line) at large ODs indicates a large suppression of the FWM process and therefore lack of amplification in that region. The situation is reversed in the dense EIT medium we initially investigated, where the probe transmission was enhanced.

We conclude by noting that in a dense atomic system it is feasible to build a memory based on the inhomogenously broadened Raman absorption that can reach close to unity efficiency while the noise and amplification due to the FWM process remains low. This result suggests that the Λ-GEM system, as has been experimentally demonstrated previously, provides efficient and noiseless storage of optical information and therefore is a good candidate for quantum information storage applications.

Part III
Optical Quantum Memory

Chapter 11

Introduction to Quantum Information Technology

"So I hope you accept Nature as She is - absurd."

Richard Feynman

The ability to coherently manipulate the quantum properties of a system allows one to treat information in a fundamentally different way. This ability can potentially provide the means for secure transmission of information or an efficient solution to computational problems for which no efficient classical algorithm is known.

Current information technology is based on classical algorithms and binary encoding. Computers that use this type of technology will soon come up against physical limitations in terms of size and speed. The integration of quantum physics and information technology is one way to keep pushing this technology forward in the future. In this chapter we introduce some basic concepts of quantum computing and information technology and discuss their potential realisation in particular systems.

11.1 Quantum Information Technology

Quantum information technology promises to revolutionise communication and computation technology in the future. Extensive research has been dedicated to this area of physics around the world and, to date, astonishing proof-of-principle experiments have been demonstrated to support the future development of such technology.

There are numerous problems that scale poorly on classical computers. As the size of the problem increases, the execution time scales exponentially. Examples include factorisation [233], travelling salesman problems [234] and database searches [235]. Quantum computers allow these problems to be solved in polynomial time [236].

According to Moore's Law, the fastest processor on the market doubles in speed about every 18 months, and typical memory capability in electronic equipment shows a similar exponential growth. This is because as electronic components get smaller they work faster. The closer electronic components can be packed on a silicon chip, the less time is required to communicate between components. Eventually, silicon will encounter practical problems, such as insulating oxide layers becoming too thin, conducting tracks becoming too narrow and transistor operations being subject to shot noise as the number of electrons becomes too small. Even if all these practical difficulties can be overcome, we will run into physical barriers.

The fundamental building blocks of matter do not behave in the same way as macroscopic or even microscopic pieces of matter; in fact they can exhibit explicit effects of

quantum mechanics. Quantum computing exploits these quantum effects, rather than trying to fight them. This technology, if realised, will revolutionise future communication and computation technology. Quantum physics offers powerful methods of encoding and manipulating information that can lead to secure communication, rapid integer factoring, and quantum simulation.

In this section we start with an overview of some important concepts of quantum theory that are applied to quantum information technology.

11.1.1 The quantum bit

The fundamental resource and basic unit of quantum information is the quantum bit (qubit), which behaves like a classical bit enhanced by the superposition principle. From a physical point of view, a qubit is represented by an ideal two-state quantum system. After measurement, the qubit is projected into a single state (classical bit), but before measurement, it is in a continuum of states and this is a main strength of quantum information. Examples of such systems include the superposition of photons with vertical and horizontal polarisation, electrons and other spin 1/2 systems (spin up and down), and systems defined by two energy levels of atoms or ions. The two-state system plays a central role in studies of quantum mechanics. It is the most simple quantum system, and in principle all other quantum systems can be modelled as a collection of qubits. A qubit can be represented as a Bloch vector in a Bloch sphere as shown in Fig. 11.1. Any point on the Bloch sphere represents a qubit with different complex probability amplitudes.

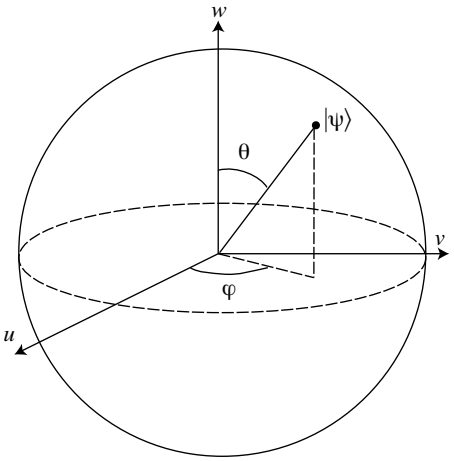

Figure 11.1: Qubit representation on the Bloch sphere

11.1.2 Quantum gates

Quantum gates are necessary for processing qubits. Like the classical NOT gate, applying the quantum NOT gate to a bit, for instance, has the effect of flipping the state of the bit. The quantum version of the NOT gate exchanges the two logical states $\alpha|0\rangle + \beta|1\rangle \rightarrow \alpha|1\rangle + \beta|0\rangle$. Other examples of quantum gates are Hadamard and Controlled-NOT(CNOT) gates. The Hadamard gate turns state $|0\rangle \rightarrow \frac{1}{\sqrt{2}}/(|0\rangle + |1\rangle)$ and $|1\rangle \rightarrow \frac{1}{\sqrt{2}}/(|0\rangle - |1\rangle)$. The CNOT gate flips the second qubit if and only if the first qubit is set to 1.

A Fredkin gate is a three-bit universal reversible gate, whose truth table is shown in Fig. 11.2 (a). The implementation of a quantum Fredkin gate as a universal gate is

(a)

a	b	c	a´	b´	c´
0	0	0	0	0	0
0	0	1	0	0	1
0	1	0	0	1	0
0	1	1	0	1	1
1	0	0	1	0	0
1	0	1	1	1	0
1	1	0	1	0	1
1	1	1	1	1	1

(b)

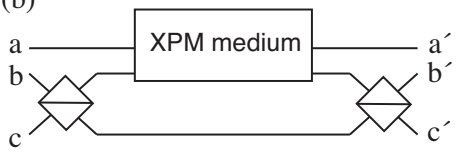

Figure 11.2: (a) The truth table of a Fredkin gate. (b) The optical circuit diagram for the implementation of a Fredkin gate using a nonlinear medium.

(a)

a	b	a´	b´
0	0	0	0
0	1	0	1
1	0	1	1
1	1	1	0

(b)

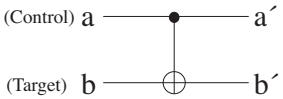

Figure 11.3: (a) The truth table and (b) circuit representation of a CNOT gate.

possible using Kerr-nonlinearity [237]. The optical circuit diagram of such a gate is shown in Fig. 11.2 (b) where a nonlinear Kerr medium is used to apply a cross phase modulation (XPM) on the input "a". One can generate the Bell states with a Hadamard gate and a CNOT gate as shown in Fig. 11.4. The first qubit is passed through a Hadamard gate and then both qubits are entangled by a CNOT gate.

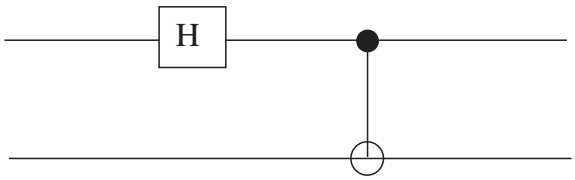

Figure 11.4: A diagram representing the simple operation needed to create Bell states using a Hadamard and a C-NOT gate.

11.1.3 Quantum computation

The rapidly growing field of quantum computing has attracted considerable interest since the work of Deutsch (1985) [238], Shor [236] and Grover [239]. A quantum computer, if one

day realised, is expected to perform certain tasks that are far beyond the power of todays classical machines. Deutsch showed how quantum information and quantum entanglement can be used to find a global property of an operation which would classically take two steps. Peter Shor in 1994 [236] formulated a framework in which the integer factorisation problem (finding prime factors of an integer N) could be efficiently solved on a quantum computer by harnessing quantum entanglement.

To date, there have been various proposals for the implementation of such computing devices. Amongst these proposals, devices based on trapped ions [240, 241, 242], electron spins, nuclear spins [243], and superconducting qubits [244] show great promises. Proof-of-principle experiments have also been accomplished, demonstrating operational quantum devices at small scales. For instance, a quantum computing device based on nuclear magnetic resonance (NMR) and using spins of nuclei in molecules as qubits has been demonstrated [245, 246]. In this case, the two qubit states were the two spins (up and down) of the nuclei in a magnetic field. NMR computing, however, seems limited to systems of less than ten-qubits, while it appears that a quantum computer that could factor a 2048-bit key would need to have at least 10^6 qubits [247]. It was shown that 30-40 qubits would suffice to perform quantum simulations of multidimensional fermionic systems [248]. A variety of solid state concepts applied to realise quantum computing devices that work based on the phenomena of superconductivity have been demonstrated [249, 243, 250, 251, 252]. Short surveys of these have been presented by Mooij (2005) [253] . Fig. 11.5 shows a few different experiments demonstrating the implementation of nano-fabricated devices for quantum information applications.

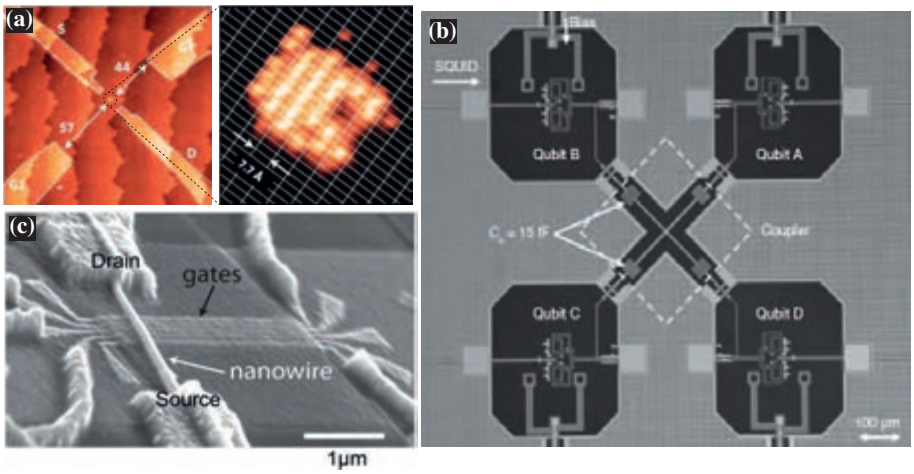

Figure 11.5: (a) An STM image of a four-terminal quantum dot device with source (S) and drain (D) leads and two in-plane gates (G1, G2). The close-up image of the central dot, on the left, showing the number of desorbed silicon dangling bonds in the dot area. Picture taken from Ref. [254]. (b) A photomicrograph of four superconducting phase qubits, fabricated with aluminium (light areas) on a sapphire substrate (dark areas). The coupler is the cross-shaped structure in the centre. The entire sample is mounted in a superconducting aluminium box and cooled to 25mK. Picture taken from Ref. [255]. (c) An SEM image of the nanowire device with gate electrodes used to electrically control qubits, and source and drain electrodes used to probe qubit states. (Image: Kavli Institute of Nanoscience at the Delft University of Technology)

Despite the progress made in the field of quantum computing, the implementation of a large number of qubits has not yet been realised, and there are many difficulties still

facing the implementation of such systems.

Scalability is perhaps the most difficult task ahead. For instance, the major difficulty with spin-based implementations of quantum computing is that they require the measurement and control of single electron spins or nuclear spins, a task that is only now on the threshold of realisation. Scalable spin-based quantum computing will probably require the development of new technologies in which single atoms can be accurately positioned to create devices with the precision necessary for quantum computation. Fortunately, several promising approaches to the fabrication of these single-atom devices are currently being explored [256].

11.1.4 Quantum communication

The fundamental difference between quantum and classical information is that cloning and measuring an unknown quantum state is impossible (due to the no-cloning theorem [21]). In general, for quantum information there is no information gain without disturbance. This fundamental difference is the basis of the application of quantum information to cryptography and secure communication.

Quantum cryptography

There are quantum protocols that Alice and Bob can exploit to share a secret random key, which they can then use to communicate privately. This is known as "quantum cryptography" [22, 257]. These protocols involve the exchange of classical and quantum information so that any attempt by an eavesdropper, Eve, to monitor the communication between Alice and Bob will be, in principle, detectable. This is because Eve cannot gain any quantum information without disturbing or adding detectable noise to the quantum communication channel. Moreover, the no-cloning theorem prohibits Eve from copying the quantum information and processing it off-line.

Quantum repeaters

Quantum communication in free space or through optical fibres is currently limited to about 100 km, due to loss and channel noise [258]. Quantum error correction can be used to protect the quantum information against noise. This requires error correction to be performed before the influence of noise exceeds about 1% [259]. For this, the error correction needs to be done at intermediate local nodes. However, the acceptable error rates for local operations are far below achievable accuracies with current technology.

The alternative approach for long-distance quantum communication is the *quantum repeater*[260]. The main function of a quantum repeater is *entanglement purification*, i.e. quantum teleportation [261, 262], and *entanglement swapping*. Entanglement swapping can be obtained, for instance, if one photon from an entangled pair is teleported between two nodes. The general idea consists of first establishing entanglement between "not-too-distant" nodes, then teleporting the entanglement from one node to the next. However, quantum processing, like entanglement swapping, is probabilistic in nature and entanglement between all of the nodes can not be established all at once. For this reason, quantum memories are an essential part of quantum repeaters to store entanglement once generated. The general principle is illustrated schematically in Fig. 11.6. A generic quantum repeater consists of $2^N + 1$ distinct nodes.

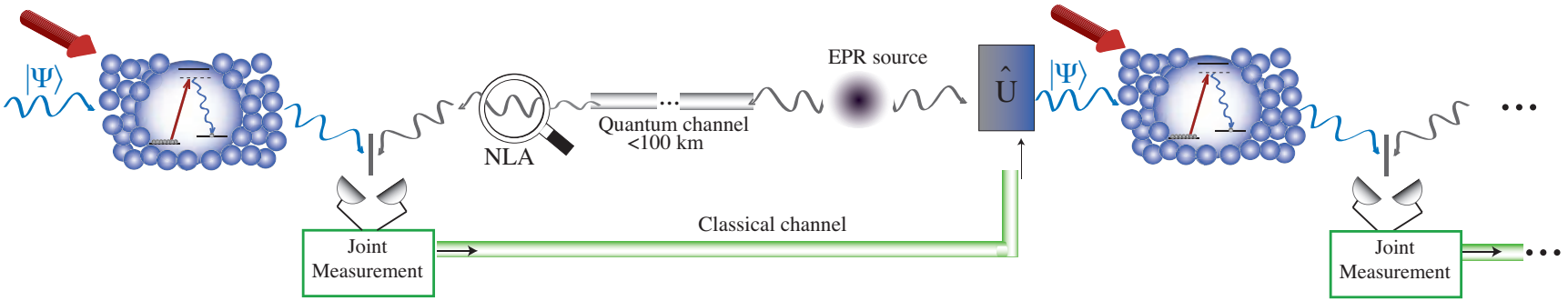

Figure 11.6: General principles of an idealised quantum repeater. Initially, entanglement is generated between neighbouring repeater stations, separated by L_0, consisting of quantum memories where the quantum state to be transferred is stored until measurement is performed. A noiseless linear amplifier (NLA) is also needed to distill the entanglement after propagation through a long channel. This entanglement connection is repeated subsequently between other nodes until the terminal quantum memory elements, separated by $L = 2^n L_0$, are entangled

The first step of the process generates entanglement between adjacent memory elements in successive nodes with probability P_0 . An entanglement connection process then extends the entanglement lengths from L_0 to $2L_0$ by means of a Bell measurement, for instance. Successful entanglements are stored in quantum memories. This entanglement connection succeeds with probability P_1 , followed by subsequent entanglement-length doublings with probabilities $P_2, ..., P_n$, until the terminal quantum memory elements, separated by $L = 2^n L_0$, are entangled.

There are several approaches to quantum repeaters including protocols based upon photon storage in atomic ensembles [136] and a scheme that uses solid-state photon emitters as the intermediate nodes of the channel [263]. Proof of principle demonstrations of the DLCZ technique has been demonstrated by different groups [138, 143, 140]. The development of a fully operational quantum repeater is a grand challenge for quantum communication and there has been progress in this field. To date, however, there has been no demonstration of such a device. We note that the implementation of a quantum memory is not only useful for quantum repeaters, but also for quantum computation.

Quantum memory criteria

To date there have been many impressive demonstrations of quantum state storage in various systems including cold atomic ensembles [264, 91, 265, 266], rare-earth ions in solid state systems [149, 130, 129], and ensemble of Rb atoms in the gaseous state [267, 268, 78, 269] to store quantum states of light. So far, the different approaches have been motivated by the degree of freedom chosen to encode the quantum state. These and many more approaches are now being actively pursued within international collaborative programmes around the world. In Chap. 3, we reviewed some of the work that has been done towards the implementation of a quantum memory in various systems. In the next chapter, we present noise measurement results and discuss the quantum properties of the GEM system.

Here we discuss the key criteria of a quantum memory and their relevance for different applications and implementations [270].

Fidelity. The precise operational meaning of fidelity depends on the specific application. For memories that store single photons, the fidelity is defined as the overlap between the input single-photon wave packet and the one that is recovered from the memory. This fidelity is conditioned on the detection of the photon. If the efficiency of the memory is low, it will reduce the rate at which information can be stored but it is still possible to achieve high fidelity storage.

For memories that are meant to store general states of light, conditional fidelity is not an appropriate concept, and one has to consider unconditional fidelities. This can be measured by overlap between the input and output states. An unconditional quantum memory can be used for information storage in either discrete or continuous variable regimes.

A quantum memory should be able to store information with a fidelity of more than 0.5, which is the classical fidelity limit. Both loss and noise can affect the unconditional fidelity. The conditional or unconditional fidelity benchmark depends on the physical system and application. Fidelities greater than the classical fidelity have been observed both in DV [130, 91] and CV [100, 230] regimes.

Efficiency. While high-recall efficiency is clearly desirable, it is not always necessary to be very close to 100 % for the memory to be useful, for example, in proof-of-principle

demonstrations of quantum memories. The conditional fidelity can be high even if the memory is a few percent efficient. However, for most applications, such as teleportation of an unknown state or fast quantum repeaters, whether in DV or CV regimes, high efficiency storage is required. Therefore, it is fair to say that the combined fidelity times efficiency must be higher than the classical limit (0.5).

To date, maximum classical efficiencies of 43% using EIT[195], 35% using AFC[128], 69% using 2-level GEM [149], 30% using Raman memory [102], and 87% using Λ-GEM have been achieved [156].

Storage time. In the context of quantum repeaters, the memory time should be longer than the time required for the generation of long distance entangled pairs. The time to generate long-distance entangled pairs on an intercontinental scale has been estimated to be on the order of seconds [271]. This imposes a lower bound on the storage time of a realistic quantum memory. A quantitative study of the effect of storage time limitations was recently performed in Ref. [272].

The coherence time in cryogenically cold crystals [90], cold atomic gases [273], and even in warm vapour cells [168, 169] is proven to reach seconds.

Bandwidth. Again the required bandwidth depends on the desired application. For quantum repeater applications, the memory bandwidth can be just as large as the source bandwidth. In general, the memory bandwidth determines the achievable repetition rates, and also the multiplexing potential.

Using the AFC technique in a thulium-doped lithium niobate waveguide a memory bandwidth of 5 GHz[130] has been observed. Implementation of the Raman memory in a warm vapour cell was also demonstrated with GHz bandwidth [102].

Multimode capacity. The capacity to store several modes is a natural capability for certain ensemble implementations. It is thus of interest to quantify the maximum number of photons (modes) that can be stored. The ability to store multiple spatial modes, i.e. to generate quantum holograms, which is inherent to atomic ensembles, is one exciting prospect.

In terms of the multi-temporal mode storage capacity, storage of 1064 modes using an AFC in crystals [201] and 20 modes using a Λ-GEM in warm vapour cells [230] has been experimentally demonstrated.

Wavelength. It is important that the wavelength of photons that propagate over long distances is within the region of small absorption in optical fibres (unless one considers free-space transmission, e.g. to satellites). Depending on the protocol considered, this may constrain the operating wavelength of the respective quantum memory. Most of the quantum storage experiments have been done around the visible range. Classical storage at telecommunication wavelengths has been done using an AFC with 0.3% efficiency [274].

A summary of quantum memory experiments demonstrated in various systems has been provided in Table 11.1.

We note here that all the criteria required for a true quantum memory have been achieved to date, but in different systems and using different wavelengths. The implementation of a quantum memory that has all the criteria for a quantum repeater in a single platform is still an open research topic.

Method	Stored quantum state	Efficiency	Storage time	Fidelity	Bandwidth
EIT	Entangled single photons [91] and squeezed optical pulses [78] at 795 nm	∼0.1 [91]	∼1μs [91]	0.92 [91] (conditional)	5.5 MHz [91]
Off-resonant Faraday interaction	Entangled squeezed state at 795 nm [100]	∼ 0.43	∼1 ms	0.52 (unconditional)	-
Raman	Coherent state at 852 nm [102]	∼ 0.3	∼1.5 μs	-	1.5 GHz
FWM	Entangled squeezed state at 795 nm [94]	-	∼ 30 ns	-	∼ 10 MHz
AFC	Entangled single photons at 795 nm [130] (883 nm[129])	0.1 [130] (0.21 [129])	∼ 7 ns [130] (200 ns [129])	0.95 [130] (conditional)	∼ 5 GHz [130] (120 MHz [129])
2-level GEM	Coherent state at 606 nm [149]	0.61	∼3 μs	-	∼ 1.6 MHz
Λ-GEM	Coherent state at 795 nm [230]	0.78	∼ 15 μs	0.98 (unconditional)	∼ 0.5 MHz
Highest performance of above techniques	-	0.87 (classical efficiency) [156]	∼ 2.3 sec (classical storage) [90]	0.98 [230] (unconditional)	∼ 5 GHz [130]

Table 11.1: The most recent successful quantum memory demonstrations in various platforms.

Chapter 12

Quantum Measurements

"Had I known that we were not going to get rid of this damned quantum jumping, I never would have involved myself in this business!"

Erwin Schrödinger

As mentioned previously, the natural bound that a quantum memory must overcome is the *classical limit* [23]. This is the storage performance that would be achieved via independent measurements of conjugate quantum observables. Attempts to simultaneously measure conjugate variables always result in quantum back-action, so this measurement-based approach for storage can never allow perfect reconstruction of the input state. To unconditionally overcome this limit, a quantum memory must have an efficiency greater than 50% and work in a way that does not involve any projective measurement in order to avoid quantum back-action. If this can be done, a new interesting performance benchmark can be surpassed, namely the *no-cloning limit* [23]. If this limit is overcome then it is guaranteed that the output of the quantum memory is the best possible copy of the original input state. For coherent states, the cloning fidelity limit is 0.68 [25].

To date there have been a number of impressive demonstrations of optical memories, which were claimed to be quantum memory [129, 130, 137, 268]. In all of these quantum memory demonstrations, the memory efficiency is around or below 30% which makes them conditional quantum memories. In order to break the classical memory limit using unconditional measurements, a minimum efficiency of 50% is required.The first unconditional quantum memory was demonstrated using the GEM technique in a cryogenic solid state system [149].

In this chapter, we present a complete tomographic reconstruction of quantum states that have been stored in the spin states of rubidium in a vapour cell operating at around 80°C. Without conditional measurements, we show recall fidelity up to 98% for coherent pulses containing around one photon. In order to unambiguously verify that our memory beats the quantum no-cloning limit we employ state-independent verification using conditional variance and signal transfer coefficients.

The relevant publication for this chapter is

Unconditional quantum memory M. Hosseini, G. Campbell, B. M. Sparkes, P. K. Lam and B. C. Buchler. Nat. Phys. 7, 794 (2011).

12.1 Quantum performance prediction

The best way to quantify the efficacy of a quantum memory will depend on the application. In order to quantify how the measured efficiency of our memory would translate into a coherent state quantum memory, we can follow the model presented by He et al. [275] where it is shown that a linear quantum memory has fidelity (F_n^c)

$$F_n^c > \frac{1}{1+\bar{n}(1-\sqrt{\eta_m})} \tag{12.1}$$

for coherent states with average photon number $\bar{n}$ and memory efficiency η_m. Given that our memory is linear, and assuming that no extra noise is added to the stored states, we can calculate the range of coherent amplitudes for which it can act as a quantum memory, as shown in Fig. 12.1. This shows, for example that we could store coherent states up to $\bar{n} = 10$ for times less than 6 μs, or states with $\bar{n}$=1 for 21 μs.

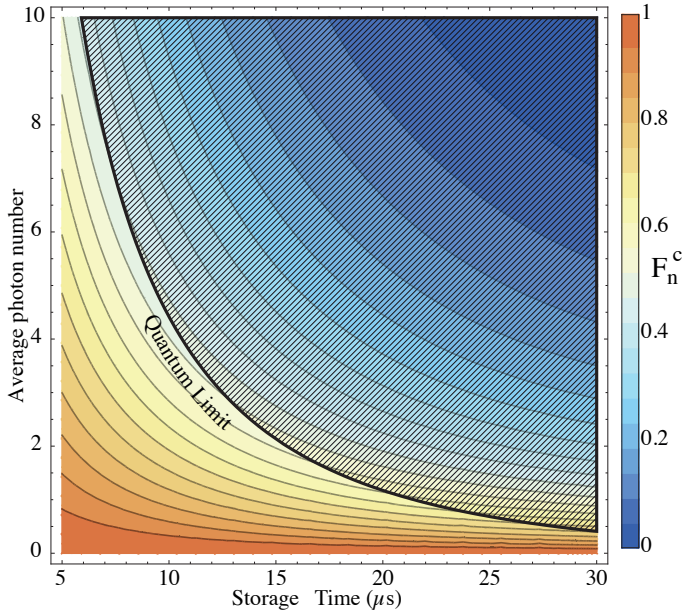

Figure 12.1: Implied quantum memory performance for coherent state storage. The quantum limit is calculated assuming the efficiency fitted to experimental data in Fig. 8.3a(i) and Eq. 12.1

12.2 Experiment and method

The experimental setup is similar to that described in Sec. 8.1 with slight modifications. Here, the signal and coupling fields, after the memory, are separated using a filtering cell [276, 91] instead of a single-mode fibre. The filtering cell containing ^{85}Rb atoms provides more than 60 dB suppression of the coupling field. The temperature of the filtering cell was set to ∼140 ^{o}C. The coupling-field one-photon detuning of 1 or 3 GHz from $F_g = 2 \rightarrow F_e = 2$ transition of the ^{87}Rb D1 line implies almost resonant interaction with $F_g = 3 \rightarrow F_e = 2, 3$ or $F_g = 2 \rightarrow F_e = 2, 3$ transition of ^{85}Rb atoms. The coupling field leakage observed through the filtering cell is well below the local oscillator power and has a different frequency and spatial mode from the signal beam. It therefore does

not contaminate the homodyne detection results. On the other hand, the signal field is well away from any atomic transitions and the absorption is low. The single-mode fibre often has substantially more leakage of the control field, depending on the alignment of the control beam.

The filtering cell attenuates the signal beam by 30% which is mostly due to lack of an anti-reflection coating on the windows of the cell and the presence of ^{87}Rb atoms in the cell. This loss could be reduced by using a pure ^{85}Rb isotope with anti-reflection-coated windows. When the coupling field was guided through the filtering gas cell at T$>$ 120^{o}C we observed purple light scattered off the cell. Using a filtering gas cell together with a cavity one can suppress the coupling field down to the single-photon level [91].

12.2.1 Noise measurement

The presence of the strong coupling field could lead to noise sources in our memory due to Raman scattering into the mode of the probe beam. To investigate these possible noise sources we measured the noise spectrum of the probe mode as shown in Fig. 12.2. With no coupling field present, we observed the shot noise of our detection system (blue) which lies 10 dB above the electronic noise floor (black). With the coupling field switched on (red), we observed no change in the noise level recorded by our heterodyne system. If there were photons added to the mode of the probe field, then we would see added noise around 8 MHz, which is the frequency offset of the heterodyne beam from the probe frequency. The absence of extra noise at this frequency is strong evidence that our memory is not prone to noise sources that could impact on quantum state storage.

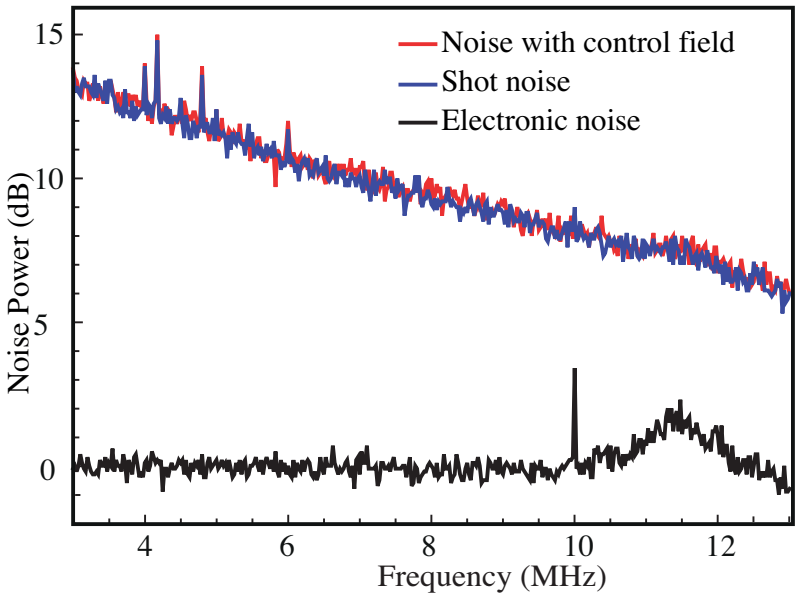

Figure 12.2: Variance of the probe field mode measured using heterodyne detection. Curves represent electronic noise (black), shot noise (blue) and noise with the coupling field switched on (red). Measurements were made with a Resolution Bandwidth=3 kHz, Video Bandwidth=30 kHz and 5 averages. The coupling beam was filtered out of this measurement using an additional gas cell containing warm ^{85}Rb.

To perform proper noise measurement of the memory and accomplish quantum state tomography we recorded more than 100,000 homodyne measurements for each input and

output state. The input pulses had a duration of 2 μs and were stored for 3 μs. The bandwidth of the pulses was matched to the chosen memory bandwidth of 0.5 MHz to maximise the single-mode efficiency of the system.

The coupling field was switched off for 1 μs during storage to minimise decoherence due to the scattering. The storage time was made sufficiently long to avoid electronic noise associated with the magnetic field switching. To determine the phase of each pulse, we sent a strong reference pulse at a different frequency 9 μs prior to the input pulse. This pulse was tuned far away from the atomic resonance so that they were fully transmitted by the memory gas cell. This was done for a range of different pulse amplitudes. The separation between the reference and the probe pulse is small compared to the time scale of phase fluctuations in the experiment, so that we can reliably infer the phase of the input and echo pulses relative to our reference pulse. The error obtained from the least-squares fit to the pulse data indicates that the phase estimation uncertainty is 29 mrad. Our measured efficiency of 78±5% therefore quantifies the memory process alone. The other efficiency parameters of the experiment will be discussed in greater detail when we consider the the quantum nature of the memory.

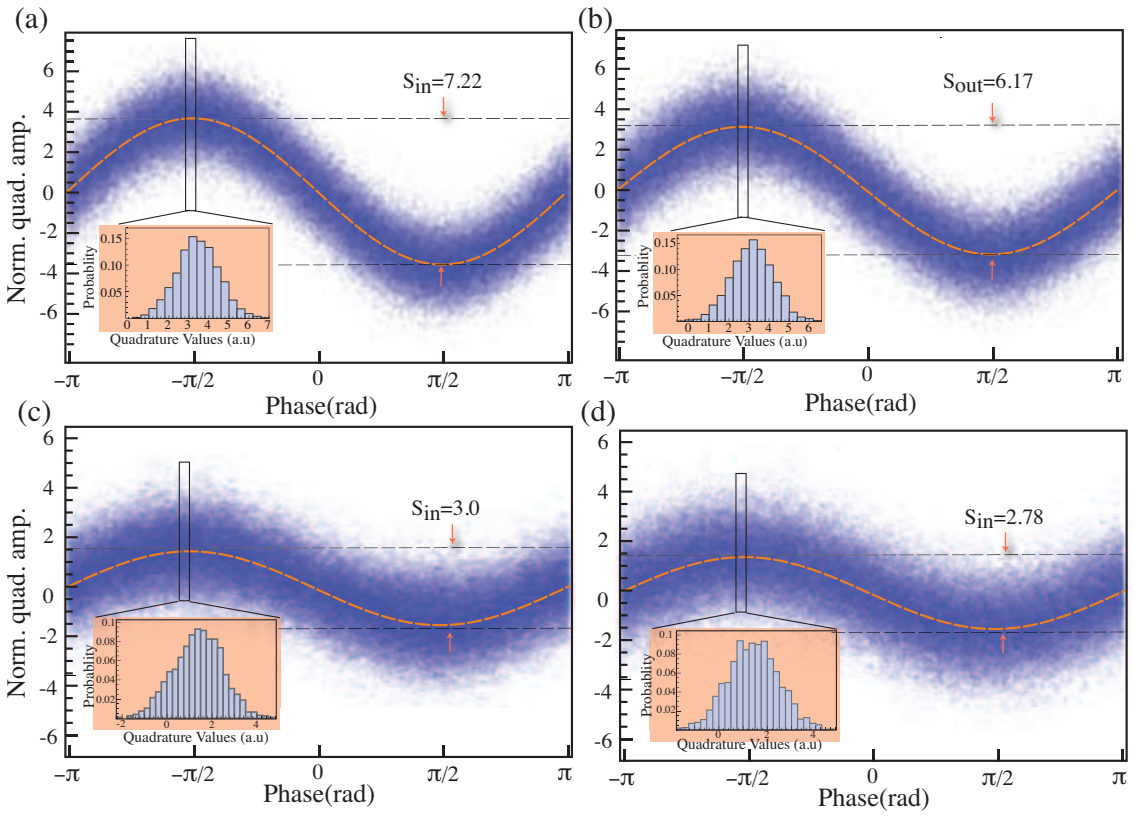

Figure 12.3: Quadrature amplitude as a function of local oscillator phase for, (a) input and (b) output pulses with mean photon number of $\langle N \rangle = 3.4$, normalised to the vacuum. Quadrature amplitude for (c) input and (d) output pulses with a mean photon number of $\langle N \rangle = 0.67$. The amplitudes of input and output signals are shown as S_{in} and S_{out}, respectively. Insets show histograms of the quadrature values at the indicated phase. The plots each show 100,000 pulse quadrature measurements.

We integrated the amplitude of the input and the echo pulses over the pulse duration

to find a quadrature value and then used the reference pulse to associate a phase with each integrated quadrature value. Fig. 12.3 (a) and (b) , (c) and (d), show the quadrature measurement results as a function of local oscillator phase for input and output pulses, respectively, with a mean input photon number of 3.4 and 0.67.

12.3 State Tomography

The quadrature measurements were used to reconstruct the density matrix elements, the results of which are plotted in Fig. 12.4 for two coherent states with different amplitudes. The iterative MaxLik method [277] (see Sec. 2.1.10) was used to reconstruct the density matrix elements of 100000 pulses obtained from a set of balanced homodyne measurements [278]. Assuming a particular density matrix ρ, one can evaluate the probability of acquiring a particular set of measurement results. The purpose of the MaxLik method is to find a density matrix that maximises the probability of obtaining the given experimental data set. In practice, the iteration algorithm is executed with the density matrix in the photon number (Fock) representation. Since the Hilbert space of optical states is of infinite dimension, the implementation of the algorithm requires its truncation so that Fock terms above a certain threshold are excluded from the analysis. The diagonal elements of the density matrix represent photon number probability amplitudes and the off-diagonal elements are coherences.

12.3.1 Photon number distribution and Wigner function

The density matrix results allowed us to investigate the photon statistics of our light pulses before and after the memory. In Fig. 12.5 (a) and (b), we plot the photon number distribution of the input and output pulses. The solid blue lines show a Poissonian distribution, fitted to the measured mean photon number of 3.4. The good agreement of our data with this model shows that our output states are also near Poissonian, as we would expect for near coherent input states. This distribution can be compared to the photon statistics that would be obtained in the case of a memory with equal efficiency but contaminated by extra noise. To do this we assume equal amounts of Gaussian noise are added to the phase and amplitude quadratures of our output state and then find the resulting photon number distributions. In Fig. 12.5 (b) we show curves that illustrate the photon statistics we would obtain assuming Gaussian noise that degrades the fidelity of our memory to the classical and no-cloning limits. This data clearly shows that our memory does not introduce significant noise to the output pulses and easily exceed the no-cloning limit.

The Poissonian distributions shown in Fig. 12.5(a) and (b) are theoretical fits using only the mean photon number calculated by summing over the relevant photon probability distribution. To obtain the photon distributions for the no-cloning and quantum limits we assume our memory is a source of Gaussian noise that is added equally to the phase and amplitude quadratures. We add just enough noise to each quadrature to reach these limits then reconstruct the photon number distributions as we did before. In the case of the no-cloning limit we assume the added quadrature variance of $2\eta - 1$ where η is the efficiency of the memory. The added noise in the case of the quantum limit can be shown to be 2η (see supplementary information in [149]. This assumption is truly valid only if the input state is a coherent state.

To get an intuitive picture from quantum-state tomography we reconstruct the Wigner function [279], which is a quasi-probability distribution in phase space. Among various

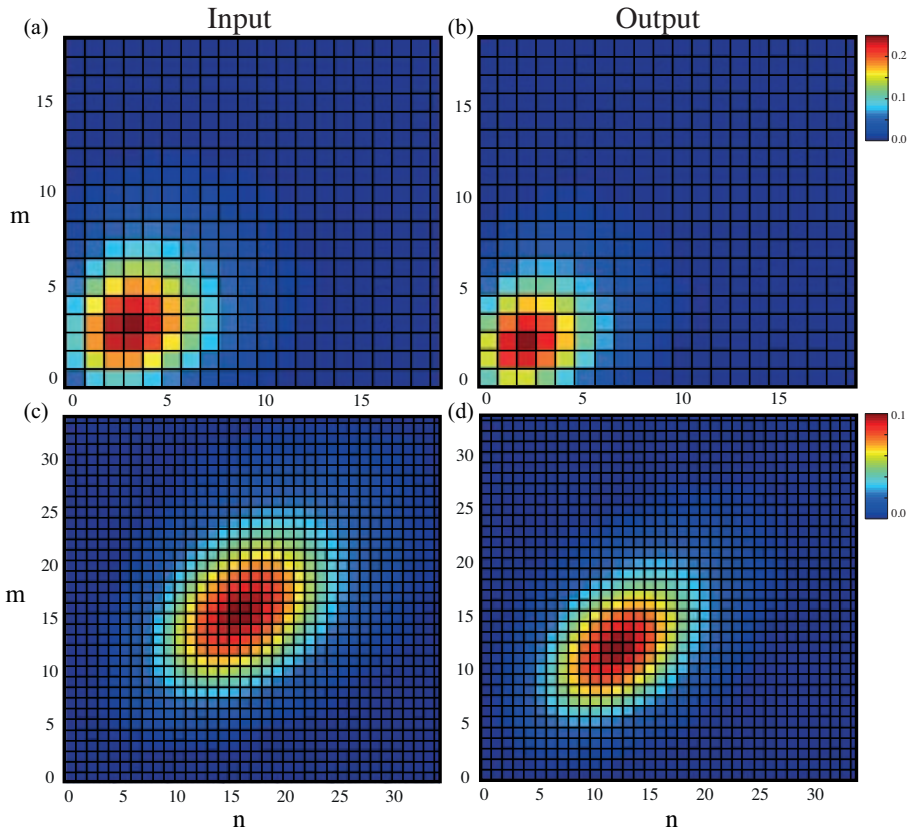

Figure 12.4: Density matrix elements for two sets of input and output pulses. (a) and (b) Density matrix elements for input and output states, respectively, with $\langle N \rangle = 3.4$ yielding a fidelity of 93%. (c) and (d) Density matrix elements for input and output states, respectively, with $\langle N \rangle = 16$ yielding a fidelity of 82%

phase space plots, the Wigner distribution is used frequently to measure probability in coordinate and momentum space. Fig. 12.5 (c)/(e) and (d)/(f) show the reconstructed Wigner functions of the input and output states with $\langle N \rangle = 3.4/\langle N \rangle = 0.67$. The projected probability distributions along the two marginal distributions, amplitude (x) and phase (p) represent a Gaussian distribution for x and p quadratures.

12.3.2 Fidelity Measurements

In order to quantitatively characterise the memory performance in the quantum regime we analyse the storage fidelity by evaluating the overlap between the input and output states. The fidelity ($\mathcal{F}$) can be computed as the overlap integral of the input and output Wigner functions, or directly from the density matrix using the equation $\mathcal{F} = |Tr(\sqrt{\sqrt{\rho_{in}}\rho_{out}\sqrt{\rho_{in}}})|^2$ [14]. After reconstruction of the density matrix for each state the fidelity can be easily calculated using this equation. These results are presented in Fig. 12.6 (a). The observed fidelity is as high as 93% for $\langle N \rangle = 3.4$ and 98% for $\langle N \rangle = 0.67$. In the limit of storing pulses with no photons, i.e. a vacuum, the efficiency of the memory no longer plays a role in determining the fidelity, since a memory with low efficiency can still

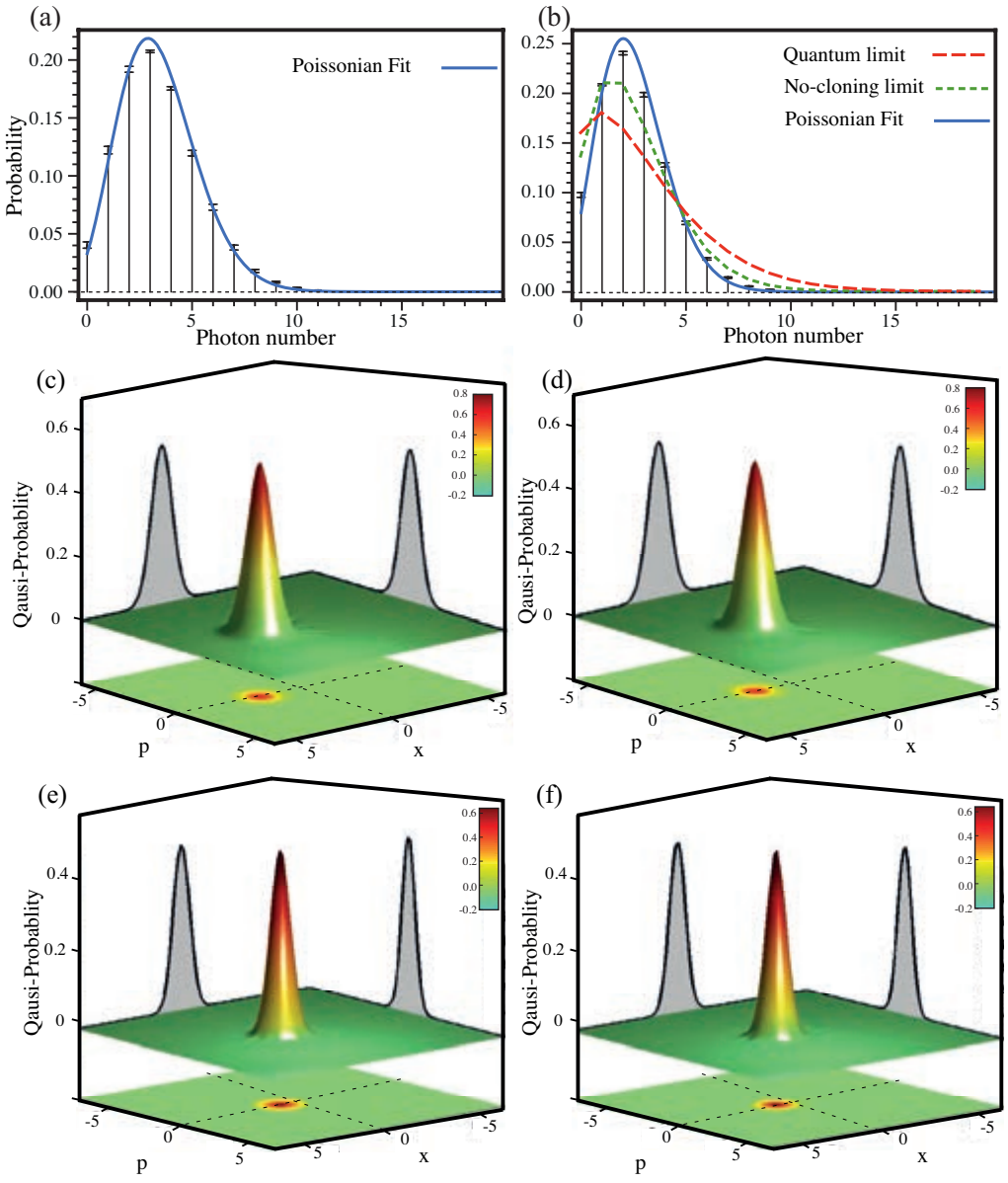

Figure 12.5: (a) and (b) Photon number distribution for input and output pulses, respectively. The blue solid lines show the fitted Poissonian distribution. The green dotted line represents the no-cloning limit and the dashed red line shows the boundary for the quantum limit. The error bars are statistical errors obtained from 100 subsets of data. (c) and (d) Reconstructed Wigner functions of input and output states for $\langle N \rangle = 3.4$. (e) and (f) Reconstructed Wigner functions of input and output states for $\langle N \rangle = 0.67$. x and p represent the amplitude and phase, respectively, of the coherent state.

output a pure vacuum state. For low photon numbers the fidelity is, however, sensitive to added noise. The high fidelity that we observe at low photon numbers is therefore indicative of a memory that does not add noise to the output state. Also shown in this plot are the classical (trace(i)) and optimal fidelity (trace(ii)) limits for coherent states of 1/2 and 0.68, respectively. The Gaussian no-cloning limit is obtained if $\delta_x = \delta_y = 0$ and $V_{out}^{\pm} = V_{in}^{\pm} + 1$. For coherent states we have $V_{in}^{\pm} = 1$, and the maximum cloning fidelity is therefore 2/3 [280]. Using a non-Gaussian cloner one can obtain slightly higher fidelity for

1-to-2 cloning of coherent states, $\mathcal{F}_{NG-cloning}$ =0.6826 [25]. All our data points are at or beyond the coherent state no-cloning limit. This is, however, only of real significance for the two smallest photon numbers where the states are, to good approximation, coherent.

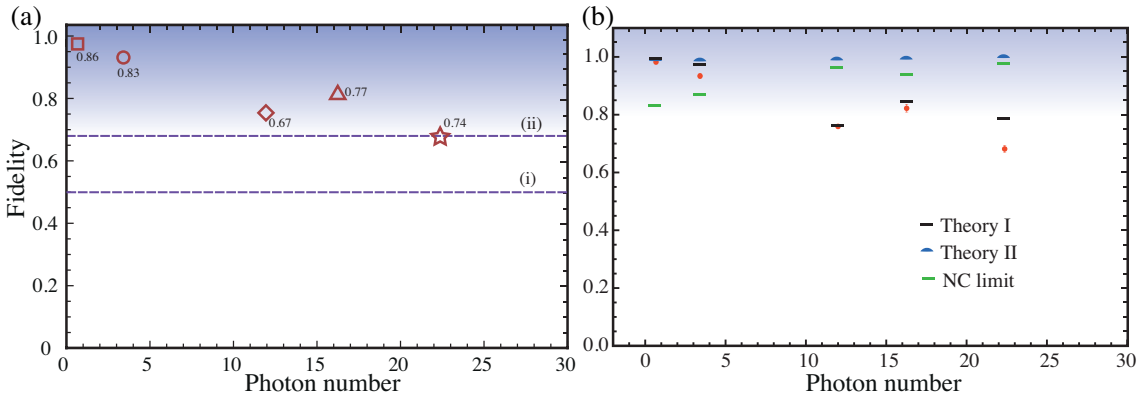

Figure 12.6: (a) Fidelity of the memory for various optical states with different photon numbers. The measured memory efficiency for each data set is shown next to each symbol. Trace (i) shows the maximum fidelity that is expected from a classical memory. Trace (ii) is the no-cloning limit of 0.68. The statistical error in measuring the fidelity is smaller than the size of the symbols. (b) Different fidelity benchmarking. The red points are the experimental data points as (a). Black lines (Theory I) are the maximum fidelity predicted by theory taking into account the input noise, efficiency and non-amplification of the state. The green lines (NC limit) are specifying the no-cloning limit taking into account the input noise and assuming linear amplifier for Eve. Finally, the blue symbols indicate the maximum fidelity that could be achieved by allowing linear amplification of experimental data and taking into account the extra noise induced via this operation.

As expected from a real experiment, our pulses have some amount of noise above the vacuum fluctuations. This added noise, mostly due to small instabilities in our cavity locking servos, increases with the photon number. Since the fidelity is highly state-dependent the quantum and no-cloning benchmarks obtained for the coherent state are not valid for states with higher photon numbers and therefore benchmarks for each state must be defined taking into account the input noise. Knowing the input/output quadrature variances, the fidelity between two optical states with Gaussian quadrature distributions [14] can also be calculated as

$$\mathcal{F} = \frac{2e^{-\frac{2\delta_x^2}{V_{in}^+ + V_{out}^+} - \frac{2\delta_y^2}{V_{in}^- + V_{out}^-}}}{\sqrt{(V_{in}^+ V_{out}^- + 1)(V_{in}^- V_{out}^+ + 1)} - \sqrt{(V_{in}^+ V_{in}^- - 1)(V_{out}^+ V_{out}^- - 1)}} \tag{12.2}$$

where $\delta_{x/y}$ is the distance between the two states in the phase space along the amplitude (x) and phase (y) axes. $V_{in/out}^{\pm}$ are the amplitude (+) and phase (-) quadrature variances of the input and output states.

In Fig. 12.6 (b) we present the different benchmarking as small lines for each state together with the experimental data (red points). To calculate the optimal memory performance (small black lines in Fig. 12.6 (b)) we used the input parameters in Table 12.1 and Eq. 12.2. We then found the distance between the input and output states and also the output noise by assuming a beamsplitter relation for the memory, where the transmis-

sivity of the beamsplitter is the efficiency of the memory. Therefore, this limit takes into account the measured input state, the measured efficiency and the absence of any additional noise other than vacuum fluctuation introduced due to the sub-unity efficiency. As can be seen in Fig. 12.6 (b), these predictions, shown as small black lines (TheoryI), are very close to the experimental points verifying negligible added noise from the memory to the output states. The red lines in this figure (NC limit) are the no-cloning limit estimated by calculating the fidelity between Eve's state and the best possible output state. In this calculation, it was assumed that Eve adds a vacuum of noise to the state by copying the state taking into account the input noise. It is worth mentioning that the experimental points and also black lines (TheoryI) were achieved without linear amplification to gain maximum fidelity (just like Eve). If we allowed ourselves to linearly amplify the output state from the memory, while taking into account the added noise, we would obtain fidelity values higher than the no-cloning limit as shown in Fig. 12.6 (b) blue lines (Theory II). This shows that with some local operations, all our data points appear to break the no-cloning limit.

$\langle N \rangle$	V_{in}^{+}	V_{in}^{-}	η	$\mathcal{F}$
0.67	1.20	1.10	0.86	0.98
3.41	1.14	1.40	0.83	0.93
12.0	1.63	4.52	0.67	0.76
16.3	1.57	2.08	0.77	0.82
22.4	2.03	7.51	0.74	0.68

Table 12.1: Experimental parameter table. Mean photon number $\langle N \rangle$, input variances ($V_{in}^{\pm}$), efficiency (η) and fidelity ($\mathcal{F}$) of different optical states used in Fig. 12.6 (a) and (b).

12.3.3 T-V representation

As the above analysis shows, the state dependent nature of the fidelity means that it is not an easy-to-use measure of the memory performance. In the case where the memory is being probed with various input states with different levels of added noise, each input state has its own unique no-cloning limit for fidelity. To unambiguously quantify the performance of our memory it would be advantageous to use a state independent criterion. This can be done using a signal-transfer and conditional-variance characterisation known as a T-V diagram. This method was originally proposed for characterising quantum non-demolition measurements [281] and later adapted to quantum teleportation [282, 283] and quantum memory [83, 284]. The conditional variance of the amplitude V^{+} and phase V^{-} quadratures is a measure of the noise added by the memory. An ideal memory adds no noise so the conditional variance between the input and output would be 0. The classical limit would be the case where the noise added by the memory is one unit of vacuum noise on each quadrature so that $V^{+} = V^{-} = 1$. The amplitude and phase signal transfer coefficients (T^{+} and T^{-} respectively) are a measure of how well the memory preserves a signal. If the signal-to-noise ratio of the output is equal to the input, as would be the case for an ideal memory, then the transfer coefficient is unity. The classical limit is $T^{+} = T^{-} = 0.5$. It can be shown that if the two quantum benchmarks of $V_{cv}^{+} \times V_{cv}^{-} \leq 1$ and $T^{+} + T^{-} \geq 1$ are satisfied then the memory device surpasses the no-cloning limit [23].

The transfer coefficient (T) and conditional variances (V) for two orthogonal quadra-

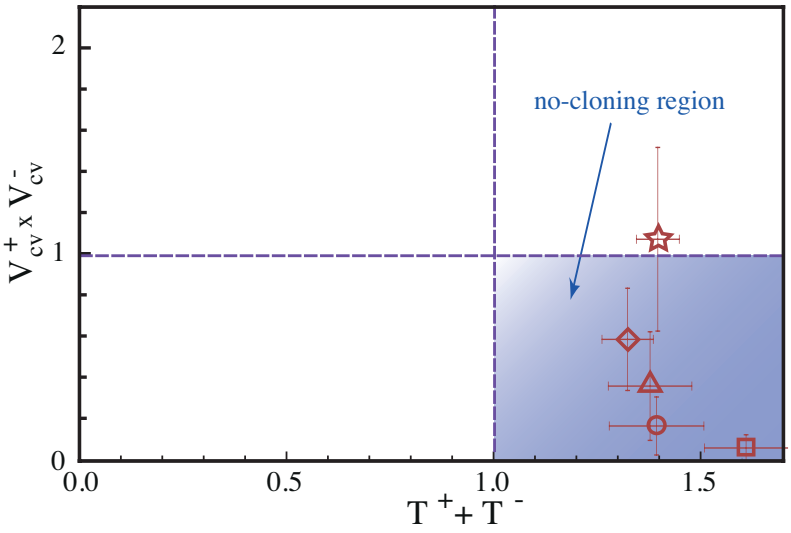

Figure 12.7: The T-V diagram based on the same raw data as Fig. 12.6 (a). The symbols used here are the same as those in Fig. 12.6 (a) to allow comparison of the data. The shaded region on the bottom-right is the no-cloning regime. The error bars represent the statistical uncertainties.

tures are defined, respectively, as $T^{\pm} = \eta/(1 + V_{out}^{\pm} - V_{in}^{\pm})$ and $V_{cv}^{\pm} = (1 - T^{\pm})V_{out}^{\pm}$ from which the two quantum limits of $V_{cv}^{+} \times V_{cv}^{-} \leq 2$ and $T^{+} + T^{-} \leq 1$ are obtained. When calculating the conditional variance it is important to account for the total detection efficiency of the experiment. In our analysis the quantum efficiency of the detectors (90%), fringe visibility of the homodyne (97%), and transmission of the signal through the filtering cell (70%) have been taken into account while calculating the conditional variances by extrapolating the variances of the input and output to the state prior to these losses. With this state-independent measurement, the results demonstrate that our system has convincingly surpassed the no-cloning limit of quantum memory for a range of photon numbers.

In the current experiment, the coherence time of the memory ($\sim$10 μs) is limited by the diffusion and collision of atoms. It was recently shown that by preparing cells with single-compound alkene-based coatings, spin relaxation times of up to a few seconds can be easily achieved even at high temperatures [168]. This spin relaxation time is comparable to the best coherence time measured in cold atomic ensembles. However, whether long coherence times in cells with alkene-based coatings can be observed in GEM system requires further investigation. In terms of the miniaturisation of these types of memories, extensive work has been done to manufacture microscopic vapour cells for alkali atoms [285, 286, 287, 288]. Hollow-core waveguides also show great promise in developing integrated coherent photonic structures[289]. All of these developments together with the results presented here suggest that Rb vapour could be a reliable and scalable platform for quantum memory.

12.4 Conclusion

In this chapter, we have shown experimental results of noise measurement and state-tomography of the λ-GEM. We have demonstrated that our gaseous memory, operating above room temperature, is capable of storing quantum information with a fidelity higher than the no-cloning fidelity limit. The simplicity of the scheme, as well as efficient and

noiseless operation of the memory, indicate its various potential applications in quantum communication technology.

Chapter 13

Nonlinear Polaritonic Interaction

In this chapter we analyse a cross-phase modulation (XPM) scheme that exhibits an enhanced nonlinearity in a Rb-based gradient echo memory system. We present numerical simulation along with a proposed experimental scheme that shows large nonlinearity at the single photon level. Furthermore, we present some preliminary experimental results of XPM between coherent states at high signal power obtained using the warm vapour cell.

13.1 Introduction

The optical Kerr effect is the case in which the electric field due to the light itself causes a variation in index of refraction, which is proportional to the local intensity of the light. The refractive index change with intensity, I, in a Kerr medium is given by

$$n = n_0 + n_2 I \tag{13.1}$$

where n_0 is the linear refractive index, and n_2 is the second-order nonlinear refractive index of the medium. The refractive index variation, $\frac{dn}{dt} = n_2 \frac{dI}{dt}$, is responsible for the nonlinear optical effect of phase modulation. This effect is present in most of the materials but only becomes significant with very intense beams or after long interaction times. When a light pulse (probe) propagates through a Kerr medium, the variation in the refractive index produces an instantaneous phase shift on the probe pulse. This effect is known as self-phase modulation (SPM). The phase shift due to SPM results in a frequency shift of the pulse due to intensity-dependent (and therefore time-dependent) phase shifts such that the front edge of the pulse shifts to lower frequencies and the tailing edge to higher frequencies, while the peak of the pulse is not shifted. The extra frequencies generated through SPM broaden the frequency spectrum of the pulse symmetrically.

Cross-phase modulation (XPM) refers to a process in which the phase of a probe pulse is modulated by the strength of another field (signal field). In the limit of extreme nonlinearity, individual photons could be persuaded to interact strongly with one another and induce cross-phase modulation (XPM). This kind of interaction is a basis of the deterministic control-not gate and phase-not gates that lie at the heart of quantum computing algorithms [290, 291]. A strong XPM has applications in creating strongly correlated states of interacting photons [292], generating macroscopic quantum superpositions [293], realising universal quantum gate operations [294, 295, 296], and providing nonlinear optical switching [297]. Below, we briefly discuss different applications of XPM at the single photon level in optics-based quantum information.

A quantum Fredkin gate can be constructed [290] based on Kerr nonlinearity and is suitable for reversible computing. The idea is that two of the inputs control whether

there is a transformation on the other input. A Fredkin gate is a three-qubit universal (reversible) gate, i.e. any other quantum gate can be constructed from this gate. To construct such a gate, large and noiseless XPM on the order of π is required. The realisation of such a large phase shift has been a great challenge for the experimentalists around the world in the past decade and the largest phase shift observed, to date, was 10^{-6} rad. Munro et al. [298] proposed that by successive weak cross-Kerr interactions between a strong coherent-state probe beam and a pair of single-photon qubits beam it is possible to realise a deterministic parity gate from which a CNOT gate can be constructed.

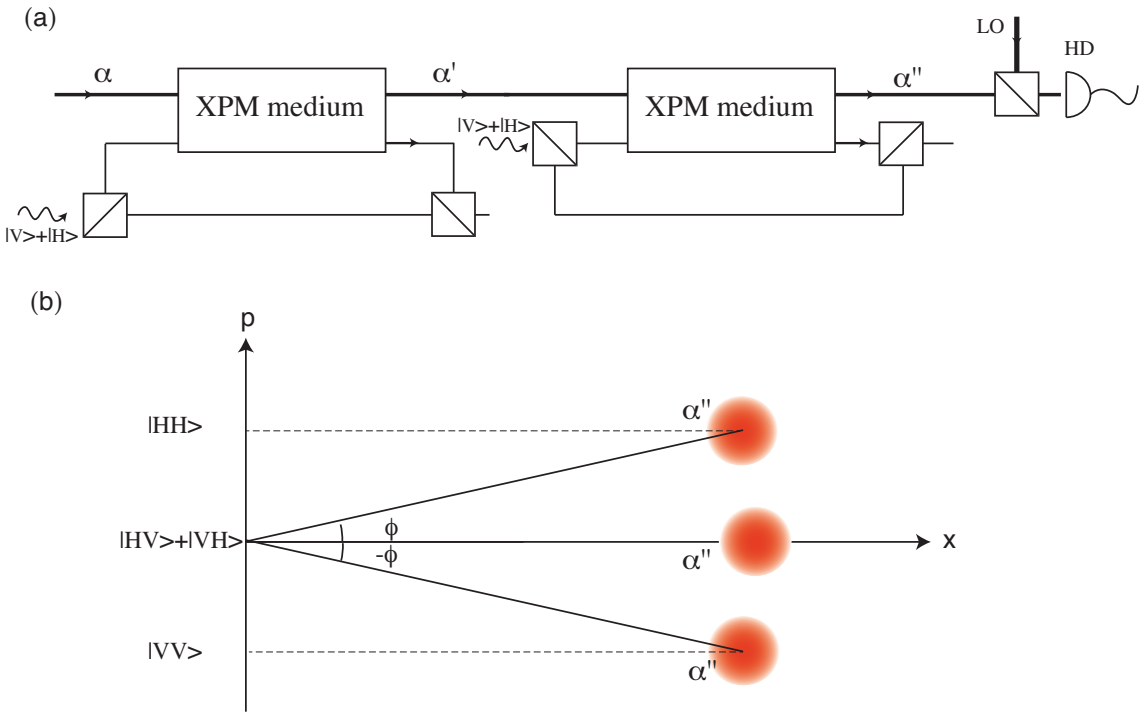

Figure 13.1: (a) Schematic experiment for generation of cluster states using a Kerr nonlinear medium. Here we assume that vertical polarization reflected from the beamsplitters gives a negative phase shift and horizontally polarized photons result in a positive phase shift. (b) A nonlinear Kerr medium can be used to generate entanglement photonic qubits via parity check done by homodyne quadrature measurement of coherent states at low nonlinearities.

To see how a Kerr medium can be used to build a parity gate, consider the setup shown in Fig. 13.1 (a). A coherent state $|\alpha\rangle$ is sent through two Kerr media together with two photons in superposition of vertical and horizontal polarisations, $1/\sqrt{2}(|V\rangle + |H\rangle)$. If the photon is in the vertical state it is reflected from the beamsplitter and introduces a negative phase shift on the coherent state, and vice versa. Homodyne measurement (HD) on the output coherent state can be seen as a parity operator which, 25% of the time, projects the state of the photons into a Bell state, i.e. $|HV\rangle + |VH\rangle$ (see Fig. 13.1(b)). Minimum displacement between possible output coherent states is necessary to guarantee distinguishability. At low nonlinearities, this can be satisfied by increasing the amplitude of the coherent state, α. A cascade of Kerr media can be used to generate highly entangled cluster states. Potentially, this should allow for a high fidelity of entanglement.

An alternative approach to quantum computation is the one-way quantum computing [299, 300] proposed by Raussendorf and Briegel, which uses continuous variables and

highly efficient measurements. This proposal is based on the generation of highly entangled cluster states [299] where a sequence of single-qubit measurements with classical feedforward of the measurement shapes the entire body of quantum computation protocol. A proof of principle experiment of this scheme has also been implemented [240]. The main difficulty of this protocol is the generation of large cluster states that can be useful for realistic problems. It was proven [291] that even weak cross-phase modulation between single photons can be used in yielding an entangling operation with a success probability greater than 1/2 (natural bound of previous scheme due to the single beam-splitter success probability) and therefore initialising cluster states. If realised, this approach could pave the way for the scalable implementation of such a scheme [301, 302, 291].

Moreover, large nonlinearity can be used to generate bright Schrödinger cat states [303]. Nonclassical properties of the quantum superposition of coherent states of certain forms have already been studied [293]. Various schemes have been suggested to produce such states, such as photon-subtracted squeezed states [304]. A familiar example of such states is the superposition of two classical-like coherent states of the same amplitude but with a phase shift of π:

$$|\psi\rangle = |\alpha\rangle + e^{i\phi}|-\alpha\rangle \tag{13.2}$$

For $\phi = 0$, Eq. 13.2 describes the even coherent state, while for $\phi = \pi$, it describes the odd coherent state.

To date, there have been various proposals aimed at realizing this strong interaction, particularly, nonlinearity in optical fibres [305], cavity quantum electrodynamics (CQED) [306, 307] and nonlinearity present in electromagnetically-induced transparency (EIT) [308, 292, 309, 310, 295]. Experiments have realised XPM in optical fibre with $\delta\phi = 10^{-7}$ rad [311] per photon, CQED with $\delta\phi = 0.5$ [312] rad and EIT systems with $\delta\phi = 10^{-6}$rad [313, 314] per photon.

In the following sections we briefly discuss and compare different methods proposed for the realisation of an experiment capable of producing large XPM at single photon level.

13.2 XPM between single photons inside nonlinear fibre

Nonlinearity in optical fibre has been shown to be an important property for manipulating and generating light in applications including soliton transmission [315], light amplification [316], all-optical switching [317], and super-continuum generation [318]. Optical fibres are also an attractive XPM medium [311]. While they may not be highly nonlinear, the interaction times can be extended simply by using longer fibres.

The experimental observation of optical nonlinearity, on the order of 10^{-7} rad, at the single photon level in 4.7 m of optical fibre was recently reported [311]. Due to the small nonlinearity in the fibre, one needs to use hundreds of kilometres of fibre to achieve phase shifts on the order of π. A single photon propagating through the fibre for a long time will disappear due to the loss in the fibre.

The XPM between single photons propagating through optical fibres relies on maximum interaction between photons; therefore one would need ideal spatial and temporal mode matching between the incoming (multimode) photons. Spatial mode matching can be resolved by precise engineering of the system. However, the temporal mode matching is a problem and seems to fundamentally limit the maximum phase shift or fidelity of the

operation [319, 320].

It is known that a typical optical fibre has a response time of τ =1-10 fs which is much shorter than the duration of a typical single photon wave packet, δt . This almost instantaneous response of the medium causes a nonlinear phase shift on a randomly-distributed-in-time portion of the probe photon. This fast-response property of optical fibres significantly reduces the overall accumulated phase shift and therefore precludes it from being useful for quantum computation applications. In a slow-response regime, on the other hand, Shapiro showed [319, 320] that the phase noise imposed due to the free-field commutator relations for the output field operators can severely degrade the fidelity of the gate operation.

13.3 XPM in EIT media

Another method of facilitating long interaction times for XPM is via light interaction with an atomic ensemble. An EIT-based XPM scheme exploits slow-light effects in an atomic ensemble to enhance the nonlinear interaction of light fields via the ac-Stark effect [321]. It has been shown that light pulses propagating through an EIT medium can exhibit strong nonlinear interactions [308, 292, 309, 310, 295] leading to XPM. A phase shift almost two orders of magnitude larger than that in optical fibres has been observed using EIT for single photons [313, 314].

Two pulses propagating under a double EIT condition can show XPM, for example, in the configuration shown in Fig. 13.2. Probe ($\mathcal{E}_p$) and signal ($\mathcal{E}_s$) fields interact with transitions $|1\rangle \rightarrow |4\rangle$ and $|2\rangle \rightarrow |4\rangle$, respectively. A double-EIT configuration can be obtained by applying a control field on the $|3\rangle \rightarrow |4\rangle$ transition and consequently the probe and signal fields can be simultaneously slowed down. In the presence of a fifth atomic level ($|5\rangle$) the signal field also off-resonantly couples to the $|3\rangle \rightarrow |5\rangle$ transition. The latter interaction can nonlinearly modulate the phase of the probe field via the ac-Stark effect.

A similar EIT-based XPM scheme was proposed by Wang et al. [309]. For the realisation of such a scheme, two control fields were used to independently control the group velocity of two light pulses. To obtain maximum nonlinearity, precise velocity matching [309, 322] between the two pulses is required. To date, similar XPM schemes based on EIT have been proposed and also experimentally implemented in ^{87}Rb atomic ensembles [292, 309, 310, 295]. The single-photon-level XPM is inferred to be about 1.3×10^{-5} rad [313].

In the EIT scenario, when a photon interacts with a single atom in a cavity or ensemble of atoms, Shapiro's simple model may not be applicable to explain the phase noise introduced on photons. The finite size of the input pulse means that it is essentially in a superposition of many temporal modes. Most of these modes will couple equally strongly to the atoms, and any nonlinearity that is strong enough to imprint a large phase shift should also be strong enough to generate large cross-spectral correlations that may distort the pulse substantially. In addition to this, there will always be a large number of empty temporal modes, also with a large coupling to the atoms, into which a photon could be emitted. It has been theoretically demonstrated that EIT-based XPM suffers from severe loss in regimes where large phase shifts are expected [323]. Gea-Banacloche [323] showed that spontaneous emission into the initially unoccupied temporal modes is responsible for the small XPM in an EIT medium. In this scenario, a large phase shift is only possible in the limit in which the pulse bandwidth matches the medium bandwidth [323]. The

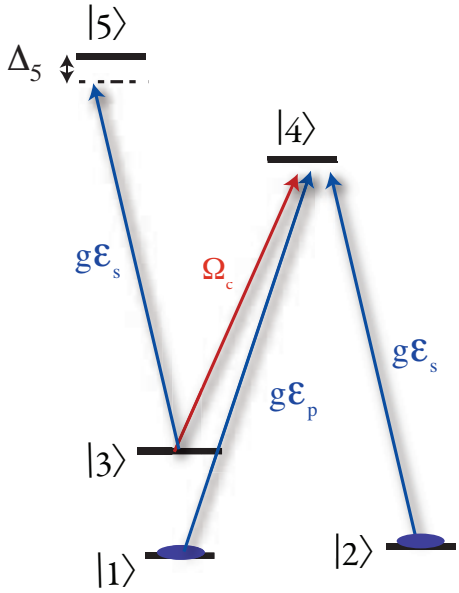

Figure 13.2: Simplified atomic level configuration for creating XPM between two light pulses ($\mathcal{E}_s$ and $\mathcal{E}_p$) under the double-EIT condition

EIT medium in this regime, however, becomes ineffective and noisy. This is because some frequency components of one light field, lying outside the EIT window, can lead to spontaneous emission that is ultimately responsible for weak and low fidelity XPM. Moreover, the storage efficiency limit of 50% [324] in EIT-based systems poses a practical limit on the fidelity of the output states.

13.4 XPM between light and atomic coherence

The temporal mode-matching matters only if the two photons are propagating through a nonlinear medium. It has been shown that nonlinear interaction can also be obtained in a memory-based XPM scheme [325, 326, 327]. When a single photon is stored inside an atomic memory, the atomic coherence can still experience a nonlinear phase shift due to another photon flying through the memory. This phase shift can then be mapped back to the electric field on the retrieval stage.

Fig. 13.3 shows a simple interaction scheme for such XPM process. The probe photon can be coherently stored inside atomic coherence, $|1\rangle\langle 2|$. The signal pulse which freely propagates through the memory, detuned from the $|2\rangle \rightarrow |3\rangle$ transition, can change the phase of the atomic coherence that can later be transferred to the recalled probe photon.

13.4.1 GEM-based XPM experiment

In this section, we present a proof-of-principle demonstration of XPM in a warm memory. The experimental setup is similar to what was described in Sec. 12.2 with slight modifications that are shown in Fig. 13.4 (a).

The probe was stored for approximately 15 μs while the coupling field was switched off. During that time, a signal field generated from a diode laser and detuned by $\delta_3 \simeq 2$ GHz from $F = 2 \rightarrow F' = 3$ of ^{87}Rb D_2 line was sent through the memory. This field was

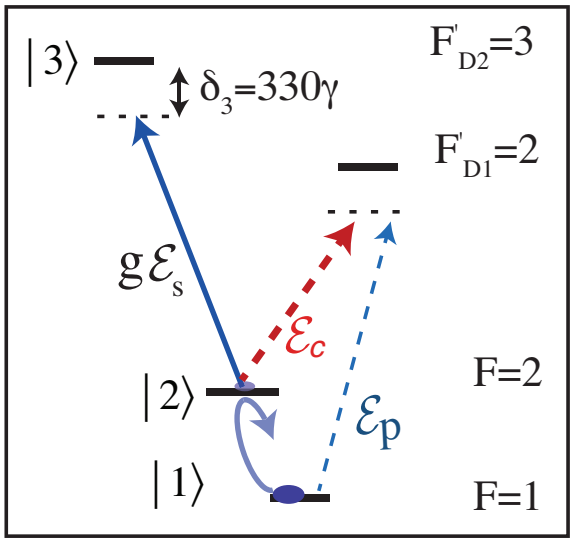

Figure 13.3: A simplified level structure where a signal pulse $\mathcal{E}_s$ interacts with the atomic coherence, generated by the probe pulse. Here, γ is the linewidth of the excited state.

counter-propagating with respect to the probe and coupling fields to avoid measurement contamination. The signal field gave rise to an ac-Stark shift of the spin coherence. On recall, therefore, the stored probe field will be phase shifted proportional to the strength and duration of the signal field. To measure the size of the phase shift, we ran two storage experiments in quick succession, without and with the signal field, as shown in Fig. 13.4 (b) (i) and (ii) respectively. A phase reference for the two recalled probe pulses was provided by a pulse that passed through the memory cell 10 μs before the start of each experiment. This reference pulse allowed us to compare the recalled probe phase with and without the signal field, as has been done in the figure.

The results of the phase shift as a function of Rabi frequency of the signal pulse is plotted in Fig. 13.5 (a), where the solid line represents the theoretical expectation calculated [325] using

$$\Phi_{XPM} = \frac{\Omega_s^2 \delta_3}{2(\gamma^2 + \delta_3^2)}\tau \tag{13.3}$$

where $\Omega_s = g\mathcal{E}_s$ is the Rabi frequency of the signal pulse and τ is its duration. This expression was derived simply by integrating the ac-Stark shift term over the duration of the pulse.

Based on the experimental data presented in Fig. 13.5 (a), we estimate a phase shift on the order of 10^{-12} rad for signal and probe fields containing single photons. In our experiment, the large detuning of the signal field (2 GHz) severely reduces the available nonlinearity, but it is necessary due to the large Doppler broadening of thermal atoms. In fact, even with this detuning the signal field leads to substantial scattering of the atomic coherence. In Fig. 13.4(b), for example, the probe recall is reduced from 53% to 7% by the signal field. Crucially, our scheme has no measurable SPM, as shown in Fig. 13.5 (b), where the recalled probe phase is seen to be independent of the probe intensity. In cold atomic ensembles [325] this detuning could be reduced by two orders of magnitude, allowing, in principle, a phase shift two orders of magnitude larger. Even if larger phase

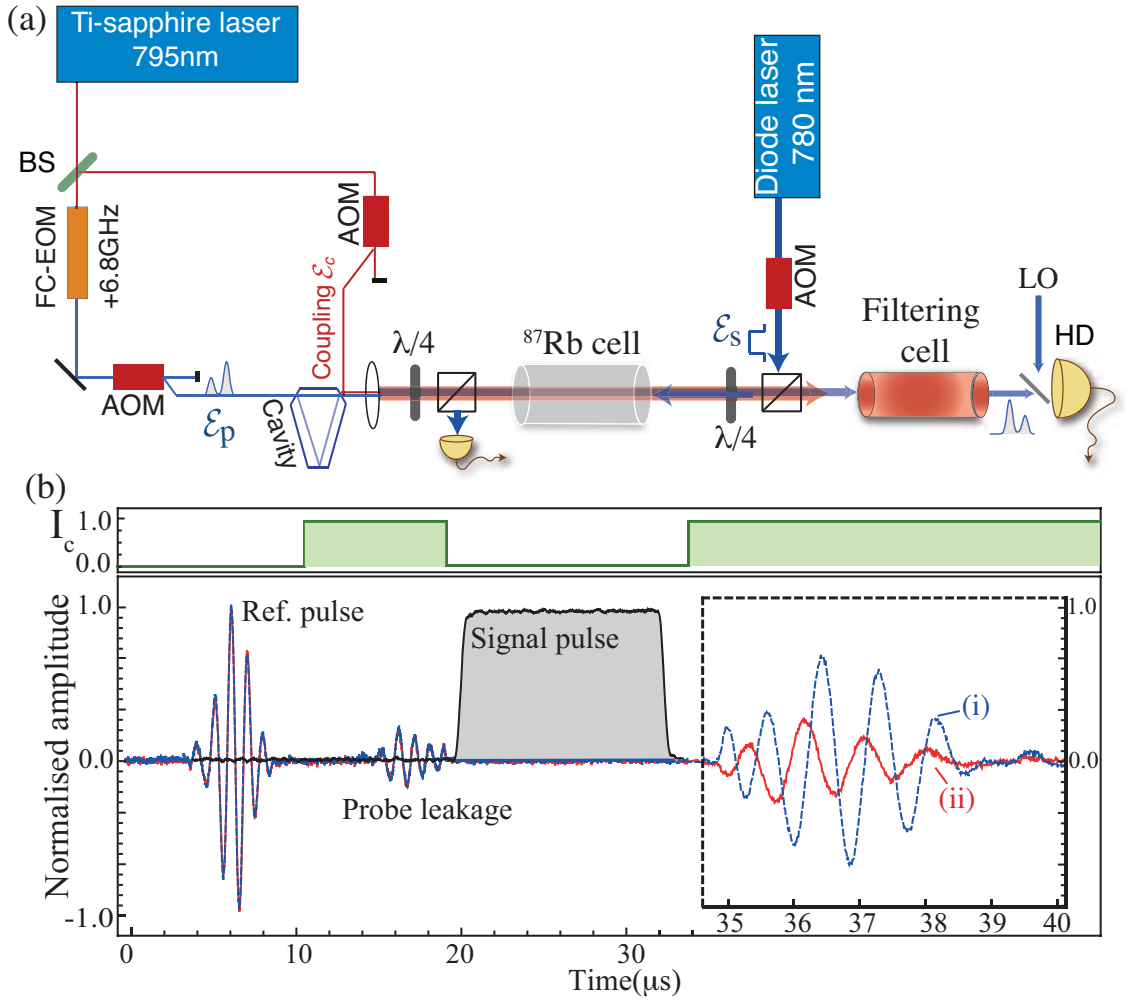

Figure 13.4: (a) Schematic experimental setup. The probe field ($\mathcal{E}_p$) is shifted by 6.8 GHz with respect to the coupling field ($\mathcal{E}_c$) using a fibre-coupled electro-optic modulator (FC-EOM) and is combined with the coupling field using a ring cavity. The counter propagating signal pulse ($\mathcal{E}_s$) at 780 nm is generated using a diode laser. The two beams are sent through the memory and filtering cell and heterodyne detection (HD) is performed afterwards. A counter-propagating signal pulse at 780 nm was used to induce the phase shift on the atomic coherence. All three beams are shaped in time using acousto-optic modulators (AOM). PBS: polarising beam splitter, $\lambda/4$ quarter wave-plate. (b) Heterodyne data showing normalised amplitude of the modulated phase reference, input and echo probe pulses. The top trace shows the switching protocol of the coupling field intensity. Traces (i) (blue) and (ii) (red) show the amplitude of $\mathcal{E}_p$ measured at the output of the memory without and with the signal pulse, respectively. Trace (ii) is taken 60 μs after (i) and overlapped using the reference pulse as a timing signal.

shifts can be achieved using cold atomic samples, this particular nonlinear interaction scheme might not be useful for single photon interactions. The signal field is not stored in the memory, meaning that the interaction time with the probe will be limited. We will now analyze a scheme in which the probe and signal fields are simultaneously stored in a double-GEM system. As before, the origin of this XPM is the ac-Stark effect, but the the available phase shift can be increased by increasing the interaction time.

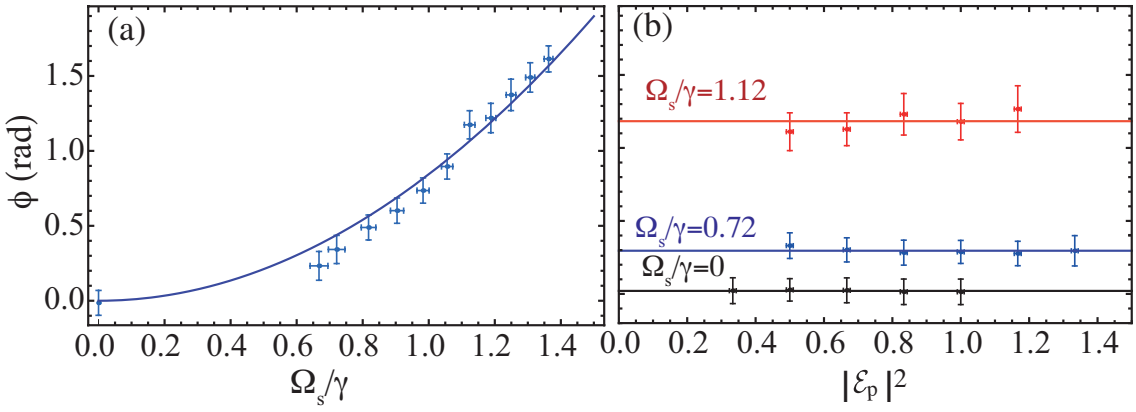

Figure 13.5: (a) Nonlinear phase shift as a function of signal pulse Rabi frequency. The solid line is the predicted theory curve. (b) Phase shift for a different signal pulse Rabi frequency as a function of peak intensity of the probe pulse normalised to the reference pulse.

13.5 XPM between two stored photons

We now propose a scheme in which the two fields (probe and signal) are simultaneously stored while exhibiting nonlinear interactions. In this scenario, it is the polariton that is phase shifted. To understand the XPM process in the memory, we use a polariton that is a superposition of the electric field, $\hat{\mathcal{E}}$ and atomic coherence, $\hat{\sigma}_{12}$, in the spatial Fourier domain [151], defined as $\hat{\psi}(t,k) = k\hat{\mathcal{E}}(t,k) + \mathcal{N}\Omega_c/\Delta\hat{\sigma}_{12}(t,k)$, where k is the spatial frequency, $\mathcal{N}$ is the effective linear atomic density, Δ is the Raman detuning from the excited state, $\hat{\sigma}_{12}$ is the atomic spin coherence and Ω_c is the coupling field Rabi frequency. During storage, the polariton evolves to higher k-values at a rate proportional to η. When using GEM for XPM, it is the polariton that will be phase shifted, leading to a phase shift of the photon echo on recall from the memory.

There are three properties of the polariton that are important to the following discussion i) The Fourier transform of the Maxwell equation gives $k\hat{\mathcal{E}}(t,k) = \mathcal{N}\hat{\sigma}_{12}(t,k)\Omega_c/\Delta$ [151]. Because the spin coherence has a constant amplitude during storage, the Maxwell equation implies that $\mathcal{E}$ is inversely proportional to k. ii) The polariton can be stopped in k-space by switching η to 0. For a pulse stored with $\eta = 0$, the group velocity of the optical component is found to be $v_g = g\mathcal{N}/k^2(\Omega_c/\Delta)^2$. iii) The polariton is purely atomic, $|\hat{\mathcal{E}}| = 0$, when the coupling field is off.

The ^{87}Rb level structure and nonlinear interaction scheme between two photons stored inside the memory are shown in Fig. 13.6. In this case the two photons (with Rabi frequencies of $g\hat{\mathcal{E}}_p$ and $g\hat{\mathcal{E}}_s$) can be stored independently in two atomic coherences, $\hat{\sigma}_{12}$ and $\hat{\sigma}_{1'2'}$, using two coupling fields with Rabi frequencies of Ω_c and Ω_c'. This can be done by introducing a linearly varying magnetic field to induce two detuning gradients with opposite slopes, resulting from the $m_f = 1$ and $m_f = -1$ Zeeman sublevels. If the coupling field on the right atomic coherence is turned off ($\Omega_c = 0$) after storage of the probe field, the photonic part of the polariton vanishes and the amplitude and phase of the probe field will be mapped to the ground-state coherence $\hat{\sigma}_{12}$.

Pulses enter the medium at slightly different times; therefore, by choosing the proper timing of the two coupling fields, it is possible to map each pulse independently in a different coherence. The coupling field Ω_c can then be turned off to map the probe photon

into $\hat{\sigma}_{12}$ and also reduce the decoherence due to the scattering during the storage time. The gradient can also be switched off in order to stop polariton evolution in k space. At a constant spatial frequency (k), the electric field's amplitude, as well as its group velocity, will remain unchanged (see Chap. 5).

The coupling field, Ω_c', will generate a slow light corresponding to the signal photon $\hat{\mathcal{E}}_s$. This slow light, as explained in the polariton description, corresponds to the photonic part of the polariton in that its strength and maximum interaction time with the atomic field can be tuned using the gradient field and the coupling beam. The slowly propagating light field can then modulate the phase of the coherence $\hat{\sigma}_{12}$. After a controllable interaction, the frequency gradient can be switched on to couple out the stored pulse. When the echo is emitted, the phase shift induced in the coherence is transferred to the output electric field. The intensity of the probe and signal fields, as well as the corresponding normal modes, are shown in Fig. 13.7 (a) and (b), respectively. The two polaritons remain at a constant spatial frequency (k) by switching the detuning gradient to zero soon after the signal pulse enters the medium.

The proposed scheme can be implemented in a cold atomic system where a long interaction time, as well as a large coupling strength can be achieved.

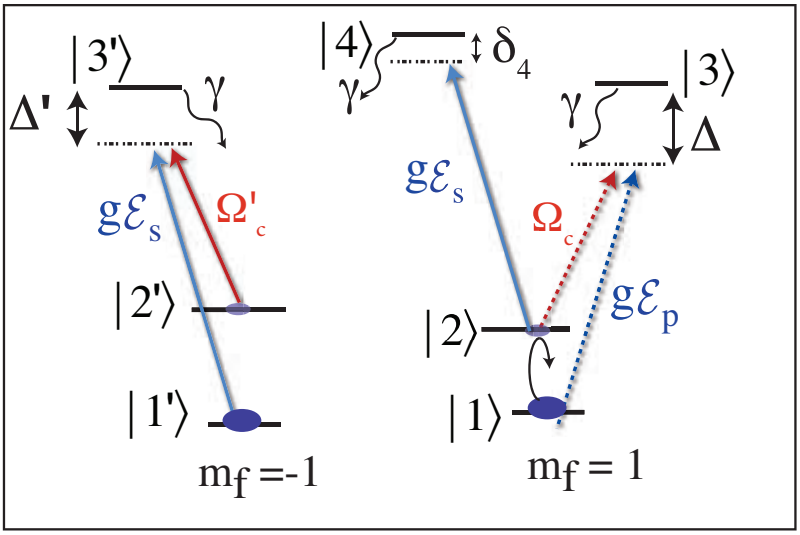

Figure 13.6: Schematic atomic-level structure of ^{87}Rb showing a scheme for the proposed nonlinear interaction. The probe $\mathcal{E}_p$ and signal $\mathcal{E}_s$ pulses arrived at different times and are independently mapped to atomic coherence $|1\rangle\langle 2|$ and $|1'\rangle\langle 2'|$ using two coupling fields Ω_c and Ω_c', respectively. The signal field can modify the phase of the atomic coherence ($|1\rangle\langle 2|$) via the ac-Stark effect.

13.5.1 Analytical solution

To find the conditional phase shift at the single-photon level, we solve the semiclassical equations of motion in two stages. Firstly, we consider the storage of two single photons (coherent states with mean photon number of 1) inside the memory. At this stage the gradient field and both coupling fields are on. Secondly, at time $t = \tau_1$ when the gradient field and the coupling field Ω is switched off, we solve the equations of motion in the steady state using the results from the first part as initial the condition to find the conditional phase shift.

The interaction Hamiltonian of the system with the level scheme depicted in Fig. 13.6 (a) can be written as

$$H_I = \frac{\hbar N}{L}\int [g\hat{\mathcal{E}}_p\hat{\sigma}_{31} + \Omega_c\hat{\sigma}_{32} + g\hat{\mathcal{E}}_s\hat{\sigma}_{42} + g\hat{\mathcal{E}}_s\hat{\sigma}_{3'1'} + \Omega_c'\hat{\sigma}_{3'2'} + H.c]dz \tag{13.4}$$

where σ_{ij} is the collective atomic spin operator, $g = \mu_{eg}\sqrt{\frac{\omega_0}{2\epsilon V\hbar}}$ is the atom-field coupling strength, and N is the total number of atoms in the quantisation volume V.

The simplified Heisenberg/Maxwell equations, assuming all of the populations are distributed between states $|1\rangle$ and $|1'\rangle$, can then be derived

$$\dot{\hat{\sigma}}_{13} = -(\gamma + i\Delta)\hat{\sigma}_{13} + ig\hat{\mathcal{E}}_p\hat{\sigma}_{11} + i\Omega_c\hat{\sigma}_{12} \tag{13.5}$$

$$\dot{\hat{\sigma}}_{1'3'} = -(\gamma + i\Delta')\hat{\sigma}_{1'3'} + ig\hat{\mathcal{E}}_s\hat{\sigma}_{1'1'} + i\Omega_c\hat{\sigma}_{1'2'} \tag{13.6}$$

$$\dot{\hat{\sigma}}_{1'2'} = -(\gamma_0 + i\delta_{1'2'}(t,z))\hat{\sigma}_{1'2'} + i\Omega_c^*\hat{\sigma}_{1'3'} \tag{13.7}$$

$$\dot{\hat{\sigma}}_{12} = -(\gamma_0 + i\delta_{12}(t,z))\hat{\sigma}_{12} + i\Omega_c^*\hat{\sigma}_{13} + ig\hat{\mathcal{E}}_s^\star\hat{\sigma}_{14} \tag{13.8}$$

$$\dot{\hat{\sigma}}_{14} = -(\gamma_0 + i\delta_{12}(t,z) + i\delta_4)\hat{\sigma}_{14} + ig\hat{\mathcal{E}}_s\hat{\sigma}_{12} \tag{13.9}$$

$$\frac{\partial}{\partial z}\hat{\mathcal{E}}_p = i\frac{gN}{2c}\hat{\sigma}_{13} \tag{13.10}$$

$$\frac{\partial}{\partial z}\hat{\mathcal{E}}_s = i\frac{gN}{2c}\hat{\sigma}_{1'3'}. \tag{13.11}$$

δ_{ij} is the two-photon detuning between level $|i\rangle$ and $|j\rangle$ that can be controlled in time and z using the external field. We also assume that the excited state decay rate γ is equal for all three excited states.

Using the steady state solution of Eq. 13.5 and spatial Fourier transform of Eq.13.10 we arrive at

$$k\hat{\mathcal{E}}_p(t,k) = \frac{gN}{2c}(\frac{\Omega_c}{\Delta})\hat{\sigma}_{12}(t,k) \tag{13.12}$$

This expression suggests that the relative phase of the electric field $\hat{\mathcal{E}}_p$ and the atomic coherence $\hat{\sigma}_{12}$ are always constant. Therefore, by tracking the atomic coherence phase one can infer the phase of the probe field at the output. The above expression also shows that the electric field amplitude linearly decreases in time as the spatial frequency k increases.

To find the phase shift induced by $\mathcal{E}_s$ during the interaction time, $\eta(\tau_1 < t < \tau_2) = 0$, we solve Eqs. 13.5 and 13.9 in the steady state, insert the results into Eq. 13.8 and obtain

$$\frac{d\sigma_{12}}{dt} = (-\gamma_0 + i\frac{|g\mathcal{E}_s|^2}{\gamma + i\delta_4})\sigma_{12} \tag{13.13}$$

The total loss and phase shift of the coherence σ_{12} during the interaction time are then respectively given by

$$\alpha = \int_{\tau_1}^{\tau_2}[\gamma_0 + \frac{|g\mathcal{E}_s(t-\tau_1)|^2\gamma}{\gamma^2 + \delta_4^2}]dt \tag{13.14}$$

$$\phi_{XPM} = \int_{\tau_1}^{\tau_2} \frac{|g\mathcal{E}_s(t-\tau_1)|^2\delta_4}{\gamma^2+\delta_4^2}dt \tag{13.15}$$

One can find a regime where the above loss term is negligible. In those regimes, the signal field amplitude inside the medium will remain constant during the interaction time, i. e. $\mathcal{E}_s(t-\tau_1) = \mathcal{E}_s(\tau_1)$. The maximum interaction time is then proportional to the medium length and inverse to the group velocity $v_g = \frac{\beta}{\eta\tau_1^2}$.

13.5.2 Numerical simulation

We performed numerical simulations using XMDS [180] to investigate the behaviour of the system considering realistic parameters. We numerically solve the Maxwell-Bloch equations of all seven atomic levels as depicted in Fig. 13.6(a) and monitor the phase of the signal pulse under different circumstances.

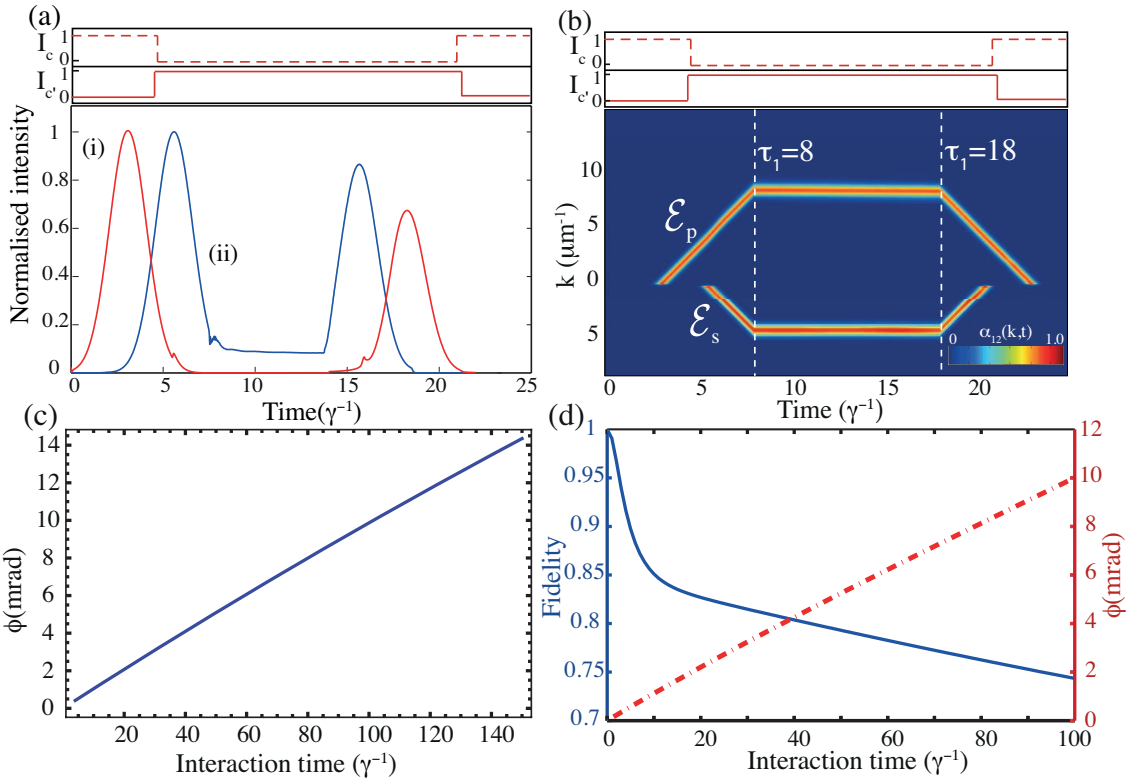

Figure 13.7: (a) Normalised intensity of the probe (i) and signal (ii) fields inside the memory, at different times, integrated over the space. The top part of the figure shows the switching protocols for the two coupling fields.(b) The total atomic coherence in spatial Fourier space (k) and time representing the evolution of two atomic fields in the $k-t$ plane. The gradient field is switched off during $8 < t < 18$. The top part of the figure shows the coupling field switching protocols. (c) Semiclassical simulation results showing a nonlinear phase shift between two coherent states with a mean photon number of one as a function of interaction time. The parameters used were: $\Omega_c = \Omega_c' = 10\gamma$, photon bandwidth= γ, $\Delta = \Delta' = 60\Omega_c$, $\delta_4 = 15\gamma$, $g = 0.085\gamma$ and number of atoms $N = 10^7$. (d) Results of quantum simulations for phase shift and phase gate fidelity as a function of interaction time. We assumed that the light is coupled to a 7-level atom with $g_{13} = g\sqrt{N}$, $g_{24} = g$, $g_{1'3'} = g\sqrt{N}$, and $\Omega_c = \Omega_c' = 20\gamma$. Other parameters are similar to the ones used in (c).

Fig 13.7 (a) shows the normalised intensity of the two fields integrated along the length of the memory at different times. As can be seen the probe field intensity drops to zero immediately after the coupling field Ω_c is switched off while the field is nonzero due to the signal pulse during the storage time because $\Omega_c' \neq 0$.

The normal modes resulting from the signal and probe fields are shown in Fig. 13.7 (b), where the spatial frequency of the two fields remains constant by switching the detuning gradient to zero soon after the signal pulse enters the medium.

We have observed a linear increase in the phase of the retrieved probe field as a function of the signal field intensity. The simulation shows no change in the phase of the probe field as its intensity increased, showing immunity to self phase modulation (SPM) [328]. The interaction strength is limited by the storage of the signal field which still has a non-zero group velocity in the memory. In order to increase the interaction strength and interaction time, one can use a pair of counter-propagating coupling fields to generate stationary light inside the memory. The application of a counter-propagating coupling field for the signal field would allow stationary trapping of the signal light (see Sec.7.3). The phase shift on the probe field due to the signal field is shown as a function of interaction time between them in Fig. 13.7 (c). Similar results have been obtained for the phase shift of a strong coherent state ($\alpha \sim 10^2$) resulting from interaction with a signal pulse with a mean photon number of one. Although the nonlinear phase shift for the proposed scheme is smaller than π, the current scheme can be used to implement parity or phase gates where the strength of the coherent states can offset the weakness of the nonlinearities [298, 291]. The simulation results suggest that $\alpha\theta > \pi$ is achievable in our scheme and therefore the error in discriminating in the final states (even and odd parity states) can be less than 10^{-3} [296, 298] which is near-optimal.

13.5.3 Quantum simulation

We also perform quantum simulations by solving the master equation numerically. The interaction scheme in this case is simplified so it can be solved using our available ultrafast computer. The quantum simulation, performed on the system during the interaction time ($\tau_1 < t < \tau_2$), yields useful information regarding the noise and gate imperfections. For this type of simulation, it is assumed that initially a photon is encoded in a coherence between $|1\rangle$ and $|2\rangle$ so the initial state of the atomic system becomes $\rho_{at} = 1/2\,(|1'\rangle\langle 1'| + |\psi_0\rangle\langle\psi_0|)$, where $|\psi_0\rangle = (|1\rangle + |2\rangle)/\sqrt{2}$. The initial state of the incoming signal photon is then given by $\rho_{ph} = |0_p, \psi_s\rangle\langle 0_p, \psi_s|$, where $|\psi_s\rangle = (|0_s\rangle + |1_s\rangle)/\sqrt{2}$, giving the total initial state $\rho(0) = \rho_{at} \otimes \rho_{ph}$. We also assume that the signal photon interaction is in the form of stationary light.

We solved the master equation including Langevin noise terms. From the resulting density operator, the conditional phase shift between a single photonic qubit in state $|\psi_s\rangle$ and the polaritonic qubit encoded in the atomic coherence $|\psi_0\rangle$ is calculated as a function of interaction time. The conditional phase shift ϕ and gate fidelity are shown in Fig. 13.7 (d) for parameters closely corresponding to the semiclassical simulations. The fidelity calculated here is that of a two-qubit controlled phase gate using single photons [329]. This fidelity is low, as expected, since the interaction between single photons is very fragile. This is not such an issue for the parity gate described above since the interaction between a single photon and a large coherent state is more robust against noise. Decoherence sources such as decay of the signal field amplitude due to Raman scattering (with lifetime of $\tau_{sc} \simeq (\Delta/2\Omega)^2/\gamma \simeq 200/\gamma$), spontaneous emission decay, and atomic spin dephasing

are included in the model. We found that the noise due to spontaneous emission is the dominant source of fidelity degradation.

13.5.4 Discussion

In the proposed scheme, far-detuned interactions, as well as tuneability and control over the strength and duration of the interaction, could potentially resolve the temporal mode-matching issue associated with other proposed XPM schemes. Although the nonlinear phase shift for the proposed scheme is smaller than π, the current scheme can be used to implement parity or phase gates where the strength of the coherent states can offset the weakness of the nonlinearities [298, 291].
Performing the experiment in a confined dipole trap system will also enhance the atom-light coupling strength by approximately three orders of magnitude due to the reduction in interaction volume, thus enhancing the phase shift by six orders of magnitude. Furthermore, interaction of atomic spin with the stopped single-photon wave packet (with duration of about $\sim$500 ns), instead of a freely propagating pulse of a 10 μs duration, can in principle enhance the phase shift per single photon by nearly two orders of magnitude. Accounting for all these enhancement factors, our experimental results support the optimal predicted phase shift of 10 mrad. The predicted phase shift is orders of magnitude larger than that available in EIT systems [314, 323].

13.6 Conclusion

We conclude by noting that, in addition to the demonstrated efficient quantum storage and capability to arbitrarily manipulate optical pulses, the versatility of GEM can be extended to implement a parity gate from which a CNOT gate can be constructed [298]. The lack of SPM and the demonstrated noiseless high-efficiency storage in our scheme suggests that the proposed method is a potential candidate for implementing practical XPM between single photons and coherent states, as well as other applications in optical quantum technology. Further multimode analysis in the Schrödinger picture is required to ensure that there are no obstacles in the realization of this scheme.

Chapter 14

Summary, Conclusion and Future Direction

"Where the storyteller is loyal, eternally and unswervingly loyal to the story, there, in the end, silence will speak. Where the story has been betrayed, silence is but emptiness. But we, the faithful, when we have spoken our last word, will hear the voice of silence."

Karen Blixen

14.1 Summary and conclusion

We have implemented an efficient and noiseless quantum optical memory using Rb vapour. We have demonstrated that more than 85% of the input light can be coherently recalled from the memory. We characterised the noise performance of the memory by storing single photon-level coherent pulses, measured the fidelity and conditional variances, and showed that the memory can in fact be used for quantum storage of optical information.

We have also demonstrated the ability of the memory in the manipulation of optical bits. These manipulations include: time-sequencing, spectral manipulation, backward retrieval, and arbitrary retrieval of optical pulses.

We have also demonstrated interference between polaritons inside the memory. The inference of light pulses with different frequencies mediated by an atomic field has also been shown.

Furthermore, we have shown a proof of principle demonstration of a conditional phase shift (non-linear phase modulation) between two coherent states. We also propose a new memory-based scheme for obtaining giant cross-phase modulation between single photons. The proposed method may ultimately pave the way for the implementation of universal quantum gates and the creation of cluster states applicable to one-way quantum computing.

14.2 Future directions

The future of the GEM project can potentially take different directions. Below we briefly mention a few experiments that can be done in future.

14.2.1 Observation of stationary light

As discussed in Chap. 7, using a pair of counter-propagating coupling fields it is possible to trap light inside the atomic sample. Experimental demonstration of this effect may

contribute to the possibility of obtaining large cross-phase modulation between single photons.

14.2.2 Simultaneous storage of two frequency sidebands

Using multiple pairs of Zeeman sublevels of the Rb ground state, it is possible, in principle, to simultaneously store multiple sideband frequencies. Storage of two sidebands can be experimentally demonstrated using a single-frequency coupling field in ^{87}Rb. Two of the Zeeman sublevels of the Hyperfine ground state $F = 1$ ($m_f = \pm 1$) should be separated by a frequency difference between the two optical sidebands. This demonstration could be useful for storage of squeezed sidebands without the need for a large memory bandwidth. A proof-of-principle demonstration of this possibility will also support the idea of enhancing low-light-level cross-phase modulation, as the scheme proposed in Chap. 13 relies on the simultaneous storage of two single photons at different frequencies.

14.2.3 Storage of a single photon, squeezing and entanglement

A quantum memory should be able to preserve entanglement after the storage and recall of information. This is crucial in the implementation of quantum repeaters. The long-term plan of the experiment is to demonstrate that the Raman GEM is capable of preserving quantum properties both in the CV and DV regimes. The CV entanglement generated by interfering two squeezed beams, as well as heralded single photons, will also be used as quantum sources to characterise the memory.

14.2.4 GEM in dipole trap

Implementation of GEM in a cold atomic sample such as a dipole trap can potentially increase the storage time to more than 3 orders of magnitude. The possibility to generate the frequency gradient required for storage using an ac-Stark gradient, instead of a magnetic field gradient, has been studied by B. Sparkes [155]. This technique will be used in the construction of the gradient echo memory in a cold atomic ensemble.

Appendix A: Experimental details

A.1 Rb vapour properties

Some of the basic physical properties of ^{87}Rb atoms are provided in Table A.1. The $5^2S_{1/2} \rightarrow 5^2P_{1/2}$ (D1 line) and $5^2S_{1/2} \rightarrow 5^2P_{3/2}$ (D2 line) transitions are the components of a fine-structure doublet.

Atomic Number	37
Neutrons and Protons	87
Relative Natural Abundance	27.83(2)%
Atomic Mass	$1.44316060(11) \times 10^{-25}$ kg
Density at 25^oC	$1.53 g/cm^3$
Melting Point	39.31^C
Boiling Point	688^oC
Vapour Pressure at 25^oC	3.0×10^{-7} Torr
Nuclear Spin	3/2
$D_1(52S_{1/2} \rightarrow 5^2P_{1/2})$ Transition Dipole Matrix Element	$2.537(3) \times 10^{-29} Cm$

Table A.1: ^{87}Rb physical properties. All values are taken from Ref. [2]

The D_2 line transition of ^{87}Rb has a wavelength of 780 nm and three hyperfine levels (F=0,1,2) in the upper state. D1 and D2 line transitions together with hyperfine and Zeeman level structure of ^{87}Rb is shown in Fig. A.1 (a). Fig. A.1 (b) shows the saturation absorption of the D2 transition line of Rb.

In a vapour cell the atomic density of Rb is highly dependent on the temperature of the cell. Atomic density of ^{87}Rb as a function of temperature is shown in Fig. A.2 for temperatures above the melting point.

A.2 Magnetic coil design

Spectral manipulation can be performed inside the memory by proper engineering of the detuning field. Rather than just inverting a simple linear gradient, we can invert different parts of the gradient at different times, add shifts to the atomic frequency spectrum, and change the recall gradient by invoking a more general atomic frequency spectrum $\eta(t, z)$. To perform this task, one should be able to generate a detuning field and switch the field at different segments of the memory independently and at different times.

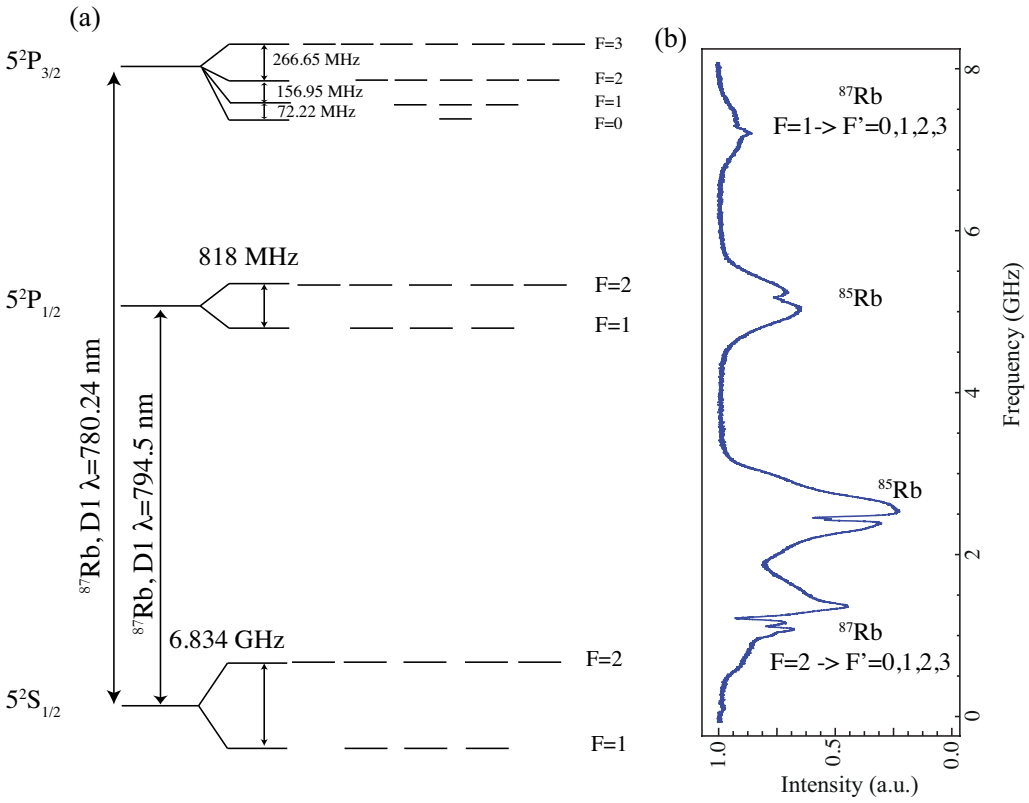

Figure A.1: (a)Atomic-level structure for the D_1 line ($5^2S_{1/2} \rightarrow 5^2P_{1/2}$) of ^{87}Rb. Two hyperfine ground states (F=1 and F=2) and two hyperfine excited states (F=1 and F=2) contains 3 and 5 Zeeman sublevels, respectively. (b) Saturation absorption of the D2 transition line of ^{87}Rb.

To generate the magnetic field that we need, we can either spatially vary the coil spacing or vary the current flowing inside the coil. Constructing the variable-pitch coil

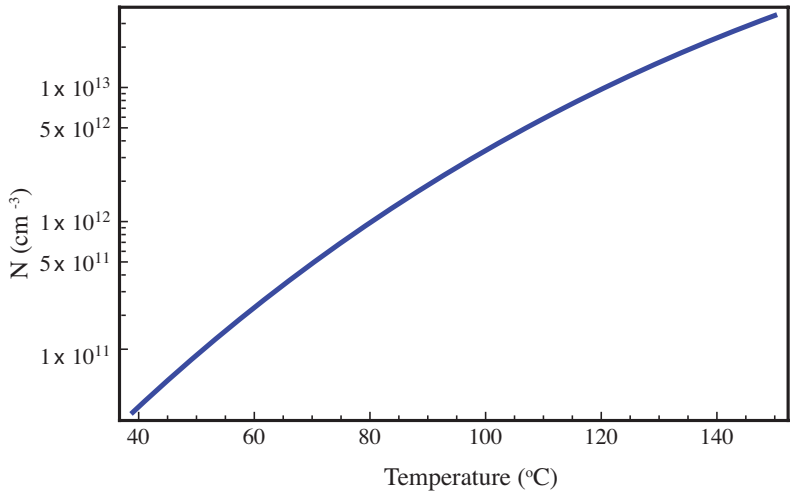

Figure A.2: Calculated number density of ^{87}Rb using the pressure-temperature relation from Ref. [2] and the ideal gas law.

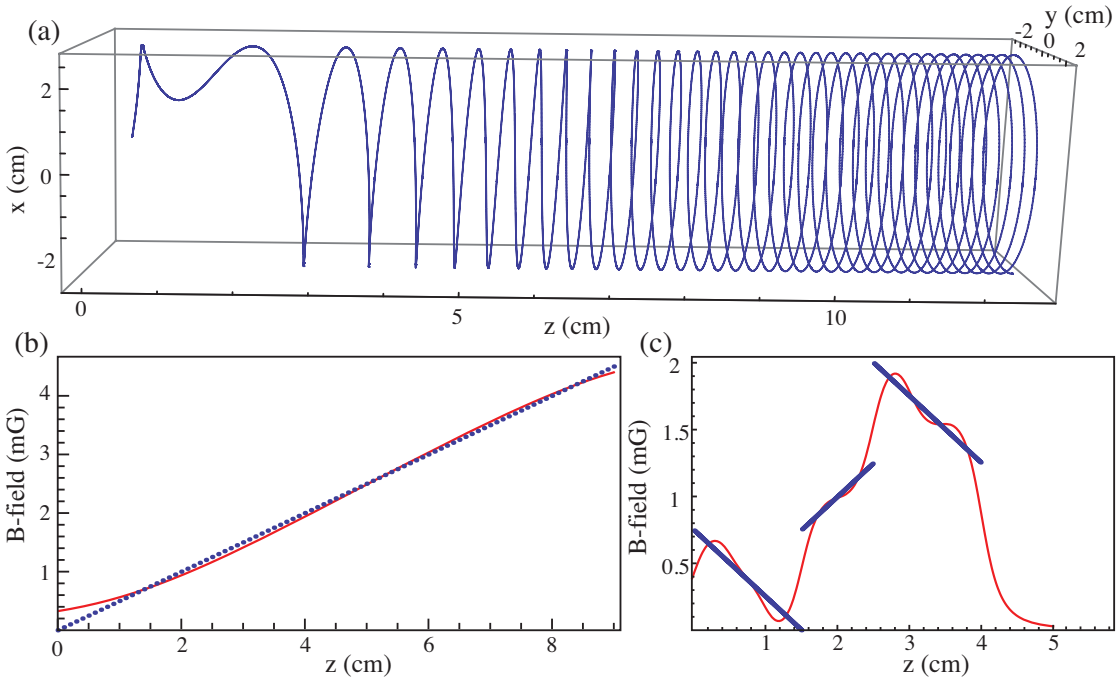

Figure A.3: (a) The shape of the solenoid required to generate a linear field as predicted by theory. (b) The ideal linearly varying magnetic field along the propagation axis (blue dotted line) and expected field (red solid line) from the solenoid shown in (a). (c) An arbitrary magnetic field along the propagation axis predicted by an 8-segmented-coil design. The solid blue line is the ideal shape and the red line is the expected field if all eight segments are placed next to each other with a particular current flowing in each segmented coil as shown in Fig. A.5 (a).

at a fixed current is simple since there is only one current to switch. The drawback is that the field is fixed since the coil spacing cannot be modulated. The advantage of the multi-segment design is that one can dynamically tune the field. The downside is that it is complicated to feed in all those different currents.

To create a magnetic field with a particular shape along the memory cell we modified a code originally written by *Simon C. Bell* in Mathematica that predicts the shape of the solenoid for particular fields.

A.2.1 Single coil design

To generate a linear magnetic field we designed a solenoid more than twice as long as the memory cell to reduce the end effects. The shape of the solenoid required to generate a linear field is shown in Fig. A.3 (a). Fig. A.3 (b) shows the ideal linearly varying magnetic field along the propagation axis (dotted line) and the expected field (red solid line) from the solenoid design shown in Fig. A.3 (a).

For fast switching of current in the coils we used a resistor in series with a super-fast solid-state switch. Fig. A.4 (a) and (b) show the switching circuit and the solid state switch used in the circuit, respectively.

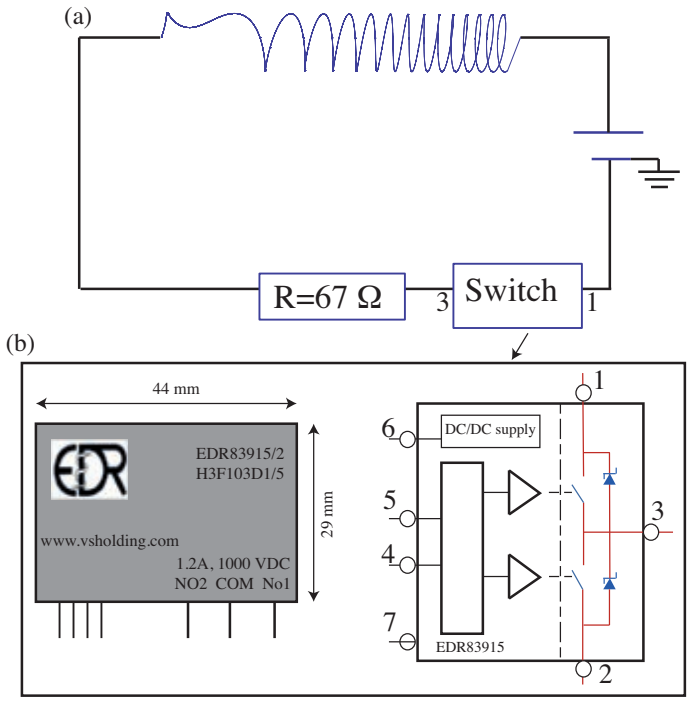

Figure A.4: (a) Switching circuit and (b) solid state super fast switch used to switch the current in the circuit. The switch was purchased from www.vsholding.com

A.2.2 Multiple coil design

A multiple coil was also designed to be used to perform the spectral manipulation experiment [330]. This design was first created with the help of *Pete Uhe*. The key to this design is to put different currents in the segments built nearly identical to each other. The schematic coil design is shown in Fig. A.5 (a). The solid line in Fig. A.5 (b) shows an arbitrary shape of the magnetic field expected from eight individual coils placed along the memory. The blue points are the magnetic field measured at the centre of the coil along the propagation axis.

A.3 Oven design for the filtering cell

An oven was designed for the filtering cell as shown in Fig. A.6(a). The aim of this design was to reduce the air current at high temperatures around the cell windows that can affect the mode matching of the homodyne detection.

A bifilar resistive wire was used as heater and designed such that the cell windows became warmer than the middle of the cell to avoid Rb condensation on the windows. The cell was mounted on two hollow cylindrical Teflon tubes to guide the laser beams. This reduced the air current around the windows. The entire setup was placed inside aluminium shielding that allowed us to fit cells with various lengths. The two holes in the middle of the shielding were to guide the air current and to make the middle of the cell colder than the windows.

A picture of the filtering cell is shown in Fig. A.6(b) in which the coupling field shone from the left is absorbed and blue light is scattered. The reason for the blue scattered light is excitation of Rb atoms to the $5D$ excited state and spontaneous emission of 420

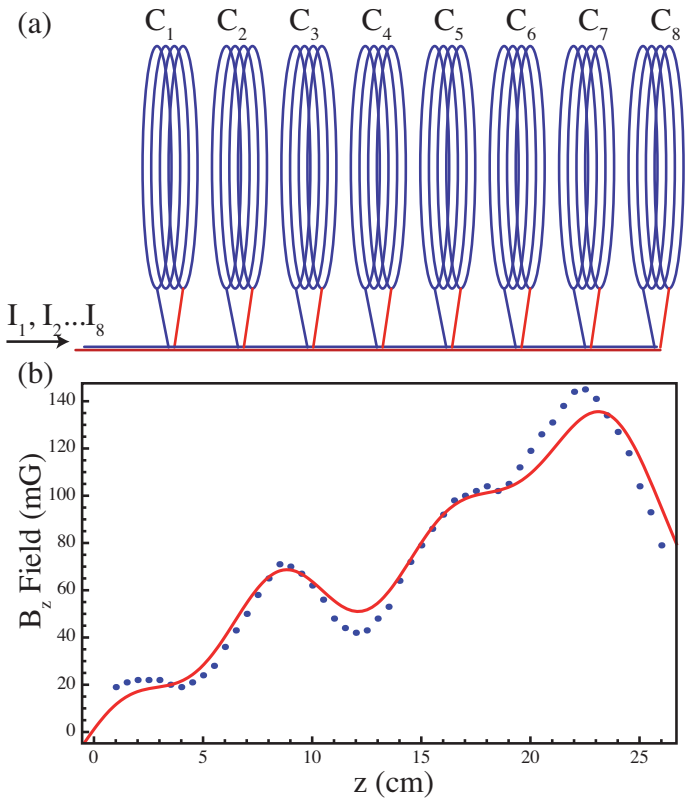

Figure A.5: (a) The schematic design of the 8-segmented coil. (b) Experimental (blue points) and expected theory (solid red line) showing the magnetic field of an eight-segmented coil with different current generating an arbitrarily field. Coil was designed and data taken by *Pete Uhe*.

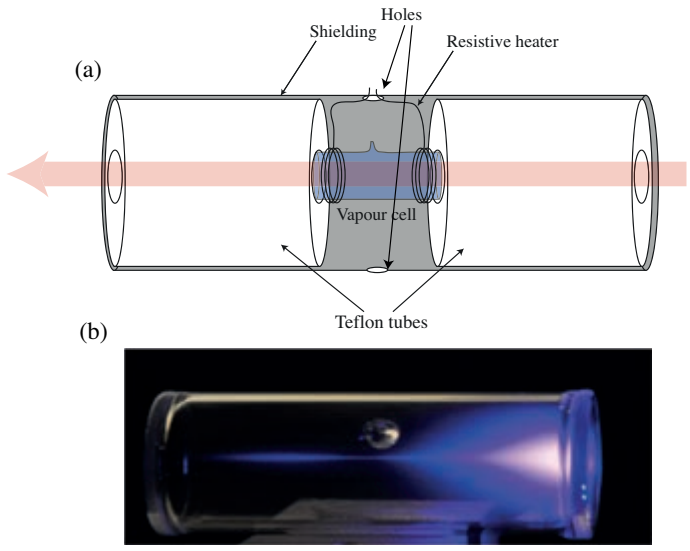

Figure A.6: (a) Schematic design of an oven for the filtering cell. (b) A picture of the filtering cell, warmed up to a temperature around 130° C, scattering blue light when exposed to 300 mW of the coupling field power.

nm light. This phenomenon is only seen at very high temperatures ($> 120°C$) where the thermal energy of the atoms is high.

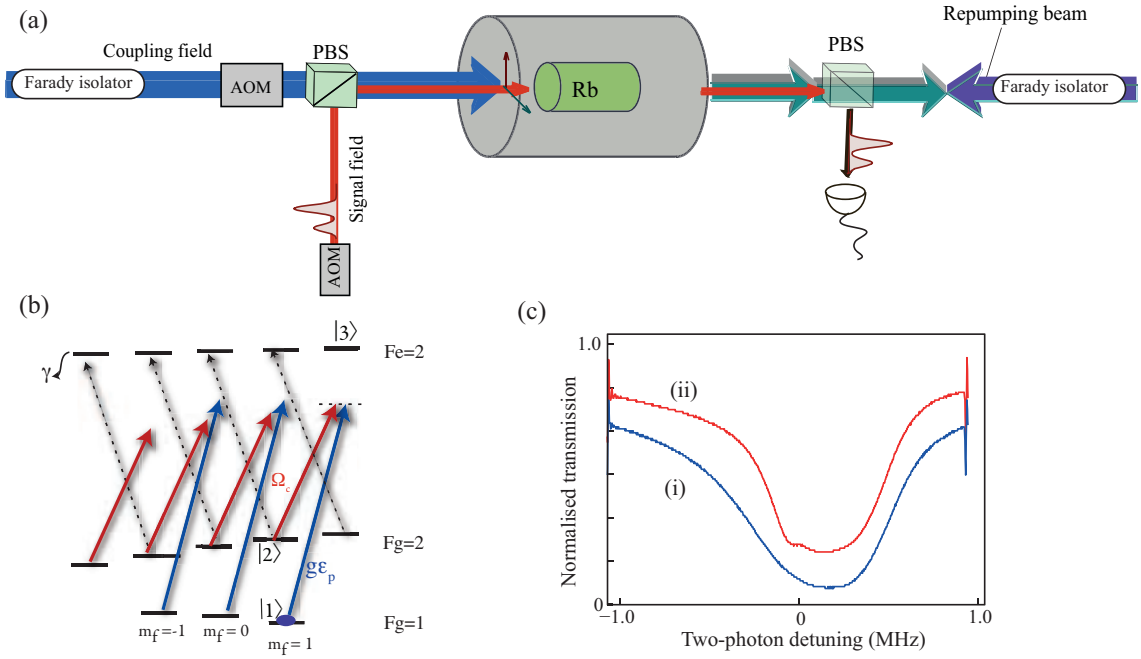

Figure A.7: (a) Schematic experimental setup showing a repumping beam backward propagating with linear polarisation. (b) Atomic level structure showing the control, probe and repumping beam transitions. (c) The Raman absorption line with (i) and without (ii) the repumping beam. The repumping also increases the incoherent absorption of the probe field.

A.4 The effect of re-pumping on storage

One of the differences between EIT and GEM is that in the case of EIT, due to resonant interaction of the control field, populations are mostly pumped to the ground state, $|1\rangle$, where the signal field is interacting. In GEM, however, off-resonant interaction of the coupling field suggests the possibility of some remaining population in other atomic states. An initial repumping can ensure that all population are in $|1\rangle$ to start with. We observed a noticeable effect by applying a repumping beam to resonantly interact with $2S_{1/2}, F = 2 \rightarrow 5P_{3/2}, F' = 2$. This effect was observed in the setup shown in Fig. A.7 (a). The repumping beam is counter-propagating with the signal and the coupling beams. The coupling field which interacts with the sample long before the probe pulse arrives will play the role of the repumping beam and move the population to either $F_g = 1, m_f = 1$ or $F_g = 2, m_f = 2$. As shown in Fig. A.7 (b), a counter-propagating resonant beam will pump most of the population from $F_g = 2, m_f = 2$ to $F_g = 1, m_f = 1$. This will considerably enhance the optical depth of the sample. The Raman lines with and without repumping beams are shown in Fig. A.7 (c). As can be seen, applying the repumping beam increases the absorption. We note here that the repumping beam should be turned off during the storage sequence in order to avoid further loss through spontaneous emission.

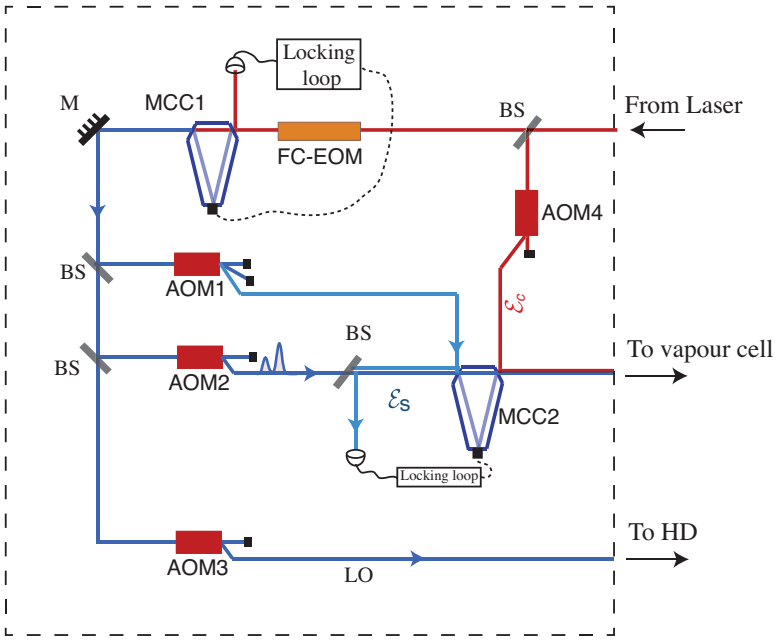

Figure A.8: Schematic representation of the experiment for combining and separating of different frequency beams. M: Mirror, BS: beam splitter, MCC: Mode cleaner cavity (or ring cavity), AOM: Acousto-optic modulator. FC-EOM: Fibre-coupled electro-optic modulator.

A.5 Combining and separating beams using ring cavities

Fig. A.8 shows how beams with different frequencies are being combined or separated via ring cavities. A laser beam going through the fibre-coupled EOM is frequency modulated at 6.8 GHz. The "-1" sideband and carrier is filtered using mode-cleaner cavity 1(MCC1) and "+1" sideband (+6.8 GHz) is transmitted through the cavity. The output of the cavity is divided into 3 parts. The first part is used to lock the second MCC after going through AOM1 and selecting the frequency-shifted beam. AOM 2, is used to generate and shape the signal beam transmitted through the MCC 2. AOM 1 and AOM 2 have different frequencies, and MCC2 is locked to the TEM_{01} mode, which allows transmission of the signal field with the TEM_{00} mode at the AOM1 frequency. This is done to avoid transmission of the coupling field through the cavity and also back-reflection of the locking beam through the cavity from the detector. The last part of the beam is used as the LO beam for homodyne detection (HD). The coupling field has a frequency difference of 6.8 GHz and is shaped via AOM 4. The coupling field is reflected from the MCC2 and together with the signal beam is guided though the vapour cell.

A.6 Optimum storage

The storage of a light pulse can be optimised in two ways. The shape of the magnetic field along the vapour cell can be designed in such a way to maximally absorb the input light pulse. This is possible by producing a Raman absorption line that matches the shape of the Fourier transformed input pulse. To generate such a Raman line, it requires precise engineering of the field as well as precise switching of the field. Alternatively, the input pulse shape can be optimised for storage by an iterative process similar to EIT

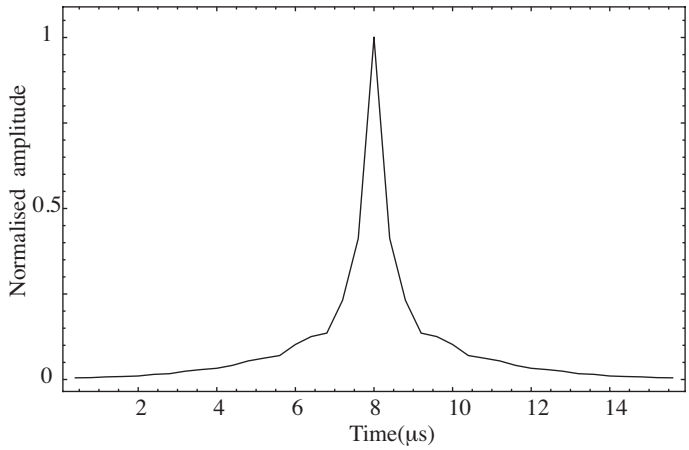

Figure A.9: Fourier transform of an experimental Raman line broadened to 500 kHz

optimisation protocol [195]. In principle, the optimum shape of the input pulse should match the Fourier transform of the broadened Raman absorption line, which in the ideal case resembles the shape of a Sinc function. The Fourier transform of the broadened Raman line (experimental) is shown in Fig. A.9.

Appendix B: AC Stark gradient echo memory in cold atoms

In this appendix we discuss an alternate gradient-creation mechanism using the ac Stark effect to provide an improvement in the flexibility of gradient-creation and field-switching times. We propose this scheme in concert with a move to cold atoms (1 mK). These temperatures would increase the storage times, and the small ensemble volumes would enable large ac Stark shifts with reasonable laser power.

This idea has been investigated in detail by Ben Sparkes and the results of this work appeared in the following article:

ac Stark gradient echo memory in cold atoms, B. M. Sparkes, M. Hosseini, G. Hetet, P. K. Lam, and B. C. Buchler, Phys, Rev. A 82 043847 (2010).

B.1 Introduction

One option for improving gradient creation and control would be to move away from magnetic fields, and the coils necessary to create them, to an ac Stark shift. This would allow for an all-optically controlled quantum memory. This gradient-creation method was first put forward by Kraus et al. [331]. Another option for improvement is to move from warm to cold atoms. The low decoherence rates in cold atomic ensembles would allow for longer storage times and large on-resonance optical depths, due to the increase in density of the atoms. Implementing these improvements in concert would be beneficial as the ac Stark effect is intensity-dependent and cold atoms can be induced to occupy small volumes, reducing the necessary laser power.

B.2 Scheme

To change an initially Gaussian beam to one with an intensity profile requires a beam shaper. These devices [for instance, deformable mirrors, phase plates, or liquid-crystal spatial light modulators (LCSLMs)] can be highly efficient (> 0.9) and can be used to create nearly any desired beam shape with a resolution on the order of 1000×1000 pixels for LCSLMs. This not only provides us with a method for optimising the ac-Stark laser intensity profile, but would also allow for spectral manipulation of the pulse to be carried out with the ability to produce complex gradients and switching arrangements.

To induce rephasing of the atomic dipoles, we must be able to invert the detunings of the atoms. There are two ways to invert the gradient generated by the ac-Stark effect. The

first method involves reversing the intensity profile along the ensemble $I(z) \rightarrow I(L-z)$. This is equivalent to the field-switching method in which by reversing the intensity profile about the centre of the trap (z = L/2), the detunings are also reversed about this point, that is, $\delta t(z) \rightarrow \delta t(L-z)$. This process involves no change in the frequency of the stored pulse with respect to the input pulse.

The second method involves switching the polarisation of the field $q \rightarrow -q$ while keeping the same intensity gradient. This is a slightly more complicated process as the detunings are no longer reversed around the centre of the ensemble, with $\delta t(z) \rightarrow \delta t(z)$. This method still results in an echo being produced; however, the stored pulse will now be frequency shifted with respect to the input pulse. This is because a switch from $\delta t(z) \rightarrow \delta t(z)$ is equivalent to a switch about the centre with an offset added. In a three-level system, this frequency shift can be overcome by altering the coupling-field frequency in such a way as to cancel the initial shift.

The first switching method would allow for different gradients but involves much longer switching times (on the order of milliseconds for LCSLMs). The second switching method would suggest itself as the easiest to implement as all that is required to switch $\delta(z)$ would be a Pockels cell, which has switching times down to nanoseconds. It would not, however, allow for different frequency gradients and consequent filtering or manipulation of the pulse.

The envisaged experiment is shown in Fig. B.1. The combination of beam shapers (BShs) and Pockels cells (PCs) shown in Fig. B.1 (a) allows for flexibility in beam shaping and fast switching times. If no spectral filtering is desired, then only PC2 and BSh1 are needed, with the beam shaper determining the shape of the gradient and the polarisation switch causing the rephasing of the atoms. To allow different gradients to be used, an extra Pockels cell PC1 and beam shaper BSh2 can be used. In this case, the second gradient can be prepared in advance and PC1 used to select which beam shaper to use. The acousto-optic modulator (AOM) can be used to switch the ac Stark beam on or off to decrease the scattering rate due to this field.

A critical parameter that must be determined is the wavelength of the ac Stark laser to be used, as this will set a limit on the maximum frequency splitting possible for a given laser power and intensity distribution, as well as the scattering rate of the system. To optimise the wavelength, one must balance the desired behaviour (i.e., frequency splitting) with the undesired effect of light scattering by the atoms.

We find that memory bandwidths on the order of MHz can be produced with experimentally achievable laser powers and trapping volumes, with high precision in gradient creation and switching times on the order of nanoseconds possible. By looking at the different decoherence mechanisms present in this system, we determine that coherence times on the order of tens of milliseconds are possible, as are delay-bandwidth products of approximately 50 and efficiencies over 90%.

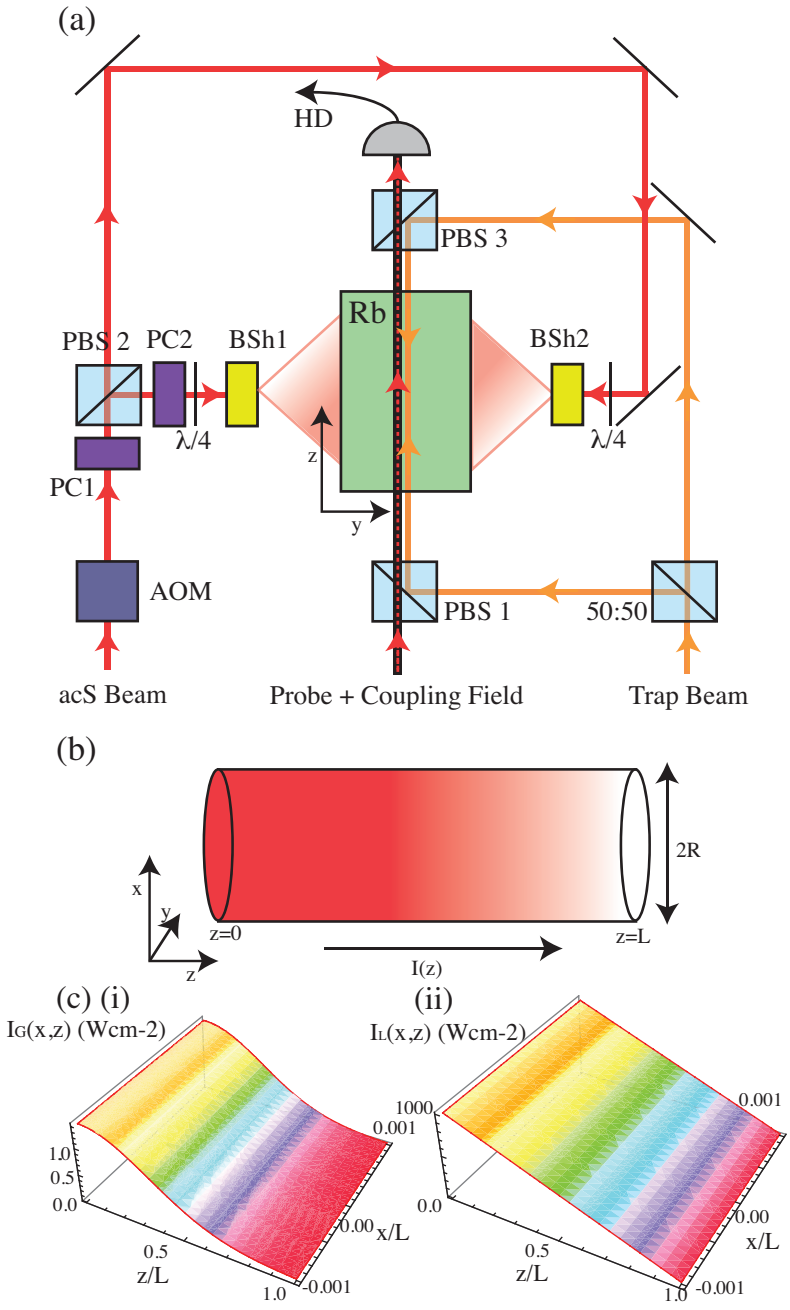

Figure B.1: The proposed experiment. (a) Envisioned setup for a GEM experiment using cold atoms and an ac Stark gradient. Rb, atomic ensemble of ^{87}Rb; 50:50, 50:50 beam splitter; PBS, polarising beam splitter; PC, Pockels cell; BSh, beam shaper; HD, heterodyne detector. The polarisations of the ac Stark and trapping fields are assumed to be linear, while optimal probe and coupling-field polarisations are discussed in Sec. III E. (b) Side-on view of the cylindrical atomic ensemble showing the direction of the intensity gradient I (z) and radius R. (c)(i) Gaussian and (ii) linear intensity profiles for the ac Stark field per unit power over the ensemble. Here L has been taken to be 1 cm and R = 10 µm, which are determined by the radius of the trapping laser.

Appendix C: XMDS programming

The eXtensible Multi-Dimensional Simulator (xmds) is open source software, developed by P. T. Cochrane, G. Collecutt, P. D. Drummond, and J. J. Hope, released under the GNU General Public License, and is written to assist in the solution of various differential equations. A high-level description of the problem at hand is written in XML (the extensible markup language) and XMDS transforms this into C language code. This code can then be compiled by a C/C++ compiler to produce a binary executable which solves the problem about as quickly and efficiently as might be achieved with code written by an expert. In this appendix we provide two sample codes written in XMDS (version 1 and 2) used to simulate an atomic memory which works based on the gradient echo technique.

C.1 Sample XMDS script

A sample xmds code provided below was used to solve the propagation of an electric field in the GEM system. This code was modified and used to simulate many other problems related to the Λ-GEM scheme.

<?xml version="1.0"?>
<!– – Example Simulations illustrating GEM Storage in Three Level Atom –– >
< author > Originally written by G. Hetet and modified by M. Hosseini < /author >

< simulation >
<! – – Each xmds simulation is enclosed within a set of *< simulation >* tags –– >
< error_check > yes < /error_check >
<! – – Optional. Whether or not to run the simulation at the half-time step as well as at the full time step and give the difference between the results. Defaults to yes –– >
< prop_dim > z < /prop_dim >

<! – – The propagation dimension of the cross propagating vector –– >
<! – – In the following part, globals are used to define any numerical constants that are useful to have globally available to all sections of code–– >
< globals >
<![CDATA[
const double $g = 1.0$;
const double *sample_length* $= 1.0$;//Length of the sample
const double *time_input* $= 3$;//mm

const double $sigma = 1.5$;
const double $inp\_hgt = 1.0$;
const double $gama = 1.0$;
const double $eta = 2$;
const double $omc = 12.0$;
const double $gama0 = 0.001$;//Normalzied to gamma
const double $gamac = 0.001$;//Normalzied to gamma
const double $timeswitchz = 10.0$;
const double $N = 5200$;
const double $delta = 700.0$;
]] >
< /globals >

<! − − The following part is a container for the other information that we are using to describe the field. If no name is given for the field, it defaults to "main". The vector is written in terms of the dimensions of the field. It is possible to define other vectors that are part of the field, but the vector of the field that is integrating is the main vector− − >

< field >
< dimensions > t < /dimensions >
< lattice > 12000 < /lattice >
< domains > (0.0, 20.0) < /domains >
< samples > 1 1 < /samples >

< vector >
< name > main < /name >
< type > complex < /type >
< components > E < /components >
$E = inp\_hgt * exp(-(t - time\_input) * (t - time\_input)/(sigma * sigma))$;
< /vector >
<! − −The CDATA section gives the C code version of what equations of motion describes.− − >
< vector >
< name > cross < /name >
< type > complex < /type >
< components > alpha12alpha13 < /components >
<![CDATA[
$alpha12 = 0.0$;//atomic coherence
$alpha13 = 0.0$;//atomic coherence
]] >
< /vector >

< /field >

<! − −In the sequence section we tell xmds how to actually perform the integration of the field. It may have as many of the other sub-elements as desired to perform the calculation. An algorithm tag is optional and will default to SIEX for stocastic simulations and to RK4EX for non-stochastic simulations. The length of the integration interval, the

total number of steps to take, and the number of samples for each output moment to take within these steps are denoted by the $< interval >$, $< lattice >$ and $< samples >$ tags respectively. The differential equation is described in terms of the C language code that xmds is to use to evolve the solution forward$-->$

$< sequence >$
$< integrate >$
$< algorithm > RK4EX < /algorithm >$
$< interval > sample\_length < /interval >$
$< lattice > 800 < /lattice >$
$< samples > 400\ 400 < /samples >$
$< vectors > maincross < /vectors >$
$<![CDATA[$
$dE\_dz = i * g * N * (alpha13);$
$]] >$
$< cross\_propagation >$
$< vectors > cross < /vectors >$
$< prop\_dim > t < /prop\_dim >$
$<![CDATA[$
double $sw = (t < timeswitchz\ ?\ -1.0 : 1.0);$
$dalpha13\_dt = (-1.0 * gama - 1.0 * gama0/2 - gamac/2 - i * delta) * alpha13 + i * g * E + i * (omc) * alpha12;$
$dalpha12\_dt = (-1.0 * gama0 - gamac - i * (sw * eta * (z - sample\_length/2) + (omc * omc)/delta)) * alpha12 + i * alpha13 * (omc);$
$]] >$
$< /cross\_propagation >$
$< /integrate >$
$< /sequence >$

$<!--$Output element: The $< output >$ element is just a container for the other tags that specify what is to be output. The $< filename >$ tag (fairly obviously) specifies the filename of the output data file. This tag is optional and defaults to the simulation name. The $< group >$ tag contains a description (and to a degree the definition) of the moments of the output data. $-->$

$< outputformat = "binary" >$

$< group >$
$< sampling >$
$< type > complex < /type >$
$< lattice > 400 < /lattice ><!--fort-->$
$< moments >$ probereal probeimag coupling $< /moments >$
$<![CDATA[$
$probereal = real(E);$
$probeimag = imag(E);$

$]] >$
$< /sampling >$
$< /group >$

```
    < group >
< sampling >
< vectors > maincross < /vectors >
< type > complex < /type >
< lattice > 400 < /lattice ><! − −fort − − >
< moments > alpreal12 alpimag12 alpreal13 alpimag13 < /moments >
<![CDATA[
alpreal12 = real(alpha12);
alpimag12 = imag(alpha12);
alpreal13 = real(alpha13);
alpimag13 = imag(alpha13);
]] >
< /sampling >
< /group >

    < /output >
< /simulation >
```

C.2 Sample XMDS2 script

XMDS2 is the second version of xmds developed to simulate more complicated systems. We used this version to simulate counter-propagating fields inside a GEM system. A sample code describing counter-propagation fields inside a three-level GEM is provided below.

```
<?xmlversion = "2.0" encoding = "UTF − 8"? >
<simulation xmds-version="2" >
< name > thlcp < /name >
< author > M.Hosseini < /author >
< description >
Three level atom example simulation. Illustrates a counter-propagating fields.
< /description >

    < features >
< benchmark/ >
< error_check/ >
< bing/ >
< fftwplan = "patient"/ >
< globals >
<![CDATA[
const real g = 1;
const real samplelength = 1; //cm
const real time_input = 2;
const real sigma = 0.5;
const real inp_hgt = 1;
const real gama = 1;
```

const real $eta = 500$;
const real $om = 30$;
const real $gama0 = 0$;
const real $gamac = 0.0$;
const real $w12 = 1.0$;
const real $timeswitchz = 5.0$;
const real $timeswitchc = 5.0$;
const real $N = 20000$;
const real $delta = 600$;
]] >
< /*globals* >
< /*features* >

<! − − In the following part, all of the dimensions used in the problem are defined, but in this case, only the dimensions of "time" and "z" are needed −− >
< *geometry* >
< *propagation_dimension* > t < /*propagation_dimension* >
< *transverse_dimensions* >
< *dimension* name="z" lattice="16000" domain="(0,1)" / >
< /*transverse_dimensions* >
< /*geometry* >

<! − − In the following part "b" stands for the backward propagating field −− >

< *vector* name="main" *initial_space* = "*z*" type="complex">
< *components* > *alpha*12 *alpha*13 *alphab*13 *alphab*12 < /*components* >
< *initialisation* >
<![*CDATA*[
$alpha12 = 0$;
$alpha13 = 0$;
$alphab13 = 0$;
$alphab12 = 0$;
]] >
< /*initialisation* >
< /*vector* >

< *vector name* = "*cross*1" *initial_space* = "*z*" *type* = "*complex*" >

< *components* >
E
< /*components* >
< /*vector* >

< *vector name* = "*cross*2" *initial_space* = "*z*" *type* = "*complex*" >

< *components* >
Eb
< /*components* >

```
    < /vector >

    <!−− Here we define what differential equations need to be solved and what algorithm
we want to use −− >
    H < sequence >
< integrate algorithm = "ARK89" interval = "10" steps = "8000"
tolerance = "1.0e − 6" >
< samples > 400 400 < /samples >

    < operators >
< operatorkind = "cross_propagation" algorithm = "RK4" propagation_dimension =
"z" >
< integration_vectors > cross1 < /integration_vectors >
<! − − You can have a dependencies tag here. −− >
< dependencies > main < /dependencies >
< boundary_conditionkind = "left" >
<![CDATA[

    E = inp_hgt ∗ exp(−(t − time_input) ∗ (t − time_input)/(2 ∗ sigma ∗ sigma));

    ]] >
< /boundary_condition >
<![CDATA[
dE_dz = i ∗ g ∗ N ∗ (alpha13);
]] >
< /operator >
< operatorkind = "cross_propagation" algorithm = "RK4" propagation_dimension =
"z" >
< integration_vectors > cross2 < /integration_vectors >
<! − − You can have a dependencies tag here. −− >
< dependencies > main < /dependencies >
< boundary_conditionkind = "right" >
<![CDATA[
Eb = 0;
]] >
< /boundary_condition >
<![CDATA[
dEb_dz = −i ∗ g ∗ N ∗ (alphab13);

    ]] >
< /operator >

    < integration_vectors > main < /integration_vectors >

    <![CDATA[
real swz = (t < timeswitchz ? − 1.0 : 1.0);
real omc = om ∗ (t < timeswitchc ? 1.0 : 0.0);
```

```
real omcb = om * (t < timeswitchc ? 0.0 : 1.0);

    dalpha12_dt = (-1.0 * gama0 - gamac + i * swz * eta * (z - samplelength/2.0) - i *
(omc*omc + omcb*omcb)/delta) * (alphab12) + i * alpha13 * (omc) + i * omcb * alphab13 *
(cos(2 * w12 * t) + i * sin(2 * w12 * t));
dalphab12_dt = (-1.0 * gama0 - gamac - i * swz * eta * (z - samplelength/2.0) - i *
(omc*omc + omcb*omcb)/delta) * (alpha12) + i * omcb * alphab13 + i * alpha13 * (omc) *
(cos(2 * w12 * t) - i * sin(2 * w12 * t));
dalphab13_dt = (-gama - 1.0 * gama0 - gamac/2 - i * delta) * alphab13 + i * g * Eb + i *
(omcb) * (alphab12);
dalpha13_dt = (-gama - 1.0 * gama0 - gamac/2 - i * delta) * alpha13 + i * g * E + i *
(omc) * (alpha12);
]] >
< /operators >
< /integrate >
< /sequence >

    < output format = "binary" filename = "thlcp.xsil" >
< group >
< samplingbasis = "z(800)" initial_sample = "yes" >
< moments > alpreal12 alpimag12 alprealb12 alpimagb12 alpreal13 alpimag13 <
/moments >
< dependencies > main < /dependencies >
<![CDATA[
alpreal12 = (alpha12 + alphab12).Re();
alpimag12 = (alpha12 + alphab12).Im();
alpreal13 = alpha13.Re();
alpimag13 = alpha13.Im();
]] >
< /sampling >
< /group >
< group >
< samplingbasis = "z(800)" initial_sample = "no" >
< moments > probereal probeimag proberealb probeimagb < /moments >
< dependencies > cross1 cross2 < /dependencies >
<![CDATA[
probereal = E.Re();
probeimag = E.Im();
proberealb = Eb.Re();
probeimagb = Eb.Im();
]] >
< /sampling >
< /group >
< /output >
< /simulation >
```

More information about XMDS programming can be found on http://www.xmds.org/

Bibliography

[1] P. Lambropoulos and D. Petrosyan, Funamentals of Quantum Optics and Quantum Information (Springer, 2006). 9, 10, 25, 34, 36

[2] D. A. Steck, Quantum and Atom Optics (available online at http://steck.us/teaching, 2007). 9, 26, 28, 30, 31, 86, 193, 194

[3] V. Giovannetti, S. Lloyd, and L. Maccone, Quantum-enhanced measurements: Beating the standard quantum limit, Science **306**, 1330 (2004). 9

[4] R. E. Slusher, L. W. Hollberg, B. Yurke, J. C. Mertz, and J. F. Valley, Observation of squeezed states generated by four-wave mixing in an optical cavity, Phys. Rev. Lett. **55**, 2409 (1985). 9

[5] L.-A. Wu, M. Xiao, and H. J. Kimble, Squeezed states of light from an optical parametric oscillator, J. Opt. Soc. Am. B **4**, 1465 (1987). 9, 16

[6] M. D. Levenson, R. M. Shelby, and S. H. Perlmutter, Squeezing of classical noise by nondegenerate four-wave mixing in an optical fiber, Opt. Lett. **10**, 514 (1985). 9

[7] P. Grangier, R. E. Slusher, B. Yurke, and A. LaPorta, Squeezed-light–enhanced polarization interferometer, Phys. Rev. Lett. **59**, 2153 (1987). 9, 16

[8] P. Grangier, J. A. Levenson, and J.-P. Poizat, Quantum non-demolition measurements in optics, Nature **396**, 537 (1998). 10

[9] W. Heisenberg, Über den anschaulichen inhalt der quantentheoretischen kinematik und mechanik, Zeitschrift für Physik **43** (1927). 11

[10] A. Einstein, B. Podolsky, and N. Rosen, Can quantum-mechanical description of physical reality be considered complete?, Phys. Rev. **47**, 777 (1935). 12

[11] E. Schrödinger and M. Born, Discussion of probability relations between separated systems, Mathematical Proceedings of the Cambridge Philosophical Society **31**, 555 (1935). 12

[12] L.-M. Duan, G. Giedke, J. I. Cirac, and P. Zoller, Inseparability criterion for continuous variable systems, Phys. Rev. Lett. **84**, 2722 (2000). 14

[13] E. Wigner, On the quantum correction for thermodynamic equilibrium, Phys. Rev. **40**, 749 (1932). 16

[14] H. Jeong, T. C. Ralph, and W. P. Bowen, Quantum and classical fidelities for gaussian states, J. Opt. Soc. Am. B **24**, 355 (2007). 16, 18, 170, 172

[15] E. C. G. Sudarshan, Equivalence of semiclassical and quantum mechanical descriptions of statistical light beams, Phys. Rev. Lett. **10**, 277 (1963). 17

[16] K. Husimi, Some formal properties of the density matrix, Proc. Phys. Math. Soc. Jpn. **22**, 264 (1940). 17

[17] P. Cochrane, G. J. Milburn, and W. J. Munro, Macroscopically distinct quantum-superposition states as a bosonic code for amplitude damping., Phys. Rev. A **59**, 2631 (1998). 18

[18] A. Ourjoumtsev, F. Ferreyrol, R. Tualle-Brouri, and P. Grangier, Preparation of non-local superpositions of quasi-classical light states., Nat. Phys. **5**, 189 (2009). 18

[19] T. C. Ralph, A. Gilchrist, and G. J. Milburn, Quantum computation with optical coherent states, Phys. Rev. A **68**, 042319 (2003). 18

[20] A. P. Lund, T. C. Ralph, and H. L. Haselgrove, Fault-tolerant linear optical quantum computing with small-amplitude coherent states., Phys. Rev. Lett **100**, 030503 (2008). 18

[21] W. Wootters and W. Zurek, A single quantum cannot be cloned, Nature **299**, 802 (1982). 18, 159

[22] C. H. Bennett and G. Brassard, Quantum cryptography: Public key distribution and coin tossing, , systems, and signal processing, in Proceedings of the IEEE International Conference on Computers, pp. 175–179, Los Alamitos, CA, 1984, IEEE Computer Society. 18, 159

[23] F. Grosshans and P. Grangier, Quantum cloning and teleportation criteria for continuous quantum variables, Phys. Rev. A **64**, 010301 (2001). 18, 165, 173

[24] N. J. Cerf, A. Ipe, and X. Rottenberg, Cloning of continuous quantum variables, Phys. Rev. Lett. **85**, 1754 (2000). 19

[25] N. J. Cerf, O. Kruger, P. Navez, R. F. Werner, and M. M. Wolf, Non-gaussian cloning of quantum coherent states is optimal, Phys. Rev. Lett. **95**, 070501 (2005). 19, 165, 172

[26] A. M. Lance et al., Quantum-state engineering with continuous-variable postselection, Phys. Rev. A **73**, 041801(R) (2006). 21

[27] H. P. Yuen, Two-photon coherent states of the radiation field, Phys. Rev. A. **13**, 2226 (1976). 22

[28] Z. Hradil, Quantum-state estimation, Phys. Rev. A **55**, R1561 (1997). 23

[29] Z. Hradil, J. Summhammer, and H. Rauch, Quantum tomography as normalization of incompatible observations, Phys. Lett. A **261**, 20 (1999). 23

[30] Z. Hradil and R. Myska, Reconstruction of diagonal elements of density matrix using maximum likelihood estimation, acta physica slovaca **48**, 1 (1998). 23

[31] I. Rabi, J. Zacharias, S. Millman, and P. Kusch, A new method of measuring nuclear magnetic moment, Phys. Rev. **53**, 318 (1938). 28

[32] A. V. Gorshkov, A. Andre, M. D. Lukin, and A. S. Sørensen, Photon storage in lambda-type optically dense atomic media. ii. free-space model, Phys. Rev. A **76**, 033805 (2007). 33

[33] A. V. Gorshkov et al., Universal approach to optimal photon storage in atomic media, Phys. Rev. Lett. **98**, 123601 (2007). 33, 47

[34] C. Cohen-Tannoudji, J. Dupont-Roc, and G. Grynberg, Atom Photon Interactions (Wiley-VCH, 2004). 34

[35] H. Tanji-Suzuki, W. Chen, R. Landig, J. Simon, and V. Vuletić, Vacuum-induced transparency, Science **333**, 1266 (2011). 34

[36] S. E. Harris, J. E. Field, and A. Imamoglu, Nonlinear optical processes using electromagnetically induced transparency, Phys. Rev. Lett. **64**, 1107 (1990). 34

[37] M. Fleischhauer, A. Imamoglu, and J. P. Marangos, Electromagnetically induced transparency: Optics in coherent media, Rev. of Mod. Phys. **77**, 634 (2005). 34, 36, 73

[38] M. Fleischhauer and M. D. Lukin, Quantum memory for photons: Dark-state polaritons, Phys. Rev. A **65**, 022314 (2002). 34, 35

[39] C. Liu, Z. Dutton, C. H. Behroozi, and L. V. Hau, Observation of coherent optical information storage in an atomic medium using halted light pulses, Nature **409**, 490 (2001). 37

[40] E. Figueroa, F. Vewinger, J. Appel, and A.I.Lvovsky, Decoherence of electromagnetically induced transparency in atomic vapor, Opt. Lett. **31**, 2625 (2006). 37

[41] N. Vermeulen, C. Debaes, and H. Thienpont, Coherent anti-stokes raman scattering in raman lasers and raman wavelength converters, Laser and Photon. Rev., 1–15 (2009) (2009). 38

[42] J. J. Sakurai, Modern Quantum Mechanics (Addison-Wesley, 1994). 38

[43] O. Landry, J. A. W. van Houwelingen, A. Beveratos, H. Zbinden, and N. Gisin, Quantum teleportation over the swisscom telecommunication network, J. Opt. Soc. Am. B **24**, 398 (2007). 42

[44] T. B. Pittman and J. D. Franson, Cyclical quantum memory for photonic qubits, Phys. Rev. A **66**, 062302 (2002). 42

[45] C. K. Hong and L. Mandel, Experimental realization of a localized one-photon state, Phys. Rev. Lett. **56**, 58 (1986). 42

[46] H. Schulte and A. Rack, Optical delay line memory, IEEE J. of Quantum Electronics **3**, 246 (1967). 42

[47] P. M. Leung and T. C. Ralph, Quantum memory scheme based on optical fibers and cavities, Phys. Rev. A **74**, 022311 (2006). 42

[48] Q. Y. He, M. D. Reid, E. Giacobino, J. Cviklinski, and P. D. Drummond, Dynamical oscillator-cavity model for quantum memories, Phys. Rev. A **79**, 022310 (2009). 42

[49] S. Lloyd, M. S. Shahriar, and J. H. Shapiro, Long distance, unconditional teleportation of atomic states via complete bell state measurements, Phys. Rev. Lett. **87**, 167903 (2001). 42

[50] T. B. Pittman, B. C. Jacobs, and J. D. Franson, Single photons on pseudodemand from stored parametric down-conversion, Phys. Rev. A **66**, 042303 (2002). 42

[51] T. B. Pittman and J. D. Franson, Cyclical quantum memory for photonic qubits, Phys. Rev. A **66**, 062302 (2002). 42

[52] T. Tanabe, M. Notomi, E. Kuramochi, A. Shinya, and H. Taniyama, Trapping and delaying photons for one nanosecond in an ultrasmall high-q photoniccrystal nanocavity, Nat. Phot. **1**, 49 (2007). 42

[53] K. Y. Song, G. Herráez, and M. . Thévenaz, Observation of pulse delaying and advancement in optical fibers using stimulated brillouin scattering, Opt. Exp. **13**, 82 (2005). 43

[54] Y. Okawachi et al., Tunable all-optical delays via brillouin slow light in an optical fiber, Phys. Rev. Lett **94**, 153902 (2005). 43

[55] Z. Zhu, D. J. Gauthier, and R. W. Boyd, Stored light in an optical fiber via stimulated brillouin scattering, Science **318**, 1748 (2007). 43

[56] G. P. Agrawal, Nonlinear Fiber Optics 3rd Ed (Academic Press, San Diego, 2001). 43

[57] J. B. Pendry, Negative refraction makes a perfect lens, Phys. Rev. Lett. **85**, 3966 (2000). 44

[58] K. L. Tsakmakidis, A. D. Boardman, and O. Hess, Trapped rainbow storage of light in metamaterials, Nature **450**, 397 (2007). 44, 45

[59] J. B. Pendryy, A. J. Holdenz, D. J. Robbinsz, and W. J. Stewartz, Low frequency plasmons in thin-wire structures, J. Phys.: Condens. Matter **10**, 4785 (1998). 44

[60] J. B. Pendry, A. J. Holden, W. J. Stewart, and I. Youngs, Extremely low frequency plasmons in metallic mesostructures, Phys. Rev. Lett. **76**, 4773 (1996). 44

[61] R. A. Shelby, D. R. Smith, and S. Schultz, Experimental verification of a negative index of refraction, Science **292**, 77 (2001). 44

[62] A. Puri and J. L. Birman, Goos-hanchen beam shift at total internal reflection with application to spatially dispersive media, J. Opt. Soc. Am. A **3**, 543 (1986). 44

[63] F. Goos and H. Hinchen, Ein neuer und fundamentales versuch zur total reflexion, Ann. Physik **6**, 333 (1947). 44

[64] Z. Jaksic, D. Vasiljevic-Radovic, M. Maksimovic, M. Sarajlic, and Z. Djuric, Nanofabrication of planar split ring resonators for negative refractive index metamaterials in the infrared range, J. Serb. Chem. Soc. **71**, 695 (2006). 45

[65] M. C. Gwinner et al., Periodic large-area metallic split-ring resonator metamaterial fabrication based on shadow nanosphere lithography, Metamaterials **5**, 400 (2009). 45

[66] E. E. Mikhailov, I. Novikova, M. D. Havey, and F. A. Narducci, Magnetic field imaging with atomic rb vapor, Opt. Lett. **34**, 3529 (2009). 46

[67] A. Peng, M. Johnsson, and J. J. Hope, Pulse retrieval and soliton formation in a nonstandard scheme for dynamic electromagnetically induced transparency, Phys. Rev. A **71**, 033817 (2005). 46

[68] M. Fleischhauer and M. D. Lukin, Dark-state polaritons in electromagnetically induced transparency, Phys. Rev. Lett. **84**, 5094 (2000). 46, 92

[69] R. N. Shakhmuratov and J. Odeurs, Two types of adiabatons in electromagnetically induced transparency, Phys. Rev. A **74**, 043807 (2006). 46

[70] R. N. Shakhmuratov and J. Odeurs, Where is teh energy of slow light stored, Coh. and Nonlin. Opt. **17**, 652 (2007). 46

[71] M. Fleischhauer, A. Imamoglu, and J. P. Marangos, Electromagnetically induced transparency: Optics in coherent media, Rev. of Mod. Phys. **77**, 634 (2005). 47

[72] M. D. Lukin, Colloquium: Trapping and manipulating photon states in atomic ensembles, Rev. of Mod. Phys. **75**, 457 (2003). 47

[73] A. B. Matsko, Y. V. Rostovtsev, O. Kocharovskaya, A. S. Zibrov, and M. O. Scully, Nonadiabatic approach to quantum optical information storage, Phys. Rev. A **64**, 043809 (2001). 47

[74] I. Novikova, N. B. Phillips, and A. V. Gorshkov, Optimal light storage with full pulse-shape control, Phys. Rev. A **78**, 021802(R) (2008). 47

[75] C. Liu, Z. Dutton, C. H. Behroozi, and L. V. Hau, Observation of coherent optical information storage in an atomic medium using halted light pulses, Nature **409**, 490 (2001). 47

[76] D. F. Phillips, A. Fleischhauer, A. Mair, R. L. Walsworth, and M. D. Lukin, Storage of light in atomic vapor, Phys. Rev. Lett. **86**, 783 (2001). 47

[77] N. B. Phillips, A. V. Gorshkov, and I. Novikova, Optimal light storage in atomic vapor, Phys. Rev. A **78**, 023801 (2008). 47

[78] J. Appel, E. Figueroa, D. Korystov, M. Lobino, and A. I. Lvovsky, Quantum memory for squeezed light, Phys. Rev. Lett. **100**, 093602 (2008). 48, 161, 163

[79] R. M. Camacho, M. V. Pack, and J. C. Howell, Low-distortion slow light using two absorption resonances, Phys. Rev. A **73**, 063812 (2006). 48

[80] J. Tidström, P. Jänes, and L. M. Andersson, Delay-bandwidth product of electromagnetically induced transparency media, Phys. Rev. (2007). 48

[81] G. Campbell, A. Ordog, and A. I. Lvovsky, Multimode electromagnetically induced transparency on a single atomic line, New J. of Phys. **11**, 106021 (2009). 48

[82] M. Shuker, O. Firstenberg, R. Pugatch, A. Ron, and N. Davidson, Storing images inwarm atomic vapor, Phys. Rev. Lett. **100**, 223601 (2008). 48

[83] G. Hétet, A. Peng, M. T. Johnsson, J. J. Hope, and P. K. Lam, Characterization of electromagnetically-induced-transparency-based continuous-variable quantum memories, Phys. Rev. A **77**, 012323 (2008). 48, 73, 173

[84] M. T. L. Hsu et al., Quantum study of information delay in electromagnetically induced transparency, Phys. Rev. Lett. **97**, 183601 (2006). 48

[85] K. Honda et al., Storage and retrieval of a squeezed vacuum, Phys. Rev. Lett. **100**, 093601 (2008). 48

[86] M. D. Eisaman et al., Electromagnetically induced transparency with tunable single-photon pulses, Nature **438**, 837 (2005). 49

[87] T. Chaneliere et al., Storage and retrieval of single photons transmitted between remote quantum memories, Nature **438**, 834 (2005). 49, 63

[88] M. D. Eisaman et al., Shaping quantum pulses of light via coherent atomic memory, Phys. Rev. Lett. **93**, 233602 (2004). 49

[89] K. S. Choi, H. Deng, J. Laurat1, and H. J. Kimble, Mapping photonic entanglement into and out of a quantum memory, Nature **452**, 67 (2008). 49

[90] J. J. Longdell, E. Fraval, M. J. Sellars, and N. B. Manson, Stopped light with storage times greater than one second using electromagnetically induced transparency in a solid, Phys. Rev. Lett. **95**, 063601 (2005). 50, 162, 163

[91] H. Zhang et al., Preparation and storage of frequency-uncorrelated entangled photons from cavity-enhanced spontaneous parametric downconversion, Nat. Phot. **5**, 628 (2010). 50, 161, 163, 166, 167

[92] M. Lettner et al., Remote entanglement between a single atom and a bose-einstein condensate, Phys. Rev. Lett. **106**, 210503 (2011). 50

[93] V. Boyer, C. F. McCormick, . E. Arimondo, 1, and P. D. Lett, Ultraslow propagation of matched pulses by four-wave mixing in an atomic vapor, Phys. Rev. Lett. **99**, 143601 (2007). 50

[94] A. M. Marino, R. C. Pooser, V. Boyer, and P. D. Lett, Tunable delay of einstein–podolsky–rosen entanglement, Nature **457**, 859 (2009). 50, 51, 143, 163

[95] R. M. Camacho, P. K. Vudyasetu, and J. C. Howell, Four-wave-mixing stopped light in hot atomic rubidium vapour, Nature Photon **3**, 103 (2009). 50

[96] B. Julsgaard, J. Sherson, J. I. Cirac, J. Fiurasek, and E. S. Polzik, Experimental demonstration of quantum memory for light, Nature **432**, 482 (2004). 51, 82

[97] M. Kitagawa and M. Ueda, Squeezed spin states, Phys. Rev. A **47**, 5138 (1993). 52

[98] C. A. Muschik, K. Hammerer, E. S. Polzik, and J. I. Cirac, Efficient quantum memory and entanglement between light and an atomic ensemble using magnetic fields, Phys. Rev. A **73**, 062329 (2006). 52

[99] J. F. Sherson et al., Quantum teleportation between light and matter, Nature **443**, 557 (2006). 52, 83

[100] K. Jensen et al., Quantum memory for entangled continuous-variable states, Nat. Phys. **7**, 13 (2010). 52, 53, 161, 163

[101] K. F. Reim et al., Towards high-speed optical quantum memories, Nat. Phot. **4**, 218 (2010). 54

[102] K. F. Reim et al., Single-photon-level quantum memory at room temperature, Phys. Rev. Lett. **107**, 053603 (2011). 54, 162, 163

[103] E. L. Hahn, Spin echoes, Phys. Rev. **80**, 580 (1950). 54

[104] I. D. Kurnit, N. Abella, and S. R. Hartmann, Observation of a photon echo, Phys. Rev. Lett **13**, 567 (1964). 54

[105] U. G. Kopvil'em and V. R. Nagibarov, (in russian), Fiz. Met. Metalloved **2**, 313 (1963). 54

[106] T. W. Mossberg, A. Flusberg, R. Kachru, and S. R. Hartmann, Total scattering cross section for na on he measured by stimulated photon echoes, Phys. Rev. Lett **42**, 1665 (1979). 54

[107] M. K. Kim and R. Kachru, Multiple-bit long-term data storage by backward-stimulated echo in eu3+:yalo3, Opt. Lett. **14**, 423 (1989). 54

[108] T. W. Mossberg, Time-domain frequency-selective optical data storage, Opt. Lett. **7**, 77 (1982). 54

[109] K. Heshami, N. Sangouard, J. Minár, H. de Riedmatten, and C. Simon, Precision requirements for spin-echo-based quantum memories, Phys. Rev. A **83**, 032315 (2011). 54

[110] W. Tittel et al., Photon-echo quantum memory in solid state systems, Laser and Photon. Rev. , 1 (2009). 54

[111] H. Lin, T. Wang, and T. Mossberg, Demonstration of 8-gbit per in areal storage density based on swept-carrier frequency-selective optical memory, Opt. Lett. **20**, 1658 (1995). 55

[112] K. Merkel et al., Multi-gigahertz radar range processing of baseband and rf carrier modulated signals in tm:yag, J. Lumin. **107**, 62 (2004). 55

[113] M. U. Staudt et al., Interference of multimode photon echoes generated in spatially separated solid-state atomic ensembles, Phys. Rev. Lett. **99**, 173602 (2007). 55, 56

[114] M. U. Staudt et al., Fidelity of an optical memory based on stimulated photon echoes, Phys. Rev. Lett. **98**, 113601 (2007). 55

[115] B. S. Ham, Ultralong quantum optical data storage using an optical locking technique, Nat. Phot. **3**, 518 (2009). 55

[116] B. Ham and J. Hahn, Ultralong photon echo storage using optical locking, arXiv:0912.2756v2 [quant-ph] (2009). 55

[117] S. A. Moiseev and B. S. Ham, Photon-echo quantum memory with efficient multipulse readings, Phys. Rev. Lett. **87**, 173601 (2001). 56, 57

[118] Y. Rostovtsev, Z. Sariyianni, and M. O. Scully, Photon echo pulse shape storage, Laser Phys **12**, 1148 (2002). 56

[119] S. A. Moiseev, V. F. Tarasov, and B. S. Ham, Quantum memory photon echo-like techniques in solids, J. Opt. B: Quantum Semiclassical Opt. **5**, S497 (2003). 56, 57

[120] S. A. Moiseev and M. I. Noskov, The possibilities of the quantum memory realization for short pulses of light in the photon echo technique, Laser Phys. Lett. **1**, 303 (2004). 56

[121] N. Sangouard, C. Simon, M. Afzelius, and N. Gisin, Analysis of a quantum memory for photons based on controlled reversible inhomogeneous broadening, Phys. Rev. A **75**, 032327 (2007). 57, 68

[122] A. L. Alexander, J. J. Longdell, M. J. Sellars, and N. B. Manson, Photon echoes produced by switching electric fields, Phys. Rev. Lett. **96**, 043602 (2006). 57

[123] M. Afzelius, C. Simon, H. de Riedmatten, and N. Gisin, Multi-mode quantum memory based on atomic frequency combs, Phys. Rev. A **79**, 052329 (2009). 58

[124] J. Nunn et al., Multimode memories in atomic ensembles, Phys. Rev. Lett. **101**, 260502 (2008). 58, 130

[125] H. de Riedmatten, M. Afzelius, M. U. Staudt, C. Simon, and N. Gisin, A solid-state light–matter interface at the single-photon level, Nature **456**, 773 (2008). 58

[126] T. Chaneliere, M. Afzelius, and J.-L. L. Gouet, Efficient light storage in a crystal using an atomic frequency comb, New J. of Phys. **12**, 023025 (2010). 58

[127] M. Afzelius et al., Demonstration of atomic frequency comb memory for light with spin-wave storage, Phys. Rev. Lett. **104**, 040503 (2010). 58

[128] A. Amari et al., Towards an efficient atomic frequency comb quantum memory, J Lumin **130**, 1579 (2010). 58, 125, 162

[129] C. Clausen et al., Quantum storage of photonic entanglement in a crystal, Nature **469**, 508 (2011). 58, 161, 163, 165

[130] E. Saglamyurek et al., Broadband waveguide quantum memory for entangled photons, Nature **469**, 512 (2011). 58, 59, 161, 162, 163, 165

[131] S. A. Moiseev and J.-L. L. Gouet, Rephasing processes and quantum memory for light: reversibility issues and how to fix them, arXiv:1108.6169v1 (2011). 59

[132] D. E. Chang, A. H. Safavi-Naeini, M. Hafezi, and O. Painter, Slowing and stopping light using an optomechanical crystal array, New J. of Phys. **13**, 023003 (2011). 60

[133] A. H. Safavi-Naeini et al., Electromagnetically induced transparency and slow light with optomechanics, Nature **472**, 69 (2011). 61

[134] S. Weis et al., Optomechanically induced transparency, Science **330**, 1520 (2010). 61

[135] V. Fiore et al., Storing optical information as a mechanical excitation in a silica optomechanical resonator, Phys. Rev. Lett. **107**, 133601 (2011). 61

[136] L.-M. Duan, M. D. Lukin, J. I. Cirac, and P. Zoller, Long-distance quantum communication with atomic ensembles and linear optics, Nature **414**, 413 (2001). 61, 161

[137] K. S. Choi, A. Goban, S. B. Papp, and S. J. van Enk andH. J. Kimble, Entanglement of spin waves among four quantum memories, Nature **468**, 412 (2010). 63, 165

[138] C. W. Chou et al., Measurement-induced entanglement for excitation stored in remote atomic ensembles, Nature **438**, 828 (2005). 63, 161

[139] C. Simon et al., Quantum repeaters with photon pair sources and multimode memories, Phys. Rev. Lett. **98**, 190503 (2007). 63

[140] B. Zhao, Z.-B. Chen, Y.-A. C. andJorg Schmiedmayer, and J.-W. Pan, Robust creation of entanglement between remote memory qubits, Phys. Rev. Lett. **98**, 240502 (2007). 63, 161

[141] R. Zhao et al., Long-lived quantum memory, Nature Photon **5**, 100 (2009). 63

[142] B. Zhao et al., A millisecond quantum memory for scalable quantum networks, Nature Photon **5**, 95 (2009). 63

[143] Y.-A. Chen et al., Memory-built-in quantum teleportation with photonic and atomic qubits, Nat. Phys. **4**, 103 (2008). 63, 161

[144] S. Moiseev and S. Kroll, Complete reconstruction of the quantum state of a single-photon wave packet absorbed by a doppler-broadened transition, Phys. Rev. Lett. **87**, 173601 (2001). 68

[145] M. Nilsson and S. Kroll, Solid state quantum memory using complete absorption and re-emission of photons by tailored and externally controlled inhomogeneous absorption profiles, Opt. Commun. **247**, 393 (2005). 68

[146] S. A. Moiseev, V. F. Tarasov, and B. S. Ham, Quantum memory photon echo-like techniques in solids, Journal of Optics B: Quantum and Semiclassical Optics **5**, S497 (2003). 68

[147] A. Alexander, J. Longdell, M. Sellars, and N. Manson, Photon echoes produced by switching electric fields, Phys. Rev. Lett. **96**, 043602 (2006). 68

[148] G. Hetet, J. J. Longdell, A. L. Alexander, P. K. Lam, and M. J. Sellars, Electro-optic quantum memory for light using two-level atoms, Phys. Rev. Lett. **100**, 023601 (2008). 68

[149] M. Hedges, J. Longdell, Y. Li, and M. Sellars, Efficient quantum memory for light, Nature **465**, 1052 (2010). 68, 125, 161, 162, 163, 165, 169

[150] J. J. Longdell, G. Hetet, P. K. Lam, and M. J. Sellars, Analytic treatment of controlled reversible inhomogeneous broadening quantum memories for light using two-level atoms, Phys. Rev. A **78**, 032337 (2008). 68

[151] G. Hetet, J. J. Longdell, M. J. Sellars, P. K. Lam, and B. C. Buchler, Multimodal properties and dynamics of gradient echo quantum memory, Phys. Rev. Lett. **101**, 203601 (2008). 68, 94, 95, 101, 113, 130, 184

[152] J. J. Longdell, G. Hetet, P. K. Lam, and M. J. Sellars, Analytic treatment of controlled reversible inhomogeneous broadening quantum memories for light using two-level atoms, Phys. Rev. A **78**, 032337 (2008). 70, 71, 102, 110, 126, 135

[153] G. Hetet, Quantum Memories for Continuous Variable States of Light in Atomic Ensembles, PhD thesis, The Australian National University, 2008. 74

[154] G. Hetet, J. J. Longdell, A. L. Alexander, P. K. Lam, and M. J. Sellars, Electro-optic quantum memory for light using two-level atoms, Phys. Rev. Lett. **100**, 023601 (2008). 74, 87, 88, 103, 104

[155] B. M. Sparkes, M. Hosseini, G. Hétet, P. K. Lam, and B. C. Buchler, An ac stark gradient echo memory in cold atoms, Phys. Rev. A **82**, 043847 (2010). 76, 192

[156] M. Hosseini, B. M. Sparkes, G. Campbell, B. C. Buchler, and P. K. Lam, High efficiency coherent optical memory with warm rubidium vapour, Nat. Commun. **2**, 174 (2010). 77, 162, 163

[157] M. Erhard and H. Helm, Buffer-gas effects on dark resonances: Theory and experiment, Phys. Rev. A **63**, 043813 (2001). 77, 80, 81

[158] A. Javan, O. Kocharovskaya, H. Lee, and M. O. Scully, Narrowing of electromagnetically induced transparency resonance in a doppler-broadened medium, Phys. Rev. A **66**, 013805 (2002). 77

[159] G. T. Purves, Absorption And Dispersion In Atomic Vapours: Applications To Interferometery, PhD thesis, Department of Physics University of Durham, 2006. 78

[160] M. Shuker et al., Angular dependence of dicke-narrowed electromagnetically induced transparency resonances, Phys. Rev. A **76**, 023813 (2007). 79, 128, 147

[161] M. D. Rotondaro and G. P. Perram, Collisional broadening and shift of the rubidium d1 and d2 lines (2s12 52p12, 52p32) by rare gases, h2, d2, n2, ch4 and cf4, J. Quant. Spec. Rad. Trans. **57**, 497 (1997). 81, 147

[162] W. Happer, Optical pumping, Rev. Mod. Phys. **44** (1972). 81, 82

[163] R. H. Dicke, The effect of collisions upon the doppler width of spectral lines, Phys. Rev. **89**, 472 (1953). 82

[164] G. Dutier et al., Collapse and revival of a dicke-type coherent narrowing in a sub-micron thick vapor cell transmission spectroscopy, Euro. Phys. Letters **63**, 35 (2003). 82

[165] A. Nagel, C. Affolderbach, S. Knappe, and R. Wynands, Influence of excited-state hyperfine structure on ground-state coherence, Phys. Rev. A **61**, 012504 (1999). 82

[166] J. Vanier, M. W. Levine, D. Janssen, and M. Delaney, Contrast and linewidth of the coherent population trapping transmission hyperfine resonance line in 87rb: Effect of optical pumping, Phys. Rev. A **67**, 065801 (2003). 82

[167] J. Vanier and C. Audoin, The Quantum Physics of Atomic Frequency Standards (IOP Publishing Ltd., 1989). 82

[168] M. V. Balabas et al., High quality anti-relaxation coating material for alkali atom vapor cells, Opt. Exp. **18**, 5825 (2010). 83, 162, 174

[169] M. V. Balabas, T. Karaulanov, M. P. Ledbetter, and D. Budker, Polarized alkali-metal vapor with minute-long transverse spin-relaxation time, Phys. Rev. Lett. **105**, 070801 (2010). 83, 162

[170] J. E. Thomas and W. W. Quivers, Transit-time effects in optically pumped coupled three-level systems, Phys. Rev. A **22**, 2115 (1980). 83

[171] A. V. Taichenachev et al., Nonlinear-resonance line shapes: Dependence on the transverse intensity distribution of a light beam, Phys. Rev. A **69**, 024501 (2004). 83

[172] D. A. Steck, Rubidium 87 d line data, available online at http://steck.us/alkalidata/ **80**, 023425 (2009). 84

[173] E. E. Mikhailov, I. Novikova, Y. V. Rostovtsev, and G. R. Welch, Buffer-gas-induced absorption resonances in rb vapor, Phys. Rev. A **70**, 033806 (2004). 86

[174] W. H. Bragg, Faraday's diary, Rev. Mod. Phys. **3**, 449 (1931). 86

[175] A. B. Matsko, I. Novikova, M. S. Zubairy, and G. R. Welch, Nonlinear magneto-optical rotation of elliptically polarized light, Phys. Rev. A **67**, 043805 (2003). 87

[176] G. Hétet et al., Photon echoes generated by reversing magnetic field gradients in a rubidium vapor, Opt. Lett. **33**, 2323 (2008). 87

[177] M. I. Stockman, Nanoplasmonics: The physics behind the applications, Phys. Today **64**, 39 (2011). 91

[178] J. Kasprzak et al., Bose-einstein condensation of exciton polaritons, Nature **443**, 409 (2006). 91

[179] S. A. Moiseev and N. M. Arslanov, Efficiency and fidelity of photon-echo quantum memory in an atomic system with longitudinal inhomogeneous broadening, Phys. Rev. A **78**, 023803 (2008). 94, 101, 102, 103

[180] G. Collecutt, P. D. Drummond, P. Cochrane, and J. J. Hope, extensible multi-dimensional simulator, Documentation and source code available from http://www.xmds.org . 95, 121, 187

[181] G. Hetet, J. J. Longdell, A. L. Alexander, P. K. Lam, and M. J. Sellars, Electro-optic quantum memory for light using two-level atoms, Phys. Rev. Lett. **100**, 023601 (2008). 103

[182] G. Campbell, A. Ordog, and A. I. Lvovsky, Multimode electromagnetically induced transparency on a single atomic line, New J. of Phys. **11**, 106021 (2009). 104

[183] M. Hosseini et al., Coherent optical pulse sequencer for quantum applications, Nature **461**, 241 (2009). 113

[184] M. Shuker et al., Ramsey-like measurement of the decoherence rate between zeeman sub-levels, Phys. Rev. A **78**, 063818 (2008). 113

[185] G. Hetet, J. J. Longdell, M. J. Sellars, P. K. Lam, and B. C. Buchler, Multimodal properties and dynamics of gradient echo quantum memory, Phys. Rev. Lett. **101**, 203601 (2008). 115, 130

[186] A. Andre and M. D. Lukin, Manipulating light pulses via dynamically controlled photonic band gap, Phys. Rev. Lett. **89**, 143602 (2002). 117, 118

[187] M. Bajcsy, A. S. Zibrov, and M. D. Lukin, Stationary pulses of light in an atomic medium, Nature **426**, 638 (2003). 118

[188] Y.-W. Lin et al., Stationary light pulses in cold atomic media and without bragg gratings, Phys. Rev. Lett. **102**, 213601 (2009). 118

[189] S. A. Moiseev and B. S. Ham, Quantum manipulation of two-color stationary light: Quantum wavelength conversion, Phys. Rev. A **73**, 033812 (2006). 118

[190] S. A. Moiseev and B. S. Ham, Quantum control and manipulation of multi-color light fields, Opt. Spectrosc. **103**, 210 (2007). 118

[191] F. Carreño and M. Antón, Coherent control of light pulses stored in a gradient echo memory, Opt. Commun. **284**, 3154 (2011). 119

[192] S. Nakamura, Y. Ueno, and K. Tajima, Femtosecond switching with semiconductor-optical-amplifier-based symmetric mach – zehnder-type all-optical switch, App. Phys. Lett. **78**, 3929 (2001). 122

[193] R. R. P. . M. L. Vilson R. Almeida, Carlos A. Barrios, All-optical control of light on a silicon chip, Nature **431**, 1081 (2004). 122

[194] X. Hu, P. Jiang, C. Ding, H. Yang, and Q. Gong, Picosecond and low-power all-optical switching based on an organic photonic-bandgap microcavity, Nat. Phot. **2**, 185 (2008). 122

[195] N. B. Phillips, A. V. Gorshkov, and I. Novikova, Optimal light storage in atomic vapor, Phys. Rev. A **78**, 023801 (2008). 125, 145, 146, 162, 200

[196] E. E. Mikhailov, I. Novikova, Y. V. Rostovtsev, and G. R. Welch, Buffer-gas-induced absorption resonances in rb vapor, Phys. Rev. A **70**, 033806 (2004). 125

[197] M. Afzelius, C. Simon, H. de Riedmatten, and N. Gisin, Multimode quantum memory based on atomic frequency combs, Phys. Rev. A **79**, 052329 (2009). 130

[198] K. Surmacz et al., Efficient spatially resolved multimode quantum memory, Phys. Rev. A **78**, 033806 (2008). 130

[199] S. A. Moiseev, S. N. Andrianov, and F. F. Gubaidullin, Efficient multimode quantum memory based on photon echo in an optimal qed cavity, Phys. Rev. A **82**, 022311 (2010). 130

[200] I. Usmani, M. Afzelius, H. de Riedmatten, and N. Gisin, Mapping multiple photonic qubits into and out of one solid-state atomic ensemble, Nat Comms **1**, 1 (2010). 130

[201] M. Bonarota, J.-L. L. Gouët, and T. Chanelière, Highly multimode storage in acrystal, New J. of Phys. **13**, 013013 (2011). 130, 162

[202] J. Tidström, P. Jänes, and L. Andersson, Delay-bandwidth product of electromagnetically induced transparency media, Phys. Rev. A (2007). 130

[203] J. Appel, K. P. Marzlin, and A. I. Lvovsky, Raman adiabatic transfer of optical states in multilevel atoms, Phys. Rev. A **73**, 013804 (2006). 133

[204] M. Fleischhauer and M. D. Lukin, Effect of large supersymmetric phases on higgs production, Phys. Rev. Lett. **84**, 22 (2000). 133

[205] M. Arend, E. Bloch, and S. R. Hartmann, Random access processing of optical memory by use of photon-echo interference effects, Opt. Lett. **18**, 1789 (1993). 133

[206] S. A. Moiseev, Time-delayed quantum interference and single-photon echo in coherent three-level systems, Quant. Elect. **31**, 557 (2001). 133

[207] M. U. Staudt et al., Interference of multimode photon echoes generated in spatially separated solid-state atomic ensembles, Phys. Rev. Lett. **99**, 173602 (2007). 134

[208] J. Appel, E. Figueroa, and A. Lvovsky, Adiabatic frequency conversion of optical information in atomic vapor, Opt. Lett. **32**, 2771 (2007). 139

[209] G. Campbell, A. Ordog, and A. I. Lvovsky, Multimode electromagnetically induced transparency on a single atomic line, New J. of Phys. **11**, 106021 (2009). 139

[210] E. Bimbard, N. Jain, A. MacRae, and A. I. Lvovsky1, Quantum-optical state engineering up to the two-photon level, Nat. Phot. **4**, 243 (2010). 140

[211] W. Tittel, J. Brendel, H. Zbinden, and N. Gisin, Quantum cryptography using entangled photons in energy-time bell states, Phys. Rev. Lett. **84** (2000). 140

[212] U. L. Andersen, R. Filip, J. Fiurášek, V. Josse, and G. Leuchs, Experimental purification of coherent states, Phys. Rev. A **72**, 060301(R) (2005). 140

[213] S. E. Harris and Y. Yamamoto, Photon switching by quantum interference, Phys. Rev. Lett. **81**, 3611 (1998). 141

[214] J.-H. Wu et al., Ultrafast all optical switching via tunable fano interference, Phys. Rev. Lett. **95**, 057401 (2005). 141

[215] H. Schmidt and R. J. Ram, All-optical wavelength converter and switch based on electromagnetically induced transparency, App. Phys. Lett. **76**, 3173 (2000). 141

[216] C. F. McCormick, V. Boyer, E. Arimondo, and P. D. Lett, Strong relative intensity squeezing by four-wave mixing in rubidium vapor, Opt. Lett. **32**, 178 (2007). 143

[217] Q. Glorieux, L. Guidoni, S. Guibal, J. P. Likforman, and T. Coudreau, Strong quantum correlations in four wave mixing in 85rb vapor, Proc. SPIE **7727**, 772703 (2010). 143

[218] V. Boyer, C. F. McCormick, E. Arimondo, and P. D. Lett, Ultraslow propagation of matched pulses by four-wave mixing in an atomic vapor, Phys. Rev. Lett. **99**, 143601 (2007). 143, 148

[219] K. Drese and M. Holthaus, Floquet theory for short laser pulses, Eur. Phys. J. D **5**, 119 (1999). 144

[220] N. B. Phillips, A. V. Gorshkov, and I. Novikova, Light storage in an optically thick atomic ensemble under conditions of electromagnetically induced transparency and four-wave mixing, Phys. Rev. A **83**, 063823 (2011). 144, 145

[221] M. D. Lukin et al., Spectroscopy in dense coherent media: Line narrowing and interference effects, Phys. Rev. Lett. **79**, 2959 (1997). 145

[222] D. A. Braje, V. B. , S. Goda, G. Y. Yin, and S. E. Harris, Frequency mixing using electromagnetically induced transparency in cold atoms, Phys. Rev. Lett. **93**, 183601 (2004). 145

[223] N. Phillips, A. Gorshkov, and I. Novikova, Slow light propagation and amplification via electromagnetically induced transparency and four-wave mixing in an optically dense atomic vapor, Journal of Modern Optics **56**, 1916 (2009). 145

[224] N. B. Phillips, A. V. Gorshkov, and I. N. and, Optimal light storage in atomic vapor, Phys. Rev. A **78**, 023801 (2009). 145

[225] V. Boyer, A. M. Marino, R. C. Pooser, and P. D. Lett, Entangled images from four-wave mixing, Science **321**, 544 (2008). 145

[226] A. B. Matsko, D. V. Strekalov, and L. Maleki, On the dynamic range of optical delay lines based on coherent atomic media, Opt. Express **13**, 2210 (2005). 145

[227] R. M. Camacho, P. K. Vudyasetu, and J. C. Howell, Four-wave-mixing stopped light in hot atomic rubidium vapour, Nature Photonics **3**, 103 (2009). 145

[228] M. D. Lukin, A. B. Matsko, M. Fleischhauer, and M. O. Scully, Quantum noise and correlations in resonantly enhanced wave mixing based on atomic coherence, Phys. Rev. Lett. **82**, 1847 (1999). 145

[229] O. Firstenberg et al., Theory of dicke narrowing in coherent population trapping, Phys. Rev. A **76**, 013818 (2007). 147

[230] M. Hosseini, B. M. Sparkes, G. Campbell, P. K. Lam, and B. C. Buchler, Unconditional room temperature quantum memory, Nat. Phys. **7**, 794 (2011). 149, 151, 161, 162, 163

[231] F. Michaud, G.-L. Gattobigio, J. W. R. Tabosa, and R. Kaiser, Interference between raman gain and four-wave mixing in cold atoms, J. Opt. Soc. Am. B **24**, A40 (2007). 151

[232] T. M. Brzozowski, M. Brzozowska, J. Zachorowski, M. Zawada, and W. Gawlik, Probe spectroscopy in an operating magneto-optical trap: The role of raman transitions between discrete and continuum atomic states, Phys. Rev. A **71**, 013401 (2005). 151

[233] T. Kleinjung et al., Factorization of a 768-bit rsa modulus, http://eprint.iacr.org/2010/006.pdf, 2010. 155

[234] A. Schrijver, On the history of combinatorial optimization (till 1960) (Handbook of Discrete Optimization, Elsevier, 2005). 155

[235] M. Boyer, G. Brassard, P. Hoyer, and A. Tapp, Tight bounds on quantum searching, arXiv:quant-ph/9605034v1 (1996). 155

[236] P. W. S. 1994, Algorithms for quantum computation: discrete logarithms and factoring, in 35th Annual Symp. Foundations Comp. Sci., pp. 124–134, Los Alamitos, CA, 1994, IEEE Computer Soc. 155, 157, 158

[237] M. A. Nielsen and I. L. Chuang, Quantum computation and quantum information (Cambridge university press, 2001). 157

[238] D. Deutsch, Quantum computational networks, Proc. R. Soc. A **400**, 97 (1985). 157

[239] G. L.K, From schrödinger's equation to quantum search algorithm, American Journal of Physics **69**, 769 (2001). 157

[240] P. Walther et al., Experimental one way quantum computing, Nature **434**, 169 (2005). 158, 179

[241] J. Chiaverini et al., Realization of quantum error correction, Nature **432**, 602 (2004). 158

[242] D. Leibfried et al., Creation of a six-atom 'schrödinger cat' state, Nature **438**, 639 (2005). 158

[243] B. E. Kane, Asilicon-based nuclear spin quantum computer, Nature **393**, 133 (1998). 158

[244] Y. Nakamura, Y. A. Pashkin, and J. S. Tsai, Coherent control of macroscopic quantum states in a single-cooper-pair box, Nature **398**, 786 (1999). 158

[245] I. L. Chuang, L. M. K. Vandersypen, X. Zhou, D. W. Leung, and S. Lloyd, Experimental realization of a quantum algorithm, Nature **393**, 143 (1998). 158

[246] L. M. K. Vandersypen et al., Experimental realization of shor's quantum factoring algorithm using nuclear magnetic resonance, Nature **414**, 883 (2001). 158

[247] K. K. Berggren, Quantum computing with superconductors, Proc. IEEE **92**, 1630 (2004). 158

[248] S. Lloyd, Universal quantum simulators, Science **273**, 1073 (1996). 158

[249] D. V. Averin, Adiabatic quantum computation with cooper pairs, Solid State. Commun. **105** (1997). 158

[250] D. P. DiVincenzo and B. Terhal, Quantum information, Phys. World **11**, 53 (1998). 158

[251] J. E. Mooij et al., Josephson persistent-current qubit, Science **285**, 1036 (1999). 158

[252] J. R. Petta et al., Coherent manipulation of coupled electron spins in semiconductor quantum dots, Science **309**, 2180 (2005). 158

[253] J. E. Mooij, The road to quantum computing, Science **307**, 1210 (2005). 158

[254] M. Fuechsle, Spectroscopy of few-electron single-crystal silicon quantum dots, Nat. Nanotech. **5**, 502 (2010). 158

[255] M. Neeley et al., Generation of three-qubit entangled states using superconducting phase qubits, Nature **467**, 570 (2010). 158

[256] J. L. O'Brien et al., Towards the fabrication of phosphorus qubits for a silicon quantum computer, Phys. Rev. **64**, 161401(R) (2001). 159

[257] P. W. Shor and J. Preskill, Simple proof of security of the bb84 quantum key distribution protocol, Phys. Rev. Lett. **85**, 441 (2000). 159

[258] E. Waks, A. Zeevi, and Y. Yamamoto, Security of quantum key distribution with entangled photons against individual attacks, Phys. Rev. A **65**, 052310 (2002). 159

[259] D. Bruss and G. Leuchs, Lectures on Quantum Information (Wiley-VCH, 2007). 159

[260] H. J. Briegel, W. Dur, J. I. Cirac, and P. Zoller, Quantum repeaters: The role of imperfect local operations in quantum communication, Phys. Rev. Lett. **81**, 5932 (1998). 159

[261] D. Bouwmeester, J.-W. P. K. Mattle, M. Eibl, H. Weinfurter, and A. Zeilinger, Experimental quantum teleportation, Nature **390**, 575 (1997). 159

[262] S. L. Braunstein and H. J. Kimble, Teleportation of continuous quantum variables, Phys. Rev. Lett. **80**, 869 (1998). 159

[263] L. Childress, J. M. Taylor, A. S. Sørensen, and M. D. Lukin, Fault-tolerant quantum communication based on solid-state photon emitters, Phys. Rev. Lett. **96**, 070504 (2006). 161

[264] R. Zhang, S. R. Garner, and L. V. Hau, Creation of long-term coherent optical memory via controlled nonlinear interactions in bose-einstein condensates, Phys. Rev. Lett. **103**, 233602 (2009). 161

[265] K. S. Choi, H. Deng, J. Laurat, and H. J. Kimble, Mapping photonic entanglement into and out of a quantum memory, Nature , 67 (2008). 161

[266] K. S. Choi, A. Goban, S. B. Papp, S. J. van Enk, and H. J. Kimble, Entanglement of spin waves among four quantum memories, Nature , doi:10.1038/nature09568 (2010). 161

[267] C. H. van der Wal nad M. D. Eisaman et al., Atomic memory for correlated photon states, Science **301**, 196 (2009). 161

[268] B. Julsgaard, J. Sherson, J. Cirac, J. Fiurasek, and E. Polzik, Experimental demonstration of quantum memory for light, Nature **432**, 482 (2004). 161, 165

[269] K. Honda et al., Storage and retrieval of a squeezed vacuum, Phys. Rev. Lett. **100**, 093601 (2008). 161

[270] C. Simon et al., Quantum memories, Eur. Phys. J. D **58**, 1 (2010). 161

[271] N. Sangouard, C. Simon, H. Riedmatten, and N. Gisin, Quantum repeaters based on atomic ensembles and linear optics, Rev. of Mod. Phys. **83**, 33 (2011). 162

[272] M. Razavi, M. Piani, and N. Lutkenhaus, Quantum repeaters with imperfect memories: Cost and scalability, Phys. Rev. A **80**, 032301 (2009). 162

[273] Y. Sagi, I. Almog, and N. Davidson, Process tomography of dynamical decoupling in a dense cold atomic ensemble, Phys. Rev. Lett. **105**, 053201 (2010). 162

[274] B. Lauritzen, J. Minar, H. de Riedmatten, M. Afzelius, and N. Gisin, Approaches for a quantum memory at telecommunication wavelengths, Phys. Rev. A **83**, 012318 (2011). 162

[275] Q. He, M. Reid, E. Giacobino, J. Cviklinski, and P. Drummond, Dynamical oscillator-cavity model for quantum memories, Phys. Rev. A **79**, 022310 (2009). 166

[276] M. D. Eisaman et al., Electromagnetically induced transparency with tunable single-photon pulses, Nature **438**, 837 (2005). 166

[277] J. Rehàcek, Z. Hradil, and M. Jezek, Iterative algorithm for reconstruction of entangled states, Phys. Rev. A **63**, 040303(R) (2002). 169

[278] A. I. Lvovsky, Iterative maximum-likelihood reconstruction in quantum homodyne tomography, J. Opt. B: Quantum Semiclass. Opt. **6**, S556 (2004). 169

[279] D. Walls and G. Milburn, Quantum Optics (Springer, Berlin, 1994). 169

[280] N. J. Cerf, A. Ipe, and X. Rottenberg, Cloning of continuous quantum variables, Phys. Rev. Lett. **85**, 1754 (2000). 171

[281] J.-P. Poizat, J.-F. Roch, and P. Grangier, Characterization of quantum non-demolition measurements in optics, Ann. Phys. Fr. **19**, 265 (1994). 173

[282] T. C. Ralph and P. K. Lam, Teleportation with bright squeezed light, Phys. Rev. Lett. **81**, 5668 (1998). 173

[283] W. Bowen et al., Experimental investigation of continuous-variable quantum teleportation, Phys. Rev. A **67**, 032302 (2003). 173

[284] J. Ortalo et al., Atomic-ensemble-based quantum memory for sideband modulations, Journal of Physics B: Atomic, Molecular and Optical Physics **42**, 114010 (2009). 173

[285] H. Kubler, J. P. Shaffer, T. Baluktsian, R. Low, and T. Pfau1, Coherent excitation of rydberg atoms in micrometre-sized atomic vapour cells, Nature Photonics **4**, 112 (2010). 174

[286] E. J. Eklunda, A. M. Shkela, S. Knappeb, E. Donleyb, and J. Kitching, Glass-blownsphericalmicrocellsforchip-scaleatomicdevices, Sensors and Actuators A **143**, 175 (2008). 174

[287] W. Yang, D. B. C. B. Wu, D. Yin, A. R. Hawkins, and H. Schmidt, Atomic spectroscopy on a chip, Nature Phot. **1**, 331 (2007). 174

[288] T. Baluktsian et al., Fabrication method for microscopic vapor cells for alkali aroms, Opt. Lett. **35**, 1950 (2010). 174

[289] B. Wu et al., Slow light on a chip via atomic quantum state control, Nature Photonics **4**, 776 (2010). 174

[290] G. J. Milburn, Quantum optical fredkin gate, Phys. Rev. Lett. **62**, 2124 (1989). 177

[291] S. G. R. Louis, K. Nemoto, W. J. Munro, and T. P. Spiller, The efficiencies of generating cluster states with weak nonlinearities, New J. of Phys. **9**, 193 (2007). 177, 179, 188, 189

[292] M. D. Lukinand and A. Imamoglu, Nonlinear optics and quantum entanglement of ultraslow single photons, Phys. Rev. Lett. **84**, 1419 (2000). 177, 179, 180

[293] M. Dakna, T. Anhut, T. Opatrny, L. Knoll, and D.-G. Welsch, Generating schrödinger-cat-like states by means of conditional measurements on a beam splitter, Phys. Rev. A **55**, 3184 (1997). 177, 179

[294] Q. A. Turchette, C. J. Hood, W. Lange, H. Mabuchi, and H. J. Kimble, Measurement of conditional phase shifts for quantum logic, Phys. Rev. Lett. **75**, 4710 (1995). 177

[295] S. Rebić et al., Polarization phase gate with a tripod atomic system, Phys. Rev. A **70**, 032317 (2004). 177, 179, 180

[296] K. Nemoto and W. J. Munro, Nearly deterministic linear optical controlled-not gate, Phys. Rev. Lett. **93**, 250502 (2004). 177, 188

[297] W. E. Williams, M. Soileau, and E. W. V. Stryland, Optical switching and n2 measurements in cs2, Opt. Commun. **50**, 256 (1984). 177

[298] W. J. Munro, K. Nemoto, and T. P. Spiller, Weak nonlinearities: a new route to optical quantum computation, New J. of Phys. **7**, 137 (2005). 178, 188, 189

[299] H. J. Briegel and R. Raussendorf, Persistent entanglement in arrays of interacting particles, Phys. Rev. Lett. **86**, 910 (2001). 178, 179

[300] R. Raussendorf and H. J. Briegel, A one-way quantum computer., Phys. Rev. Lett. **86**, 5188 (2001). 178

[301] Q. Lin and B. He, Efficient generation of universal two-dimensional cluster states with hybrid systems, Phys. Rev. A **82**, 022331 (2010). 179

[302] S. G. R. Louis, K. Nemoto, W. J. Munro, and T. P. Spiller, Weak nonlinearities and cluster states, Phys. Rev. A **75**, 042323 (2007). 179

[303] E. Schrödinger, Die gegenwärtige situation in der quantenmechanik, Naturwissenschaften **23**, 812 (1935). 179

[304] M. S. Kim, E. Park, P. L. Knight, and H. Jeong, Nonclassicality of a photon-subtracted gaussian field, Phys. Rev. A **71**, 043805 (2005). 179

[305] M. J. F. Digonnet, R. W. Sadowski, H. J. Shaw, and R. H. Pantell, Resonantly enhanced nonlinearity in doped fibers for low-power all-optical switching: A review, Opt. Fib. Tech. **3**, 44 (1997). 179

[306] S. Xiao-Qiang, C. Li, and Z. Shou, Three-qubit fredkin gate based on cavity quantum electrodynamics, Chinese Physics B **18**, 3258 (2009). 179

[307] C.-Y. Chen, M. Feng, and K.-L. Gao, Toffoli gate originating from a single resonant interaction with cavity qed, Phys. Rev. A **73**, 064304 (2006). 179

[308] C. Ottaviani, S. R. S, D. Vitali, and P. Tombesi, Quantum phase-gate operation based on nonlinear optics: Full quantum analysis, Phys. Rev. A **73**, 010301 (2006). 179, 180

[309] Z. B. Wang, K. P. Marzlin, and B. C. Sanders, Large cross-phase modulation between slow copropagating weak pulses in rb, Phys. Rev. Lett. **97** (2006). 179, 180

[310] L. Deng and M. G. Payne, Gain-assisted large and rapidly responding kerr effect using a room-temperature active raman gain medium, Phys. Rev. Lett. **98** (2007). 179, 180

[311] N. Matsuda, R. Shimizu, Y. Mitsumori, H. Kosaka, and K. Edamatsu, Observation of optical-fibre kerr nonlinearity at the single-photon level, Nature Photonics **3**, 95 (2010). 179

[312] I. Fushman et al., Controlled phase shifts with a single quantum dot, Science **320**, 769 (2008). 179

[313] H.-Y. Lo et al., Electromagnetically-induced-transparency-based cross-phase-modulation at attojoule levels, Phys. Rev. Lett. **83**, 041804 (2011). 179, 180

[314] B.-W. Shiau, M.-C. Wu, C.-C. Lin, and Y.-C. Chen, Low-light-level cross-phase modulation with double slow light pulses, Phys. Rev. Lett. **106**, 193006 (2011). 179, 180, 189

[315] L. Mollenauer, R. H. Stolen, and J. P. Gordon, Experimental observation of picosecond pulse narrowing and solitons in optical fibers, Phys. Rev. Lett. **45**, 1095 (1980). 179

[316] M. Nakazawa, Y. Kimura, and K. Suzuki, Efficient er-doped optical fiber amplifier pumped by a 1.48 mic.m ingaasp laser diode., App. Phys. Lett. **54**, 295 (1989). 179

[317] M. Asobe, T. Kanamori, and K. Kubodera, Ultrafast all-optical switching using highly nonlinear chalcogenide glass fiber, IEEE Photon. Technol. Lett. **4**, 362 (1992). 179

[318] J. K. Ranka, R. S. Windeler, and A. J. Stentz, Visible continuum generation in air – silica microstructure optical fibers with anomalous dispersion at 800 nm., Opt. Lett. **25**, 25 (2000). 179

[319] J. H. Shapiro, Single-photon kerr nonlinearity do not help quantum computation, Phys. Rev. A **73**, 062305 (2006). 180

[320] J. H. Shapiro, Continuous-timecross-phasemodulation and quantum computation, New J. of Phys. **9**, 16 (2007). 180

[321] H. Schmidt and A. Imamoglu, Giant kerr nonlinearities obtained by electromagnetically induced transparency, Opt. Lett. **21**, 1936 (1996). 180

[322] D. Petrosyan and G. Kurizki, Symmetric photon-photon coupling by atoms with zeeman-split sublevels, Phys. Rev. A **65**, 033833 (2002). 180

[323] J. Gea-Banacloche, Impossibility of large phase shifts via the giant kerr effect with single-photon wave packets, Phys. Rev. A **81**, 043823 (2010). 180, 189

[324] S. Zhang, S. Zhou, M. M. T. Loy, G. K. L. Wong, and S. Du, Optical storage with electromagnetically induced transparency in a dense cold atomic ensemble, Opt. Lett. **36**, 4530 (2011). 181

[325] Y.-F. Chen, C.-Y. Wang, S.-H. Wang, and I. A. Yu, Low-light-level cross-phase-modulation based on stored light pulses low-light-level cross-phase-modulation based on stored light pulses, Phys. Rev. Lett. **96**, 043603 (2006). 181, 182

[326] C.-Y. Wang et al., Low-light-level all-optical switching, Opt. Lett. **31**, 2350 (2006). 181

[327] W.-H. Lin, W.-T. Liao, C.-Y. Wang, Y.-F. Lee, and I. A. Yu, Low-light-level all-optical switching based on stored light pulses, Phys. Rev. A **78**, 033807 (2008). 181

[328] L. G. Joneckis and J. H. Shapiro, Quantum propagation in a kerr medium: lossless, dispersionless fiber, J. Opt. Soc. Am. B **10**, 1102 (1993). 188

[329] P.-M. L. Yan Xia, Jie Song and H.-S. Song, Efficient implementation of the two-qubit controlled phase gate with cross-kerr nonlinearity, J. Phys. B **44**, 079804 (2011). 188

[330] B. C. Buchler, M. Hosseini, G. Hétet, B. M. Sparkes, and P. K. Lam, Precision spectral manipulation of optical pulses using a coherent photon echo memory, Opt. Lett. **35**, 1091 (2010). 196

[331] B. Kraus et al., Quantum memory for nonstationary light fields based on controlled reversible inhomogeneous broadening, Phys. Rev. A **73**, 020302(R) (2006). 201